11-9-2021

Ionospheric F-Layer Dipole Flute Instability Effects on Electromagnetic Scattering in a Magnetohydrodynamic Plasma

Andrew J. Knisely

IONOSPHERIC F-LAYER DIPOLE FLUTE INSTABILITY EFFECTS ON ELECTROMAGNETIC SCATTERING IN A MAGNETOHYDRODYNAMIC PLASMA

DISSERTATION

Andrew J. Knisely, Civ

AFIT-ENG-DS-21-M-009

DEPARTMENT OF THE AIR FORCE
AIRUNIVERSITY

AIR FORCE INSTITUTE OF TECHNOLOGY

Wright-Patterson Air Force Base, Ohio

AFIT-ENG-DS-21-M-009

IONOSPHERIC F-LAYER DIPOLE FLUTE INSTABILITY EFFECTS ON ELECTROMAGNETIC SCATTERING IN A MAGNETOHYDRODYNAMIC PLASMA

DISSERTATION

Presented to the Faculty

Department of Electrical and Computer Engineering

Graduate School of Engineering and Management

Air Force Institute of Technology

Air University

Air Education and Training Command

In Partial Fulfillment of the Requirements for the

Degree of Doctor of Philosophy

Andrew J. Knisely, BS, MS

September 2021

AFIT-ENG-DS-21-M-009

IONOSPHERIC F-LAYER DIPOLE FLUTE INSTABILITY EFFECTS ON ELECTROMAGNETIC SCATTERING IN A MAGNETOHYDRODYNAMIC PLASMA

Andrew J. Knisely, BS, MS

Committee Membership:

Dr. Andrew J. Terzuoli
Chair

Dr. Larry W. Burggraf
Member

Maj Daniel J. Emmons, PhD
Member

ADEDEJI B. BADIRU, PhD
Dean, Graduate School of Engineering and Management

AFIT-ENG-DS-21-M-009

Abstract

The ionosphere has significant impact on radio frequency (RF) applications such as satellites, over-the-horizon radar, and commercial communication systems. The dynamic processes effecting the behavior of the ionic content leads to a variety of instabilities that adversely affect the quality of RF signals. In the F-layer ionosphere, flute instability persists, appearing as two radial regions of high and low density perturbations elongated along the earth's geomagnetic field lines. The sizes of flute structures are comparable to the wavelengths in the high frequency spectrum. The objective is to characterize the high frequency scattering of an incident field by developing a 3D propagation model that incorporates a phase cube coupled ray tracer approach to discretize the phase effects of a two-fluid magnetohydrodynamic (MHD) dipole flute density perturbation model. A single fluid MHD model simulates a variety of plasma flow and shear effects to alter the ideal flute's physical features, creating a subset of unique flutes. A unique phase screen approach is presented to generate stochastic flute density maps. The phase power spectrums reveal a power law relationship similar to Kolmogorov turbulence. The electric field propagation results demonstrate that specific arrangements of the flutes can cause weak to strong scattering conditions. Additional frequency domain analysis of the received field scattering functions demonstrates the existence of parabolic scintillation arcs, significant broadening in the doppler power spectrum, and narrow coherence bandwidths indicating frequency selectivity in the propagation channels that adversely impact the quality of high frequency electric fields.

Acknowledgments

First and foremost, I would like to thank Dr. Andrew Terzuoli for making this possible from the beginning. The guidance, wisdom, and perspective on this process and on life in general have been invaluable to me, and I am forever grateful. I would like to especially thank Dr. Terzuoli's wife, Rhonda, for taking the time to meticulously review this dissertation page by page and providing the edits that were crucial to the organization and interpretation of this document. Thank you to Maj. Daniel Emmons for providing his immense knowledge of ionospheric studies and for establishing correspondence with the AFRL/RYMF PPSL team that catalyzed this research. Thank you to Dr. Larry Burggraf for your time reviewing and providing guidance on this dissertation and other technical papers I have authored. I would like to thank Paul Gilgallon and the AFRL Rome team for providing initial sponsorship in this research that led to the development of critical propagation algorithms required for the multiple phase screen models. The work completed on the V/W signal effects from HANEs generated valuable technical publications in the IEEE community. Thank you to the PPSL team members; Dr. Vladimir Sotnikov, Matthew Rustad, and Nathan Zechar for our routine conversations and for providing direction. Some of the research assistants that helped me in the beginning; Shawn McTaggart, Alena Brand, Ryan Kinkade, Eric Harris, and Cameron Brown, thank you for your time and contributions. Finally, I would like to thank my family for their support and encouragements as I have continued to accomplish my goals in life. It has made a difference. Thank you!

Andrew J. Knisely

Table of Contents

Page

List of Figures

Page

List of Tables

Page

IONOSPHERIC F-LAYER DIPOLE FLUTE INSTABILITY EFFECTS ON ELECTROMAGNETIC SCATTERING IN A MAGNETOHYDRODYNAMIC PLASMA

I. Introduction

1.1 Problem Statement

The F-layer ionosphere can significantly influence the propagation properties of signals that are critical to the commercial and military communication and surveillance infrastructure [1]. The nonlinear stage of interchange instability in the F-layer ionosphere leads to the generation of coherent density vortices that coexist amongst short scale density irregularities [2]. Driven by Rayleigh Taylor instability, these density vortices take the form of flute-like structures as they oscillate along the earth's magnetic field lines [2]. The small scale sizes of flute structures are comparable to the wavelengths of high frequency (HF) electromagnetic waves propagating through the medium and results in significant scattering. This effect impacts the reliability of radio frequency systems that utilize the F-layer propagation channel. Current computational models that characterize ionospheric propagation through plasma structures do not account for these specific flute-like irregularities but rather generalize the propagation medium to a Kolmogorov turbulence power spectrum. Additionally, little is known regarding the frequency selective nature of flute turbulent propagation channels including scintillation, amplitude fading, refractivity, and their unique power spectrums. Characterizing these metrics requires investigating a variety of flute structures over a plethora of frequencies in the

high frequency regime and using a variety flute density perturbation arrangements within the propagation channel.

1.2 Scope and Research Goals

Early research examined anomalous transport in magnetic confinement devices, in which flute instability is caused from the magnetic field curvature confining the plasma. This motivated the need for analytic approaches to deriving vortex solutions from nonlinear flute mode equations [3]. It was determined that the dipole flute structure was the most common vortex solution obtained from the 2D equations along with an infinite possible family of solutions [3]. As computational capabilities have evolved, recent research has successfully demonstrated the ability to numerically model the flute instability by using a two-fluid magnetohydrodynamic approximation of the plasma's electron and ion species to derive nonlinear differential equations that describe the evolution of the flute perturbation density gradients during the interchange instability process as shown in [1,3,4] and illustrated in Figure 1. These numerical results show that over the period of the interchange, random initial perturbations grow in vorticity and become streamer-like during the linear phase before the perturbation amplitude exceeds the threshold for modulation instability and transition to zonal flow perturbations in which the nonlinear vortex structures form [2]. The notion of modulational instability and electromagnetic wave scattering cross-section of plasma flute modes was examined in [4] for finite Larmor radius, low beta plasmas. Results demonstrated that the flute's scattering cross section increases as the flute radius increases and the incident wave frequency decreases. Additionally, the maximum growth rate of the modulational instability is

achieved where zonal flows are being generated and can lead to the formation of large scale structures in low beta plasma [4].

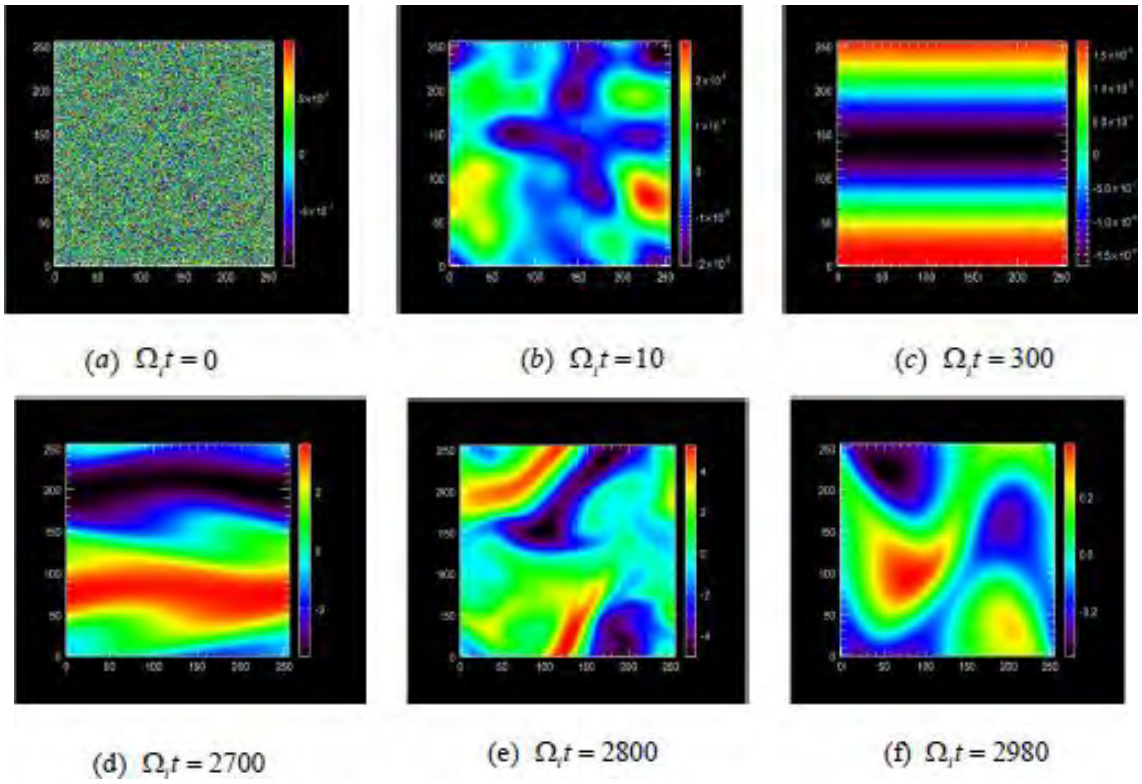

Figure 1. [2] Linear Stage of Interchange (top row) and Nonlinear Stage of Interchange (bottom row) evolving in time.

The research conducted in [1] continued to apply the finite Larmor approximation and considered a weakly inhomogeneous high beta plasma derivation of flute modes in which electromagnetic scattering was evaluated in a particle-in-cell (PIC) model. The PIC model results demonstrated that the maximum of the differential scattering cross section corresponds to small scattering angles, and larger variations in the density perturbation amplitudes will produce a larger scattering cross section.

This current research effort began in 2016 with sponsorship provided by Paul Gilgallon from the The Air Force Research Lab (AFRL) Rome, New York branch. The

objective was to develop propagation algorithms that characterize the V/W band signal scintillation effects caused by natural or artificial disturbances in the ionosphere. These propagation models intended to aide the design and development of environmentally assured satellite communication systems by providing a macroscopic characterization of the Kolmogorov plasma turbulence influenced by these disturbances and determine their broad impact on the signal characteristics. Upon completion of the propagation algorithm development for the Rome effort, the motivation transitioned towards the studies of the AFRL/RYMF branch at Wright-Patterson Air Force Base (WPAFB) to further the application of the finite Larmor flute structure for a finite beta plasma configuration in terms of its inclusion in a large scale macroscopic propagation model that characterizes the flute structures coexistence with ambient irregularities defined by a Kolmogorov spectrum. Application of the single vortex solution determined by perturbation analysis of two-fluid magnetohydrodynamic nonlinear equations is desired. The vortex solution is straightforward to characterize and practical for applications involving extrinsic effects. Multiple phase screen (MPS) models have historically been applied as a computationally efficient method to determine the forward scatter effects over long propagation ranges in lieu of full wave propagation models that require extensive sampling on a finite domain. However, many MPS models apply a generalized power spectrum such as Kolmogorov to derive phase effects caused by the ionospheric irregularities that cascade from several kilometers down to a few meters in scale size. Incorporation of flute structures in an MPS model will allow for long range propagation analysis of the scattering phenomenology for specified flute map configurations that could exist in nature. Additionally, the MPS model can be adapted to examine temporal characteristics of pulse modulated realizations

along the electric field. The temporal analysis will characterize the bandwidth coherence and time delay effects. The scattering function calculations acquired from the mutual coherence of the electric field realizations will provide a frequency domain analysis of the scattered energy distribution profiles in relation to the pulse time delay and doppler frequency along the receiver plane. Additional secondary calculations include the time/doppler delay, jitter, spread, coherence bandwidth, and spatial coherence. These results intend to establish a baseline expectation that can be applied to identify the potential presence of flute structures amongst other irregularities during the process of data collections and measurements at real-world ionosphere observatory sites such as Alaska's High-frequency Active Auroral Research Program (HAARP) or the Arecibo Observatory Radio Telescope in Puerto Rico. The Air Force Research Lab Plasma Physics Sensory Lab (PPSL) intends to utilize the propagation algorithms and flute density perturbation models developed in this dissertation as a supplement to existing modeling and simulation techniques with intent to develop environmentally assured HF systems required for optimal performance in prominent flute propagation channels.

1.3 Limitations, Challenges, and Assumptions

A key challenge is to develop an MPS model to characterize the forward scatter caused specifically by the flute structures. This requires numerical derivation of the flute structure phase power spectrum to enable the formulation of phase screens that are unique to the flute density perturbations. The ideal flute structure applied in the previous research efforts [1,4] is not likely to exist in reality. Consequently, an alternate subset of flute perturbation solutions should be considered to observe differences in their

respective scattering characteristics. Generating the unique solutions will come from modifying the initial ideal flute perturbation solution in a quasi-neutral plasma using a single fluid magnetohydrodynamic model to simulate velocity shear and Rayleigh Taylor effects that morph the flute structure's appearance within an unstable plasma. As stated previously, an infinite family of dipole flute solutions exist, therefore, a threshold must be applied to limit the test matrix to a subset of flutes for the MPS model analysis. A classification process must also be established based on the physical features of the flute structure such as the shape, uniformity, and symmetry. The density maps of the flute structures will be characterized on quantities, arrangements, and their total phase power spectrum.

The MPS model will incorporate refractivity effects caused by rapidly changing density gradients of the flute as the field propagates through the structure. This metric is not a common calculation for typical MPS models. The propagation angles required for vectorizing the electric field prior to phase cube passage will be determined by ray tracing through the layers of density maps. A three dimensional propagation model has significant computational limitations in the number of samples applied to the sequence of phase cubes. This in turn will affect the fidelity of the flute density gradient variations along the phase screens and the features of the scattered electric field. A key assumption coinciding with the density gradients are the size and the strength of the density perturbation. Literary reviews and consultation with researchers in this area of study have limited the flute structure dimension to sizes that are comparable to electric field wavelengths in the high frequency spectrum. The intensity of the perturbations shall be no more than 25% of the maximum ambient electron density distribution. In addition to

the primary forward scatter model, the backscatter is observed using full wave techniques. The significant limitation as stated previously is the sampling requirements to achieve a stable numerical scheme and to acquire meaningful solutions of the electric field's propagation through the flute density map. As a result, the backscatter electric field propagation distance will be limited to the dimensions of the flute structure density map.

The final limitation is the scarcity of real-world data collections that specifically address the existence of flute structures. Currently, available data collections in general do not decipher the instability mechanisms present when the electron density samples are measured. Attempting to examine incoherent scatter radar (ISR) maps could take considerable amounts of time to distinguish features that are characteristic of flute scattering, especially without initially determining the potential features that could define their existence or prevalence. The phase screen method has historically been an excepted method to provide realistic simulations of ionospheric scattering as determined in comparisons to observatory data collections. Due to the limitations of real world data collections, alternative theoretical methods comparable to the MPS solutions will be the primary approach to validate the calculations in each numerical model. The results analyzed in Chapter 5 will have more qualitative value than quantitative until relationships can be established with respect to real data collections.

1.4 Resource Requirements

Numerical analysis is foundation to many of the techniques addressed in this dissertation. MATLAB is the primary software application to develop and apply the numerical algorithms for the calculations described in the previous sections. The Air Force

Research Lab Sensors Directorate, RYMF branch and ITARnet facility at the Air Force Institute of Technology (AFIT) has additional computational resources available to execute multiple simulations simultaneously if required.

1.5 Organization

The remainder of the document is organized in six chapters that cover the development, application, and analysis of the numerical propagation algorithms. Chapter 2 provides the background and theory necessary to derive the ideal flute structures and their alternative solutions. The propagation algorithms for the MPS model and full wave model are derived in addition to the ray tracing algorithm. An explanation of the calculations for pulse coherence and the scattering functions spectrum are also provided. Chapter 3 describes the process of developing phase screens and phase cubes necessary to approximate the propagation channel and characterize the flute's total phase power spectrum. Chapter 4 focuses on the development of the propagation models used in this dissertation by incorporating the phase cubes and ray tracing techniques with the slow varying envelope wave equations. Initial tests include the polarization features of the scattered field along the flute structure and the backscatter characteristics obtained from the full wave technique. Chapter 5 provides an analysis of the flute structure scattering characteristics such as scintillation, time delay, channel coherence bandwidth, and doppler characteristics utilizing the pulse coherence model and the 3D phase cube - ray trace algorithms. Chapter 6 provides a conclusion, remarks, and suggestions for future work.

II. Background and Theory

This chapter provides the theory and principles that are applied to the computational models and analysis referenced throughout this document. The breakdown description of the ionosphere is introduced to describe the general characteristics and phenomenon that contribute to the formation of plasma irregularity structures. Emphasis is placed on the F-layer portion of the ionosphere where the flute instability resides. The computational aspects of modeling the ionosphere's impact on radio frequency (RF) propagation are examined. These concepts include modeling the ionosphere's electron density fluctuation power spectrum, multiple phase screen theory, Maxwell's equations, and descriptions of measurable radio frequency signal characteristics such as scintillation and the doppler-delay power spectrum of the scattered electric field.

The key mechanisms of the flute instability are introduced through process descriptions of gradient drifts and Rayleigh Taylor instability. A mathematical description of plasma behavior is introduced in the single fluid magnetohydrodynamic (MHD) plasma approximation in which momentum and continuity equations describe plasma motion. This framework establishes an application for disturbances acting on the initial ideal dipole flute structure leading to imperfections and irregularity. A two-fluid MHD description of the flute structure behavior is applied to yield nonlinear equations that represent the electrostatic potential and density perturbations of the ideal dipole flute solution. Finally, a variety of unique dipole flute structure solutions are generated from the single fluid MHD model, implemented in density perturbation maps, and applied in the phase screen techniques described in the following chapter.

2.1 Ionosphere

The ionosphere is an atmospheric layer between the altitudes of 60 kilometers and 2000 kilometers that contains free ions and electrons [5]. The terrestrial ionosphere at all latitudes has the tendency to separate into stratified layers: *D*, *E*, and *F* (see Figure 2). The electron content structure of the ionosphere during day time hours can be described as steadily increasing from 100 kilometers to 300 kilometers (*E* and *F* layers), whereas the content begins to decline and decrease at altitudes greater than 300 kilometers [5]. During night hours, the electron content in the *E* layer (100-150 kilometers) decays [5].

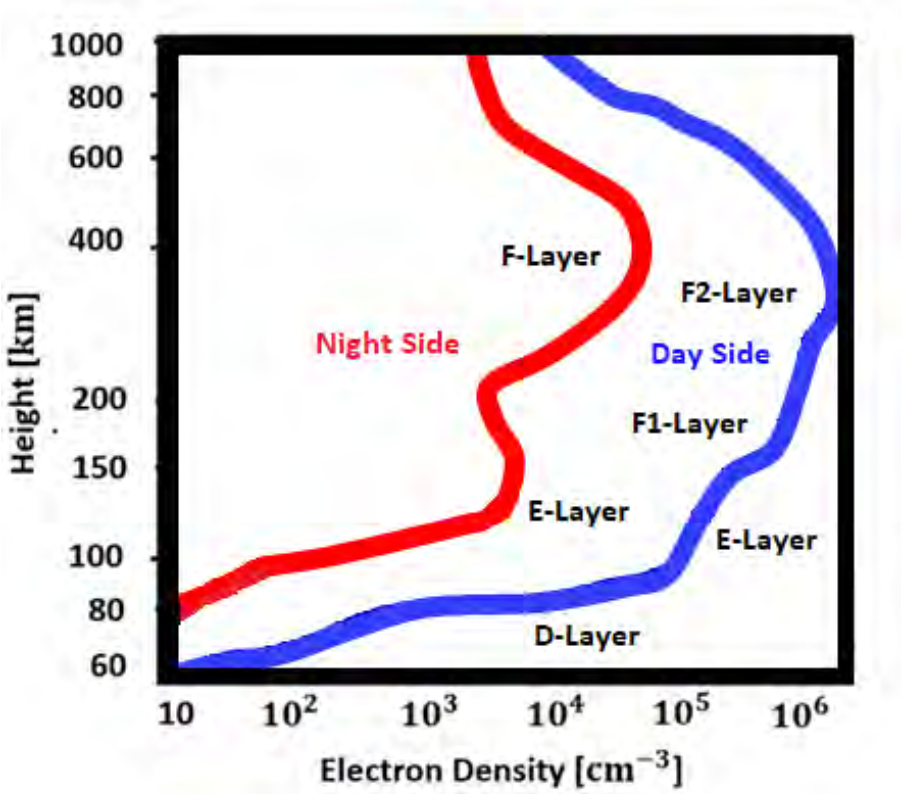

Figure 2. Typical Electron Density Distribution of D, E, and F Layers

The main source of plasma for the ionosphere is photoionization of neutral molecules via solar EUV and soft X-ray radiation, in which, the ions produced undergo

chemical reactions with the neutrals, recombine with the electrons, and diffuse to either higher or lower altitudes [6]. A disturbance to the ionosphere can cause a change in the distribution of the electron content. A common natural occurrence that can contribute to this alteration are geomagnetic storms. Geomagnetic storms result from a compression of the magnetosphere due to the arrival of solar wind discontinuity causing the electric fields, currents, and particle precipitation to increase as a large amount of energy is deposited into the ionosphere [6]. At mid-latitudes, the wind speeds increase and drive the F region plasma toward higher altitudes which can result in ionization enhancements from which the enhanced neutral winds and composition variations penetrate toward the equatorial region [6]. The high latitude ionosphere (aurora and polar regions) is critical to the solar-terrestrial energy transfer process in which it controls the conductivity at the base of far reaching magnetic field lines and provides a plasma source for the magnetosphere [7]. Experimental observations have revealed that from the auroral zone into the polar cap, the medium contains structures with scale sizes ranging from hundreds of kilometers down to centimeters as a result of the high latitude ionospheric plasma instabilities caused by several sources of free energy such as density gradients, velocity shears, electric fields, convective currents, and neutral winds [7]. Conditions in the high-latitude ionosphere are complicated by the diminished role of direct solar radiation in electron density production, and the enhanced role of energetic particle precipitation [7]. The plasma convection from the magnetosphere also effects the high latitude electron density distribution which include the nighttime F-layer trough, large scale patch transport, and thin high density blobs in the auroral region [8].

2.2. Radio Frequency Observations of Irregularity Structures

Observations of radio wave reflections from the ionosphere has revealed that the ionosphere's refractive index depends on frequency and electron density. The critical frequency of the ionosphere is the maximum frequency reflected at vertical incidence as determined by the maximum electron density in the medium [8]. Below this critical frequency, all the other frequencies are reflected from the bottom side ionosphere regardless of the angle of incidence whereas above the critical frequency, the radio waves may refract at normal incidence, escape without reflection, or reflect for sufficiently oblique angles [8]. Effective scatter from field aligned irregularities occurs only at or near normal incidence to the magnetic field lines, thus implying that HF waves must first be directed at or refracted to normal incidence before they can be effectively scattered by field aligned irregularities [8]. These characteristics will be addressed in Chapter 4, when examining the ray trace interaction with a flute perturbation.

Transmissions through the ionosphere under severe disturbance conditions can lead to significant disruptions in the propagating signal. The local electric field governs the movement of the plasma as the particles also act as sources contributing to the electric field [5]. A group of electrons in the plasma will move in response to the wave field, altering the local concentration of the electric charge, thereby making their own contribution to the electric field [5]. Vertical sounding experiments in which radar echoes from a frequency sweep of transmitted pulses have been analyzed to determine the spread of the received pulses caused by the ionosphere [9]. Incoherent Scatter Radars (ISRs) are used to characterize the ionospheric plasma fluctuations that cause backscatter of energy. Radio satellites have also been used as sources to study scintillations on a global scale

[9]. There is a large body of evidence, based upon satellite scintillation measurements, satellite in situ electron density measurements, and radar backscatter measurements, that ionospheric F region electron density irregularities are well described by a power law wavenumber spectrum [8]. Figure 3 shows a composite spectrum that summarizes the intensity of ionospheric irregularities as a function of wavenumber over a wide spatial scale.

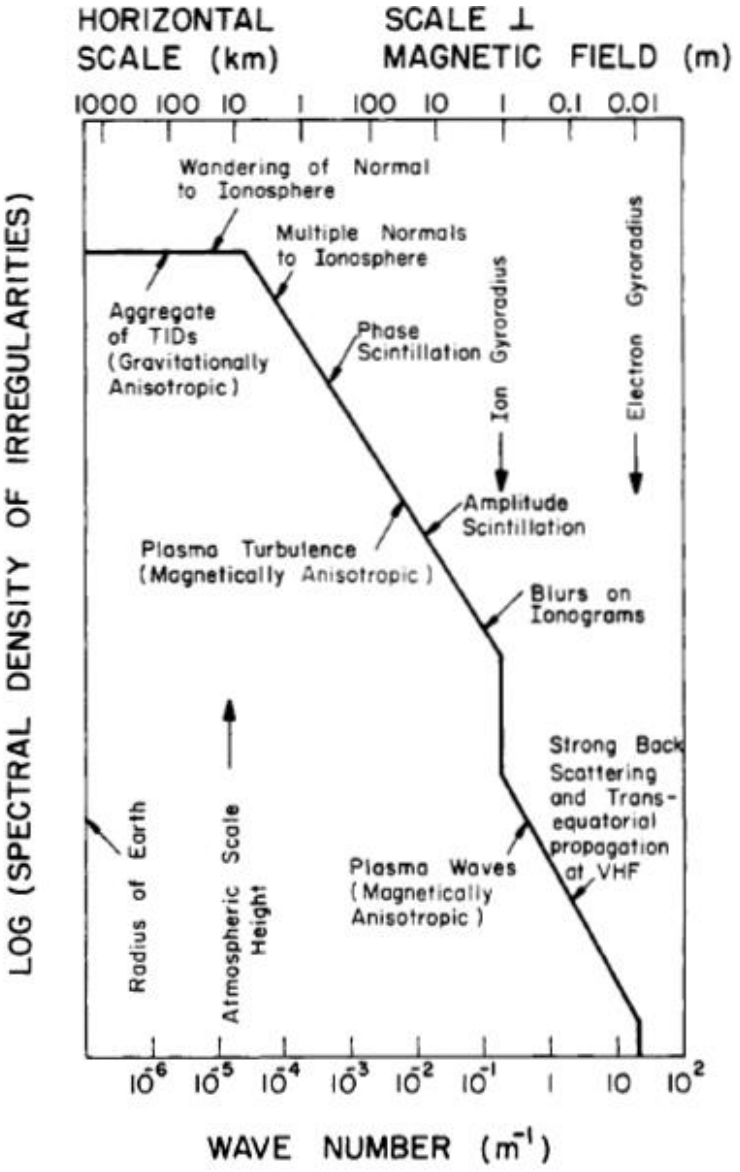

Figure 3. [9] Composite Spectrum of Ionospheric Irregularities over a Spatial Wavenumber Scale

In contrast to the large scale irregularities mostly contributing to phase fluctuations, small scale irregularities (100 meters to kilometers) mainly affect the amplitude of radio signals [10]. The existence of small scale turbulence has been deduced from the observation of scintillations in the transmission of HF signals [11]. Under conditions of small phase spectral index, small-scale irregularities dominate and scatter the wave through large angles which consequently induce large delay values.

Several mechanisms have been proposed to generate the small scale plasma turbulence in the high latitude F-region. Large scale irregularities are believed to be created by particle precipitations, turbulent mixing, or plasma detached from the denser low latitude plasma regions by a rapidly changing convection pattern [11]. These blobs are a source of density gradients transverse to the earth's magnetic field in which the smaller scale irregularities develop through a nonlinear cascading process towards smaller wavelengths [11]. These observations have led to the hypothesis that interchange processes such as the gradient drift and current convective instabilities play a major role in structuring the high latitude plasma [11]. It is important to distinguish between different types of turbulence events and to establish the spectral index of the density fluctuations in addition to the relation between the occurrence of the turbulence and the electromagnetic parameters of the irregularities within the medium.

2.3. Multiple Phase Screen Theory

A statistical characterization of the irregularities can be used to model the ionospheric scintillation phenomenon. A key concept to this methodology is the description of the diffraction process. This process depends on the random deviations of

the phase front curvature, which in turn is determined by the size and strength distributions of the irregularities [9]. It is reasoned that the contribution to the phase fluctuation comes from many irregularities along the propagation line of sight [12]. The theory of the random slab of irregularity fluctuations is assumed to be a Gaussian random field with zero mean. As the wave propagates through a slab of irregularities, only the phase is affected by the random fluctuations in the refractive index [9]. After the wave has emerged from the random slab, its phase front is randomly modulated and the distorted wave front will set up an interference pattern resulting in amplitude fluctuations [9]. These slab of irregularities can be compressed down to a thin screen of samples that contribute to changing the phase of the incident wave [12]. Figure 4. illustrates this thin screen sample process.

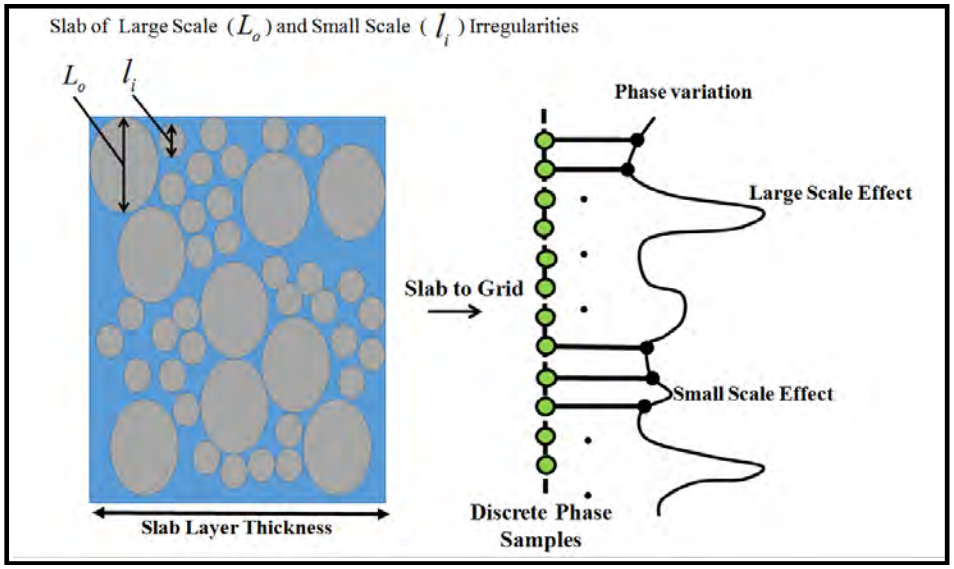

Figure 4. Random Slab Layer of Irregularities Compressed to a Grid of Phase Varying Samples

The screen model is widely used since it includes most of the physics of scattering in an extended inhomogeneous medium and is also mathematically tractable [12]. To get interference, the screen must be illuminated by a radiation field of high spatial coherence,

i.e., radiation from a point like source [12]. If the phase deviations are small, the wavefront will remain relatively coherent across each irregularity which acts to focus or defocus the rays (as illustrated in Figure 5) [9]. When the irregularities are strong, the phase deviations may become so intense that the phase fronts are no longer coherent as the irregularities lose their ability to focus and defocus the rays [9].

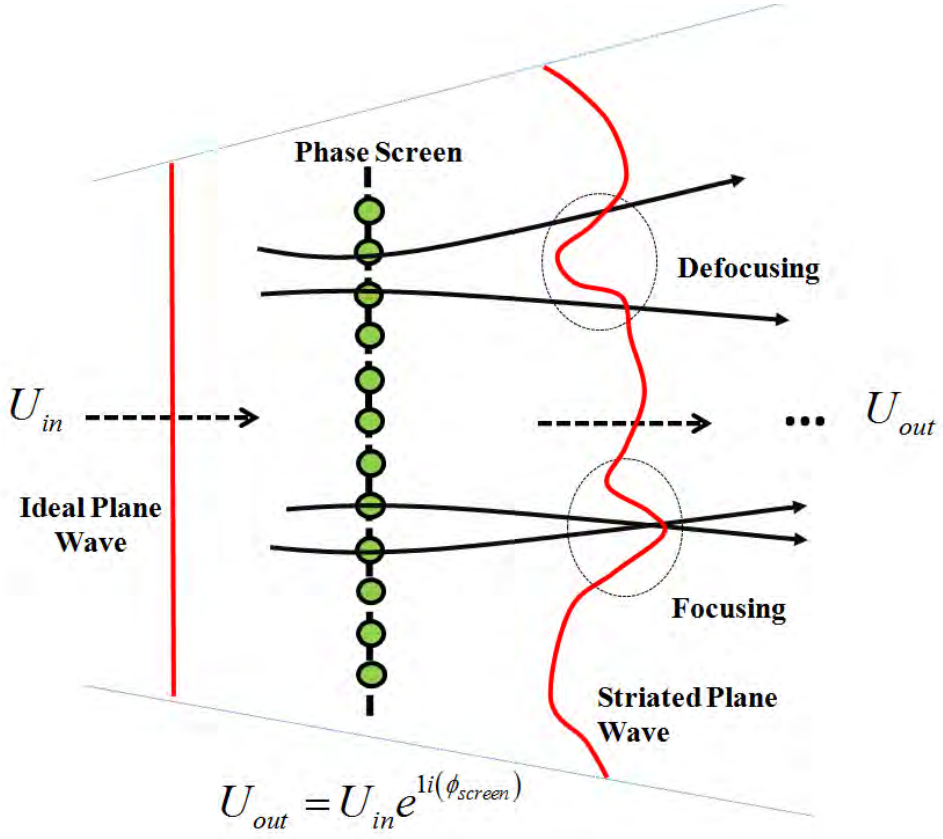

Figure 5. Focusing and Defocusing of Rays resulting from the Exponential Phasor Modulation of the Incident Field

A series of these refractive screens applied to modulate the incident field is defined as a multiple phase screen (MPS) model. A critical concept to MPS theory is the phase power spectrum that describes the nature of the phase fluctuations derived from in-situ electron density measurements [9]. In the frequency domain, random realizations of this power spectrum are averaged to formulate idealistic phase shifts that occur along the

propagation path. The following chapter provides clarity to this concept, describing the mathematical process of deriving phase screens in relation to the power spectrum. The following section focuses on important concepts of wave propagation required to derive the multiple phase screen propagation algorithm.

2.4. Wave Propagation

In the field of Electromagnetics, the planar wave is commonly used as an initial waveform to observe deviations in magnitude and phase induced by the propagation medium. The planar electromagnetic (EM) wave is simple to characterize and can be modeled analytically by means of phasor algebra in the time harmonic form. The following formulation demonstrates the mathematical representation of the plane wave in rectangular coordinates as denoted by the subscript *R*:

$$\overline{r_R} = x\hat{x} + y\hat{y} + z\hat{z}\,, \tag{2.1}$$

where $\overline{r_R}$ represents the position vector which points outward from an initial coordinate position into a final coordinate position. Note that the over bar notation represents a vector and the under bar represents that it is a complex value.

$$\overline{\underline{\gamma}_R} = \underline{\gamma}_x\hat{x} + \underline{\gamma}_y\hat{y} + \underline{\gamma}_z\hat{z}\,, \tag{2.2}$$

$\overline{\underline{\gamma}_R}$ represents the complex propagation vector where:

$$\underline{\gamma}_x\left(\bar{r}\right) = \alpha_x\left(\bar{r}\right) + i\beta_x\left(\bar{r}\right) \qquad \underline{\gamma}_y\left(\bar{r}\right) = \alpha_y\left(\bar{r}\right) + i\beta_y\left(\bar{r}\right) \qquad \underline{\gamma}_z\left(\bar{r}\right) = \alpha_z\left(\bar{r}\right) + i\beta_z\left(\bar{r}\right). \tag{2.3}$$

The α_R variable represents the attenuation parameter and β_R variable represents the propagation parameter. The attenuation parameter is the direction of the maximum rate of

amplitude change. Attenuation acting nonparallel to the propagation path can produce non-uniformity in the plane wavefronts. The uniform plane waves exist when attenuation is either parallel to the propagation vector or not present at all. Attenuation will not be applied in the simulations presented in this dissertation. Therefore, each successive wavefront has equal amplitude and phase. The propagation parameter is the direction of maximum rate of phase change. The loci of equi-angles form planes as shown in Figure 6. The plane waves can be found as the solutions of the Helmholtz wave equation:

$$\left[\nabla^2 + \beta^2 n^2\right]\underline{\bar{E}}\left(\bar{r}\right) = 0 \quad . \tag{2.4}$$

where n is the refractive index of the medium. This equation can be characterized as a time-harmonic, homogenous vector equation derived from the homogenous, isotropic, and source free region form of Maxwell's equations.

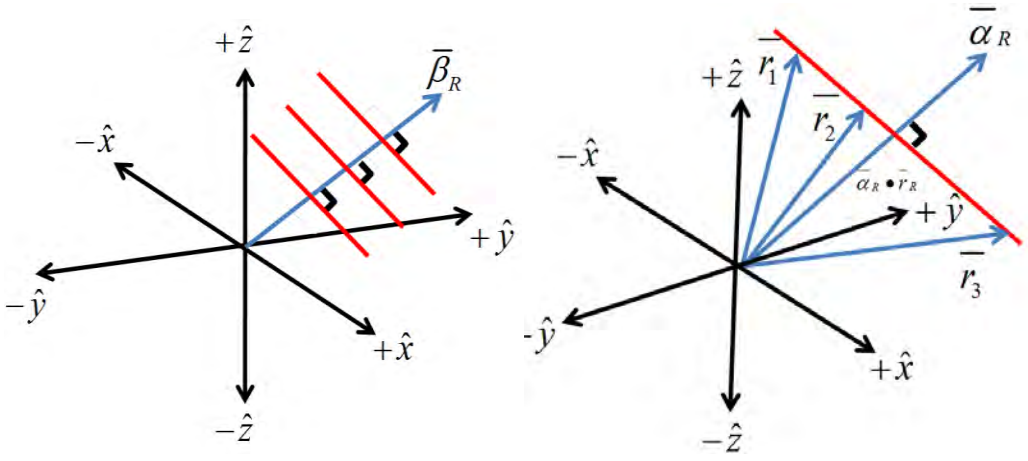

Figure 6. Planar Wavefront Parameters Illustration

Often solutions that cannot be determined analytically are instead approximated numerically on a finite domain. In the case of the Helmholtz equation, difficulty on the finite domain can arise in numerically modeling phase changes over small wavelengths or

long propagation distances. If there are rapid variations in phase during propagation, many samples of the discretized domain must be taken per wavelength, especially to accommodate the subtle refractivity changes within an anisotropic medium. For a high frequency simulation, this can be an expensive computational task as more wavelengths require additional sampling to acquire meaningful solutions. An approximation to the Helmholtz equation is often practiced to avoid this limitation. The method begins by assuming that the derivative with respect to the propagation direction (r) of the amplitude function "U" is a slow varying function (envelope) as long as the transverse length scale is much greater than the wavelength**:**

$$\left|\frac{\partial^2 \underline{\underline{U}}}{\partial r^2}\right| \ll \left|\beta \frac{\partial \underline{\underline{U}}}{\partial r}\right| \ll \left|\beta^2 \underline{\underline{U}}\right| .$$

(2.5)

These conditions are favorable for forward stepping algorithms. As the sampling requirements for the EM wave's phase is minimized, the emphasis becomes the slow varying envelope in the amplitude of the waveform.

$$\underline{\underline{E}} = \underline{U}(z) e^{-\underline{\gamma}_z z},$$

(2.6a)

$$\text{For } \nabla^2 \underline{\underline{E}} = \left[\frac{\partial^2}{\partial x^2} + \frac{\partial^2}{\partial y^2} + \frac{\partial^2}{\partial z^2}\right]\left[\underline{U}(z) e^{-\underline{\gamma}_z z}\right],$$

(2.6b)

$$\text{let } \nabla_\perp{}^2 = \frac{\partial^2}{\partial x^2} + \frac{\partial^2}{\partial y^2} \text{ and } \frac{\partial^2}{\partial z^2}\left[\underline{U}(z) e^{-\underline{\gamma}_z z}\right] = \left[\frac{\partial^2}{\partial z^2}\underline{U}(z) - 2\gamma_z \frac{\partial}{\partial z}\underline{U}(z) + \gamma_z{}^2 \underline{U}(z)\right] e^{-\underline{\gamma}_z z},$$

(2.6c)

Substitution into Scalar Helmholtz equation and assuming a uniform plane wave condition; α=0, yields:

$$\left(\nabla_{\perp}^{2}+\frac{\partial^{2}}{\partial z^{2}}-2i\beta\frac{\partial}{\partial z}\right)\underline{U}(z)+\beta^{2}\left(n^{2}-1\right)=0 \quad . \tag{2.7}$$

The paraxial assumption is that the wavefront deviation relative to the direction of propagation is very small. The angle is in fact small enough to assume that the wave is parallel to its optical axis, hence the term paraxial. Therefore, the second order derivative in the propagation direction can be eliminated in addition to assuming free space medium ($n = 0$):

$$\left(\nabla_{\perp}^{2}-2i\beta\frac{\partial}{\partial z}\right)\underline{U}(z)=0 \quad . \tag{2.8}$$

In this instance, the direction of propagation is z and wavefront electric field vector is along the x -y plane. The process is replicated in the other propagation directions as the 2D field vector planes are perpendicular to the propagation vector. The final form of the paraxial approximation of the Helmholtz equation is presented:

$$\left(\left[\frac{\partial^{2}}{\partial x^{2}}+\frac{\partial^{2}}{\partial y^{2}}\right]-2\underline{\gamma}\frac{\partial}{\partial z}\right)\bar{\underline{U}}(z)=0 \quad . \tag{2.9}$$

This parabolic wave equation (PWE) can be characterized as a second order, linear, homogenous differential equation.

The numerical technique for solving the parabolic wave equation is the spectral method. From herein, the focus is on the mechanism of the spectral method and phase screen technique. The spectral method involves converting the input function to the

frequency space. Over the unbounded physical space, for any complex exponential, there are infinitely many other complex exponentials that match it on the physical space grid. These are known as "aliases" of spatial frequency (*K*). Consequently, it suffices to measure wave numbers for the grid in an interval of length $2\pi/\Delta x$ over the interval $[-\pi/\Delta x, \pi/\Delta x]$. A fourier series represents a function on a bounded interval as a sum of complex exponentials at discrete wave numbers. The wavenumber *K* is bounded because *x* is a discrete set of samples. *K* is continuous in the fourier space as *x* is unbounded in the physical space.

The theory of fourier series is utilized to develop the notion of spectral differentiation. The fourier series is a sequence of waves where each wave represents a mode. The interpolant is required for spectral differentiation to occur and is provided by the inverse fourier transform. On the domain, $x \in [0, L)$, where *L* is the length of the spatial grid,

$$\phi_L(x) = e^{i(2\pi/L)Kx}, \tag{2.10}$$

represents the global basis trigonometric function. The fourier series is presented in the following:

$$U(x) = \sum_{k=-\infty}^{\infty} a_k \phi_k(x), \tag{2.11a}$$

where *U* has compact support as $U \in C^P$ along the closed interval:

$$K \in [-\pi/\Delta x, \pi/\Delta x]. \tag{2.11b}$$

The trigonometric basis element passes the orthonormal property, which allows for:

$$\langle f,g\rangle = \begin{cases} 0, & m \neq K \\ 1, & m = K \end{cases}$$

(2.11c)

Taking the inner product of the trigonometric basis elements with the fourier series of the input function:

$$\left\langle \phi_m(x), U(x) \right\rangle = \left\langle \phi_m, \sum_{k=-\infty}^{\infty} a_k \phi_k(x) \right\rangle .$$

(2.12a)

Re-arranging the terms and simplifying:

$$= \sum_{k=-\infty}^{\infty} \langle \phi_m, \phi_k \rangle a_k = \sum_{k=-\infty}^{\infty} (\delta_{mk}) a_k ,$$

(2.12b)

for $m = k$ $= a_m$, continuous fourier coefficients.

The continuous fourier transform representation is:

$$a_m = \langle \phi_m, u \rangle = (1/2\pi) \int_0^{2\pi} v(x_j) e^{-im(x_j)} dx ,$$

(2.13)

$m = k$ is where f(x) and g(x) are equal for each j and no aliasing occurs. The discrete representation is:

$$\hat{a}_n = (1/N) \sum_{j=0}^{N+1} \vec{u}(x_j) e^{-2\pi(i)(j)n/N} = fft(U) .$$

(2.14)

The fourier coefficients are now related to the basis functions and the inverse fourier transform is written as:

$$\vec{u}(x_j) = \sum_{n=-N/2+1}^{N/2} \hat{a}_n e^{i(n)(x_j)} = ifft(\hat{a}_n) .$$

(2.15)

Using the orthonormal property (on the trigonometric basis) and showing the discrete fourier transform satisfies the orthonormal condition:

$$\left\langle e^{i(m)(x_j)}, e^{i(n)(x_j)} \right\rangle_N = \delta_{m,n} .$$

(2.16)

The discrete form is written as:

$$\left\langle f, \vec{g} \right\rangle = \frac{1}{N} \sum_{j=0}^{N-1} \bar{F}_j g_j .$$

(2.17)

Substitution of the trigonometric basis into the orthonormal property and simplifying:

$$\left\langle e^{i(m)(x_j)}, e^{i(n)(x_j)} \right\rangle_N = \frac{1}{N} \sum_{j=0}^{N-1} e^{-i(m)(x_j)} e^{i(n)(x_j)} = \frac{1}{N} \sum_{j=0}^{N-1} \left(e^{i(2\pi/N)(n-m)} \right)^j .$$

(2.18)

Showing that the discrete inverse fourier transform representation satisfies orthonormality:

$$\hat{a}_n = \left\langle e^{i(n)(x_j)}, \sum_{n=-\infty}^{\infty} e^{i(m)(x_j)} \right\rangle_N = \sum_{m=-\infty}^{\infty} \left\langle e^{i(n)(x_j)}, e^{i(m)(x_j)} \right\rangle_N a_m = \sum_{m=-\infty}^{\infty} (1) a_m .$$

(2.19)

where $n \in [-N/2+1, N/2], \quad m \in [-\infty, \infty]$.

The grid increments are now established to minimize aliasing effects. The spectral periodic grid is defined as $K_x = [-N/2 : \Delta n : N/2](2\pi/L)$

Re-writing the fourier coefficients formula:

$$\hat{a}_n = \frac{1}{N} \sum_{j=0}^{N+1} \vec{u}(x_j) e^{i(K)(x_j)} .$$

(2.20)

Take the derivative in the fourier space, the fourier mode is realized:

$$\frac{\partial \hat{a}_n}{\partial x} = iK\left(\frac{1}{N}\sum_{j=0}^{N+1}\vec{u}\left(x_j\right)e^{i(K)(x_j)}\right) = iK\left(\hat{a}_n\right) \quad . \tag{2.21}$$

Applying the fourier mode conversions to the hyperbolic wave equation:

$$\left[\frac{\partial^2}{\partial x^2}+\frac{\partial^2}{\partial y^2}\right]A(z)+\left[\frac{\partial^2}{\partial z^2}-2i\beta\frac{\partial}{\partial z}\right]A(z)=0 \quad . \tag{2.22}$$

Let $\hat{A} = fft(A)$

Apply the fourier mode substitutions: $\frac{\partial^2}{\partial x^2} = iK_{xy}\left(iK_{xy}\hat{A}(z)\right) = -K_{xy}^2\hat{A}(z)$.

Substitution of this property into the parabolic wave equation second order variable with respect to *x:*

$$\frac{\partial}{\partial z}\hat{A}(z)+\frac{1}{2i\beta}\left[K_{xy}^2\right]\hat{A}(z)=0 \quad . \tag{2.23}$$

The first order differential equation can be solved directly using integration:

$$\frac{\partial}{\partial z}\hat{A}(z) = -\frac{1}{2i\beta}\left[K_{xy}^2\right]\hat{A}(z) \quad . \tag{2.24}$$

Isolate the wave field term $\hat{A}(z)$ and the differential with respect to *z* and integrate on both sides.

$$\int\frac{1}{\hat{A}(z)}\partial\hat{A}(z) = -\int_{Z_1}^{Z_2}\left(\frac{1}{2i\beta}\right)K_{xy}^2\partial z \quad , \tag{2.25}$$

$$\ln\left(\hat{A}(z)\right) = -\frac{1}{2i\beta}K_x^2\left(Z_2-Z_1\right)+C \quad . \tag{2.26}$$

The solution is realized in the spatial frequency domain:

$$\hat{A}(z) = \hat{A}_o(z) e^{-\frac{1}{2i\beta} K_x^2 (Z_2 - Z_1)} . \tag{2.27}$$

For the hyperbolic case (2.28), a pseudo spectral method is applied:

$$\frac{\partial}{\partial z}\hat{A}(z) - \frac{1}{2i\beta}\left[\frac{\partial^2}{\partial z^2}\hat{A}(z)\right] + \frac{1}{2i\beta} K_{xy}^2 \hat{A}(z) = 0 . \tag{2.28}$$

This equation can be solved using finite differences:

$$-\frac{1}{2i\beta}\left[\frac{\hat{A}^{n+1} - 2\hat{A}^n + \hat{A}^{n-1}}{\Delta z^2}\right] + \left[\frac{\hat{A}^{n+1} - \hat{A}^n}{\Delta z}\right] + \frac{1}{2i\beta} K_{xy}^2 \hat{A}^{n+1} = 0 . \tag{2.29a}$$

Isolate the forward pointing spatial steps and the current and previous spatial steps and combine the like terms:

$$-\left(\frac{1}{2i\beta}\right)\left[\hat{A}^{n+1} - 2\hat{A}^n + \hat{A}^{n-1}\right] + \Delta z\left[\hat{A}^{n+1} - \hat{A}^n\right] + \frac{\Delta z^2}{2i\beta} K_{xy}^2 \hat{A}^{n+1} = 0 , \tag{2.29b}$$

$$\hat{A}^{n+1}\left[1 - (2i\beta)\Delta z - \Delta z^2 K_{xy}^2\right] + \left[-2 + (2i\beta)\Delta z\right]\hat{A}^n + \hat{A}^{n+1} = 0 , \tag{2.29c}$$

$$\hat{A}^{n+1} = \frac{\left[-2 + (2i\beta)\Delta z\right]\hat{A}^n - \hat{A}^{n-1}}{\left[1 - (2i\beta)\Delta z - \Delta z^2 K_{xy}^2\right]} . \tag{2.29d}$$

In the parabolic and hyperbolic cases, the inverse fourier transform converts the solution to the spatial position domain:

$$U(z) = ifft\left(\hat{A}(z)\right) . \tag{2.30}$$

Figure 7 demonstrates the spectral method propagation mechanism with phase screen interaction using four input wave samples as an example.

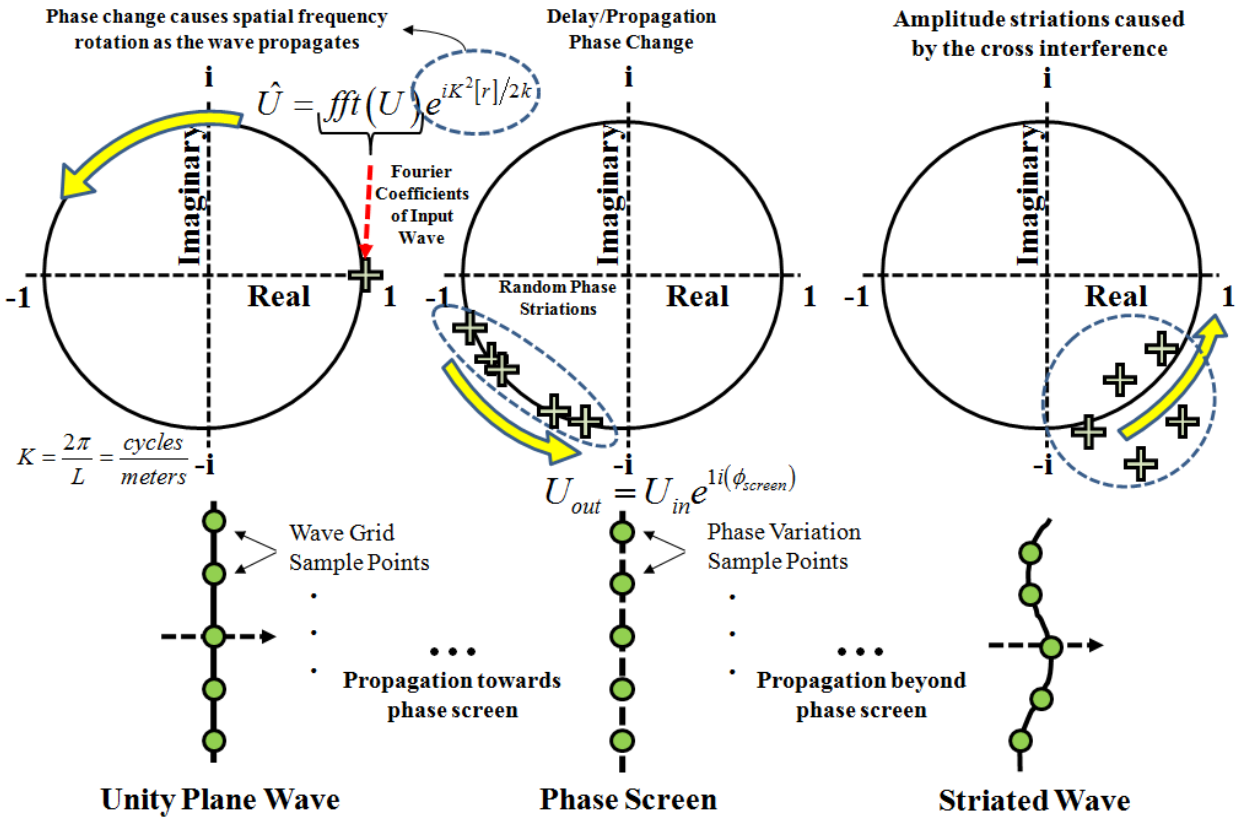

Figure 7. Spectral Method MPS Propagation Process

The fourier transform of the ideal plane wave maps to a pure real value of unity on the complex plane for each sample. As the wave propagates towards the phase screen, the phase change in the wave translates to a rotational change in the spatial frequency domain along the complex plane with equal magnitude. A greater phase change amounts to a higher spatial frequency in which more rotations (or cycles) occur per unit distance. The initial encounter with a phase screen causes a summation of unique random phase fluctuations with the pre-existing phase from the propagation delay, leading to a separation between the fourier coefficient sample points along the contour of the complex

map. This can be thought of as a phase striation. As the wave propagates beyond the phase screen, constructive and deconstructive interference translates to fourier coefficients mapping towards the interior and exterior of the complex map contour as they continue to rotate around the complex plane during the propagation sequence. Deconstructive interference from defocusing of the waves causes the fourier coefficients to reside more interior of the complex map contour and exterior for constructive interference. The scintillation index is the normalized variance of intensity fluctuations caused by the phase screens that intend to model irregularities in the ionosphere. It is defined by the following formula:

$$S_4 = \sqrt{\frac{\langle I^2 \rangle - \langle I \rangle^2}{\langle I \rangle^2}}, \tag{2.31}$$

where the intensity is defined by I, and the average is defined by $\langle\ \rangle$. The intensity is the absolute square of the electric field acquired from the parabolic wave equation solutions. This is an important metric to quantifying the effect of the disturbance the ionosphere induces on a propagating waveform. In addition to scintillation effects, the multiple phase screen technique can also be applied to determine the coherence between a set of pulse modulated parabolic wavefront realizations in terms of time delay and bandwidth.

2.5. Pulse Coherence

An important aspect of a high frequency propagation channel is the effect of small-scale ionization structures that cause signal decorrelation in space, frequency, and time. This involves calculating realizations of the receiver plane samples over multiple frequencies

defined within a bandwidth centered about the signal's carrier frequency. The single sideband-single carrier (SSB-SC) modulation scheme represents a transmission of information to a receiver using a refined form of amplitude modulation that applies a bandwidth twice the maximum frequency of the original baseband signal. Figure 8 shows the particular pulse modulation function applied to the receiver signal in the frequency domain. The resulting integration of the frequency domain function, described in equation (2.32a), is a band limited triangular pulse in the time domain.

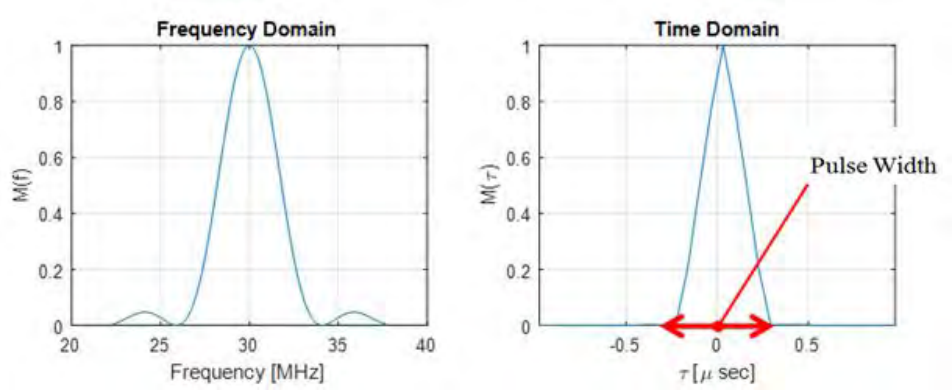

Figure 8. SSB-SC Triangular Pulse Time and Frequency Domain Representations

$$M(f)=\begin{cases}\frac{T_c}{2}\left[\operatorname{sinc}\left(2\pi f_c T_c \diagup 4\right)\right]^2 & if \quad |f|\le\frac{Bw}{2}\\ else \quad 0\end{cases},$$

(2.32a)

where $M(f)$ is the amplitude of the modulation waveform at a particular frequency *f*, $U(x,z_r,f)$ is the PWE realization, T_c is the pulse duration, f_c is the carrier frequency, and *Bw* is the frequency bandwidth. The span of the frequencies centered about the carrier is defined by:

$$f=-\frac{Bw}{2}+f_c:\Delta f:\frac{Bw}{2}+f_c,$$

(2.32b)

where $\Delta f = 1/T$ is the frequency index with respect to the total time duration beyond the pulse width. The sample index for time and frequency is defined respectively as:

$$\Delta\tau = T/M \quad (2.33) \qquad Bw = 1/\Delta\tau \quad (2.34)$$

M is the samples for the delay increment, and $\Delta\tau$ is the delay increment, and T is the total time duration. The time duration τ_d of the pulse grid is defined as:

$$\tau_d = -\frac{T}{2} : \Delta\tau : \frac{T}{2} . \quad (2.35)$$

The time domain representation of the pulse is acquired by applying an inverse fourier transform to the amplitude modulated field realization using Equation (2.36).

$$v(x, z_r, \tau) = \frac{1}{2\pi} \int_{-Bw/2}^{Bw/2} M(f) U(x, z_r, f) \; e^{1i(2\pi f)} df \quad (2.36)$$

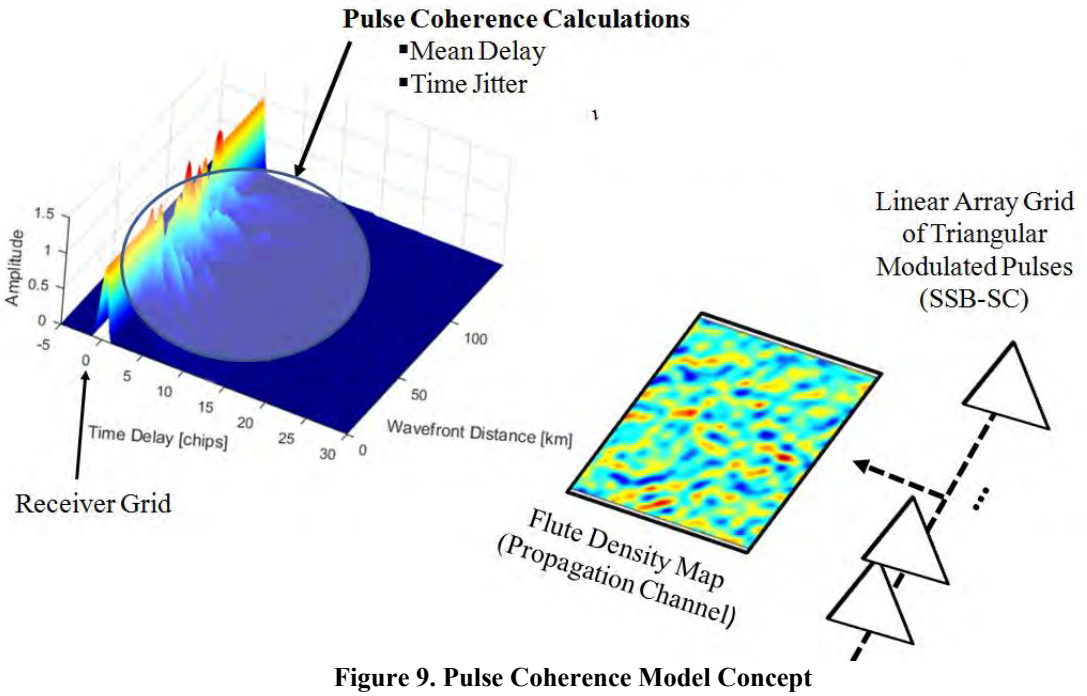

Figure 9. Pulse Coherence Model Concept

Figure 9 shows the concept of the pulse coherence model in which a linear grid of triangular pulses are propagated across a stochastic map of flute structures. The term $v(x, z_r, \tau)$ can be characterized as a space and time dependent response of a system to an external excitation. From this parameter, temporal moments can be applied to capture the different individual features of these pulse response curves.

$$m_k(x) = \frac{\int_0^{\infty} t^k \left| v(x, z_r, \tau) \right|^2 dt}{m_0^*(x)}, \tag{2.37}$$

where:

t^k is a monomial of order *"k"* used as a base function, and

$m_0^*(x)$ is the normalization using the zeroth moment which makes $v(x, z_r, \tau)$ a function with density properties similar to a probability density function.

$$m_0^*(x) = \int_0^{\infty} t^0 \left| v(x, z_r, \tau) \right|^2 dt, \tag{2.38}$$

The integration of the temporal base and response functions measures the overall response strength with respect to time. The initial moment yields the overall time delay with respect to the bulk of pulses along the receiver grid:

$$\langle \tau \rangle = \langle \tau^1 \rangle. \tag{2.39}$$

The second moment captures the dispersion or jitter between the pulses:

$$\sigma_\tau^2 = \left\langle \tau^2 \right\rangle - \left\langle \tau \right\rangle^2 . \tag{2.40}$$

An important calculation that stems from the inverse of the jitter is the coherence bandwidth. The coherence bandwidth determines the frequency selective nature of the propagation channel. A high coherence bandwidth suggests that the pulses are generally subjected to similar amplitude fading characteristics (flat fading) whereas a low coherence bandwidth refers to two or more pulses exhibiting unique amplitude fade properties (frequency selective). A theoretical approach to validating the phase screen technique for calculating the pulse coherence statistics has been proposed in [23]. The derivation begins with the concept of wave function coherence in which the mutual coherence of its complex envelope is multiplied with a temporal monomial of order *n* and integrated with respect to time to determine the low order statistical properties.

$$\left\langle \left\langle t^n (r) \right\rangle \right\rangle = \int_{-\infty}^{\infty} \left\langle A(r,t) A^*(r,t) \right\rangle t^n dt, \qquad n = 0,1,2... \tag{2.41}$$

where A is the slow varying complex envelope acquired at a propagation distance r and time t. The A term can be described by its complex carrier more specifically as:

$$A(r,t) = \int_{-\infty}^{\infty} M(f) U(r,s) e^{i(2\pi ft - (\Delta k) z)} df \tag{2.42}$$

where s is the spatial span of the wavefront, and $\Delta k = k - k_c$ is the change in the wave number based on the carrier frequency and frequencies (f) in the carrier envelope, and U is the received field realizations from the parabolic wave equation.

Substitution of this form into the temporal moment relation:

$$\left\langle\left\langle t^n(r)\right\rangle\right\rangle = \int_{-\infty}^{\infty}\left\langle \int_{-\infty}^{\infty} M(f)U(r,f_1)e^{i(2\pi ft-(\Delta k)z)}df \int_{-\infty}^{\infty} M^*(f)U^*(r,f_2)e^{-i(2\pi ft-(\Delta k)z)}df \right\rangle t^n dt$$

(2.43)

Combine like terms:

$$\left\langle\left\langle t^n(r)\right\rangle\right\rangle = \left\langle\left\langle \int\int_{-\infty}^{\infty}\int M(f)M^*(f)\left[U(r,f_1)U^*(r,f_2)\right]t^n e^{i(2\pi(f_1-f_2)t-(\Delta k_1-\Delta k_2)z)}df_1df_2 \right\rangle\right\rangle t^n dt$$

(2.44)

The mutual coherence function arises from pulse distortions and is defined by:

$$\Gamma(\Delta r,\Delta f) = \left\langle U(r,f_1)U^*(r,f_2)\right\rangle.$$

(2.45)

Rewriting with Mutual Coherence relation:

$$\left\langle\left\langle t^n(r)\right\rangle\right\rangle = \left\langle\left\langle \int\int_{-\infty}^{\infty}\int M(f)M^*(f)\left[\Gamma(\Delta r,\Delta f)\right]t^n e^{i(2\pi(f_1-f_2)t-(\Delta k_1-\Delta k_2)z)}df_1df_2 \right\rangle\right\rangle t^n dt$$

(2.46)

The solutions for the mutual coherence function can be acquired using the parabolic diffraction method described in the next section.

$$\frac{\partial\Gamma(\omega,\vec{\mathrm{r}},z)}{\partial z} + \left(\frac{ik_d}{2k_o^2}\right)\left(\frac{\partial^2\Gamma(\omega,\vec{\mathrm{r}},z)}{\partial x^2}\right) + \frac{1}{2}\Gamma(\omega,\vec{\mathrm{r}},z)A_p(\vec{\mathrm{r}}) = 0.$$

(2.47)

Additionally, the phase structure function of the medium is approximated by the correlation function integration of the homogenous random field.

$$A_\xi(\vec{r}) = \int_{-\infty}^{\infty} B_\xi(\vec{r},z)dz.$$

(2.48)

The approximation of the phase structure function description of the ionosphere found in [13] is given by:

$$A_\xi(\vec{r}) = -(1/4)\left[\left(k_1^2\beta_1^2 + k_2^2\beta_2^2\right)A_\xi(0) - 2k_1\beta_1 k_2\beta_2 A_\xi(\vec{r})\right] \tag{2.49}$$

where β is the wave propagation constant.

The temporal moments method approximates the solution by the transformation:

$$\Gamma = \exp(\Psi + \phi) \tag{2.50}$$

where $\Psi = -\left(k_1^2\beta_1^2 + k_2^2\beta_2^2\right)A_\xi(0)z/8 \cdot$

The solution to ϕ is determined when the Transformation (2.50) is inserted into the parabolic diffraction Equation (2.47) and solved, obtaining the Rytov solution:

$$\phi \simeq \frac{j\pi k_1^2 k_2^2 \beta_1\beta_2}{\Delta k}\int_{-\infty}^{\infty}\int \Phi_\xi(\vec{\kappa}_T, 0)\left[1 - \exp\left(j\Delta k\vec{\kappa}_T^2 z/2k_1k_2\right)\right]\exp\left(-j\vec{\kappa}_T \bullet \vec{r}\right)d^2\vec{\kappa}_T/\vec{\kappa}_T^2 \tag{2.51}$$

where $\Phi_\xi(\vec{\kappa}_T, \vec{\kappa}_Z)$ is the spatial spectrum of the random field and the fourier transform of the correlation function B_ξ, and $\vec{\kappa}$ represents the spatial frequencies. Various solutions of ϕ are obtained when the structure function approximation and ϕ term order is expanded by multiple terms:

$$A_\xi(\vec{r}) = A_0 + (A_2)(\vec{r})^2 + (A_4)(\vec{r})^4 + \ldots.$$

$$\phi(\vec{r}) = \phi_0 + (\phi_2)(\vec{r})^2 + (\phi_4)(\vec{r})^4 + \ldots.$$

Given these equations, the propagation of waves in random media are intimately related to the correlation spectrum of the random field. Substituting ϕ back into the parabolic diffraction equation (2.47) and solving, a hierarchy set of equations are obtained. The set of ϕ terms are:

$$\phi_0\left(\vec{r}=0\right)=k_2^2\beta_2^2A_0\,L/4 \tag{2.52a}$$

$$\phi_1\left(\vec{r}=0\right)=\left(-j/4\right)k_2\beta_2^2A_2L\left(2z-L\right)+\left(1/4\right)k_2^2\beta_2\left(b_1-\beta_2\right)A_0L \tag{2.52b}$$

$$\begin{aligned}\phi_2\left(\vec{r}=0\right)=\left(1/4\right)k_2\beta_2\left(b_2-b_1\right)A_0L-\left(j/4\right)k_2\beta_2b_1A_2L\left(2z-L\right)\\-\left(2/3\right)\beta_2^2A_4L\left(L^2-3Lz+3z^2\right)\end{aligned} \tag{2.52c}$$

where b_n is the expansion terms of the propagation constant, z is the propagation distance to the receiver, and L is the thickness of the irregularity structure. Additionally, the expansion on the correlation function yields:

$$A_0=\left(2\pi r_o/\kappa_o\right)^{1/2}\sigma_\xi^2\,K_{(p-2)/2}\left(\kappa_o r_o\right)\Big/K_{(p-3)/2}\left(\kappa_o r_o\right) \tag{2.53a}$$

$$A_2=-\left(\pi\kappa_o/2r_o\right)^{1/2}\sigma_\xi^2\,K_{(p-4)/2}\left(\kappa_o r_o\right)\Big/K_{(p-3)/2}\left(\kappa_o r_o\right) \tag{2.53b}$$

$$A_4=-\left(\pi\kappa_o^3/2r_o^3\right)^{1/2}\sigma_\xi^2\,K_{(p-6)/2}\left(\kappa_o r_o\right)\Big/K_{(p-3)/2}\left(\kappa_o r_o\right) \tag{2.53c}$$

where r_o is the inner scale of the spectrum, κ_o is the inverse of the outer scale, K is the Hankel function, σ_ξ^2 is the variation in the electron density fluctuations, and p is the order of the power spectrum. The equations that represent the approximate solution of the mutual coherence function becomes:

$$\Gamma_0 = 1 \tag{2.54a}$$

$$\Gamma_1 = \left(-j/4\right) k_2 \beta_z^2 A_2 L\left(2z - L\right) \tag{2.54b}$$

$$\begin{aligned}\Gamma_2 = \left(-1/8\right) k_2^2 \left(\beta_z - b_1\right)^2 A_o L - \left(j/4\right) k_2 \beta_2 b_1 A_2 L\left(2z - L\right) \\ -\left(2/3\right)\beta_2^2 A_4 L\left(L^2 - 3Lz + 3z^2\right) \\ -\left(1/96\right) k_2^2 \beta_2^2 A_2^2 \left(24z^2 - 28Lz + 9L^2\right)\end{aligned} \tag{2.54c}$$

Applying these terms to the stochastic temporal moments integral (2.41), the solutions for time delay and time jitter are:

$$\left\langle \tau \right\rangle = \beta \sigma_\phi^2 \left(2z - L\right)\left|A_2\right| / 4\pi\omega_o A_o \tag{2.55}$$

$$\begin{aligned}\sigma_\tau^2 = t^2\left(0\right) + \sigma_\phi^2 / \omega_o^2 + \frac{\sigma_\phi^4 \lambda^2 A_2^2}{24\pi^2 \omega_o^2 A_0^2}\left(12z^2 - 16Lz + 6L^2\right) \\ + \frac{\sigma_\phi^2 \lambda^2 A_4}{2\pi^2 \omega_o^2 A_0}\left(3z^2 - 3Lz + L^2\right)\end{aligned} \tag{2.56}$$

where $t^2\left(0\right) = \int_0^\infty t^k \left|m\left(\tau\right)\right|^2 d\tau \Big/ \int_0^\infty \left|m\left(\tau\right)\right|^2 d\tau$, and m is the triangular pulse modulator spectrum.

The final component to the multiple phase screen approach resides in the frequency domain analysis of the received parabolic wave realizations. The secondary power spectrum measurements, also known as the scattering function or doppler-delay function is critical to ascertaining the spread of the energy as a result of scattering caused by ionospheric irregularities.

2.6. Channel Scattering Function

Phenomena caused by scattering of pulsar radiation in the interstellar medium have long been used to study small scale structure in the electron density. Pulsars are the primary source of information of the smallest scale structure in the interstellar medium [14]. The chief observable phenomena from these pulsars are intensity fluctuations in time and frequency, angular broadening, pulse broadening, and arrival time variations. Intensity variations are usually quantified using the dynamic spectrum, intensity versus time and frequency, from which its two-dimensional correlation function estimates the characteristic bandwidth and timescale for the scintillations [14]. It is worth noting that the MPS model applied in this research will not have any time dependency. Instead, the spatial samples along the wavefront sample grid will account for a spatial evolution (time harmonic) rather than a time evolution of the waveform.

Occasional periodic fringes in the dynamic spectrum are quantified using a two dimensional fourier analysis of the dynamic spectrum. These fringes appear as discrete features in the secondary spectrum and are explained as the interference between two or more scattered images. Arcs appear as enhanced power (at very low levels) along parabolic curves extending out from the origin well beyond the normal diffractive feature [12]. In the MPS model developed in the following chapter, the spectrum emitted by a sequence of uniform plane waves is significantly modulated by interference caused by the flute density map and changes in terms of space (instead of time) due to variations in the medium and pulsar.

According to [12], some of the most notable characteristics of the parabolic arcs are the following:

1. Scintillation arcs are faint, but they are ubiquitous and persistent when the secondary spectrum has adequate dynamic range and high frequency and time resolution.
2. The arcs often have a sharp outer edge, although in some cases (e.g., Fig. 10c) the parabola is a guide to a diffuse power distribution. There is usually power inside the parabolic arc but the power falls off rapidly outside the arc except in cases where the overall distribution is diffuse.
3. In contrast to the symmetrical shape typical of the arc outline, the amplitude of the arc can be highly asymmetric for a given frequency and can show significant substructure.
4. A particularly striking form of substructure consists of inverted arclets with apices that lie along or inside the main arc outline.
5. Although a single scintillation arc is usually present for each pulsar, there are possible cases in which multiple scintillation arcs are seen.
6. The arcs arise in small angle scattering from the square law dependence of the delay on angle of scattering and do not depend on the dispersive nature of the interstellar plasma.

The delay-doppler maps shown in Figure 10 demonstrate the various properties observed in the pulsar radiation measurements of the small scale irregularity structures that cause prominent fringe effects in the delay-Doppler power spectrum distribution.

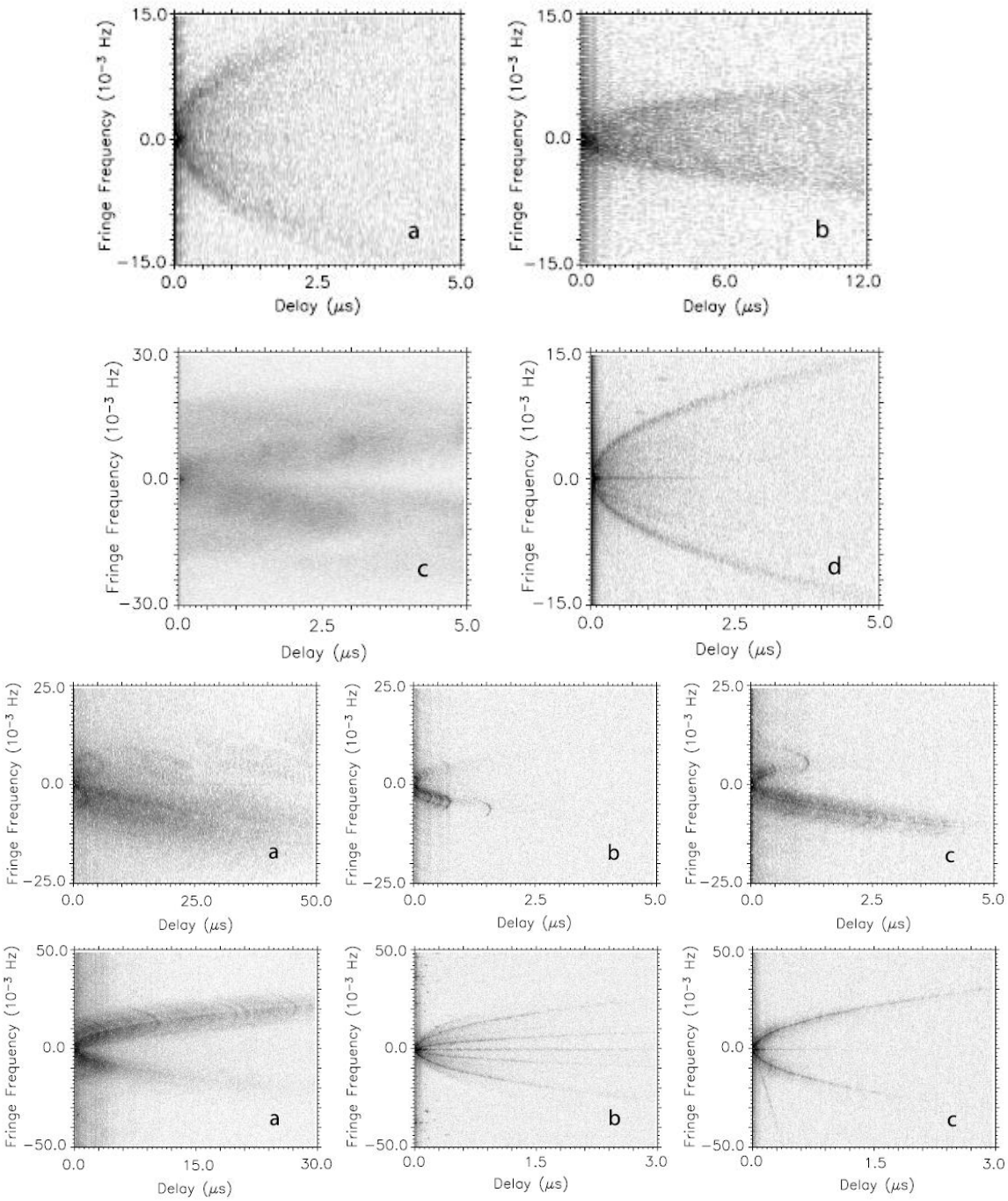

Figure 10. [12] Maps of Parabolic Arcs from Pulsar B1133+16 collected at Arecibo Observatory

Channel probe measurements can be used to provide an approximation to the channel scattering function. The channel scattering function is a concept that arises in the modeling of random scatter channels and describes the way in which signal energy is

redistributed in delay and doppler as a result of distortion introduced by the transmission channel [8]. The delay spread is a normal result of propagation via the dispersive ionospheric medium and is significantly enhanced by multipath or scatter effects when the medium is irregular and the irregularity structure is spatially extensive [8]. Doppler spread is a consequence of the spatial variability of the MPS channel and also related to the bulk motion of the irregularity regions in the ionosphere and their turbulent internal motions. Under conditions of high integrated strength of turbulence, a low phase spectral index indicating relatively dense small-scale irregularities, produces pronounced range spreading [14].

This range spreading is an expected occurrence for the stochastic flute density maps developed in Chapter 3. Conversely, when the spectral index is high, strong focusing/defocusing by large-scale irregularities causes increased doppler spreading. This phenomenon will be further examined in Chapter 5 for comparisons between the large scale Kolmogorov structure and flute structure phase cubes effecting the scattering function. However, in the Kolmogorov structure case, the spectral index will not be considerably high for the large scale phenomenon in order to avoid masking the flute structure's scattering effects. Therefore, the doppler spreading may not be significant if at all for the large scale irregularities in comparison to the flute structures.

Calculation of the scattering function begins with comparing two position-two frequency components of the parabolic wave equation realizations. The cross correlation function of the complex fields in the direction transverse to the direction of propagation describes the loss of coherence of an initially coherent wave propagating in a turbulent medium. The objective is to examine the similarities of samples along the wavefront grid

as a function of frequency. These similarities involve projecting the realizations as vectors in which the correlation becomes the projection of the two vectors.

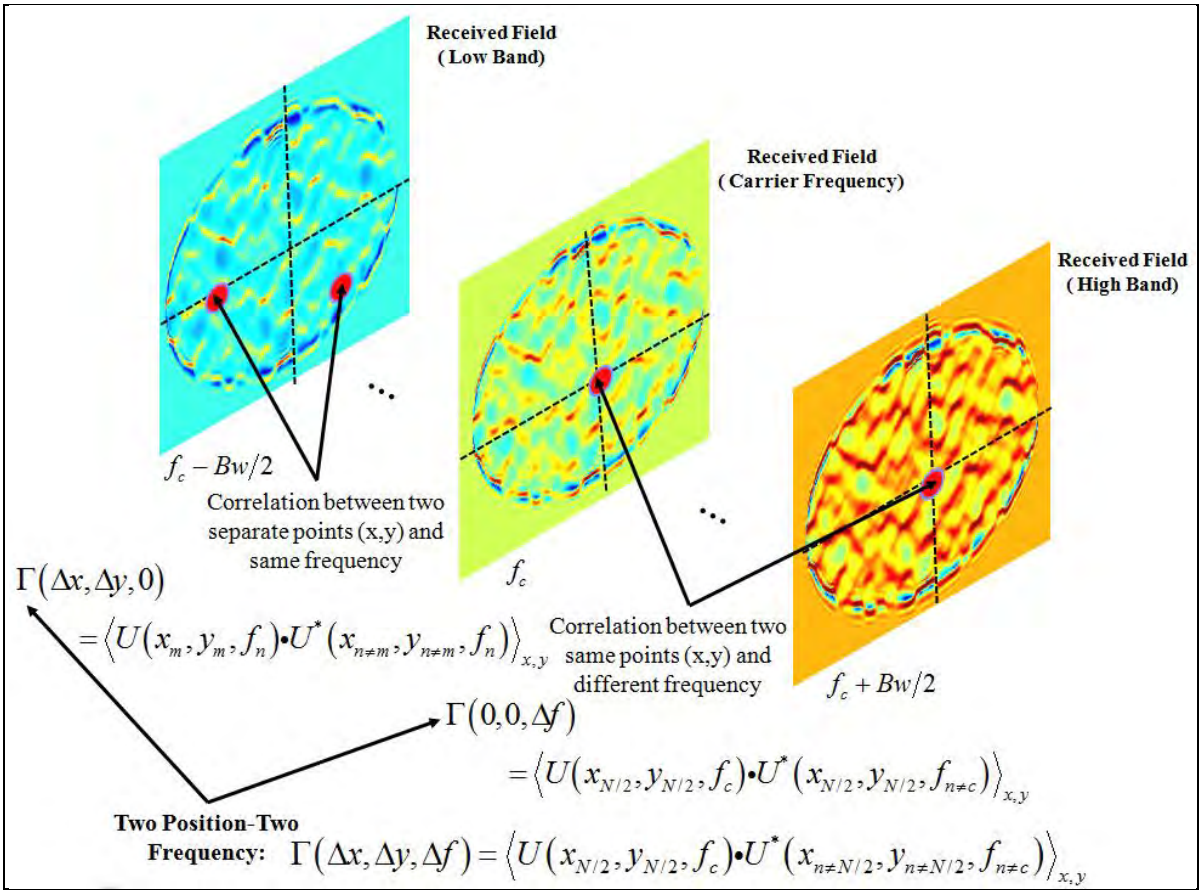

Figure 11. Two Position - Two-Frequency Mutual Coherence Functions

The angle between the two vectors is required, as determined when taking the complex conjugate of one of the two realizations:

$$\Gamma(\Delta x, \Delta y, \Delta f) = \left\langle U(x_{N/2}, y_{N/2}, f_c) \bullet U^*(x_{n\neq N/2}, y_{n\neq N/2}, f_{n\neq c}) \right\rangle_{x,y} \tag{2.57a}$$

$$= \left\langle \left| U(x_{N/2}, y_{N/2}, f_c) \right| e^{1i\phi_c} \bullet \left| U(x_{n\neq N/2}, y_{n\neq N/2}, f_{n\neq c}) \right| e^{-1i\phi_n} \right\rangle_{x,y} \tag{2.57b}$$

$$= \left\langle \left| U\left(x_{N/2}, y_{N/2}, f_c\right) \right| \left| U\left(x_{n\neq N/2}, y_{n\neq N/2}, f_{n\neq c}\right) \right| \mathrm{e}^{1i(\phi_c - \phi_n)} \right\rangle_{x,y} \tag{2.57c}$$

where $\emptyset_c - \emptyset_n$ is the phase difference. Figure 11 shows the spectrum of the two-dimensional received field realizations acquired from using a multiple phase screen model. The two frequency-two position mutual coherence function is developed by comparing the resulting realizations at different points along the spatial grid and the frequency spectrum relative to the carrier frequency realization at the central point on the grid map.

An alternative technique to compare against the phase screen based calculations of the doppler-spread is the Parabolic Diffraction Method (PDM) proposed by L.J. Nickisch [8]. The Nickisch approach requires a specification of the background ionosphere for purposes of ray-path determination and uses a multiple thin-screen diffraction model to simulate the effects of the irregular ionosphere. By allowing the diffraction properties and the drift velocity of the medium to vary from screen-to-screen, Nickisch is able to simulate the effects of a non-uniformly irregular medium. Using this technique he has been able to reproduce scattering functions measured on a polar path. The formulation starts with determining the mutual coherence function through use of the parabolic wave equation, in which substitution of the mutual coherence definition (2.57c) is followed by the Markov approximation to yield the final form.

$$\frac{\partial \Gamma\left(\omega, \vec{\mathrm{r}}, z\right)}{\partial z} + \left(\frac{ik_d}{2k_o^2}\right)\left(\frac{\partial^2 \Gamma\left(\omega, \vec{\mathrm{r}}, z\right)}{\partial x^2}\right) + \Gamma\left(\omega, \vec{\mathrm{r}}, z\right) P\left(\vec{\mathrm{r}}\right) = 0 \tag{2.58}$$

,

$\lambda_1 = C/f_c$ is the wavelength evaluated at the carrier frequency of the modulated wave, $\lambda_2 = C/f_i$ is the wavelength evaluated at a frequency that is being evaluated against the carrier frequency in the coherence calculation, and k_o is the associated wavenumber. $k_d = 2\pi/\lambda_1 - 2\pi/\lambda_2$ is the differential wavenumber. The phase structure function of the electron density fluctuations is approximated as a quadratic function. The formulation is based on the power spectrum of phase fluctuations for a slope of 3.

$$P(\vec{r}) = \frac{\lambda_1^2 \sigma_\phi^2}{8}\left[\frac{k_d^2}{\pi^2 L_x} + 2\left(k_1^2\right)\left(r^2\right)\left(\log\left(\frac{L_o}{l_i}\right)2\pi^2 L_o^2 L_x\right)\right], \tag{2.59}$$

where, σ_ϕ^2 is the root mean square phase deviation, L is the layer thickness, L_o is the outer scale, l_i is the inner scale, and *r* is the spatial span of the quadratic function transverse to the direction of propagation.

The numerical technique applied to solve the PDM equation is a pseudo spectral technique to convert the equation to the frequency domain and apply the implicit backward Euler scheme to solve the ordinary differential equation. Starting with the finite difference approximation of the spatial derivatives with respect to the propagation direction *z* and the spectral fourier mode conversion of the second order derivative with respect to the spatial span in the transverse direction *x*:

$$\frac{\hat{\Gamma}^{n+1} - \hat{\Gamma}^n}{\Delta z} - \left(\frac{ik_d}{2k_o^2}\right)\left(K_x^2\right)\hat{\Gamma}^{n+1} + \frac{1}{2}P(K)\hat{\Gamma}^{n+1} = 0, \tag{2.60}$$

in which the fourier conversion to the input function is defined by: $\hat{\Gamma}^n = fft(\Gamma^n)$.

The algebraic manipulations of isolating the forward stepping terms (n+1) from the current spatial step (n) results in the following form:

$$\hat{\Gamma}^{n+1} = \frac{\hat{\Gamma}^n}{\left[1 + \Delta z\left(\frac{ik_d}{2k_o^2}\right)\left(K_x^2\right) - \Delta z\frac{1}{2}P(K)\right]}. \tag{2.61}$$

The solution is realized by converting the output function to the spatial position domain using an inverse fourier transform: $\Gamma^{n+1} = ifft(\hat{\Gamma}^{n+1})$.

The Khinchin-Kolmogorov Theorem states that the spectral decomposition of an autocorrelation function of a wide sense stationary random process is given by the power spectral density. In essence, the mutual coherence represents the correlation between realizations of the received field with respect to position and frequency, as determined assuming a wide sense stationary process of phase screens to sample the ionospheric irregularities. The spectral decomposition involves the fourier transform of the mutual coherence spatial components to provide a solution in terms of spatial frequency and inverse fourier transform the frequency components to yield the relationship of the power distribution to time delay of the received signal.

$$S\left(K_x, K_y, \tau\right) = \int_{-B_w/2}^{B_w/2}\int_{-L_y}^{L_y}\int_{-L_x}^{L_x} \Gamma\left(\Delta x, \Delta y, \Delta f\right) e^{i2\pi f\tau}\, dx dy df. \tag{2.62}$$

Important mathematical relationships can be calculated from the scattering function (see Figure 12) to provide useful information regarding the power delay profile, doppler power spectrum, frequency correlation function, and the spatial correlation function.

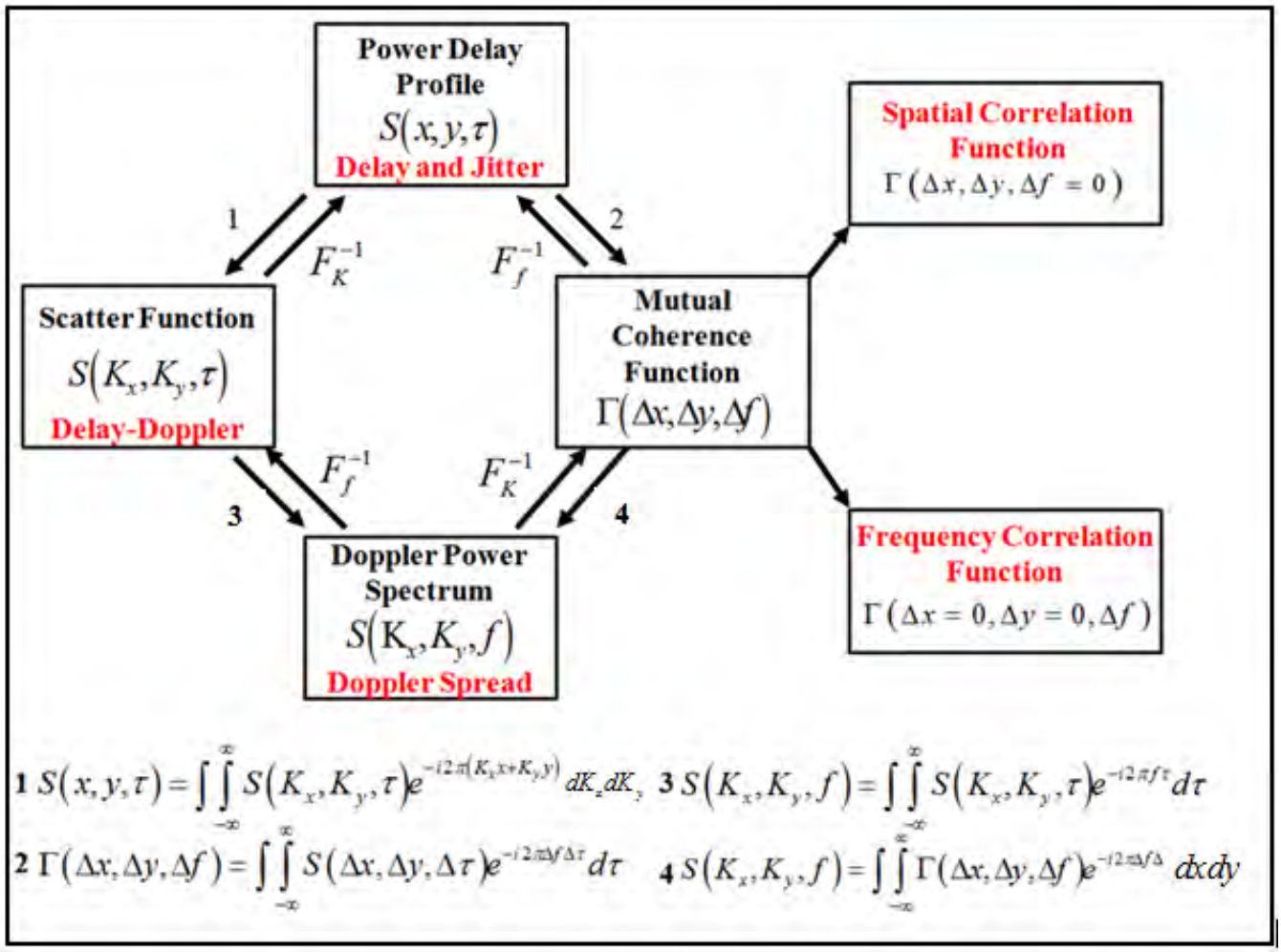

Figure 12. Scattering Function Secondary Calculation Fourier Transform Relationships

The application of MPS models to acquire the important metrics described in this section requires a fundamental understanding flute structure behavior. The key source of ionospheric irregularities are plasma instabilities. Computationally modeling the behavior of these plasma instabilities depends on the descriptions that define the nature of the particle behavior. In this research effort, a macroscopic treatment of the plasma instability is desired. The motions of the individual particles within the flute plasma instability is not a concern, however, the collective electron and ion particle behavior during the plasma instability must be considered to determine their contribution to an incident electric field

over propagation distances that relate to radio occultation systems or satellite communications. The macroscopic approach applied to describe the convective plasma process caused by either gradient drifts or Rayleigh Taylor instability is the MHD approximation. The following section introduces this theory and its application to describe the flute mode generation in an unstable plasma.

2.2 Magnetohydrodynamic Plasma and Flute Structure Formation

This section describes the numerical approximation of the flute structures by initially defining the critical equations that characterize a single fluid MHD plasma. This is followed by a description of the flute structure formation process based on electron and ion particle behavior. The flute structures are derived using perturbation analysis that converts complex two-fluid MHD nonlinear equations into alternate functions whose solutions are generalized over a finite domain. Finally, an unstable single fluid MHD model is applied to an ideal flute structure to model extrinsic disturbances that lead to alternative forms of flute structures. A framework is established in a classification method to define the flutes as linear, quasi-linear, or nonlinear modes based on each structure's physical appearance as a result of the plasma's evolution. These flutes will be implemented in various configurations on a density map applied to the propagation models presented in Chapter 4 to investigate their impact on coherent pulse signals.

2.2.1 Single-Fluid Magnetohydrodynamic Plasma

In the MHD approximation, plasma is approximated as a single, finite pressure, electrically conducting fluid. The macroscopic treatment of the plasma provides an

approximate understanding of its behavior. Particle motion in the two-fluid system is described by the individual species' mean velocities and pressure. Electric current is induced in the conductor which, by Lenz's law, creates its own magnetic field that tends to cancel the original, externally supported field, thereby, in effect, excluding the magnetic field lines from the conductor [15]. Conversely, when the magnetic field penetrates the conductor and the conductor is moved out of the field, the induced field reinforces the applied field, resulting in the lines of force dragged along with the conductor in the direction of the flow [15]. Naturally, if the conductor is a fluid with complex motions, the ensuing magnetic field distribution can become quite complex, and the current will build up until its growth is balanced by ohmic dissipation [15]. Additionally, when currents are induced by a motion of a conducting fluid through a magnetic field, a Lorentz force will act on the fluid and modify its motion.

The governing equations for an MHD plasma are the continuity and momentum equations. The continuity equation states that the rate at which mass enters the system is equal to the rate at which mass leaves the system plus the accumulation of mass within the system [16]. The time derivative is the accumulation (or loss) of mass in the system, while the divergence term is the difference in in-flow vs. out-flow.

$$\partial\rho/\partial t + \nabla\bullet\left(\rho\bar{U}\right) = 0 \tag{2.63}$$

The equation of momentum as shown in (2.64) describes the motion of the plasma, where the time derivative is the convective derivative defined using the center of mass velocity. It also relates the current density and the plasma velocity. The gradient of the pressure is

the average force per unit volume inside the fluid. The J × B term describes the Lorentz force acting on the fluid to modify its motion.

$$\rho\left[\partial\bar{U}/\partial t + \bar{U}\bullet\nabla\bar{U}\right] = \bar{J}\times\bar{B} - \nabla P \tag{2.64}$$

where, ρ is the fluid density, $\bar{U}$ is the velocity of the fluid, and P is the pressure applied to the fluid. In static MHD, $\nabla P = \bar{J}\times\bar{B}$, in which no flow velocity is observed [17]. In dynamic equilibrium, $\nabla\times\left(\bar{J}\times\bar{B}\right)\neq 0$, and therefore, the magnetic force is not conserved. Since the flow is incompressible, the density is constant, and independent of space and time, simplifying the mass continuity equation to a volume continuity equation in which $\nabla\bar{U} = 0$ is incompressible flow [17].

The formulation of a single fluid MHD model begins with the mathematical description of two common instability mechanisms; Rayleigh Taylor followed by the Kelvin Helmholtz instability. It is important to note that the Lorentz force is not applied in these calculations and the forces are predefined. Figure 13 shows the unstable configuration of the Rayleigh Taylor instability that occurs at the interface of high and low density regions in which the heavy density layer perturbs into the lighter density later when a disturbance is present at the interface.

$$\left[\partial\bar{U}/\partial t + \bar{U}\bullet\nabla\bar{U}\right] = -\frac{1}{\rho}\nabla P - g\hat{y} \tag{2.65}$$

Applying a fictitious gravity term on the momentum equation in the *y*-direction:

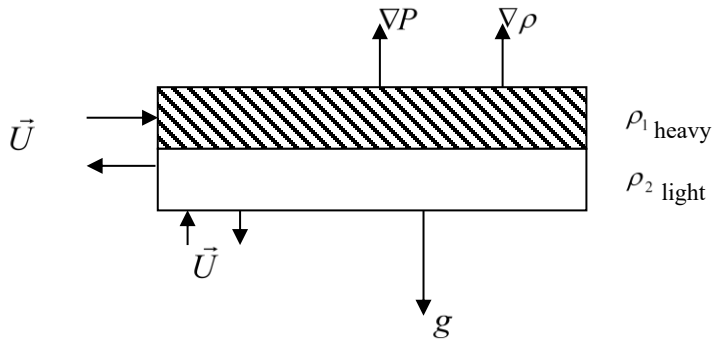

Figure 13. Force Configuration for Rayleigh Taylor Instability

The pressure gradient balances with the force of the gravity component on the right side of the Equation (2.66). Pressure in then calculated by integrating this force balance equation with respect to the y-direction (2.67).

$$\nabla P = -\rho g \hat{y} \tag{2.66}$$

$$P(\vec{r},t) = \int_{y}^{h} \rho(x,y',t) g dy' \tag{2.67}$$

Integration of velocity with respect to time will yield the spatial changes of the density with respect to time. A detailed description applying similar formulary and numerical modeling for MHD instability can be found in [18]. The advection density is solved using the following steps. Solving for the velocity term in the *x*-direction:

$$\vec{U}_{x1} = \frac{1}{\rho}\left[\frac{\vec{P}_{x1} - \vec{P}_{xo}}{\Delta x}\right]\Delta t + \vec{U}_{xo} \tag{2.68}$$

Solving for the velocity term in the $\hat{y}$ direction:

$$\vec{U}_{y1} = \left(\frac{1}{\rho} \left[\frac{\vec{P}_{y1} - \vec{P}_{yo}}{\Delta y} \right] - g\hat{y} \right) \Delta t + \vec{U}_{yo} \tag{2.69}$$

Declare the initial perturbations along the interface of the densities in the x and y direction.

$$\vec{U}_{xo} = \partial\Phi / \partial x \qquad (2.70a)$$

$$\vec{U}_{yo} = \partial\Phi / \partial y \qquad (2.70b)$$

These density perturbations take the form of a sinusoid along the x-direction with a radial frequency of crests (2.71):

$$\Phi(x) = A\sin(\omega x + \pi/2) \tag{2.71}$$

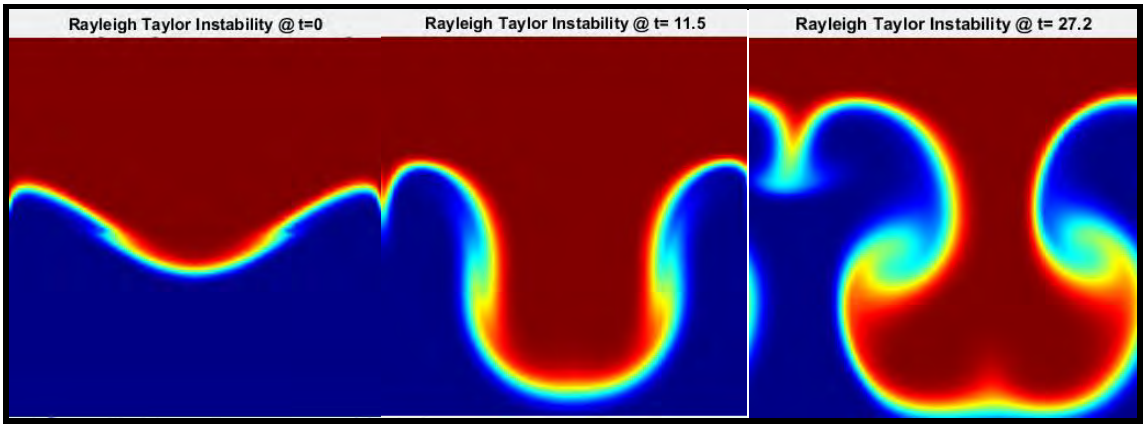

Figure 14. Rayleigh Taylor Instability Sequence

Figure 14 shows the time lapse of an initial sinusoidal perturbation at the interface of the density layers. Driven by the dominant gravitational force, the heavy (red) density layer sinks into the light (blue) density layer and a spatial exchange of density layers occurs. As the exchange evolves the velocity vector in the x-direction coupled with the force of gravity creates minor vorticity at the edges of the interface.

In the case of Kelvin Helmholtz instability, the gravity term magnitude is reduced and the velocity terms become the dominant contributor to create shear flow. Figure 15 shows the unstable configuration between two density layers.

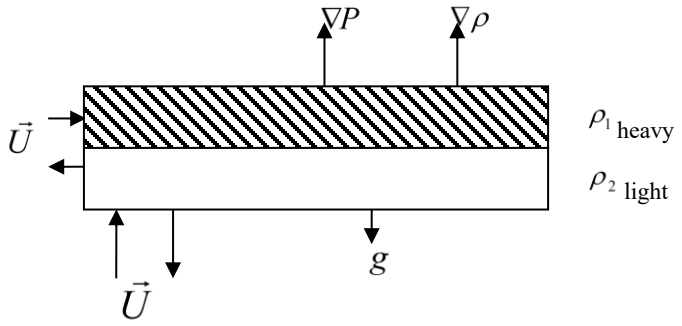

Figure 15. Force Configuration for Kelvin Helmholtz Instability

An important step in the process of solving the single fluid MHD equations is the Helmholtz Hodges decomposition (HHD). HHD is applied to decouple the pressure and velocity fields and to keep the error of the respective terms from interfering with each other [19]. The theorem itself states that any field vector can be decomposed uniquely into curl-free (irrotational) and divergence free (incompressible) components [19].

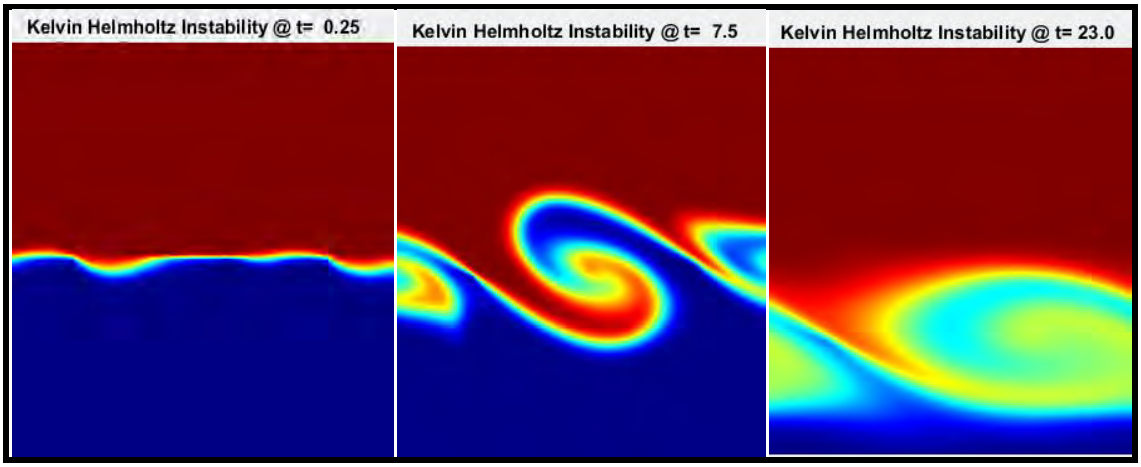

Figure 16. Kelvin Helmholtz Instability Sequence

The continuity relation for divergence free is to set the divergence free component equal to zero. Applying orthogonality and substitute the continuity property into the relation

will yield the recognizable Poisson equation for the Helmholtz potential. Projection methods model the fluid motion by taking small steps in time. For each time step, the velocity from the previous time step is used to update the previous velocity. The decomposition process begins with the following velocity vectors in the *x* and *y* directions:

$$\left.\begin{aligned}\vec{U}_{x1} &= \vec{U}_{x0}^{k+1} + \nabla\phi^{k+1} \\ \vec{U}_{y1} &= \vec{U}_{y0}^{k+1} + \nabla\phi^{k+1}\end{aligned}\right\} \tag{2.72}$$

ϕ is scalar field called Helmholtz potential and $\vec{U}^{k+1}$ is the divergence free component of $\vec{U}_x$ (or $\vec{U}_y$).

$$\vec{U}_x^{k+1} = \vec{U}_{x1} - \left(\frac{\phi_{x1} - \phi_{x0}}{\Delta x}\right) \tag{2.73}$$

$$\vec{U}_y^{k+1} = \vec{U}_{y1} - \nabla\phi_y \tag{2.74}$$

A plasma accelerated by a magnetic field pressure may cause instability on the natural equilibrium of the plasma. A gravity force or the influence of a magnetic field will cause the disturbance to grow in the plasma and subsequent separation of charges, leading to the drift velocity that enhances the initial disturbance. The application of this single fluid MHD model will demonstrate the nonlinear formation of the linear flute perturbation under the influence of gravity, pressure, and drift velocities. Turbulent effects will cause irregularities in the flute structure.

2.3. Flute Instability

This section presents the background mechanism from which the flute instability arises. It is important to understand the behavior of electrons and ions particle behavior within the plasma in relation to a local magnetic field. The relationship between gradient drift instability and flute mode formation is addressed. The flute instability theory will lead to the formulation of two-fluid MHD nonlinear equations to model the density gradients of a dipole structure.

2.3.1 Ionospheric Gradient Drifts and the Rayleigh Taylor Instability

The mechanisms of the F-layer Ionosphere include strong thermospheric neutral winds that create upward dynamo currents and establish a vertical polarization field in which positive and negative charges accumulate at the top and bottom boundaries of the field [20]. These positive and negative charges create an electric field that interacts with the horizontal magnetic field at and near the geomagnetic dip equator with a resultant drift velocity that sets the ionospheric plasma into motion [20]. This motion includes low latitude plasma rising above the geomagnetic dip equator until it is slowed down by pressure forces. As a result of this momentum loss, the plasma begins to move along the magnetic field lines under the forces of gravity and pressure gradients and eventually becomes deposited at the higher dip equator latitudes in both hemispheres [20].

The Rayleigh Taylor Instability is a possible explanation for interchange between the high and low density layers within the equatorial region of the F-layer Ionosphere. The driving mechanism of this instability is a gravitational force acting perpendicular to the ambient magnetic field on an inverted density gradient. The collisional Rayleigh

Taylor instability modes in the Earth's ionosphere tend to evolve into plasma bubbles that extend upward from the bottom side to the topside of the F-layer [21].

2.3.2 Plasma Particle Behavior

In order to define the causes of a flute instability, the gradient drifts of electrons and ions must be understood. Ions in plasma absorb electromagnetic radiation and increase in kinetic energy. The magnetic field bends the ions path into a circular orbit known as the Larmor radius. This circular trajectory is also present in electrons in which it rotates in the opposing direction relative to the ion. A difference in the Larmor radii of ions and electrons leads to a difference in trajectories. Therefore, their drift velocities differ and builds up a charge separation out of phase due to particle drifts such as the result from the gravitational force, or an applied constant acceleration. The gradient drift motion is the most common form of a single–particle behavior in a plasma. The added electric field is perpendicular to the uniform magnetic field, causing the ion to decelerate when it moves upward whereas the electron will then be accelerated in its upward motion [22]. This results in a smaller instantaneous Larmor radius for the electron and a larger Larmor radius for the ion. The opposite takes place in downward motions. The overall effect will be a drift motion in the E x B direction for both the ion and the electron, a fundamental aspect of the gradient drift instability [22].

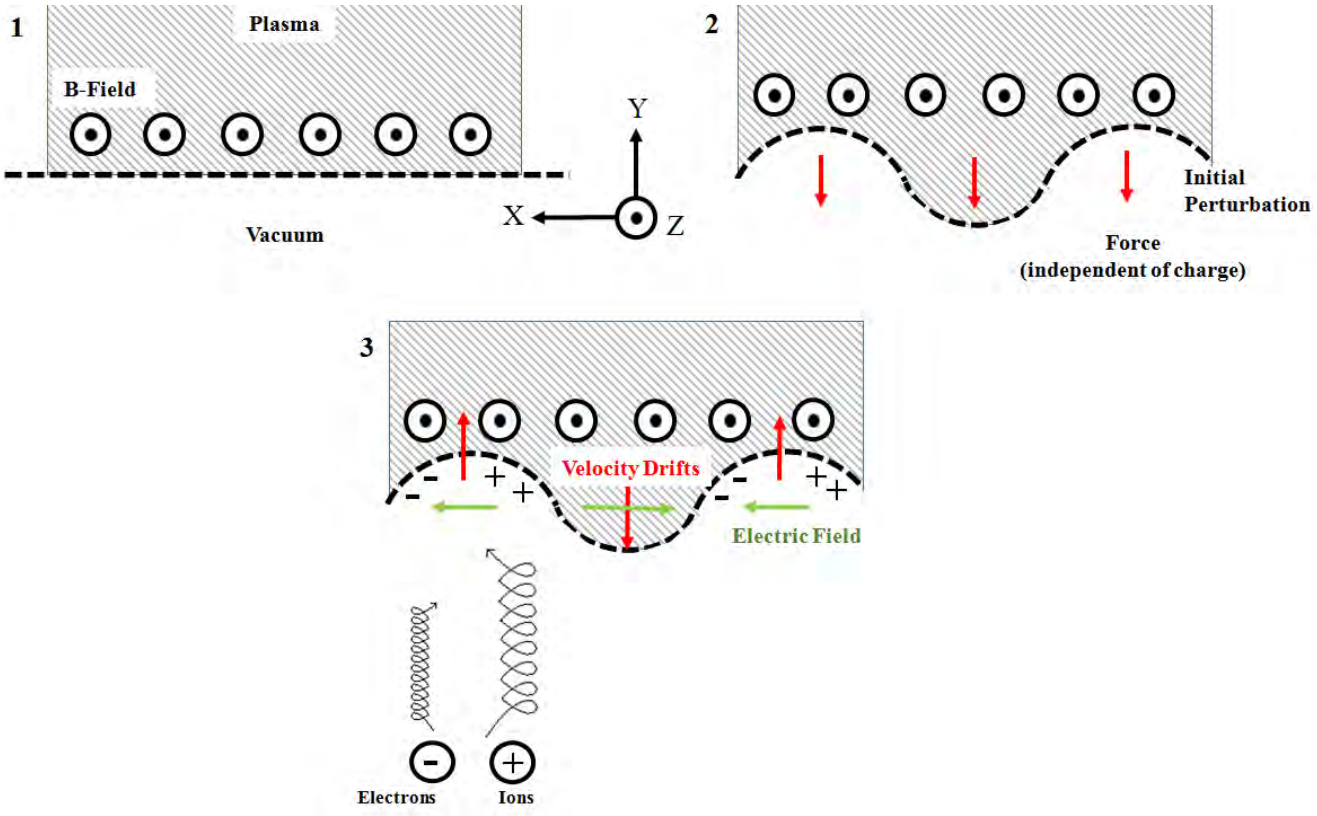

Figure 17. Gradient Drift Instability Mechanisms

2.3.3 Flute Formation and Conditions

Flute modes occur as low frequency electrostatic oscillations of non-uniform magneto plasma in which their frequency is significantly lower than the ion cyclotron frequency [23]. They also occur from the drift instability and grow in the direction that is perpendicular to the equilibrium magnetic field in the magnetized plasmas [2]. The flute modes become unstable due to the combined effects of the density inhomogeneity and the curvature of the magnetic field [23]. The formation of a flute structure is initialized when a gravitational force is applied to a small density perturbation, causing the ions to drift. A separation of charge occurs from this drift, forming an electric field. The gradient drift velocity varies based on the different species of the plasma due to magnetic field

curvature [4]. The instability arises from the drift motion in the radial direction, bringing particles from the denser plasma core. A velocity shear and non-uniform electron flow will occur in the presence of a non-uniform electric field and an external magnetic field [4].

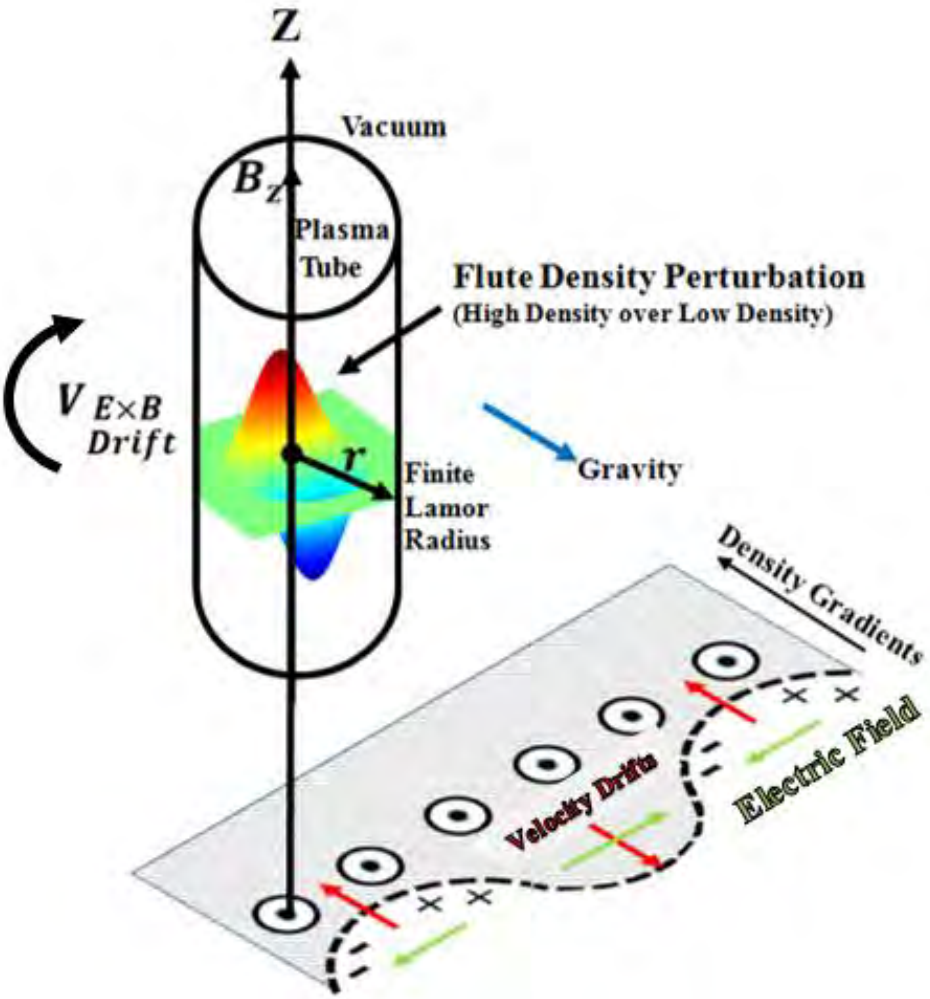

Figure 18. Flute Perturbation Generated from Gradient Drifts

It is important to note that in relation to the terrestrial high latitude (auroral) magnetosphere and ionosphere, lower hybrid fluctuations are usually found along geomagnetic field lines and/or anisotropic electron distributions as well as strong sheared

plasma flows driven by structural electric fields in the vicinity of small scale auroral arcs [2].

2.3.4 Two-Fluid Magnetohydrodynamic Scheme and the Ideal Flute Solution

This section provides a general description of the derivation of the flute structures from two-fluid MHD equations in a finite beta plasma whose solutions are approximated in a finite domain with prescribed boundary conditions. Further detailed information on this mathematical process can be found in [4]. The parameters for the MHD model are defined in Figure 19. The general equilibrium force and velocity vectors referenced in the MHD nonlinear systems of equations are defined in relationship to a Cartesian coordinate grid.

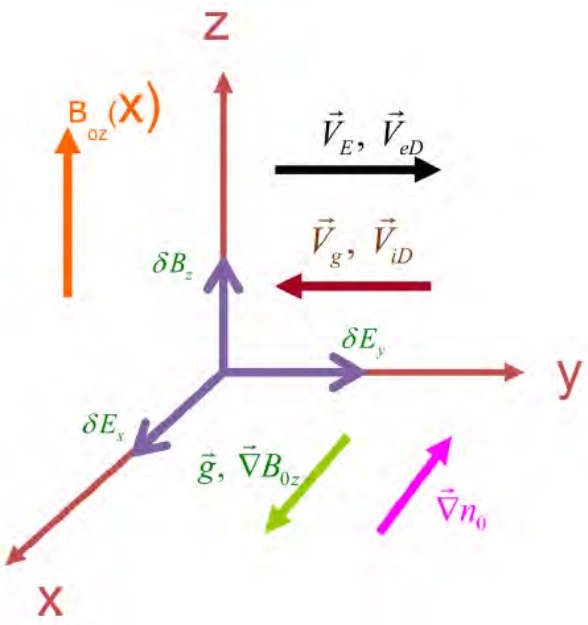

Figure 19. [1] Interchange Mode Vector Components

The initial state of the plasma is assumed to be in equilibrium until a small perturbation is applied in which the interchange oscillations are added to the physical equilibrium

quantities. Let δn represent interchange oscillations, n_o represent the equilibrium plasma density, P_o is the equilibrium pressure, B_o is the equilibrium magnetic field, *g* is the fictitious gravitational force, and T_j is the plasma temperature for the species *j*. Re-writing in terms of the electrostatic potential and gravitational acceleration, the governing non-linear equations of motion iterative solutions for the electrostatic potential $\Delta_\perp \Phi$, density δn, and the magnetic field δB_z in a high beta plasma are shown in (2.75 *a*, *b*, and *c*). Variables within these formulas are defined in Appendix A.1.

$$\frac{\partial \Delta_\perp \Phi}{\partial t} - \frac{V_{Ti}^2}{\omega_{ci}} \left[\frac{\left(-\frac{1}{n_o}\frac{dn_o}{dx} \right) + \frac{\beta}{2}\left(-\frac{1}{n_o}\frac{dn_o}{dx} \right) + \frac{g\beta_i}{2V_{Ti}^2}}{1+\frac{\beta}{2}} \right] \frac{\partial \Delta_\perp \Phi}{\partial y} + \frac{gB_{0z}}{n_{i0}c} \left(1 + \frac{\rho_i^2 \frac{\beta_e}{2}}{1+\frac{\beta}{2}} \Delta_\perp \right) \frac{\partial \delta n}{\partial y}$$

$$- \frac{V_{Ti}^2}{\omega_{ci} c} \left(\frac{\partial \Delta_\perp \delta B_z}{\partial t} + \frac{g}{\omega_{ci}} \frac{\partial \delta B_z}{\partial y} \right) - \frac{g}{\omega_{ci}} \left(\frac{\partial \Delta_\perp \Phi}{\partial y} + \frac{V_{Ti}^2}{\omega_{ci} c} \frac{B_{0z}}{n_{io}} \frac{\partial \Delta_\perp \delta n}{\partial y} \right)$$

$$= \frac{V_{Ti}^2}{\omega_{ci} n_{0i}} \vec{\nabla}_\perp \bullet \left(\frac{\partial \vec{\nabla}_\perp \Phi}{\partial x} \left[\frac{\partial \delta n}{\partial y} \right] - \frac{\partial \vec{\nabla}_\perp \Phi}{\partial y} \left[\frac{\partial \delta n}{\partial x} \right] \right) + \frac{c}{B_{0z}} \left(\frac{\partial \Delta_\perp \Phi}{\partial x} \left[\frac{\partial \Phi}{\partial y} \right] - \frac{\partial \Delta_\perp \Phi}{\partial y} \left[\frac{\partial \Phi}{\partial x} \right] \right)$$

(2.75a)

$$\frac{\partial \delta n}{\partial t} + \frac{c}{B_{oz}} \frac{-\frac{1}{n_0}\frac{dn_0}{dx} + \frac{1}{B_{0z}}\frac{dB_{0z}}{dx}}{1+\frac{\beta}{2}} \frac{\partial \Phi}{\partial y} - \frac{\beta_e}{\beta_i} \frac{V_{Ti}^2}{\omega_{ci}} \left[\frac{\frac{1}{B_{0z}}\frac{dB_{0z}}{dx} - \frac{\beta}{2}\frac{1}{n_0}\frac{dn_0}{dx}}{1+\frac{\beta}{2}} \right] \frac{\partial \delta n}{\partial y}$$

$$= \frac{c}{B_{0z}} \left[\frac{\partial \delta n}{\partial x}\frac{\partial \Phi}{\partial y} - \frac{\partial \delta n}{\partial y}\frac{\partial \Phi}{\partial x} \right]$$

(2.75b)

$$\delta B_z = \frac{\beta}{2} \delta n$$

(2.75c)

Equations (2.75a) and (2.75b) can be re-written in the following dimensionless form:

$$\frac{\partial \Delta\varphi}{\partial t} = A_1 \frac{\partial \Delta\varphi}{\partial y} + A_2 \frac{\partial \Delta\delta n}{\partial t} - g\frac{\partial \delta n}{\partial t} + \left[\frac{\partial \Delta\varphi}{\partial x}\frac{\partial \varphi}{\partial y} - \frac{\partial \Delta\varphi}{\partial y}\frac{\partial \varphi}{\partial x}\right] + \tau\left(\left[\frac{\partial \Delta\delta n}{\partial x}\frac{\partial \varphi}{\partial y} - \frac{\partial \Delta\delta n}{\partial y}\frac{\partial \varphi}{\partial x}\right] + \left[\frac{\partial^2 \delta n}{\partial x^2}\frac{\partial \varphi}{\partial x\partial y} - \frac{\partial \delta n}{\partial x\partial y}\frac{\partial^2 \varphi}{\partial y^2}\right] + \left[\frac{\partial \delta n}{\partial x\partial y}\frac{\partial^2 \varphi}{\partial y^2} - \frac{\partial^2 \delta n}{\partial y^2}\frac{\partial \varphi}{\partial y\partial x}\right]\right) \tag{2.76a}$$

$$\frac{\partial \delta n}{\partial t} = A_3 \frac{\partial \delta n}{\partial y} - \frac{\left[-\frac{1}{n_0}\frac{dn_0}{dx} + \frac{1}{B_{0z}}\frac{dB_{0z}}{dx}\right]}{\left(1+\frac{\beta}{2}\right)}\frac{\partial \varphi}{\partial y} + \left[\frac{\partial \delta n}{\partial x}\frac{\partial \varphi}{\partial y} - \frac{\partial \delta n}{\partial y}\frac{\partial \varphi}{\partial x}\right] \tag{2.76b}$$

The variable definitions include:

$$A_1 = \tau\frac{\left(-\frac{1}{n_{0x}}\frac{dn_{0x}}{dx} - \frac{1}{B_{0z}}\frac{dB_{0z}}{dx}\frac{\beta}{2}\right)\left(1-\frac{\beta}{2}\right)}{1+\frac{\beta}{2}} + g \tag{2.77a}$$

$$A_2 = \left[\frac{1}{1+\frac{\beta}{2}}\right]\left(g\left(1+\beta_i+\frac{\beta_e}{2}+\frac{\beta^2}{4}\right) + \frac{\beta}{2\tau}\left(-\frac{1}{n_{0x}}\frac{dn_{0x}}{dx} + \frac{1}{B_{0z}}\frac{dB_{0z}}{dx}\frac{\beta}{2}\right)\right) \tag{2.77b}$$

$$A_3 = \frac{\left(-\frac{1}{n_{0x}}\frac{dn_{0x}}{dx} - \frac{1}{B_{0z}}\frac{dB_{0z}}{dx}\frac{\beta}{2}\right)}{1+\frac{\beta}{2}} \tag{2.77c}$$

τ is the ratio of electron and ion temperature.

Perturbation analysis is applied to simplify the system of equations by use of arbitrary functions in which the plasma inhomogeneities are treated as small parameters of the first order, and using a circularly symmetric solution with arbitrary radial profile as the zeroth order solution [3]. Steady state solutions to the nonlinear system of equations are acquired for the streamlines of a flute structure that is propagating along the *y*-axis at a constant velocity.

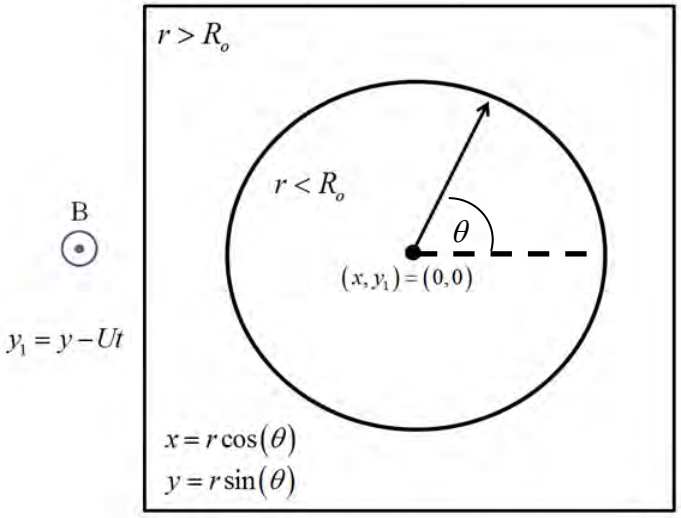

Figure 20. Flute Perturbation Boundaries in the Cylindrical Coordinates Domain

Solutions to these functions are determined by converting the *(x, y)* plane to polar coordinates. The change of variables allows for the simplification of the system of equations by use of arbitrary functions. The plane is partitioned into two regions; one that is less than the characteristic radius and the other that is greater than the characteristic radius. For the inner region of the circle: $(r < R_o)$ the electrostatic potential and density perturbation solutions are approximated using the functions (2.78a, b) that satisfy (2.76a, b):

$$\varphi = C_1 J_1(br)\cos(\theta) + \left(\frac{F_1}{b^2}\right) r\cos(\theta) \tag{2.78a}$$

$$\delta n = DC_1 J_1(br)\cos(\theta) + \left(D\left(\frac{F_1}{b^2}\right) + F_2 \right) r\cos(\theta) \tag{2.78b}$$

For the outer region: $(r > R_o)$ the electrostatic potential and density perturbation solutions are approximated using the functions that also satisfy (2.76a, b):

$$\varphi = C_2 K_1(hr)\cos(\theta) \tag{2.79a}$$

$$\delta n = HC_2 K_1(hr)\cos(\theta) \tag{2.79b}$$

At the boundary of the circle, the following conditions must be satisfied:

$$\varphi_{in}(R_o) = \varphi_{ext}(R_o) \quad (2.80a) \qquad \delta n_{in}(R_o) = \delta n_{ext}(R_o) \quad (2.80b)$$

$$\left.\frac{\partial \varphi_{in}}{\partial r}\right|_{r=R_o} = \left.\frac{\partial \varphi_{ext}}{\partial r}\right|_{r=R_o} \quad (2.80c) \qquad \left.\frac{\partial^2 \varphi_{in}}{\partial r^2}\right|_{r=R_o} = \left.\frac{\partial^2 \varphi_{ext}}{\partial r^2}\right|_{r=R_o} \quad (2.80d)$$

The ratio of the density to potential outside of the vortex

$$H = k_{aps} / (U + A_3)\beta_+ \tag{2.81a}$$

The length scale outside of the vortex: $h = \sqrt{H(g_{norm}) / (U + A_1 + H(A_2))}$ (2.81b)

The variable "*b*" describe the modal structure of the vortex.

The following relation is derived from the boundary conditions:

$$-\frac{h}{b} = \frac{K_2(hR_o)J_1(bR_o)}{K_1(hR_o)J_2(bR_o)} \tag{2.82}$$

where J_1 is the Bessel function of the first kind and K_1 is the modified Bessel function of the second kind.

The coefficient of the linear portion of the potential:

$$F_1 = \frac{b^2\left(\left(U + A_1\right) + D\left(A_2 + \frac{g}{b^2}\right)\right)}{\left(1 + \tau D\right)} \tag{2.83a}$$

Additional linear coefficient of the linear portion of the density perturbation:

$$F_2 = \left(H - D\right)\left(U + A_3\right) \tag{2.83b}$$

In which the intermediate coefficient is defined by:

$$D = \frac{\left(\left(U + A_3\right)\left(h^2/b^2 + 1\right) - U - A_1\right)}{A_2 + \frac{g}{b^2} - \tau\left(U + A_3\right)\left(h^2/b^2 + 1\right)} \tag{2.83c}$$

The coefficient of the Bessel portion of the potential region $\left(r < R_o\right)$ is defined as:

$$C_1 = -\frac{F_1/b^2 + F_2/\left(D - H\right)}{J_1\left(bR_o\right)}R_o \tag{2.83d}$$

Coefficient of the Bessel portion of the potential $\left(r > R_o\right)$ defined as:

$$C_2 = -\frac{-F_2 R_o}{\left(D - H\right)K_1\left(hR_o\right)} \tag{2.83e}$$

Additionally, the following flute vortex parameters are defined as follows:

- Normalized drift velocity $U = U/v_{ti}$, normalized Speed of Light: $c_p = c/v_{ti}$ normalized gravity constant: $g_{norm} = g/r_i\omega_{ci}^2$
- Normalized density scale length: $k_{norm} = k_n\left(r_i\right)$, and the normalized characteristic radius to ion Larmor radius: $R_{ON} = R_o/r_i$

The total plasma beta is comprised of the electron and ion betas: $\beta = \beta_e + \beta_i$. The plasma betas are defined as:

$$\beta_+ = 1 + \beta/2 \qquad \beta_- = 1 - \beta/2 \qquad \beta_s = 1 + \beta_i + \beta_e/2 + \left(\beta^2\right)/4$$

Figure 21 shows a plot of an ideal dipole flute structure solution acquired from the arbitrary functions. Many possible solutions exist based on the selection of "*b*", the modal structure. The "*b*" value is selected to yield the dipole structure.

The dipole solution consists of two vortices, each centered around stagnation points that are similar in appearance. One vortex is has a positive density distribution while the other is negative. There is a sharp, continuous edge that forms around the density profile at the characteristic radius, which makes this flute non-adiabatic. An interior separatrix contour is present down the middle of the two vortices, dividing the two regions.

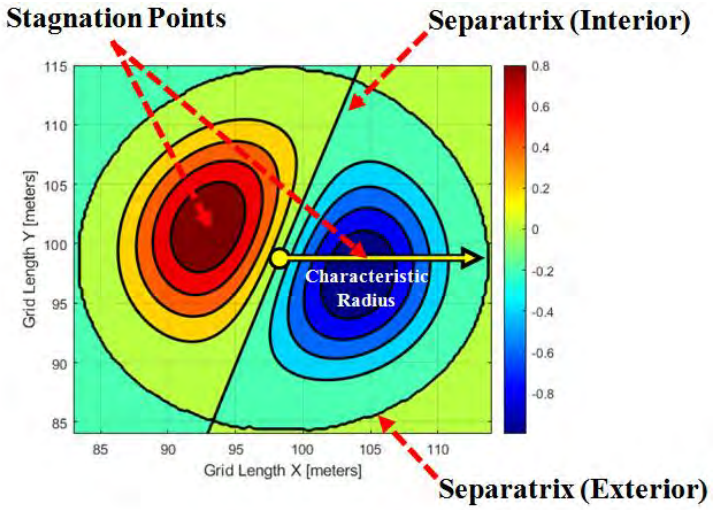

Figure 21. Ideal Flute Density Perturbation Features

The outer separatrix divides the high amplitude region of the flute density from the remainder of the medium in which the density amplitude approaches zero. The

characteristic radius defines the limit of the exterior separatrix separating the interior and exterior regions. The vortices' radial profile appears to be non-monotonous in which rotating counter-flows exists within the interior of the characteristic radius. It is suggested by [3] that these counter-flows are destabilizing.

2.3.4 Alteration of Flute Structures

Multiple free energy sources for instabilities coexist in magnetized plasmas with density gradient and velocity shear. Inhomogeneous flows such as poloidal mean sheared flow, zonal flow, and toroidal rotations are driven intrinsically and/or externally [24]. Strong inhomogeneity of the perpendicular flow can be a free energy source of the Kelvin-Helmholtz (KH) instability and interchange mode [24]. In this research effort, a single fluid MHD model is developed and applied to investigate pressure and gravitational forces to drive the shear and flow instabilities coexisting with an initial flute density perturbation.

There is a large group of characteristic frequencies depending on the local state at a given point within the plasma. The individual particle motion is directly associated with collisional phenomena, as given by the characteristic frequencies and relaxation times of ionization, excitation, recombination, attachment, charge exchange, elastic collisions, fusion reactions, and other types of elementary processes [25]. The use of the MHD approximation limits the model to macroscopic plasma behavior such as drift waves. Drift waves due to pressure gradients and equivalent gravitation fields, to associated transverse electric fields are characterized by certain wave lengths and frequencies. The drift motions couple to growing flute-like electrostatic or electromagnetic disturbance in

the plasma caused from the anti-parallel guiding centre motions of ions and electrons in a gravitational field and involves finite Larmor radius and other high order effects [25]. The shear flow is externally fixed with an imposed driver, as would arise from non-ambipolar losses in the background plasma [25]. The simulation applied in this research assumes that a space-charge separation exists initially, which produces an initial E × B shear flow. Based on the behavior of the interacting plasma flows during the interchange process, it is believed that presence and dynamics of the vortices may strongly affect the macroscopic behavior of the turbulence.

The presence of shear in the flow of neutral fluids and plasmas gives rise not only to instability of the sheared layer, i.e., the Kelvin-Helmholtz (K-H) instability, but also to stabilization of other instabilities, such as the interchange mode Rayleigh-Taylor instability [26]. The presence of zonal and shear flow mechanisms around flute structures is modeled using the single fluid MHD model as shown in Figure 22. The flute structure is placed in the center of a neutral density layer that is enclosed with a heavy layer on top and a lighter layer on the bottom. Initially, these layers are in a static equilibrium, in which the pressure gradients that compress the density layers are balanced. A sinusoidal disturbance is applied at the interface to initiate the MHD instability. The apriori velocity moves the density in opposite directions along the x axis, creating the zonal flow. Gravity acts along the y - axis, perpendicular to the velocity vectors. The trigged instability causes the density layers to mix as the force of gravity and the velocity flow interact to create a shear flow. The shear flow tends to dominate the crests of the density layers that were initially caused by the sinusoidal perturbation. The flute structure succumbs to these interactions between the density layers, causing the stagnation points to morph in shape.

Variations in the sinusoidal perturbation will influence the location and severity of the shear flow, and the morphology of the initial flute structure.

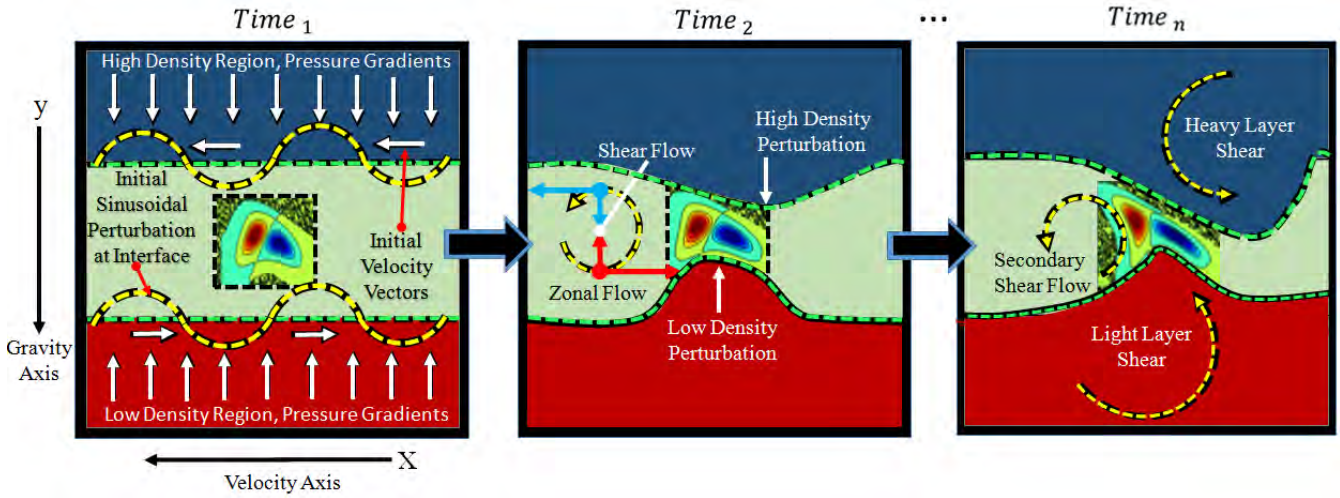

Figure 22. Single Fluid MHD Process

It is important to distinguish the types of dipole flute structures that potentially exist in nature accordingly to their physical characteristics including shape, uniformity, and symmetry. The characteristics can be generalized to the process from which the flute structures form during the interchange instability. Examples include the linear, quasi-linear, and nonlinear stages. The following are properties for the Linear flute mode characteristics (see Figure 23):

1.) Strictly identical stagnation point shapes

2.) Symmetric stagnation about the interior separatrix

3.) Uniform exterior separatrix with symmetry over the interior separatrix

4.) Linear interior separatrix

The Quasi-Linear flute mode characteristic is a uniform exterior separatrix with a symmetry not with respect to interior separatrix as seen in Figure 24. All other flutes that do not satisfy the linear or quasi linear characteristics are considered nonlinear modes

(see Figure 25). Figure 26 shows an organized array of flutes that could exist due to the persistence of zonal flows and suppression of shear flows during the interchange process.

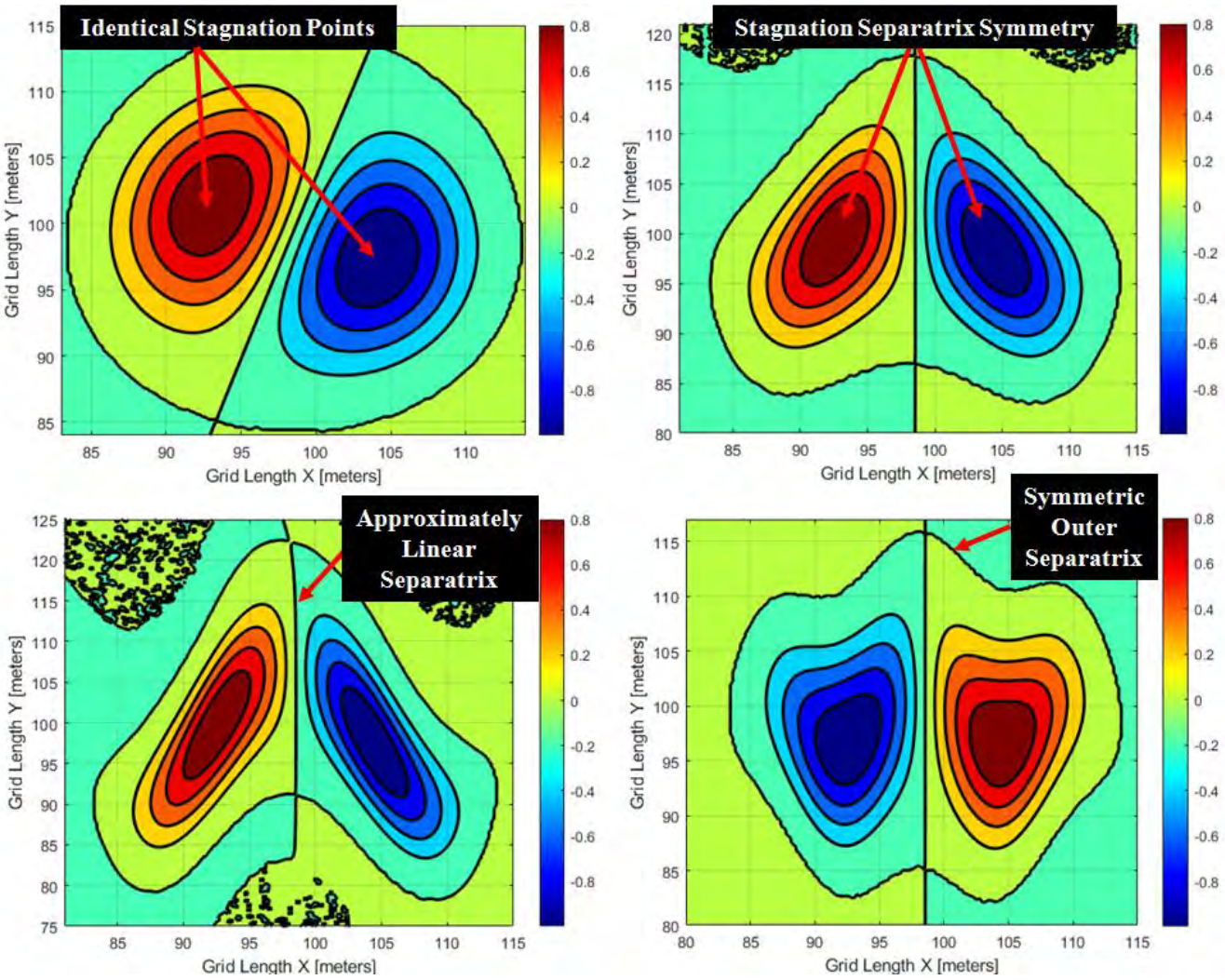

Figure 23. Examples of Linear Flute Modes

The previous sections have demonstrated the mathematical rigor for deriving the dipole flute structure from two-fluid MHD nonlinear equations. Application of the single fluid MHD model yields modified flute structures with unique symmetry and uniformity properties. These flute structures are possible forms that could exist in the F-layer ionosphere depending on the progression of interchange instability.

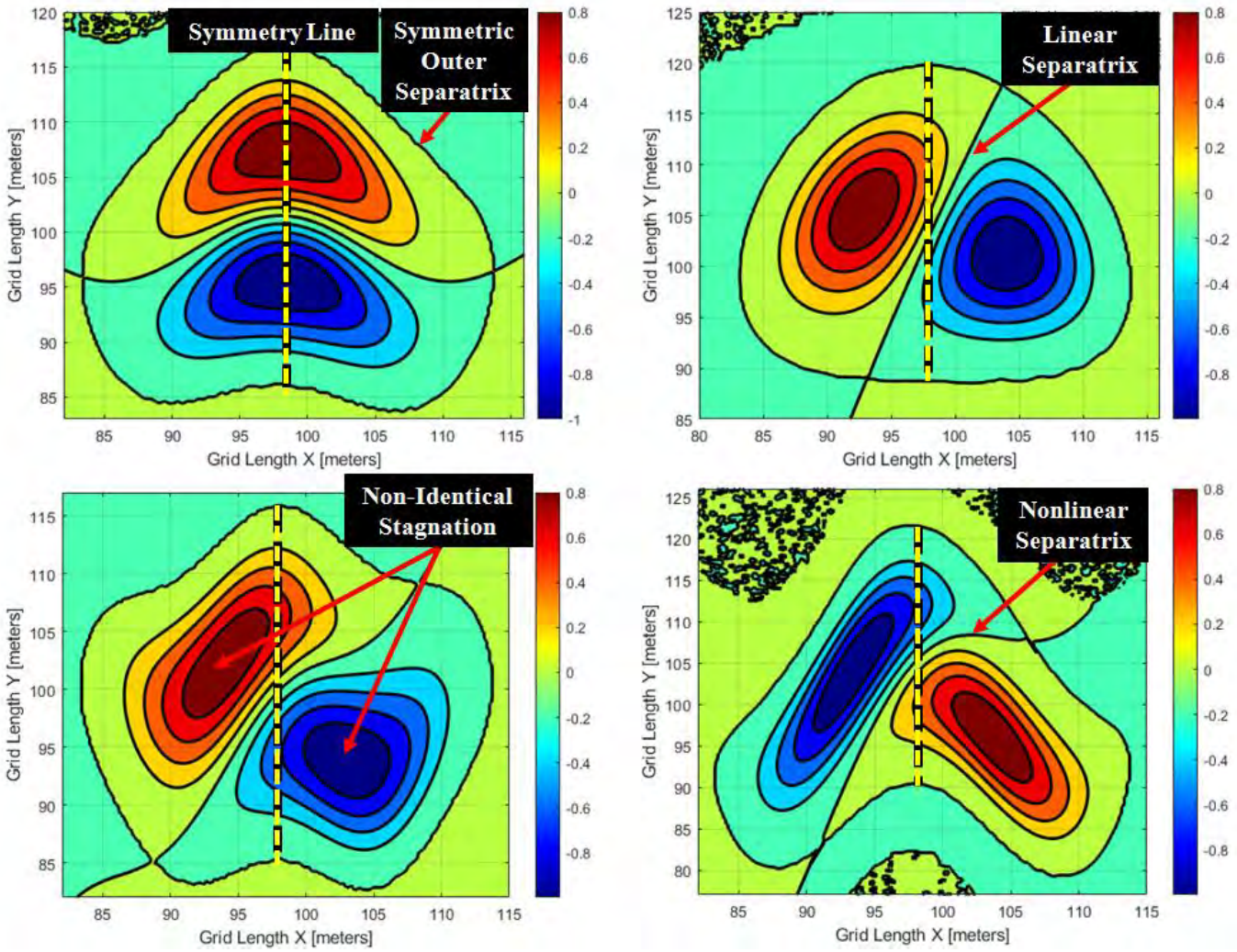

Figure 24. Examples of Quasi-Linear Flute Modes

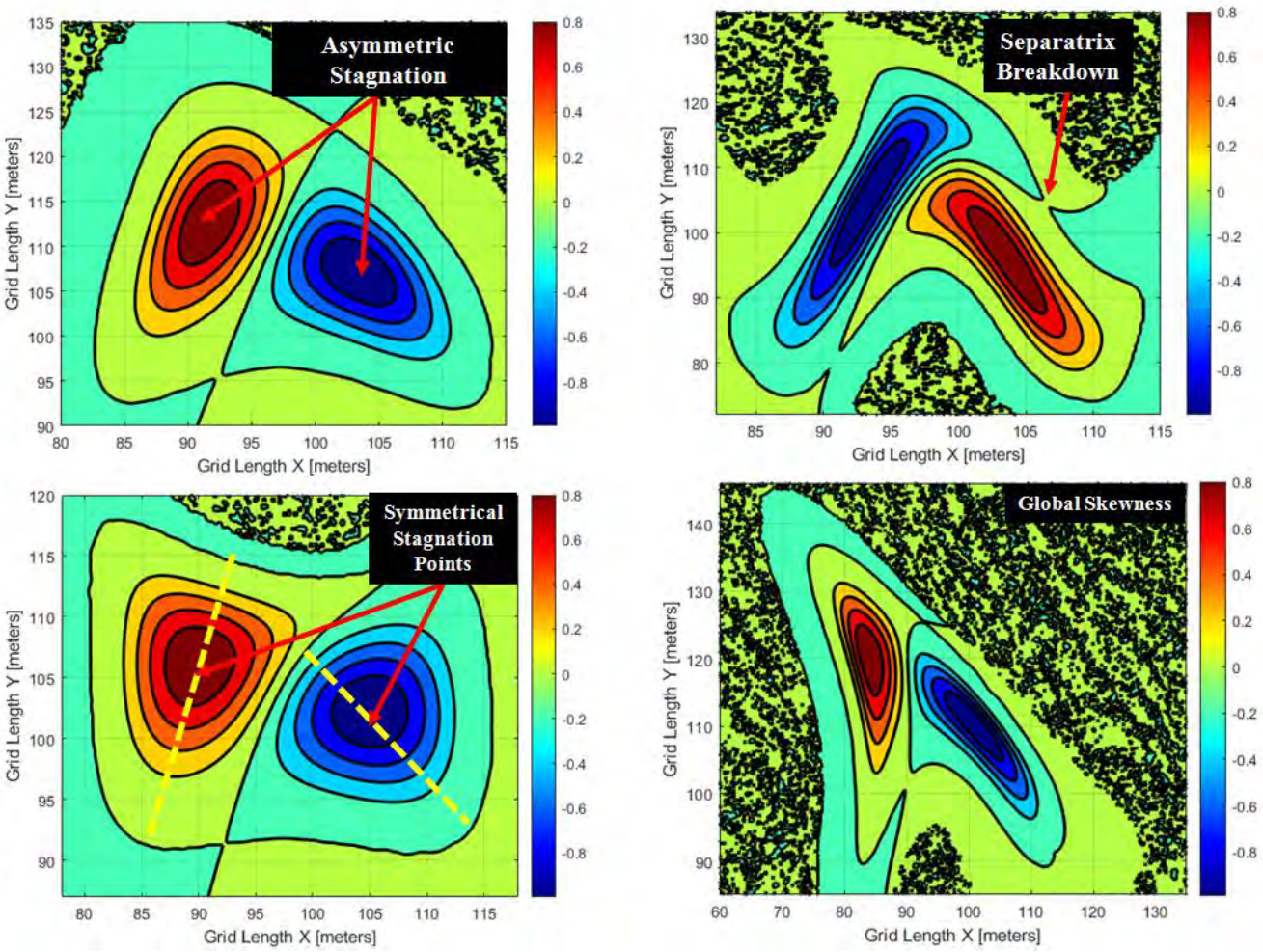

Figure 25. Examples of Nonlinear Flute Modes

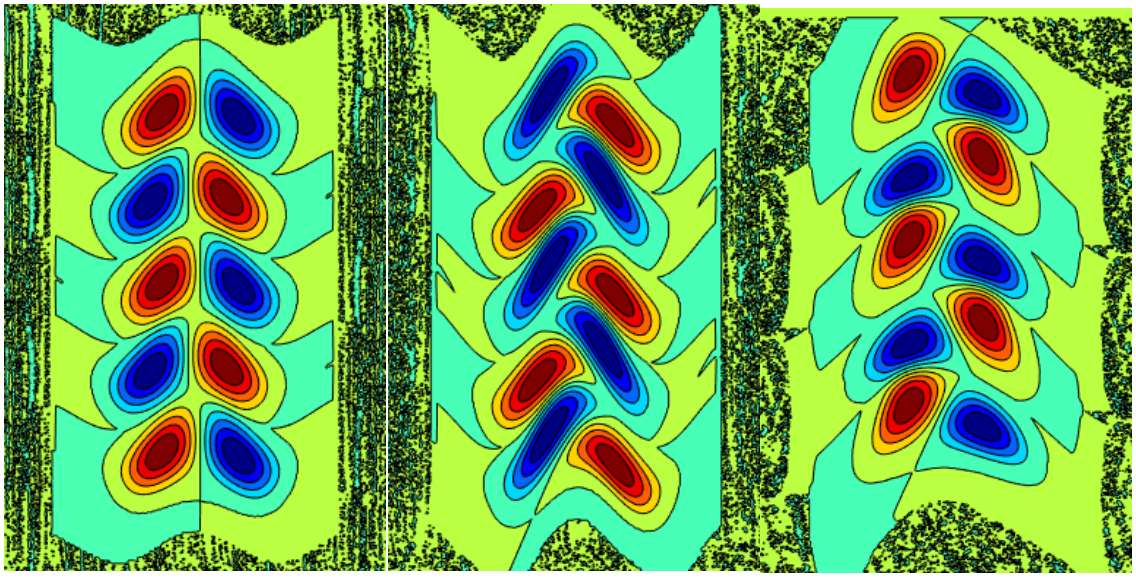

Figure 26. Organized Flute Arrays: Linear (left), Quasi-linear (middle), and Nonlinear (right)

2.5 Summary

This chapter presented the theory required to understand the formation and significance of flute structures in the F-layer ionosphere. MHD is critical to the numerical modeling of both the flute structure behavior and other macroscopic plasma instabilities that can alter a flute structure's features. A subset of unique flute structures are characterized by linear, quasi-linear, and nonlinear features in relation to each flute's interior/exterior separatrix, stagnation points, and symmetry. The spectral method is a fast and effective way to discretize the slow varying envelope approximation of the Helmholtz wave equation over a finite domain. The following chapter will continue to evolve the phase screen concept through incorporation of the MHD derived flute structures and the expanded phase cube geometry.

III. DEVELOPMENT OF PHASE CUBES AND FLUTE SCREENS

The development of a forward scatter propagation model begins with the derivation of phase screens and phase cubes using the autocorrelation of random Gaussian distributed phase lags and the Kolmogorov power spectrum to describe the ambient nature of density fluctuations in the ionosphere. An analytic calculation of the flute structure perturbation power spectrum is presented to determine stochastic realizations for a variety of flute densities over a finite sampling grid. These screen realizations are derived for one and two dimensional cases to enable cross-verification prior to implementing a three-dimensional propagation configuration. The three dimensional phase cube structure concept is further evolved to model the ideal and stochastic flute structures and to enable comparison of the frequency and scintillation characteristics for a variety of flutes as addressed in the following chapters.

3.1 Kolmogorov Phase Screen Development

The development of phase screens begins with relating the power spectral density of the electron density fluctuations to a phase power spectrum approximation. The phase (ϕ) relationship starts with the formulation of the optical path length along the propagation path (r) within the propagation medium.

$$\phi(r) = -(\beta)(r_e) \int_{-\Delta r/2}^{\Delta r/2} \Delta N_e(r) dr \tag{3.1}$$

where β is the propagation wavelength, and $\Delta N_e(r)$ is the change in electron density with respect to the spatial propagation change in $\Delta r = (\Delta x, \Delta y, \Delta z)$, r_e is the classical electron radius, and the negative sign represents the direction along the propagation path. Integration of this formula yields:

$$\phi(r) = -(\beta)(r_e)\left[\Delta N_e(r)\right]\Delta r \tag{3.2}$$

Next, the autocorrelation of the phase is determined by convolution with a biased or perturbed version of itself to examine similarities between the realizations at different locations within the medium. The following is the convolution relation equation applied to the phase terms:

$$(f * g)(\xi) = \int_{-\infty}^{\infty} f^*(r) g(r+\xi)\, dr \tag{3.3}$$

Convolution $f * g$ provides the probability density function of the sum of two independent random variables. If the correlation coefficient is calculated for all lags, $\xi = 0, 1, 2, \cdots \mathrm{N}-1$, the resulting series is called the autocorrelation series. The ensemble average $\langle\ \rangle$ of the phase samples are taken with respect to the collective random lags. The autocorrelation of phase is determined in the following manner:

$$B_\phi = \left\langle \phi(r)\, \phi^*(r+\xi) \right\rangle \tag{3.4}$$

Substitute the optical path length phase formula into the autocorrelation relationship:

$$B_\phi = \left\langle \left(-(\beta)(r_e) \int_{-\Delta r/2}^{\Delta r/2} \Delta N_e(r)\, dr \right) \left(-(\beta)(r_e) \int_{-\Delta r'/2}^{\Delta r'/2} \Delta N_e(r')\, dr' \right) \right\rangle \tag{3.5}$$

where $r' = r + \xi$

Re-arrange the terms to form the double integral:

$$B_{\phi} = \left[(\beta)(r_e) \right]^2 \left(\int_{-\Delta r/2}^{\Delta r/2} \int_{-\Delta r'/2}^{\Delta r'/2} \left\langle \Delta N_e(r) \Delta N_e(r' + \xi) \right\rangle dr dr' \right) \tag{3.6}$$

Let $B_{N_e}(r', \xi)$ represent the autocorrelation of the change in the electron density:

$$B_{N_e}(r', \xi) = \left\langle \Delta N_e(r) \Delta N_e(r' + \xi) \right\rangle \tag{3.7}$$

The transform applied to relate the autocorrelation of the electron density to the phase autocorrelation is given by the double integral:

$$B_{\phi} = \left[(\beta)(r_e) \right]^2 \left(\int_{-\Delta r/2}^{\Delta r/2} \int_{-\Delta r'/2}^{\Delta r'/2} B_{N_e}(r', \xi) dr dr' \right) \tag{3.8a}$$

Integrate with respect to *r*:

$$B_{\phi} = \left[(\beta)^2 (r_e)^2 \right] (\Delta r) \left(\int_{-\Delta r'/2}^{\Delta r'/2} B_{N_e}(r', \xi)\, dr' \right) \tag{3.8b}$$

The electron density fluctuations cannot statistically be represented in the spatial position domain, but rather the spatial frequency domain where the power spectrum resides. Therefore, the fourier transform of the autocorrelation function of the phase B_{ϕ} is used to obtain the power spectral density (frequency spectrum). The fourier transform relationship between the spatial frequency (*K*) and spatial position (*r*) domains is given by:

$$F(K) = \int_{-\infty}^{\infty} f(r) e^{-iKr} dr \tag{3.9}$$

This relationship is applied to create the autocorrelation and power spectral density. Substitution of phase power spectral density and autocorrelation variables into this formula yields:

$$S_{\phi}\left(K_r\right) = \int_{-\infty}^{\infty} B_{\phi}\left(r\right) e^{-iKr} dr$$

(3.10)

Substitute the autocorrelation function with respect to electron density into this fourier transform relationship yields a direct correspondence to the phase power spectrum:

$$S_{\phi}\left(K_r\right) = \int_{-\infty}^{\infty} \left[\left(\beta\right)^2 \left(r_e\right)^2\right] \left(\Delta r\right) \left(\int_{-\infty}^{\infty} \left[B_{N_e}\left(r', \xi\right) dr' \right] \right) e^{-iKr} dr$$

(3.11a)

Re-arrangement of terms:

$$S_{\phi}\left(K_r\right) = \left[\left(\beta\right)^2 \left(r_e\right)^2\right] \left(\Delta r\right) \int_{-\infty}^{\infty} \left(\int_{-\infty}^{\infty} \left[B_{N_e}\left(r', \xi\right) \right] \right) e^{-iKr} dr' dr$$

(3.11b)

The fourier transform of the electron density autocorrelation is the power spectral density of the electron density fluctuation.

$$S_{N_e}\left(K_r\right) = \int_{-\infty}^{\infty} B_{N_e}\left(r\right) e^{-iKr} dr$$

(3.11c)

Substitution of this identity into (3.11b) yields the relationship between the power spectrum electron density to the phase power spectral density:

$$S_{\phi}\left(K_r\right) = \left[\left(\beta\right)^2 \left(r_e\right)^2\right] \left(\Delta r\right) S_{N_e}\left(K_r\right)$$

(3.11d)

where $S_{N_e}\left(K_r\right)$ is considered a pre-calculated power spectrum that analytically models the irregularities as a power spectrum function of scale sizes. The Kolmogorov power spectrum is defined in equation (3.12).

$$S_{N_e}(K_x,K_y,K_z)=\frac{\sigma_{N_e}^2(2\pi)^{-1/2}l_i^2(l_i/L_o)^{(m-2)/2}K_{m/2}\left(l_i\sqrt{K_x^2+K_y^2+K_z^2+1/L_o^2}\right)}{K_{(m-2)/2}\left(l_i/L_o\right)\left(l_i\sqrt{K_x^2+K_y^2+K_z^2+1/L_o^2}\right)^{m/2}} \tag{3.12}$$

where σ_{Ne}^2 is the electron density variance, L_o is the outer scale of the plasma, l_i is the inner scale of the plasma, K_x, K_y, and K_z are the spatial frequencies of the phase screen grid points corresponding to the *x, y,* and *z* directions respectively, *m* is the slope of the power spectral density, and K_n is the Bessel function of order *n*. The second order moment of the phase is realized by letting $\xi=0$. This is known as the variance relation to the electron density fluctuation. The variance in the electron density changes with respect to the distance between sample points along the propagation path.

$$\sigma_{N_e}^2=\left[\left(\beta\right)^2\left(r_e\right)^2\right]\left(\Delta r\right)\int_{-\Delta r'/2}^{\Delta r'/2}B_{N_e}\left(r',\xi=0\right)dr' \tag{3.13}$$

Figure 27 shows the relationship between the normalized power spectrum and the increase in the phase variance. The increased order of magnitude in the phase variance causes a similar increase in the magnitude power spectrum, while maintaining the slope of 3. This is the typical slope of the Kolmogorov power spectrum that accurately represents ambient turbulence caused by the ionic content of the ionosphere.

Utilizing the ideal phase power spectrum, statistical realizations can be created from a random distribution of lags that are representative of electron density fluctuations that correspond to phase changes in the spatial position domain. These lags are created using a Gaussian distributions of zero mean and a variance of unity. The number of realizations of a distribution correspond to the number of phase screen realizations needed for a statistical average to create the ideal phase screen realization.

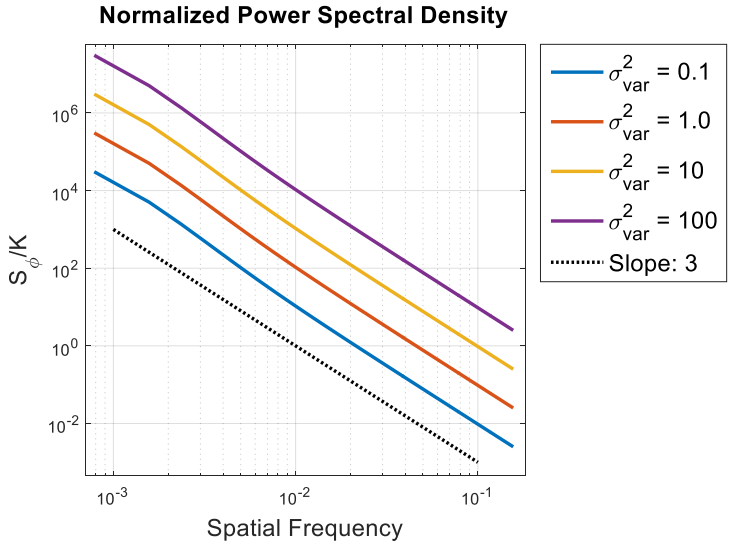

Figure 27. Power Law PSD

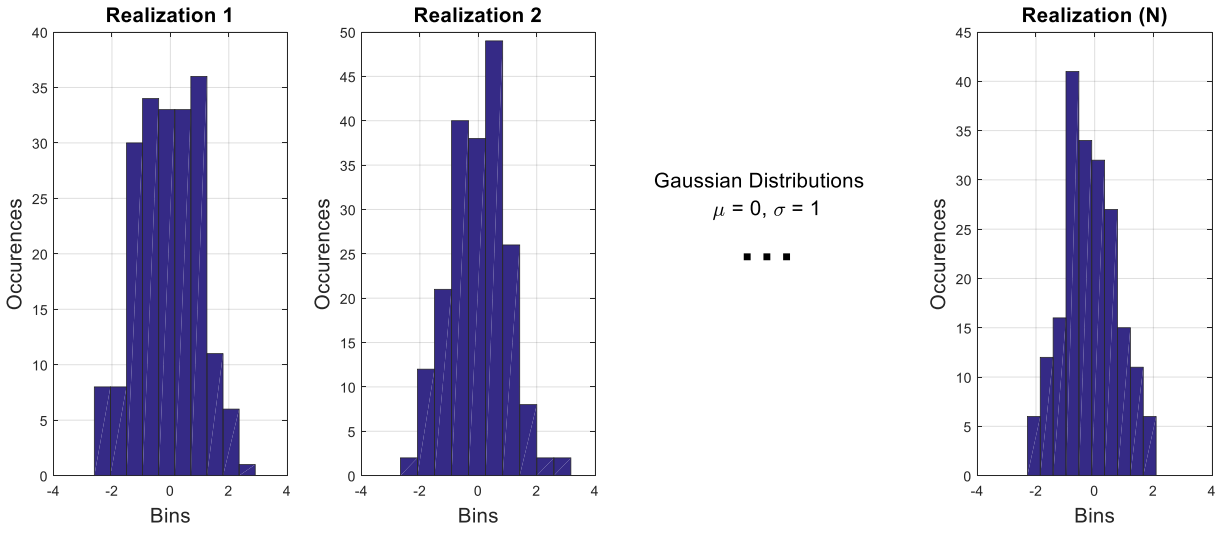

Figure 28. Random Gaussian Distributions

The lags are applied by cross correlating the power spectrum phase values with the random values to vectorize the inputs into real and imaginary components.

$$c_q = \sqrt{1/2}\left(G_r + iG_i\right) \tag{3.14}$$

where G_r and G_i are independent vectors of Gaussian distribution of values.

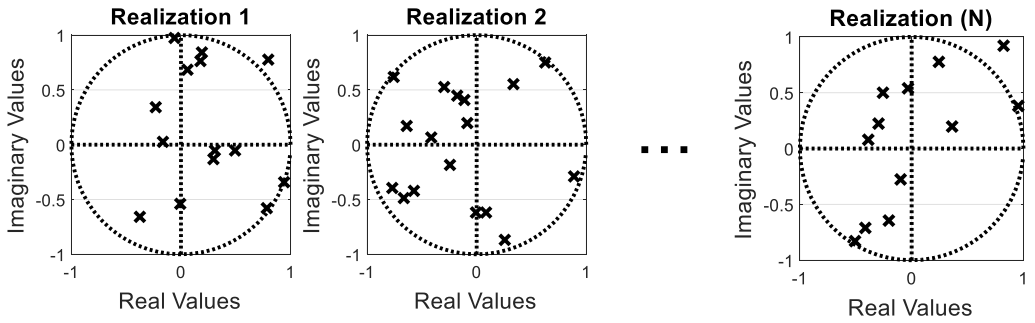

Figure 29. Random Realizations of Gaussian Distributed Complex Values

The fourier transform of the autocorrelation is equivalent to the absolute square of the fourier transform of the input phase samples. The absolute square of the fourier transform of the phase is equivalent to the phase power spectral density:

$$S_\phi\left(K_r\right) = \left|\int_{-\infty}^{\infty} \phi(r) e^{-iKr}\, dr\right|^2 \tag{3.15a}$$

Substitution of the discrete fourier transform in three dimensions yields:

$$S_\phi\left(m_1\Delta K_x, m_2\Delta K_y, m_3\Delta K_z\right) = \left|\sum_{m_1=0}^{M-1}\sum_{m_2=0}^{N-1}\sum_{m_3=0}^{P-1} \phi(\Delta x, \Delta y, \Delta z) e^{-i2\pi[A]}\Delta K\right|^2 \tag{3.15b}$$

where:

$$\Delta K = \Delta K_x \Delta K_y \Delta K_z = 2\pi \Big/ \left(L_x L_y L_z\right) \qquad n_1 = 0,\ldots,M-1$$
$$m\Delta K = m_1\Delta K_x, m_2\Delta K_y, m_3\Delta K_z \qquad n_2 = 0,\ldots,N-1$$
$$A = \left(m_1 n_1 / M\right) + \left(m_2 n_2 / N\right) + \left(m_3 n_3 / P\right) \qquad n_3 = 0,\ldots,P-1$$

$L_{x,y,z}$ are the lengths of the phase cube sample grid. *M*, *N*, and *P* are the number of samples that span each dimension. The significance of these parameters is stated later in this section for the one dimensional phase screen case.

Applying the necessary operations on the left side of the equation to create equivalency on the right side.

$$\left(\frac{S_\phi\left(m_1\Delta K_x, m_2\Delta K_y, m_3\Delta K_z\right)}{\Delta K} \right)^{1/2} = \left| \sum_{m_1=0}^{M-1}\sum_{m_2=0}^{N-1}\sum_{m_3=0}^{P-1} \phi\left(\Delta x, \Delta y, \Delta z\right) e^{-i2\pi[A]} \right| \tag{3.16}$$

Multiply the left side by the wide sense stationary complex Gaussian realizations constant, canceling the negative phasor on the right side of the equation and apply the series summation required to sum the independent realizations together and divide by the number of realizations to create an average:

$$\sum_{q=1}^{Q} c_q \left(\frac{S_\phi\left(m_1\Delta K_x, m_2\Delta K_y, m_3\Delta K_z\right)}{\Delta K} \right)^{1/2} \Big/ Q = \left| \sum_{m_1=0}^{M-1}\sum_{m_2=0}^{N-1}\sum_{m_3=0}^{P-1} \phi\left(\Delta x, \Delta y, \Delta z\right) e^{-i2\pi[A]} \right| \tag{3.17}$$

This relation demonstrates the equivalency of the left side formulation with the average of the phase lags that are modeled using the Gaussian random distributions. The right side shows the discrete fourier transform of the phase realizations. This operation is reversed by applying an inverse fourier transform to both sides of the equation, resulting in the spatial position domain phase realization. This solution will be identical for the one and two dimensional cases. The difference between each dimension is the number of ΔK terms corresponding to the dimensional span.

$$B\sum_{m_1=0}^{M-1}\sum_{m_2=0}^{N-1}\sum_{m_3=0}^{P-1}\left(\left[\sum_{q=1}^{Q}c_q\left(\frac{S_\phi\left(m_1\Delta K_x, m_2\Delta K_y, m_3\Delta K_z\right)}{\Delta K}\right)^{1/2}\Big/Q\right]e^{i2\pi[A]}\right)=\phi(x,y,z) \tag{3.18}$$

where, $B=\left(\frac{1}{M-1}\right)\left(\frac{1}{N-1}\right)\left(\frac{1}{P-1}\right)$

Proper sampling of an irregularity through the application of a phase screen requires that the following screen grid conditions are satisfied:

1.) Sample Grid: L > 5 L_o

2.) Sample index: $\Delta x \le \frac{l_i}{3}$

Condition 1 ensures that the grid is long enough to sample the large scale irregularity and Condition 2 ensures that there are enough points to adequately sample the smallest irregularity.

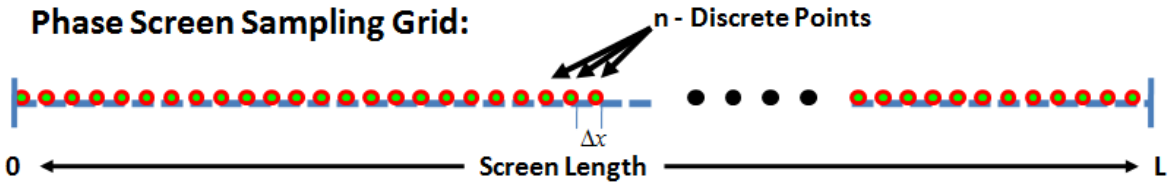

Figure 30. One dimensional Phase Screen Sampling Grid

The simulations utilized in this research effort assumes an outer scale of 1000 meters for large scale structures. Therefore, the grid length for the Kolmogorov screen is 8000 meters or eight times the outer scale. A significant constraint is the number of samples used along the phase screen grid which will limit the smallest dimensions of irregularities sampled. A three dimensional phase cube model will limit this factor due to the computational expense accrued when sampling the irregularities over multiple dimensions. It is therefore necessary to keep the sample size small in order to minimize

this issue by increasing the size of the inner scale. An inner scale of 200 meters is established for the smaller scale structures. An added benefit is that this ensures that the flute structures investigated in this research are the smallest sampled structures represented on a phase screen grid.

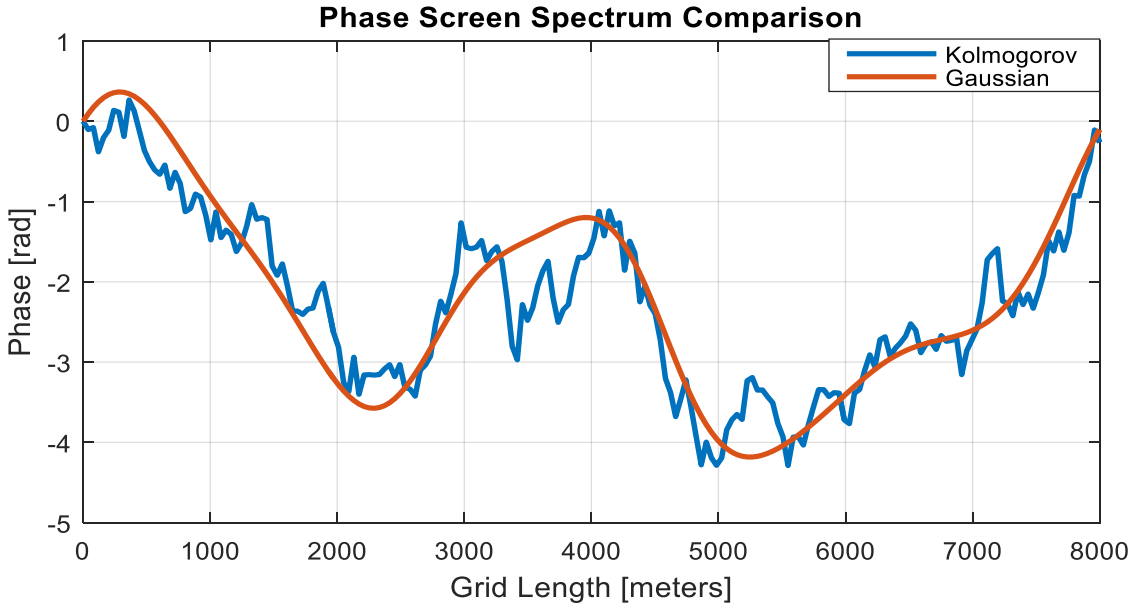

Figure 31. One dimensional Phase Screen Realizations

Figure 31 shows the comparison between a phase screen realization formulated using the Kolmogorov spectrum and a realization that uses a Gaussian spectrum using identical random lags. This plot demonstrates general agreement of the phase fluctuations and confirms proper programming and implementation of the numerical techniques. The 2D realizations of the phase screens are shown in Figure 32. The phase increases correspond to the increase from the second moment phase variance that represents the severity of the density fluctuations observed between the inner and outer scale irregularities.

Figure 33 shows the volume of the phase realization determined from the three dimensional Kolmogorov power spectrum. The continuity of the irregularities in each dimension is notable. It is expected that the phase cube arrangement will create a prolonged phase change to an incident electric field compared to the field interaction with a single phase screen sample.

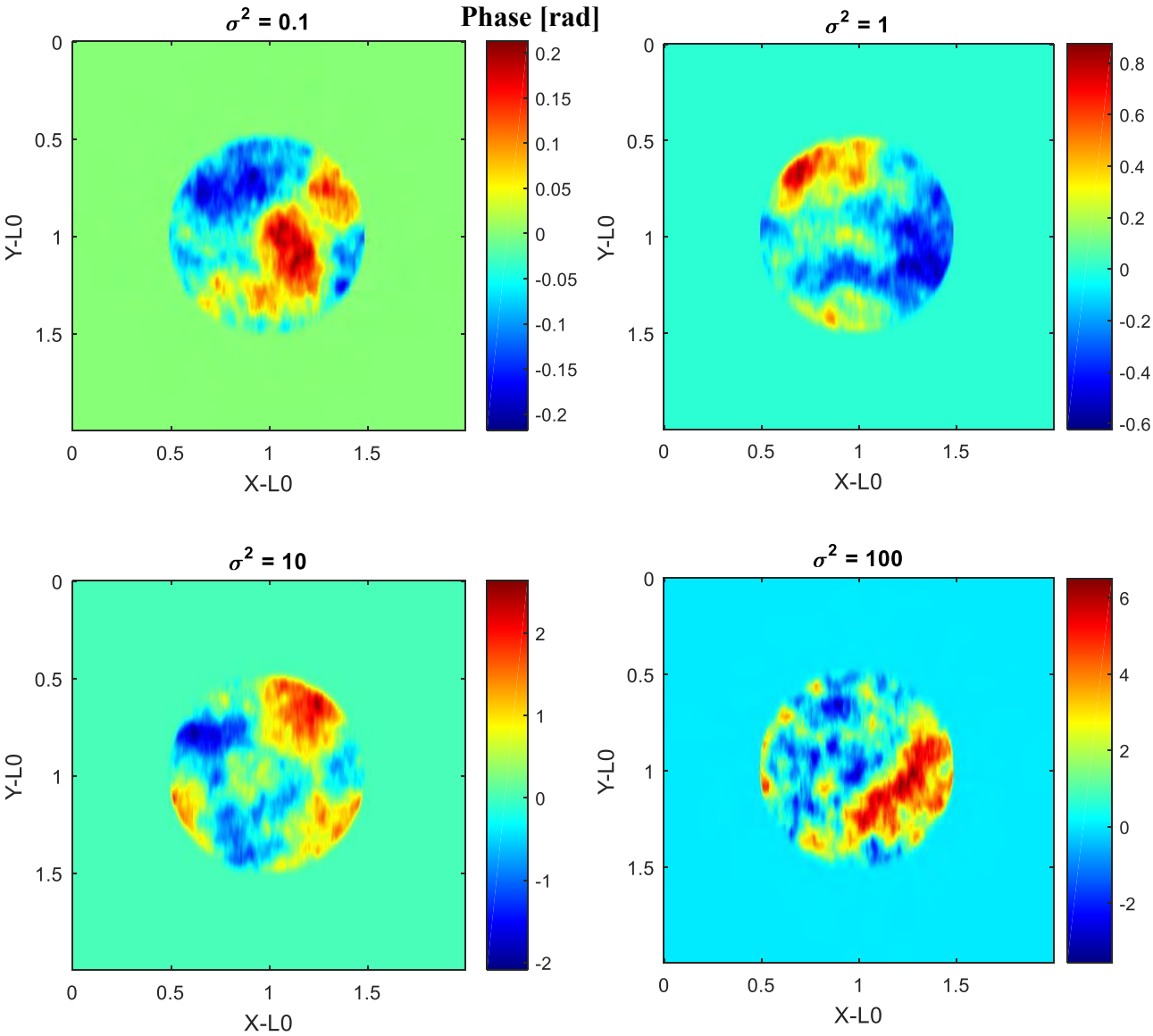

Figure 32. Two-Dimensional Phase Screen Realizations with Varied Phase Variance

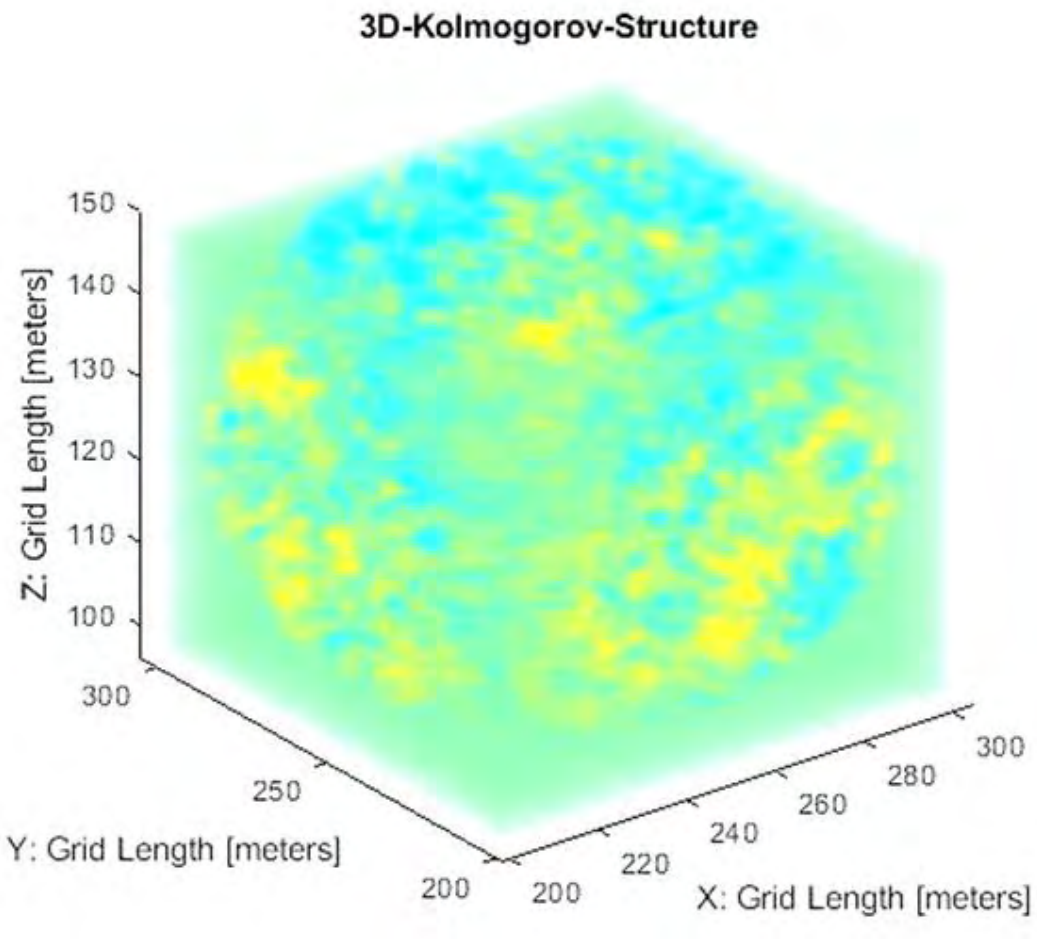

Figure 33. Kolmogorov Phase Cube

The plots in Figure 34 show the analysis of each phase screen/cube's realizations averaged extrema over the change in phase variance. The median is consistently close to zero, indicating an adequate sampling of the random Gaussian distribution of values with zero mean. The extrema appear to deviate equally away from zero as phase variance increases. The larger phase variances result in a greater possible range of phase values. Consequently, the standard deviation of the phase increases exponentially in relation to the increase in the phase variance.

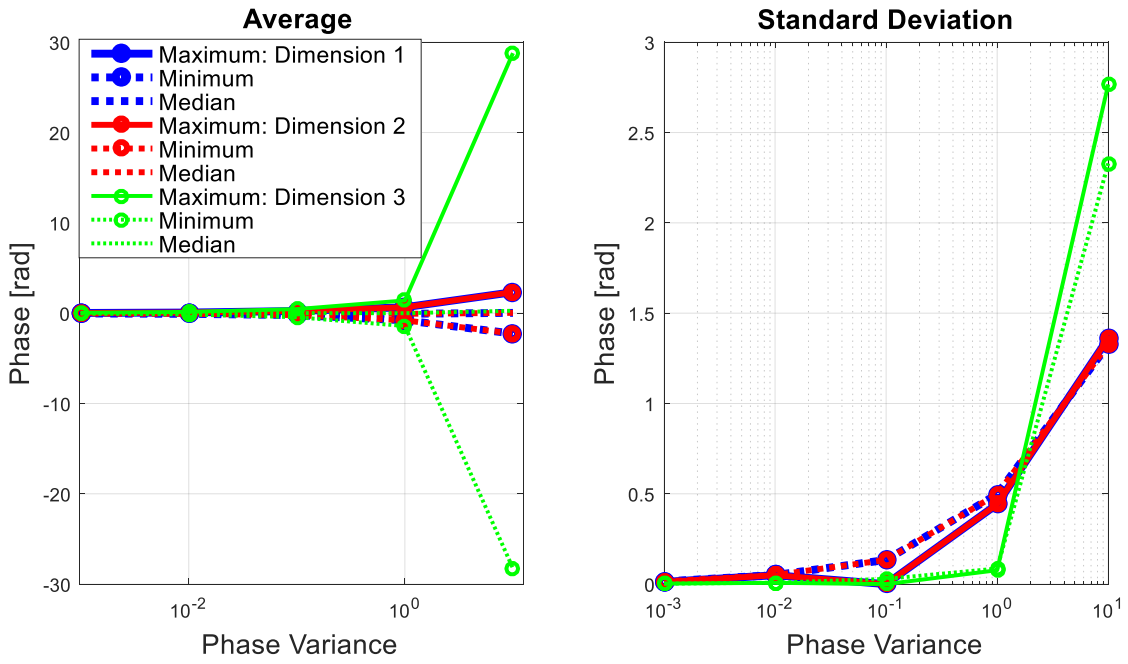

Figure 34. Phase Extrema

The phase screens and phase cubes developed in this section demonstrate desired characteristics for representing the slab layer of irregularities. However, the implementation of the phase screen concept in terms of electromagnetic wave scattering is validated through the comparison to weak scattering theory concept developed by Salpeter discussed in the following chapter. The next section further extends the power spectrum concepts to derive stochastic realizations of flute perturbation structures.

3.2 Ideal Flute Structure Phase Screen and Phase Cube Development

The stochastic representation of the ideal flute structure begins with the phase representation of the ideal flute structure and deriving a corresponding power spectrum in the spatial frequency domain. This notion is the reverse operation of the procedure described in the previous section in which the Kolmogorov power spectrum was provided. The ideal flute structure investigated in this section has a characteristic radius

of 22 meters. This dimension is accepted as an adequate characterization of the typical size for small scale irregularities observed in the F-layer ionosphere. The grid length of the flute structure is the length of the diameter of the flute (44 meters). A single dipole flute structure grid has 226 samples in its two dimensional cross-section. A maximum of 1004 grid samples is applied to a global density map that is inclusive of multiple flute structures. The sample limitation is strictly computational and applicable in all three dimensions.

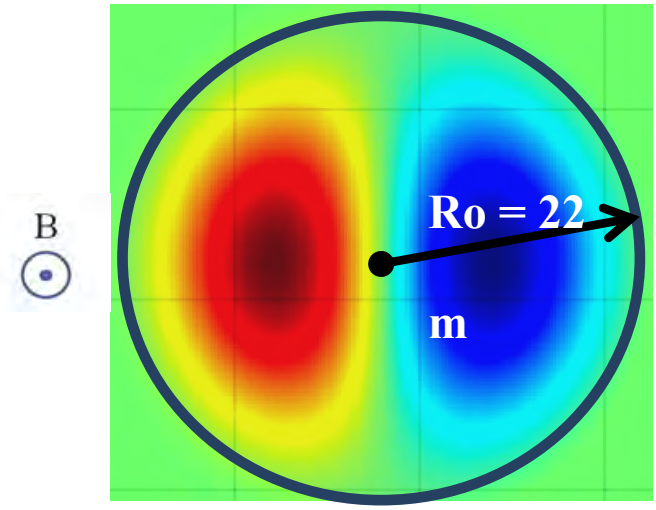

Figure 35. Ideal Flute Structure

The following formulation and analytics determines the physical length of the flute perturbation sample grid. Let $N_{\Delta x}$ and $N_{\Delta y}$ equate to 1004 samples. A proportion can be established to scale the propagation grid from a single flute structure.

$$\frac{V_d}{N_{fl}} = \frac{D_L}{N_{\Delta x,\Delta y}} \tag{3.19a}$$

where V_d is the flute vortex diameter, N_{fl} is the samples for a single flute, $N_{\Delta x,\Delta y}$ is the samples for the propagation grid in the *x* and *y* dimensions, and D_L is the minimum grid length. Solving for D_L:

$$\frac{\left(N_{\Delta x,\Delta y}\right)V_d}{N_{fl}} = D_L \tag{3.19b}$$

Based on the sampling restrictions for this research effort, the physical grid length of a typical density map is:

$$D_L = \frac{\left(1004[samples]\right)\ \ 44[meters]}{226[samples]} \simeq 196[meters]$$

This dimension will adequately sample 4 flute structures aligned abreast.

The following optical path length based calculations are applied to the density perturbations on a two dimensional screen in the *x* (3.20a), *y* (3.20b), and *z* (3.20c) directions:

$$\phi_{x\left(N_y \times N_z\right)} = \left(C/f\right) r_e N_{frac} \mu_{Den} \left(\Delta x\right) \phi_{x\left(N_y \times N_z\right)} \tag{3.20a}$$

$$\phi_{y\left(N_x \times N_z\right)} = \left(C/f\right) r_e N_{frac} \mu_{Den} \left(\Delta y\right) \phi_{y\left(N_x \times N_z\right)} \tag{3.20b}$$

$$\phi_{z\left(N_x \times N_y\right)} = \left(C/f\right) r_e N_{frac} \mu_{Den} \left(\Delta z\right) \phi_{z\left(N_x \times N_y\right)} \tag{3.20c}$$

where C is the speed of light, f is the frequency, r_e is the classical electron radius, N_{frac} is the magnitude of the density perturbation, μ_{Den} is the background density, ϕ is the phase term for the medium, and the Δ is the distance between the grid of samples in a direction along the flute structure. This delta term is simply calculated as the grid length divided by the number of samples along the grid.

Solving the one dimensional form of the equation for the phase of a dipole flute perturbation at the extrema of the density perturbation yields the following profile:

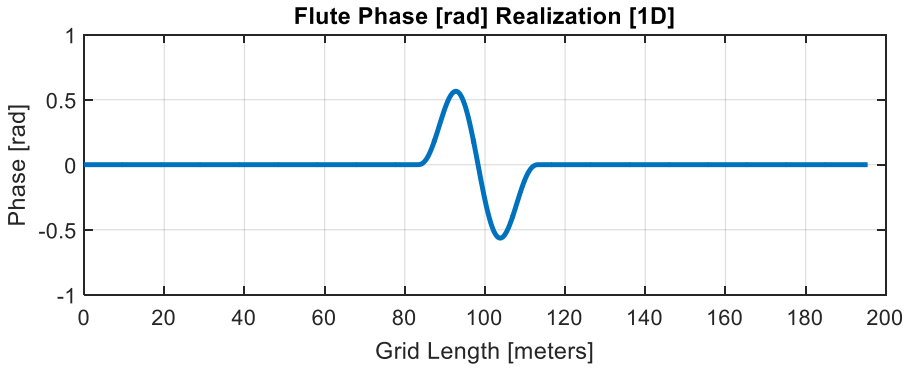

Figure 36. Ideal Flute Perturbation One Dimensional Phase Screen

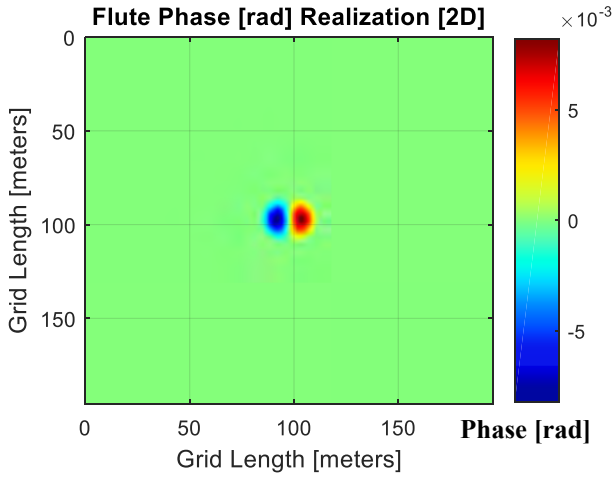

Figure 37. Ideal Flute Perturbation Two Dimensional Density Map

The phase has an abrupt increase and decrease within the flute diameter and approaches zero beyond the diameter outward towards the ends of the grid length. The two dimensional perspective of the electron density distribution in shown in Figure 37. In this case, the phase is solved across the entire electron density gradient map of the flute in the lateral (*x*-*y*) direction.

A three dimensional representation of the flute requires multiple phase screens to sample the horizontal and vertical aspects of the flute density perturbation in each direction. The phase screens that represent the lateral (*x* or *y* direction) propagation are created by taking segments of the 2D map and repeating the gradient from that segment along the elongated portion of the 2D phase screen. The following figure illustrates this process:

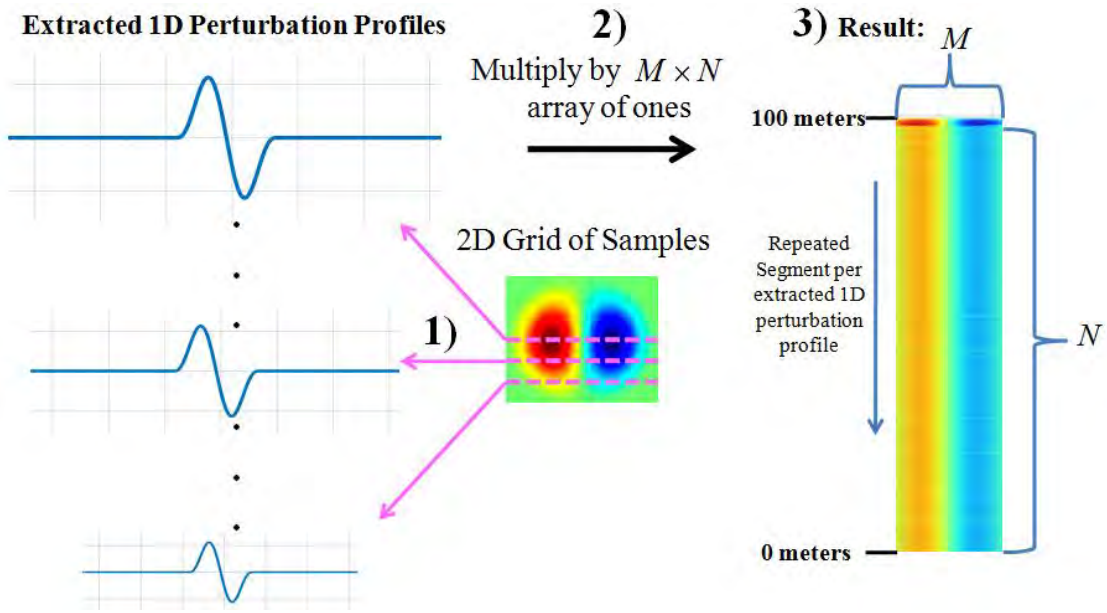

Figure 38. Flute Elongation Process

The one dimensional perturbations extracted from the two dimensional map are multiplied by a two dimensional array of ones that spans the *X*-*Z* (or *Y*-*Z*) plane. The

array of ones creates a repetition of the density gradients in the *z*-direction as the perturbation gradients extend in the *x* or *y* direction. This process is applied in each dimension as shown in Figure 39 in which the sequence of two dimensional phase screens oriented in their respective lateral propagation orientations.

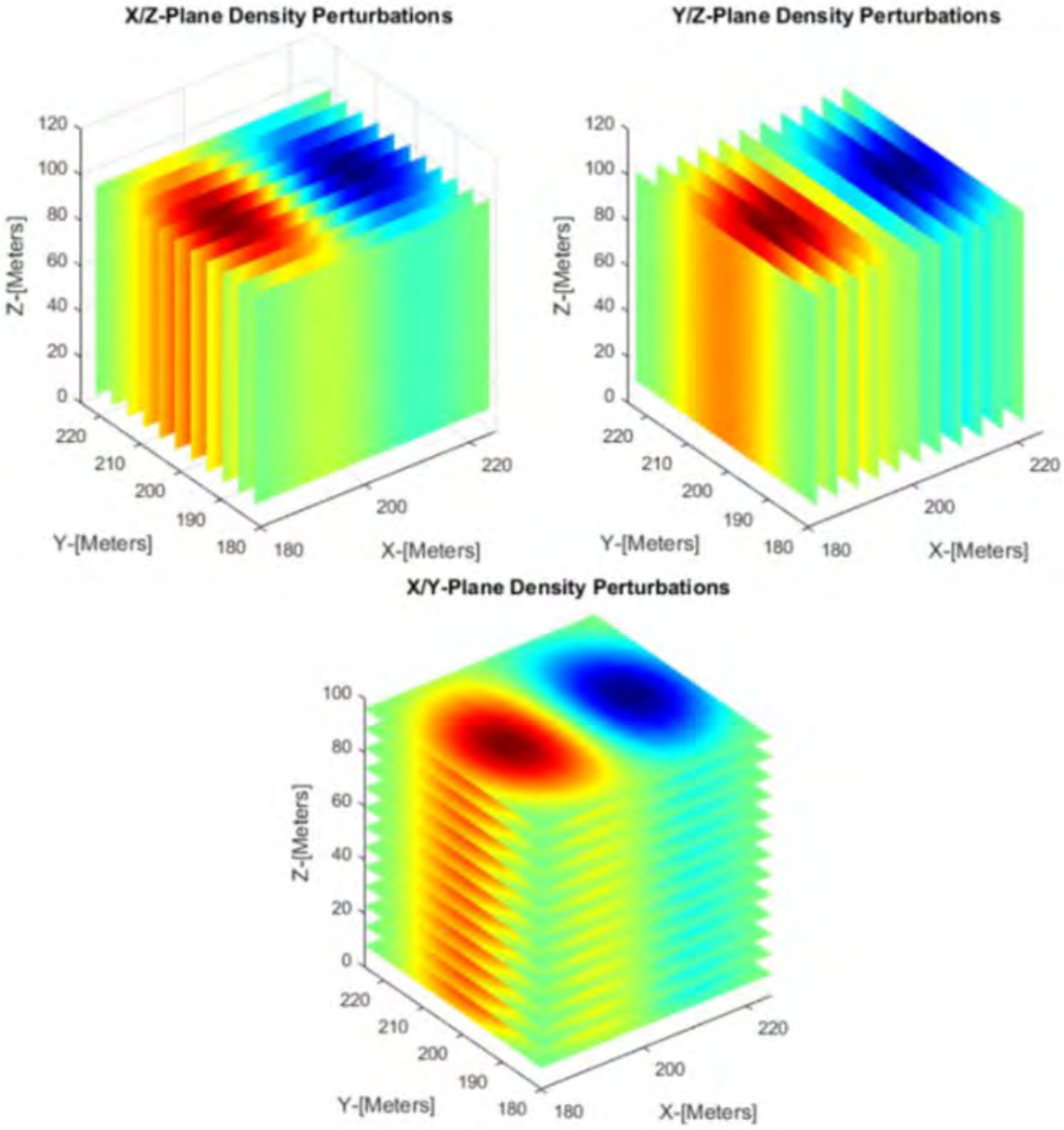

Figure 39. Two-Dimensional Phase Screen Flute Structure Arrangements in the *X, Y*, and *Z* Directions

The spacing between screens relates to the desired number of screens used to sample the flute. Approximately 100 phase screens are used to sample the lateral (x/y) directions at a spacing of approximately 1.95 meters of free space between each screen. Formulation of the elongated portion of the flute involves taking 251 two dimensional lateral profile screens and stacking them in the *z* direction, maintaining a free space separation distance of approximately 0.4 meters between each screen as it is assumed that the elongated dimension of the flute is approximately 100 meters. Combining all the two dimensional screen orientations into a singular cube structure is shown in Figure 40. This structure of screens represents the full three dimensional elongated flute. This form of discretization is computationally expensive and therefore limits the flute sampling to 1004 samples in each dimension.

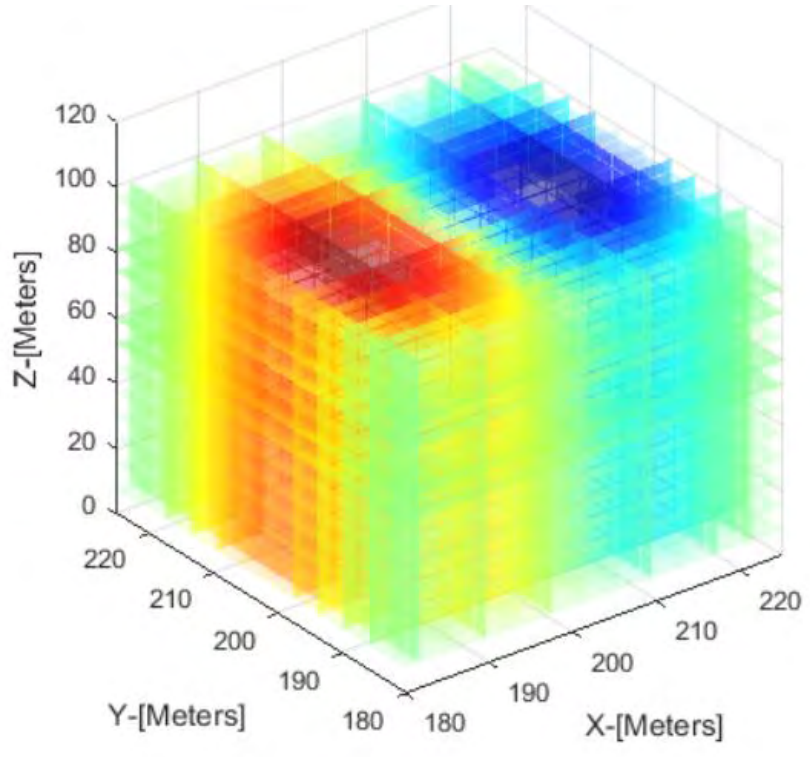

Figure 40. Ideal Flute Structure Phase Cube

3.3 Stochastic Flute Structure Phase Screen and Phase Cube Development

It is desired to study scattering and diffusion through multiple, randomly located vortex structures. The stochastic phase screen representation of the flute structures begins with deriving the power spectral density from the autocorrelation of a phase distribution observed from the ideal form of the flute structure. Calculation of the autocorrelation function is determined from the spatial frequency domain representation of the flute density perturbation $\delta_n\left(K_x, K_y\right)$.Starting with the analytic definition of the dipole flute structure:

$$\begin{aligned}\delta_n(x,y) = &\begin{pmatrix} 1 & x \geq 0 \\ -1 & x < 0 \end{pmatrix} \left[rD_c J_1(br) + D_F r \right] \\ &+ \begin{pmatrix} 1 & x \geq 0 \\ -1 & x < 0 \end{pmatrix} rH_c K_1(hr) \\ &+ \begin{pmatrix} 1 & x \geq 0 \\ -1 & x < 0 \end{pmatrix} rH_c K_1(hr) e^{2(R-r_1)d_f}\end{aligned} \tag{3.21}$$

The sum of the three terms represent the interior stagnation points, immediate exterior of the outer separatrix and the extended exterior of the outer separatrix, respectively.

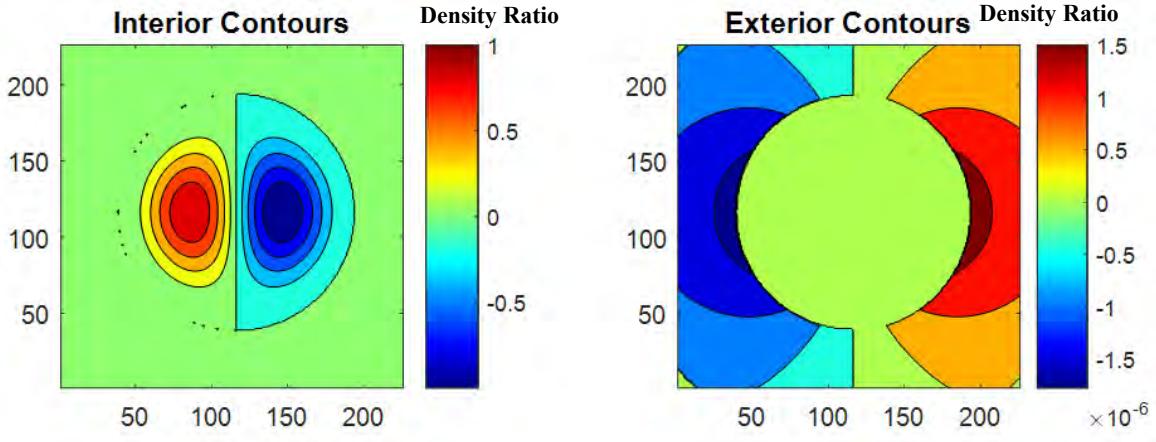

Figure 41. Interior (Left) and Exterior (Right) Contours of the Ideal Flute Density Perturbation

The radii of the three regions are defined as:

$$r = \begin{cases} r_1, & r \le R_o \\ r_2, & 2R_o \ge r > R_o \\ r_3, & r > 2R_o \end{cases}$$

The Bessel functions in these calculations are represented as a Frobenius series approximation. The Bessel function of the first kind and order 1 is approximated as:

$$J_1(z) = \sum_{m=0}^{\infty} \frac{(-1)^m}{m!\Gamma(m+2)} \left(\frac{z}{2}\right)^{2m+1}$$

(3.22a)

The Bessel function of the second kind and order 1 is approximated as:

$$K_1(z) = \frac{\sum_{m=0}^{\infty} \frac{1}{m!\Gamma(m)} \left(\frac{z}{2}\right)^{2m-1} - \sum_{m=0}^{\infty} \frac{1}{m!\Gamma(m+2)} \left(\frac{z}{2}\right)^{2m+1}}{\sin(\pi) + 0.001}$$

(3.22b)

The coefficients that build the density map of the flute perturbations are defined in the following:

1.) Outer streamlines of the density potential:

$$H_c = \left(\frac{SK_{aps}}{U + A_3\beta_+}\right)\left(-F_2 R_{ON} \Big/ \left(D - \left(\frac{SK_{aps}}{U + A_3\beta_+}\right)\right)\right)$$

(3.23a)

2.) Interior streamlines of the density potential:

$$D_C = \frac{\begin{array}{r}\left[-D\left(b^2\left(U + A_1 + A_2 D\right) + D\,g_{norm}/S\right)\Big/\left(S + \left(1 + \tau D\right)\right)\right]\ldots \\ \cdot R_{ON}\left(D - \left(\frac{SK_{aps}}{U + A_3\beta_+}\right)\right)\Big/ b^2 + \left[\left(\frac{SK_{aps}}{U + A_3\beta_+}\right) - D\right]\left(U + A_3\right)/S\end{array}}{\left(D - \left(\frac{SK_{aps}}{U + A_3\beta_+}\right)\right) J_1\left(bR_{ON}\right)}$$

(3.23b)

3.) Intermediate calculations for the streamline coefficients:

$$E = -hJ_1\left(bR_{ON}\right)K_2\left(hR_{ON}\right)\Big/\left(bK_1\left(hR_{ON}\right)J_2\left(bR_{ON}\right)\right) \tag{3.24a}$$

$$D = \left(\left(Sb^2\right)\left(U + A_3\right)\left(E + 1\right) - U - A_1\right)\Big/\left(SA_2b^2 + g_{norm} - \tau\left(U + A_3\right)\left(E + 1\right)b^2\right) \tag{3.24b}$$

$$h = \sqrt{\left(\frac{SK_{aps}}{U + A_3\beta_+}\right)g_{norm}\Big/\left(U + A_1 + \left(\frac{SK_{aps}}{U + A_3\beta_+}\right)A_2\right)} \tag{3.24c}$$

R_{ON} is the normalized characteristic radius to the ion Larmor radius, *h* is the length scale of the outer portion of the vortex, *b*is the mode of the flute structure Bessel Solution, K_{aps} is the total density scale length, A_1, A_2, and A_3, are intermediate calculation coefficients defined in the appendix, β_+ is the positive portion of the plasma beta, g_{norm} is the gravity constant normalization, *U* is the velocity of the flute structure, and D_F describes the decay factor of the perturbation:

$$D_F = \frac{\begin{array}{l}\left(\left(b^2\right)\left(U + A_3\right)\left(E + 1\right) - U - A_1\right)\Big/\left(A_2b^2 + g_{norm} - \tau\left(U + A_3\right)\left(E + 1\right)b^2\right)\ldots \\ \cdot\left[b^2\left(U + A_1 + A_2D\right) + Dg_{norm}\Big/\left(1 + \left(1 + \tau D\right)\right)\right]R_{ON}\end{array}}{b^2}\ldots$$
$$+\left[\left(\frac{K_{aps}}{U + A_3\beta_+}\right) - D\right]\left(U + A_3\right) \tag{3.24d}$$

Substituting the Bessel function series solutions into the density perturbation equation:

$$\delta(r)=\left[\begin{matrix}-1 & x<0\\ 1 & x\geq 0\end{matrix}\right\}r_1D_c\sum_{m=0}^{\infty}\frac{(-1)^m}{m!\Gamma(m+2)}\left(\frac{br+D_Fr}{2}\right)^{2m+1}\cos(\theta)\right]$$
$$+\left[r_2H_c\frac{\sum_{m=0}^{\infty}\frac{1}{m!\Gamma(m)}\left(\frac{hr}{2}\right)^{2m-1}-\sum_{m=0}^{\infty}\frac{1}{m!\Gamma(m+2)}\left(\frac{hr}{2}\right)^{2m+1}}{\sin(\pi)+0.001}\cos(\theta)\right]$$
$$+\left[r_3H_c\frac{\sum_{m=0}^{\infty}\frac{1}{m!\Gamma(m)}\left(\frac{hr}{2}\right)^{2m-1}-\sum_{m=0}^{\infty}\frac{1}{m!\Gamma(m+2)}\left(\frac{hr}{2}\right)^{2m+1}}{\sin(\pi)+0.001}\cos(\theta)\right]e^{(2R_o-r)d_f}$$

(3.25a)

Converting the cylindrical components to rectangular:

$$\delta(x,y)=\left[\begin{matrix}-1 & x<0\\ 1 & x\geq 0\end{matrix}\right\}r_1D_c\sum_{m=0}^{\infty}\frac{(-1)^m}{m!\Gamma(m+2)}\left(\frac{b\sqrt{x^2+y^2}+D_F\sqrt{x^2+y^2}}{2}\right)^{2m+1}\cos(\theta)$$
$$+\frac{\pi H_c\left(r_2+r_3e^{\left(2R_o-\sqrt{x^2+y^2}\right)d_f}\right)}{2\left(\sin(\pi)+0.001\right)}\left[\begin{matrix}\sum_{m=0}^{\infty}\frac{1}{m!\Gamma(m)}\left(\frac{h\sqrt{x^2+y^2}}{2}\right)^{2m-1}\\ -\sum_{m=0}^{\infty}\frac{1}{m!\Gamma(m+2)}\left(\frac{h\sqrt{x^2+y^2}}{2}\right)^{2m+1}\end{matrix}\right]\cos(\theta)$$

(3.25b)

The discrete fourier transform relationship to convert the density perturbation to the frequency domain:

$$\delta(K_x,K_y)=\frac{1}{N}\sum_{x=0}^{N-1}\sum_{y=0}^{N-1}\delta(x,y)e^{-2i\frac{\pi}{N}(K_xx+K_yy)}$$

(3.26a)

The important property of autocorrelation between the frequency domain spatial frequency and its complex conjugated is defined by:

$$\delta\left(K_x,K_y\right)\delta^*\left(K_x,K_y\right)=\delta\left(K_x,K_y\right)\left\lfloor \mathrm{Re}\left[\delta\left(K_x,K_y\right)\right]-j\,\mathrm{Im}\left[\delta\left(K_x,K_y\right)\right]\right\rfloor$$

(3.26b)

Substituting the discrete fourier transform into the conjugate relationship above:

$$\delta\left(K_x,K_y\right)\delta^*\left(K_x,K_y\right)=\frac{1}{N}\sum_{x=0}^{N-1}\sum_{y=0}^{N-1}\delta(x,y)e^{-2i\frac{\pi}{N}\left(K_xx+K_yy\right)}\left\lfloor \begin{array}{l}\mathrm{Re}\left(\frac{1}{N}\sum_{x=0}^{N-1}\sum_{y=0}^{N-1}\delta(x,y)e^{-2i\frac{\pi}{N}\left(K_xx+K_yy\right)}\right)\\ -j\cdot\mathrm{Im}\left(\frac{1}{N}\sum_{x=0}^{N-1}\sum_{y=0}^{N-1}\delta(x,y)e^{-2i\frac{\pi}{N}\left(K_xx+K_yy\right)}\right)\end{array}\right\rfloor$$

(3.26c)

Reducing the real and imaginary components of the fourier transformation:

$$\delta\left(K_x,K_y\right)\delta^*\left(K_x,K_y\right)=\left(\frac{1}{N}\sum_{x=0}^{N-1}\sum_{y=0}^{N-1}\delta(x,y)e^{-2i\frac{\pi}{N}\left(K_xx+K_yy\right)}\right)\left\lfloor \begin{array}{l}\left(\frac{1}{N}\sum_{x=0}^{N-1}\sum_{y=0}^{N-1}\delta(x,y)\cos\left(-2\frac{\pi}{N}\left(K_xx+K_yy\right)\right)\right)\\ -j\cdot\left(\frac{1}{N}\sum_{x=0}^{N-1}\sum_{y=0}^{N-1}\delta(x,y)\sin\left(-2\frac{\pi}{N}\left(K_xx+K_yy\right)\right)\right)\end{array}\right\rfloor$$

(3.26d)

Recombining to acquire the phasor form on the conjugate component:

$$\delta\left(K_x,K_y\right)\delta^*\left(K_x,K_y\right)=\left(\frac{1}{N}\sum_{x=0}^{N-1}\sum_{y=0}^{N-1}\delta(x,y)e^{-2\frac{\pi}{N}\left(K_xx+K_yy\right)}\right)\left[\left(\frac{1}{N}\sum_{x=0}^{N-1}\sum_{y=0}^{N-1}\delta(x,y)e^{2\frac{\pi}{N}\left(K_xx+K_yy\right)}\right)\right]$$

(3.26e)

From numerical observations of the spatial frequency domain of the density perturbations and its conjugate, it is revealed that:

$$\delta\left(K_x,K_y\right)=\delta^*\left(K_x,K_y\right)$$

(3,.26f)

Therefore, the multiplication of both terms' series reduces to:

$$\delta\left(K_x,K_y\right)\delta^*\left(K_x,K_y\right)=\delta\left(K_x,K_y\right)^2=\left(\frac{1}{N}\sum_{x=0}^{N-1}\sum_{y=0}^{N-1}\delta\left(x,y\right)e^{-2\frac{\pi}{N}\left(K_x x+K_y y\right)}\right)^2 \tag{3.26g}$$

Applying the discrete inverse fourier transform to yield the autocorrelation function:

$$B_\phi\left(x,y\right)=\frac{A}{N}\sum_{K_x=0}^{N-1}\sum_{K_y=0}^{N-1}\delta\left(K_x,K_y\right)\delta^*\left(K_x,K_y\right)e^{2i\frac{\pi}{N}\left(K_x x+K_y y\right)} \tag{3.27}$$

where $A=\left(C/f\right)r_e N_{frac}\mu_e\Delta xy$ is the conversion from the density perturbation to phase. Substitution of the autocorrelation function into the discrete fourier transform relationship to yield the power spectral density function:

$$S_\phi\left(K_x,K_y\right)=\frac{1}{N}\sum_{x=0}^{N-1}\sum_{y=0}^{N-1}\left[\frac{A}{N}\sum_{K_x=0}^{N-1}\sum_{K_y=0}^{N-1}\left[\delta\left(K_x,K_y\right)^2\right]e^{2i\frac{\pi}{N}\left(K_x x+K_y y\right)}\right]e^{-2i\frac{\pi}{N}\left(K_x x+K_y y\right)} \tag{3.28}$$

The complete solution relating the flute density perturbation to the power spectrum is:

$$S_\phi\left(K_x,K_y\right)=\frac{1}{N}\sum_{x=0}^{N-1}\sum_{y=0}^{N-1}\left[\frac{A}{N}\sum_{K_x=0}^{N-1}\sum_{K_y=0}^{N-1}\left[\left(\frac{1}{N}\sum_{x=0}^{N-1}\sum_{y=0}^{N-1}\delta\left(x,y\right)e^{-2i\frac{\pi}{N}\left(K_x x+K_y y\right)}\right)^2\right]e^{2i\frac{\pi}{N}\left(K_x x+K_y y\right)}\right]e^{-2i\frac{\pi}{N}\left(K_x x+K_y y\right)} \tag{3.29}$$

The frequency domain analysis of the flute's power spectrum is similar to the mathematical description for the Kolmogorov structure. Random lags are established from a Gaussian distribution applied independently to two variables that combine to create a complex set of values that satisfy the wide sense stationary condition. These random lags correlate the power spectrum normalized by spatial frequency around a unit

circle. The fourier transform of the phase lags are approximated by the transform that relates the PSD and autocorrelation functions. The inverse fourier transform of this realization results in the spatial domain representation of the phase lags of the flute structure.

As previously applied in the Kolmogorov derivation, the two-dimensional discrete transform relationship between the autocorrelation and power spectral density requires isolating the phase term. The discrete inverse fourier transform relation between the power spectral density and the phase realization is:

$$\phi\left(\Delta r,\Delta s\right)=B\sum_{m_1=0}^{M-1}\sum_{m_2=0}^{N-1}\left[\left(\sum_{q=1}^{Q}c_q\left[\frac{S_\phi\left(m_1\Delta K_r,m_2\Delta K_s\right)}{\Delta K_r\Delta K_s}\right]^{\frac{1}{2}}\right)\Big/Q\right]e^{i2\pi[A]}\Delta K_r\Delta K_s \tag{3.30}$$

where, $B=\left(\frac{1}{M-1}\right)\left(\frac{1}{N-1}\right)$

$$\Delta K_r\Delta K_s=2\pi/\left(L_rL_s\right) \qquad n_1=0,...,M-1$$
$$m\Delta K=m_1\Delta K_r,m_2\Delta K_s \qquad n_2=0,...,N-1$$
$$A=\left(m_1n_1/M\right)+\left(m_2n_2/N\right)$$

c_q is the randomly generated complex set of values that creates unique realization of the phase power spectrum, and the power spectrum relation to the flute perturbation:

$$S_\phi\left(m_1\Delta K_r,m_2\Delta K_s\right)=$$
$$\frac{1}{N}\sum_{x=0}^{N-1}\sum_{y=0}^{N-1}\left[\frac{A}{N}\sum_{K_x=0}^{N-1}\sum_{K_y=0}^{N-1}\left[\left(\frac{1}{N}\sum_{x=0}^{N-1}\sum_{y=0}^{N-1}\delta\left(x,y\right)e^{-2i\frac{\pi}{N}\left(K_xx+K_yy\right)}\right)^2\right]e^{2i\frac{\pi}{N}\left(K_xx+K_yy\right)}\right]e^{-2i\frac{\pi}{N}\left(K_xx+K_yy\right)} \tag{3.31}$$

In summary, the process of deriving the stochastic phase screen realization from the initial flute density perturbation can be described in a six step process.

1.) Acquire the dipole flute approximation from the perturbation analysis of the nonlinear two-fluid MHD equations:

$$\delta(x,y)=\begin{matrix}-1 & x<0\\ 1 & x\geq 0\end{matrix}\Bigg\} r_1 D_c \sum_{m=0}^{\infty}\frac{(-1)^m}{m!\Gamma(m+2)}\left(\frac{b\sqrt{x^2+y^2}+D_F\sqrt{x^2+y^2}}{2}\right)^{2m+1}\cos(\theta)$$
$$+\frac{\pi H_c\left(r_2+r_3 e^{\left(2R_o-\sqrt{x^2+y^2}\right)d_f}\right)}{2\left(\sin(\pi)+0.001\right)}\left[\begin{matrix}\sum_{m=0}^{\infty}\frac{1}{m!\Gamma(m)}\left(\frac{h\sqrt{x^2+y^2}}{2}\right)^{2m-1}\\ -\sum_{m=0}^{\infty}\frac{1}{m!\Gamma(m+2)}\left(\frac{h\sqrt{x^2+y^2}}{2}\right)^{2m+1}\end{matrix}\right]\cos(\theta) \tag{3.32}$$

2.) The autocorrelation of the density perturbation is accomplished using a discrete inverse fourier transform on the perturbation and its conjugate component, thus providing the measure of similarity between the x and y components of the perturbation:

$$B_\phi(x,y)=\frac{A}{N}\sum_{K_x=0}^{N-1}\sum_{K_y=0}^{N-1}\delta(K_x,K_y)\delta^*(K_x,K_y)e^{2i\frac{\pi}{N}(K_x x+K_y y)} \tag{3.33}$$

3.) Applying the discrete fourier transform to the autocorrelation function to yield the power spectrum:

$$S_{\phi}\left(K_x, K_y\right) = \frac{1}{N}\sum_{x=0}^{N-1}\sum_{y=0}^{N-1}\left[B_{\phi}\left(x,y\right)\right]e^{-2i\frac{\pi}{N}\left(K_x x + K_y y\right)} \tag{3.34}$$

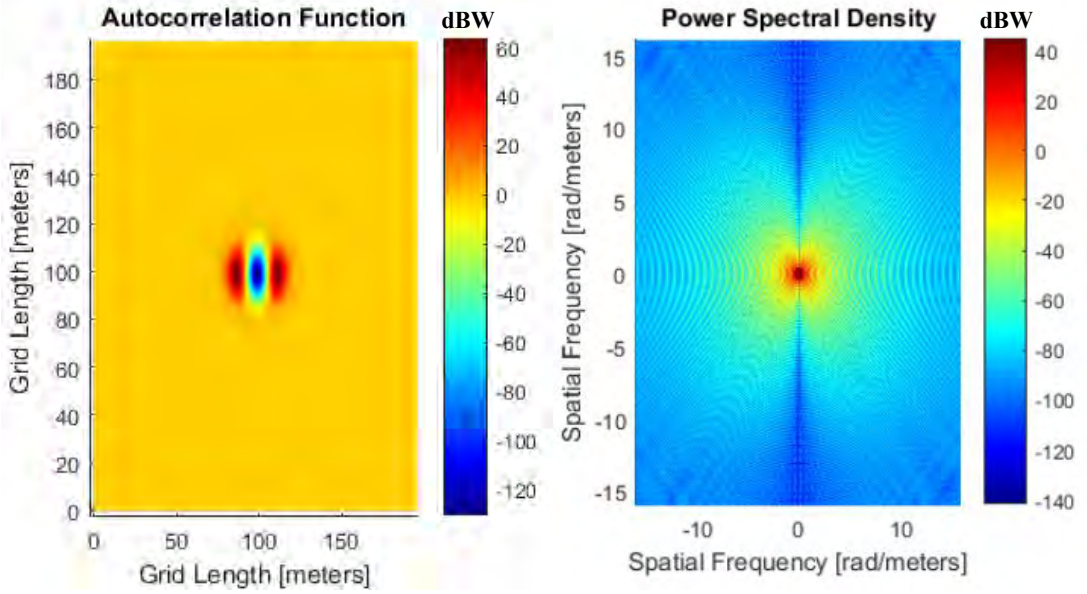

Figure 42. 2D Autocorrelation Function (Left) corresponding to 2D Power Spectrum (Right)

4.) Create the random lags from the Gaussian distributions (ref. Figure 28).

5.) Cross correlate the power spectrum phase values with the random values to vectorize the inputs into real and imaginary components (ref. Figure 29).

6.) Apply the inverse fourier transform of the averaged power spectrum realizations:

$$\phi\left(x,y\right) = B\sum_{m_1=0}^{M-1}\sum_{m_2=0}^{N-1}\left[\left(\sum_{q=1}^{Q}c_q\left[\frac{S_{\phi}\left(m_1\Delta K_x, m_2\Delta K_y\right)}{\Delta K_x \Delta K_y}\right]^{\frac{1}{2}}\right)\Big/ Q\right]e^{i2\pi[A]}\Delta K_x \Delta K_y \tag{3.35}$$

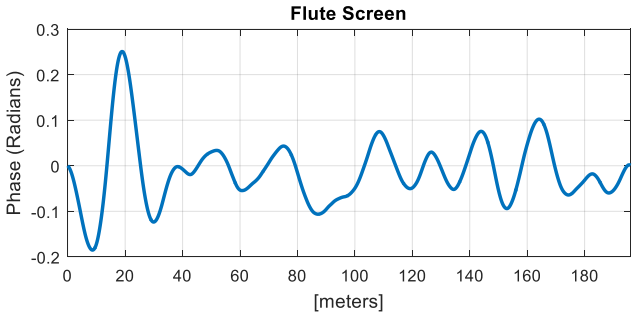

Figure 43. One Dimensional Flute Phase Screen

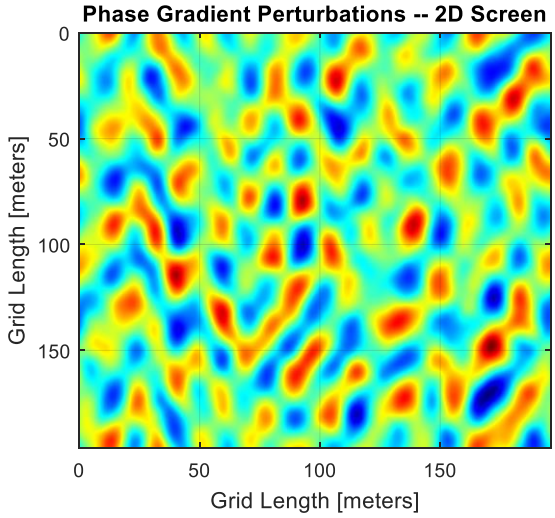

Figure 44. 2D Flute Phase Screen

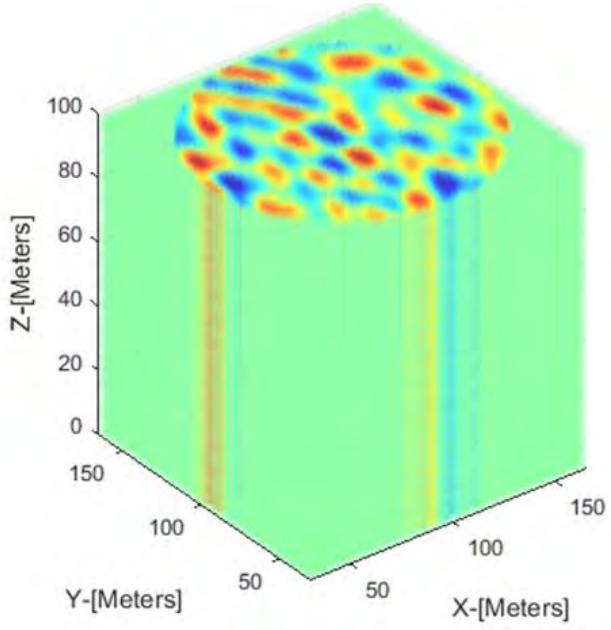

Figure 45. 3D Flute Phase Cube

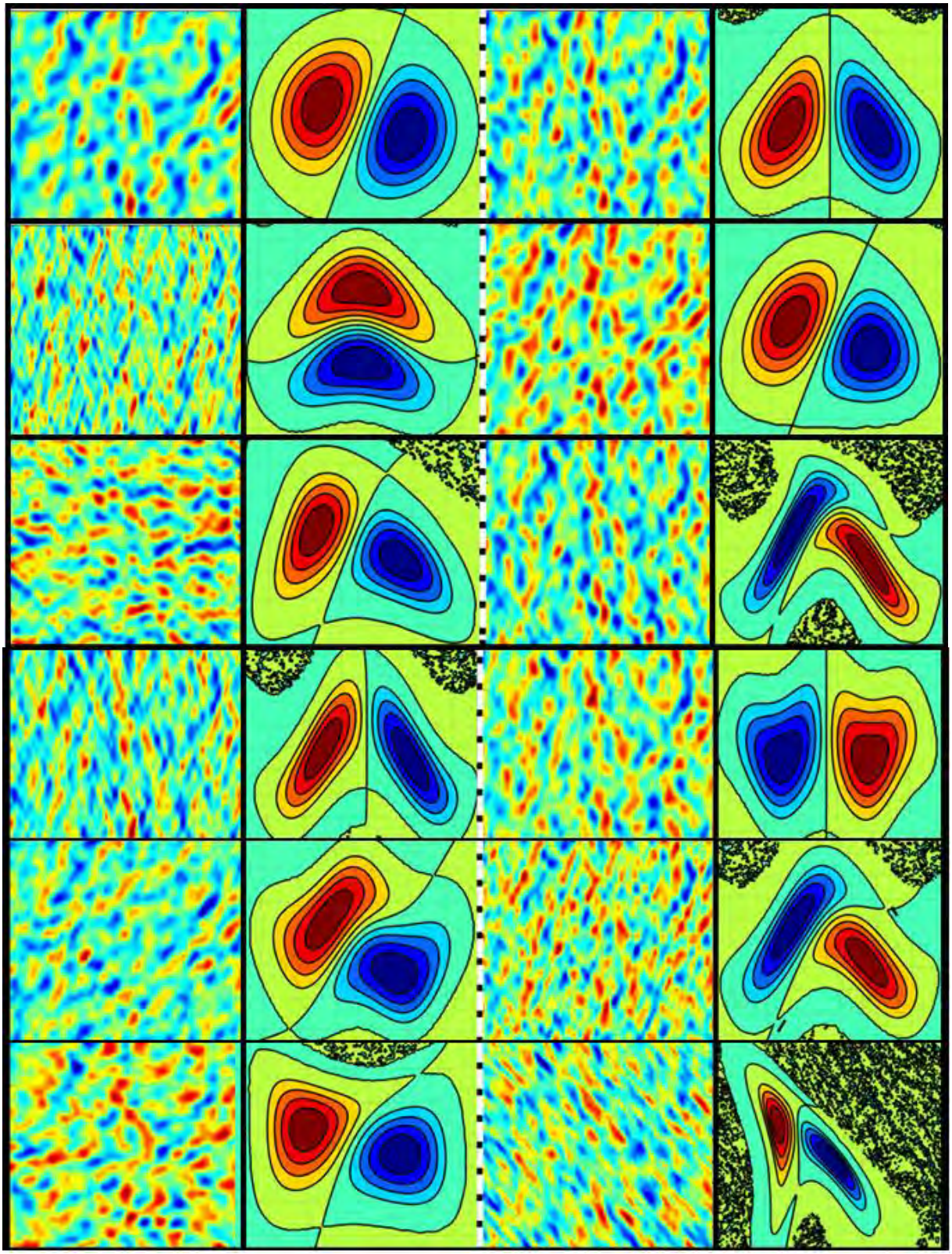

Figure 46. 2D Stochastic Flute Density Maps with corresponding flute structures applied during the autocorrelation process

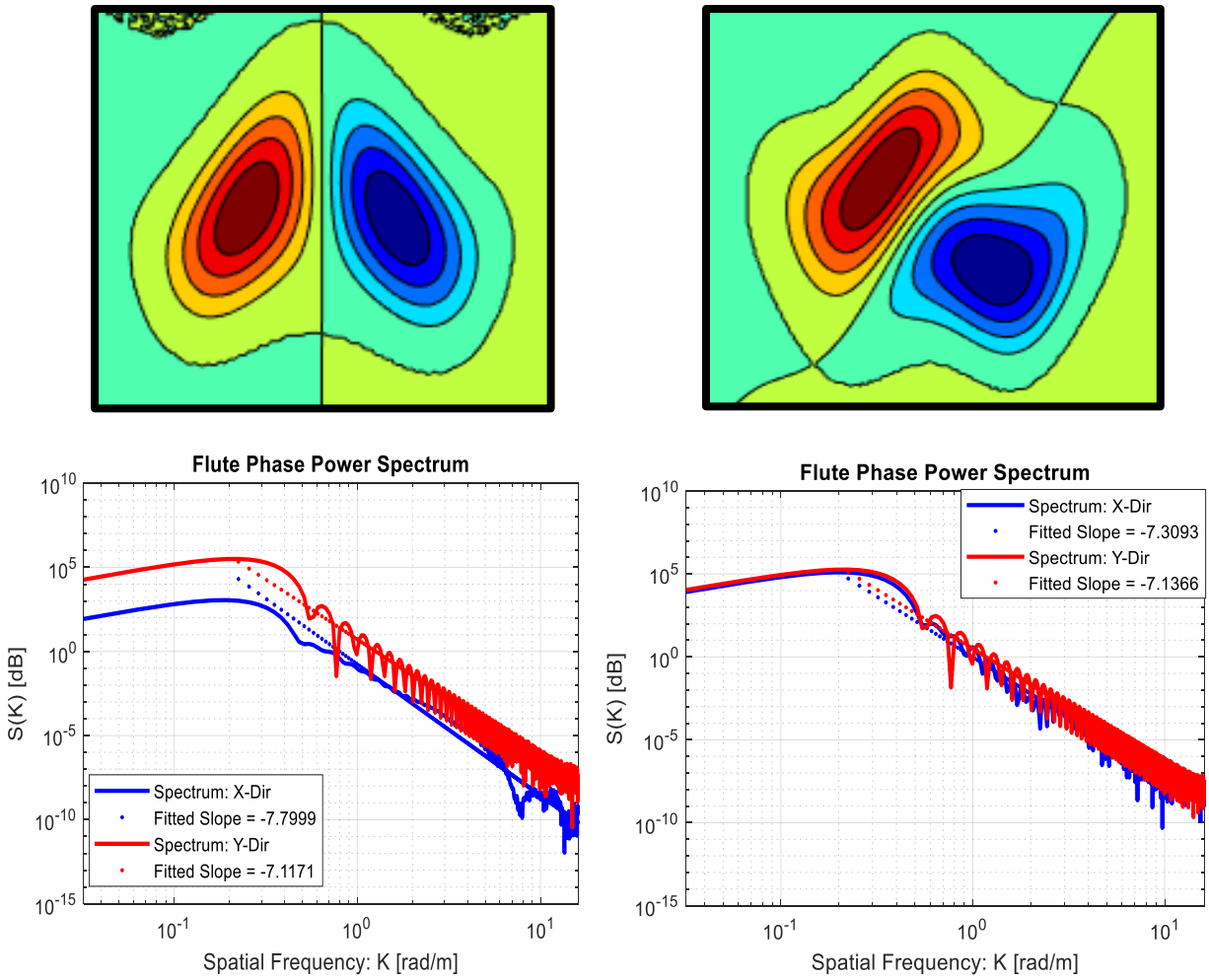

Figure 47. Flute Structure Power Spectrums

Figures 43 and 44 show the one and two dimensional stochastic flute phase screens, respectively. Note in the 2D plot the variations in the flute density gradients, sizes, and shapes. Some of the stagnation points are well defined while others appear faded. The phase cube representation of this stochastic flute map is shown in Figure 45. It is developed based on the steps previously described in the previous section using a compilation of two dimensional phase screens. The technique described in this section is applied to a variety of singular flute structures that are generated from the single fluid MHD model discussed in the previous chapter. Figure 46 illustrates the variety of

stochastic flute density maps generated from the random sampling of each flute's power spectrum. Note the variations in shape and orientation of the flute structures.

Examining the power spectrum distributions, it is apparent that they follow a power law in which the energy cascades in a decaying slope as the spatial frequency increases. This cascade of energy dissipates towards the smaller scale size irregularity structures at a slope that is more than two times the typical slope of the Kolmogorov power spectrum. For the flute structure on the left, the stagnation points are symmetric about the *y*-axis. The effect on the power spectrum is shown in the calculation with respect to the *x*-direction, where the overlap causes a cancellation effect. For the flute structure on the right, a direct alignment is not present in the *x* or *y* directions, as the interior separatrix is relatively diagonal. Therefore, the power spectrums for each direction are relatively identical.

The flute structure on the left has uniform and symmetric stagnation points with respect to the y-axis. The alignment of these stagnation points are near perfect, and causes the most significant decline in the overall power spectrum calculated in the *y*-direction. Therefore, the energy does not cascade by a particularly steep slope, as it does in the x-direction, where the stagnation points appear abreast relative to the *x*-axis. For the flute on the right, the non-uniformities in the stagnation points create more variable decays with respect to the direction of the power spectrum calculation. The energy decay is minimal in the x-direction as stagnation points have the most overlap, causing a phase cancellation.

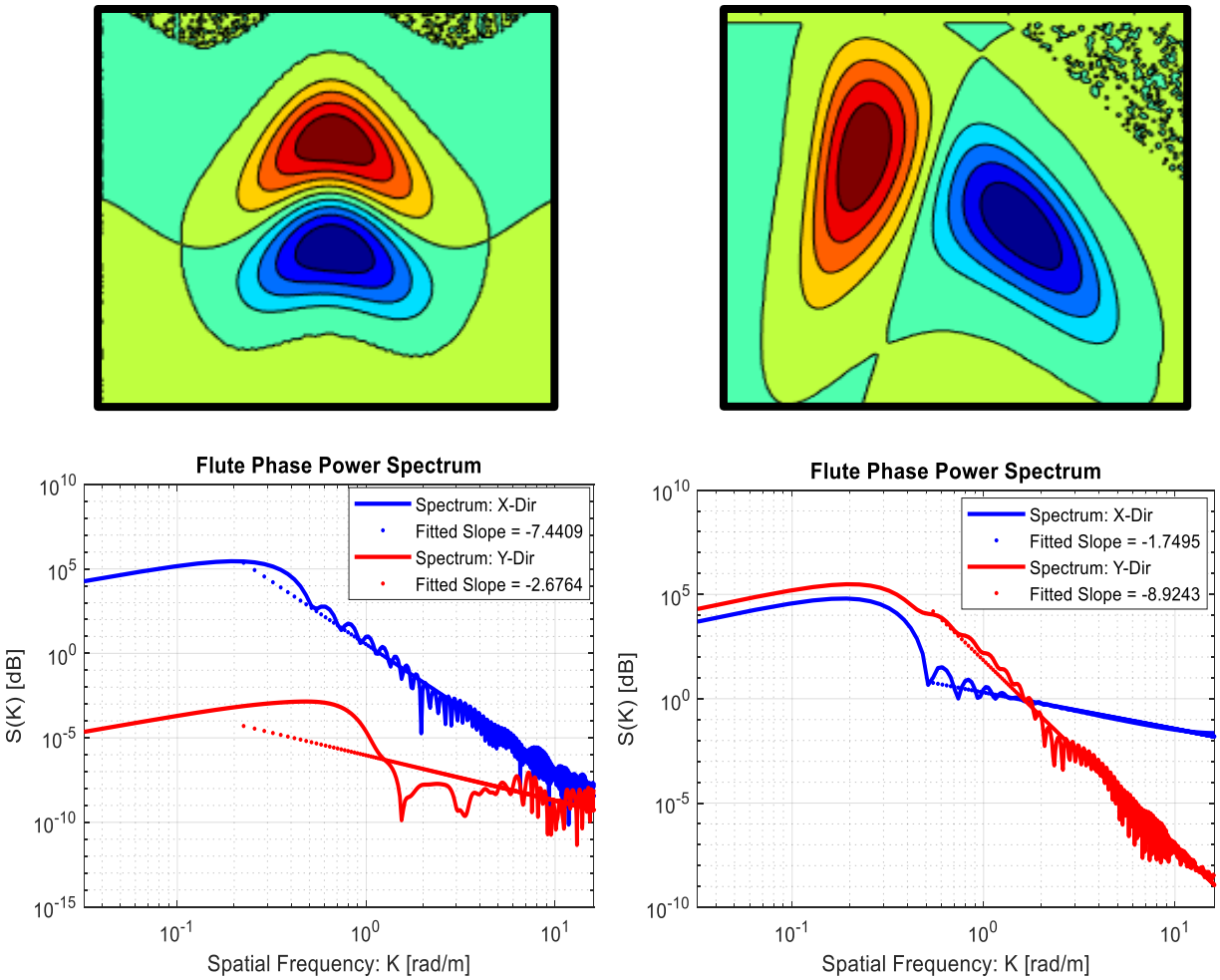

Figure 48. Flute Structure Power Spectrums

Similar properties are also observed for flute arrays. In the case of the nonlinear mode array on the right, the non-uniformitys in the *x* and *y* directions causes the slopes of the energy decay to be unique in comparison to the relatively consistent slopes obersved on the linear flute array on the left. In general, if the flute structures are aligned in a particular direction, the power spectum will weaken the most in that direction.

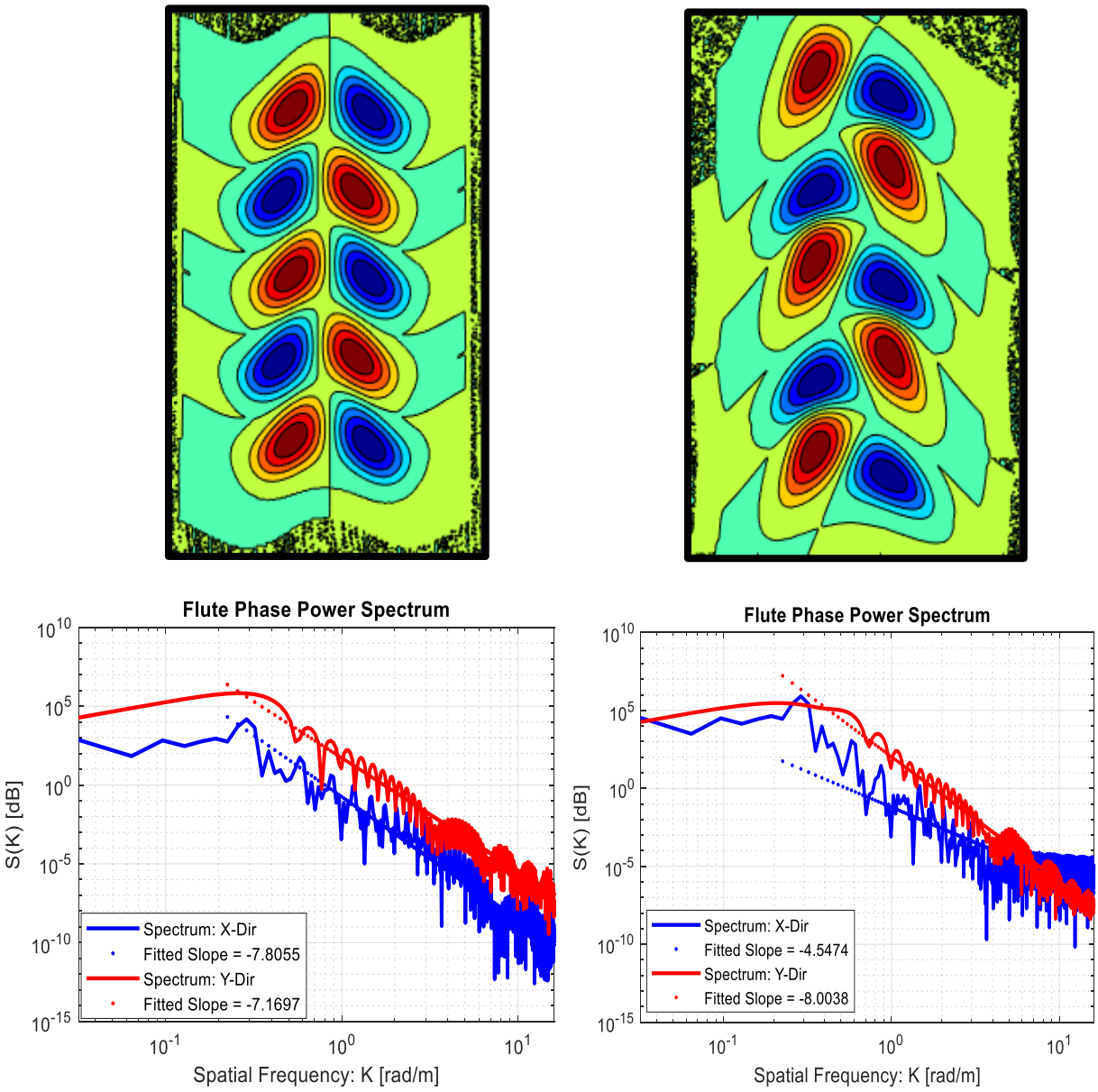

Figure 49. Flute Array Power Spectrums

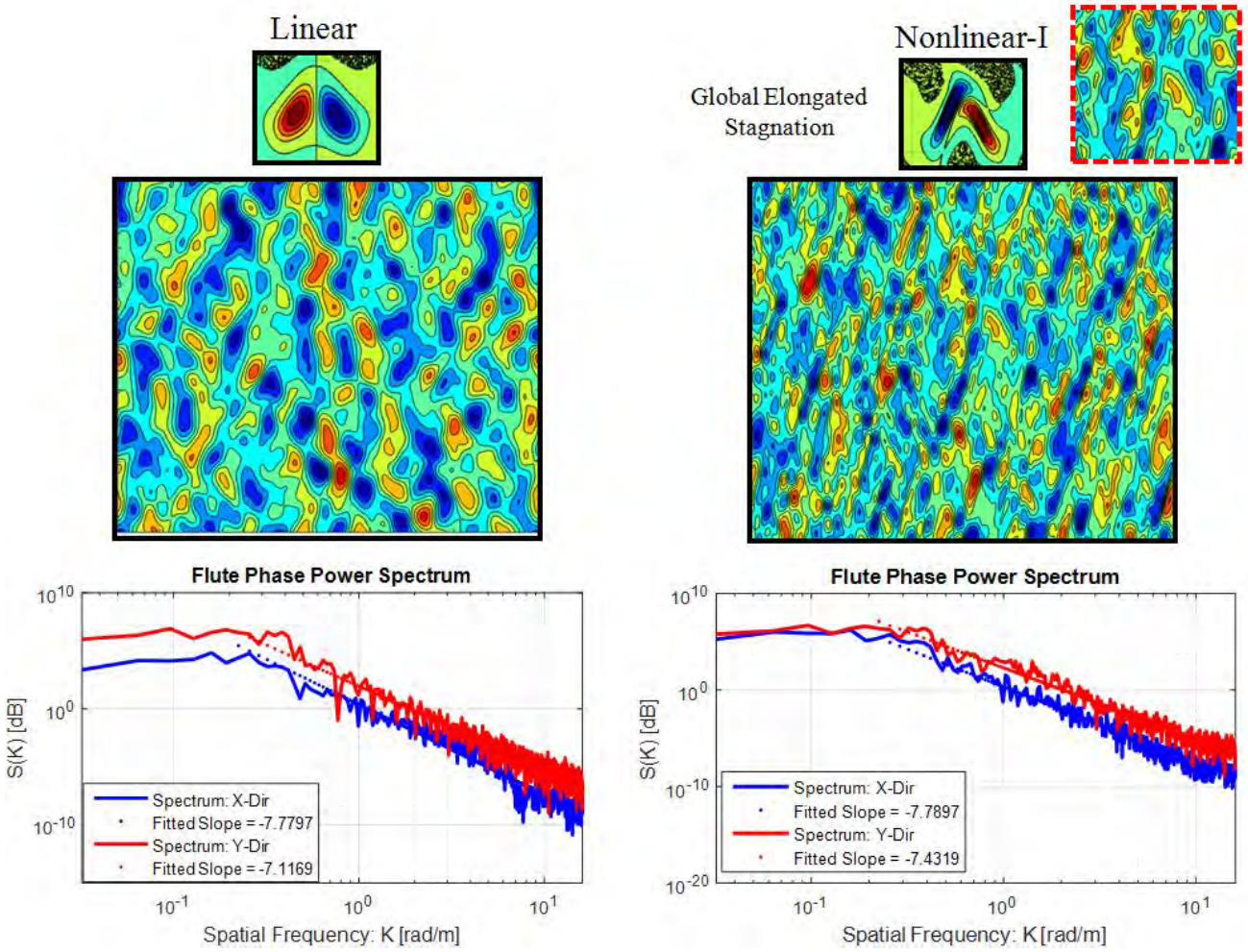

Figure 50. Stochastic Flute Power Spectrums

Figure 50 shows the stochastic map representation of two singular flute structures and their corresponding flute power spectrums. The power spectrum distributions have identical slopes in the *x* and *y* directions. The stagnation points have similar alignment with repsect to the *y*-axis. It is also noteworth that the nonlinear flute on the right appears to be more elongated than the flute on the left. This elongation impacts the stochastic map on a global basis, in which the random flute realizations are elongated despite the variability in the sizes and contours of the density perturbations.

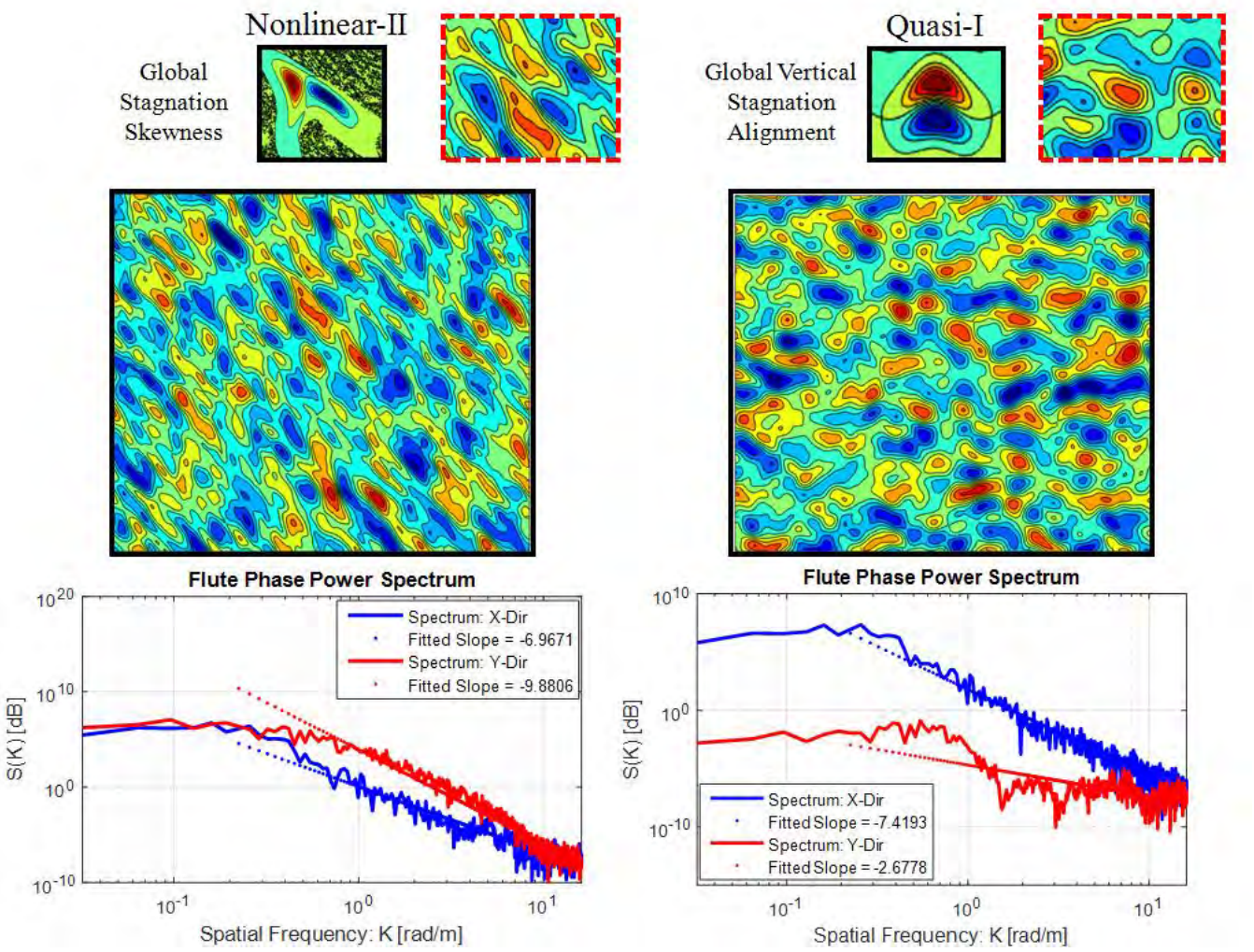

Figure 51. Stochastic Flute Power Spectrums

In Figure 51, there is a global skewness in the single nonlinear flute structure that also leads to a global skewness in the corresponding stochastic map. The orientation of the flute structure on the right biases the stagnation points along the y-axis. Consequently, the global bias appears to create a vertical alignment of the flute structures on the stochastic map. Skewness and stagnation causes more ambiguity in the power spectrum distributions with respect to the *x* and *y* directions, effecting their magnitude and slopes.

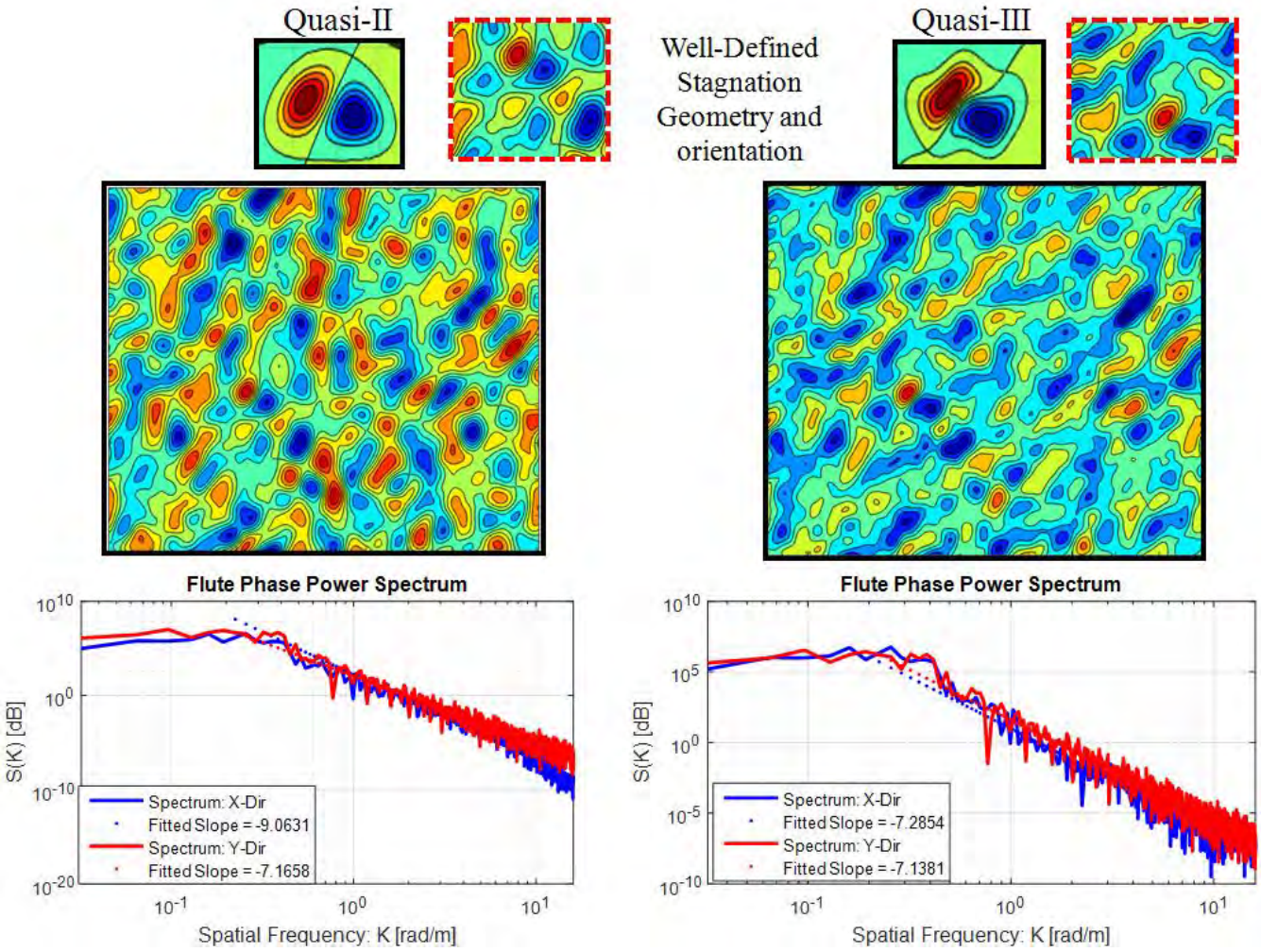

Figure 52. Stochastic Flute Power Spectrums

In the quasi-linear flute cases shown in figure 52, the stagnation geometries are very well-defined and prevalent in the stochastic maps of the flute. The characteristics such as the ideal flute orientation with respect to the positive and negative stagnations points are clearly identifiable in the stochastic map. As the stagnation points are equally biased in the *x* and *y* directions, the corresponding power spectral density distributions are identical in either direction.

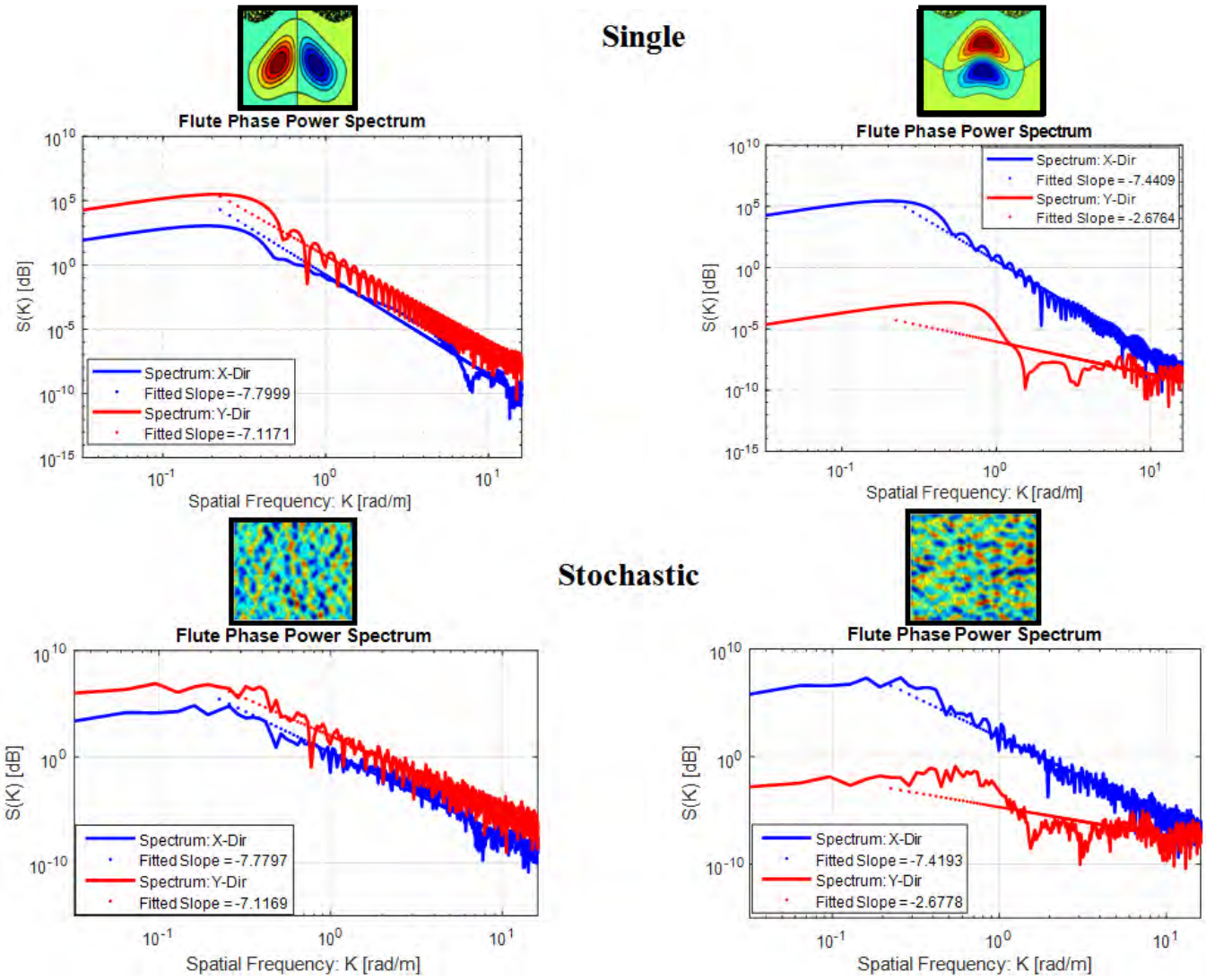

Figure 53. Single Flute vs. Stochastic Flute Power Spectrums

A key observation in figure 53 is that the stochastic representation of the singular flute structure maintains an identical power spectral density distribution, albiet, with more fluctuations due to the random sampling from the gaussian distributions. The significance is that the forward scatter propagation characteristics will rely on the physical nature of the flute structure density maps in terms of shaping, positioning, and orientations without much ambiguity in the wave number energy dissipation when comparing isolated and

stochastic flute map results. This mitigates implications brought about by the stochastic generation of flute structures with unrelatable power spectrum characteristics, which would otherwise add more variables to the analysis.

3.4 Summary

This chapter presented the derivations of the Kolmogorov phase screen and phase cube structures by presenting the foundational process of randomly sampling a Gaussian distribution and creating a complex map of the power spectrum realizations. This concept is extended to the application of flute structure irregularities in which the density perturbation is initially known and the power spectrum is calculated from the autocorrelation of the perturbation samples. The three dimensional phase cube concept was developed from careful arrangement of two dimension phase screens oriented in the x, y, and z directions. Power spectrum distribution plots revealed that the orientation of the stagnation points and overall uniformity of the flute structure effects the magnitude of the power spectrums and dissipation of energy. Stagnation overlap with respect to the direction of the power spectrum calculation will reduce the magnitude of the power spectrum and lessen the slope of the energy decay. These properties will be examined further in the propagation models developed and applied in the remainder of this document.

The following chapter focuses on implementing the phase cube structures in a forward scatter propagation model coupled with ray tracing to account for the refractive nature of medium and providing a realistic distribution of field vector quantities with respect to the propagation direction.

IV. FORWARD SCATTER PROPAGATION MODEL

This chapter addresses the structure and functionality of the forward scatter propagation algorithms developed to model the scattering effects that occur within a flute structure channel. Initially, this chapter provides solutions of the two-dimensional received field when applying a Gaussian lens or a single phase screen as the scattering structure to provide a baseline on the forward scatter solutions. The validation process of the model includes comparisons of the generalized power spectrum calculations acquired from the multiple phase screen (MPS) model and compared to the Parabolic Diffraction Method (PDM) as introduced in chapter 2. The backscatter calculations of the flute structure scattering is also compared to the forward scatter solutions over identical propagation domain parameters. This is necessary to determine scattering features that are otherwise unaccounted in the phase screen approximation of flute perturbations. The temporal stochastic moment technique is compared to the phase screen model's pulse coherence calculations to validate the time delay and time jitter calculations determined at the receiver plane of the MPS model. Finally, the phase cube model of the flute structure is coupled with ray tracing to account for the refractive properties of the medium during the propagation process. An analysis of the refractivity for a variety of perturbation intensities and incident angles are presented.

4.1 Solutions of the Forward Scatter Propagation Algorithms

Initial testing and observation of the propagation algorithm functionality is accomplished by applying an exponential phasor to the incident electric field in the form

of a Gaussian lens or phase screen. Figure 54 illustrates the propagation model that is applied in this section to demonstrate the phase screen effects on scattering of the incident wave. The down range receiver plane at the end of the propagation path is where the wave solution is realized.

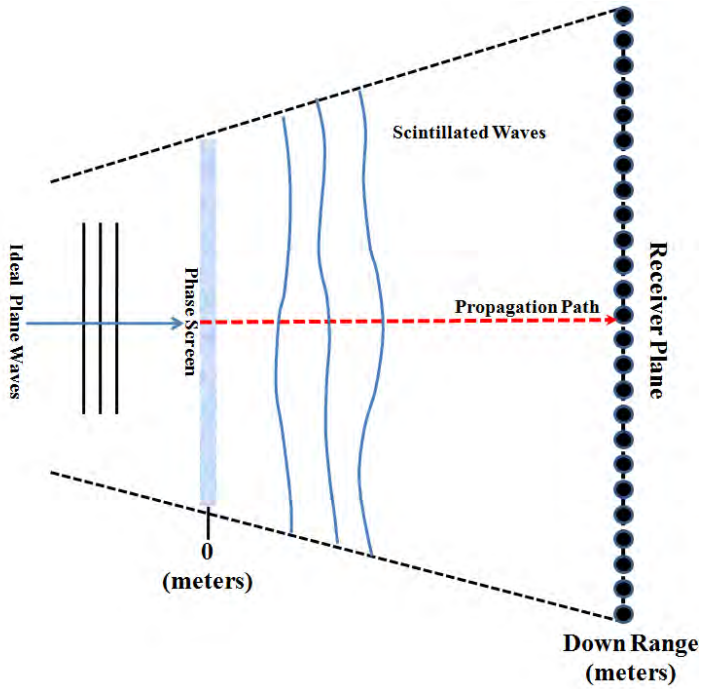

Figure 54. Typical Propagation Model Arrangement

In two-dimensional space, the phase screen realization is compared to a deterministic convergent Gaussian Lens realization that is given by:

$$\phi = \phi_o e^{-(x+y)^2/r_o^2} \tag{4.1}$$

where ϕ_o is the initial phase of the lens, x and y are the dimensions of the lens, and r_o is the lens focus parameter. The phase terms for either the Gaussian lens or the phase screens are applied in the form of an exponential phasor:

$$A(z) = A_o(z) e^{1i(\Delta z)\phi_{phase}} \tag{4.2}$$

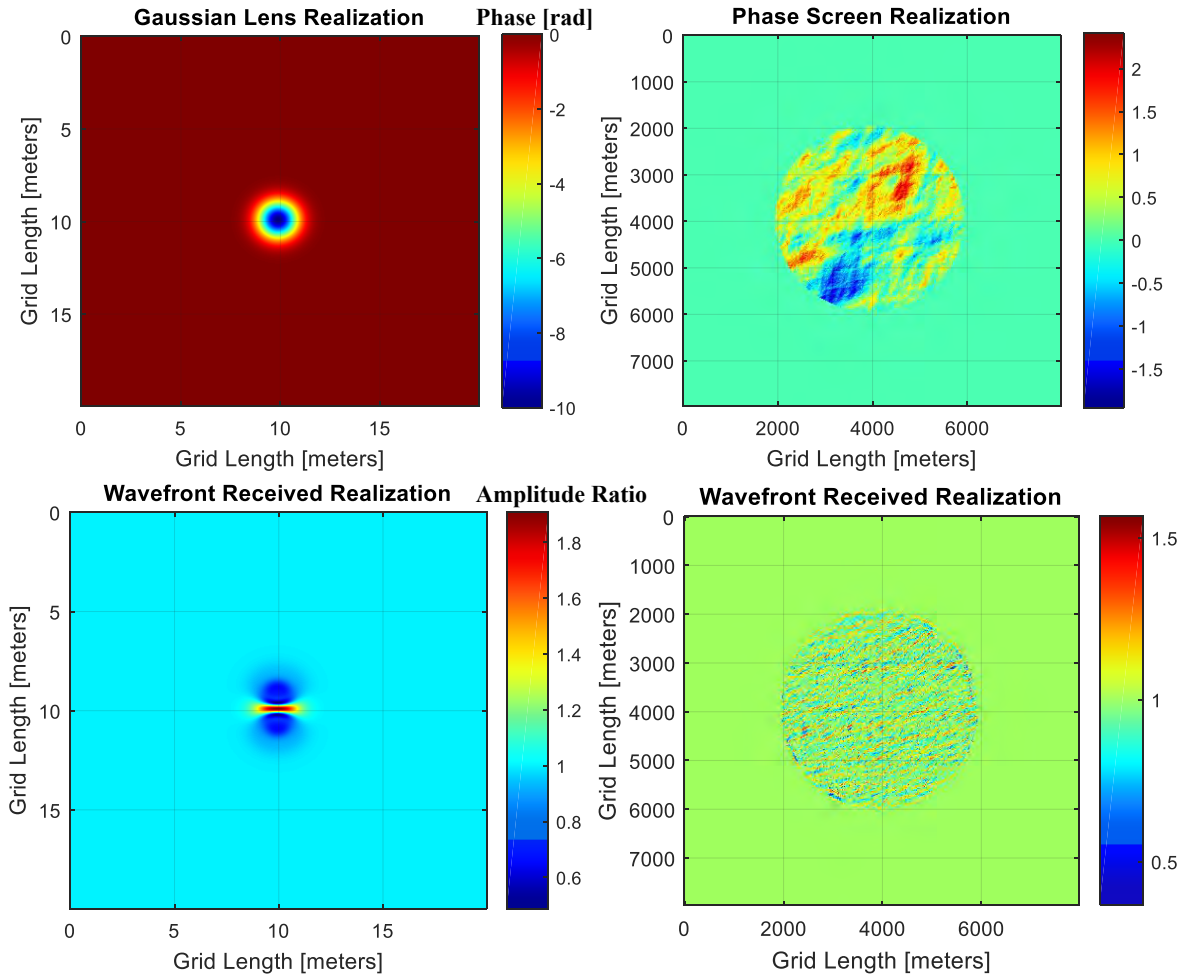

Figure 55. 2D Gaussian Lens (Left) and Kolmogorov Screen Phase (Right) with Corresponding Received Field Amplitude Ratios (Below)

The propagation distance of the incident wave beyond the lens is 0.5 meters, while the propagation beyond the phase screen realization is 5 kilometers. It can be seen that the convergent Gaussian lens results in a peak intensity where the focusing caused by the constructive interference is most intense. The propagation through a phase screen yields a dense combination of constructive and destructive interference from the large and small scale irregularity structures modeled by the Kolmogorov spectrum.

The average extrema and standard deviations are evaluated at a propagation distance of 5 kilometers to determine the relationship of the received wavefront

amplitude in comparison to the increase in the phase variance of the phase screen. In each case of the one and two dimensional propagation problems, there is consistency in the exponential (or logarithmic) rate of change in the average amplitude across the wavefront grid at the receiver as the phase variance increases. The corresponding standard deviations generally increase exponentially as well. This consistency is an expectation that provides an initial confidence for the numerical implementation of the wave equations. Additionally, this corresponds to the screen's phase variations observed in Chapter 3. A greater variation in the standard deviation is a result of the increasing dispersion in the phase samples from within the Kolmogorov power spectrum.

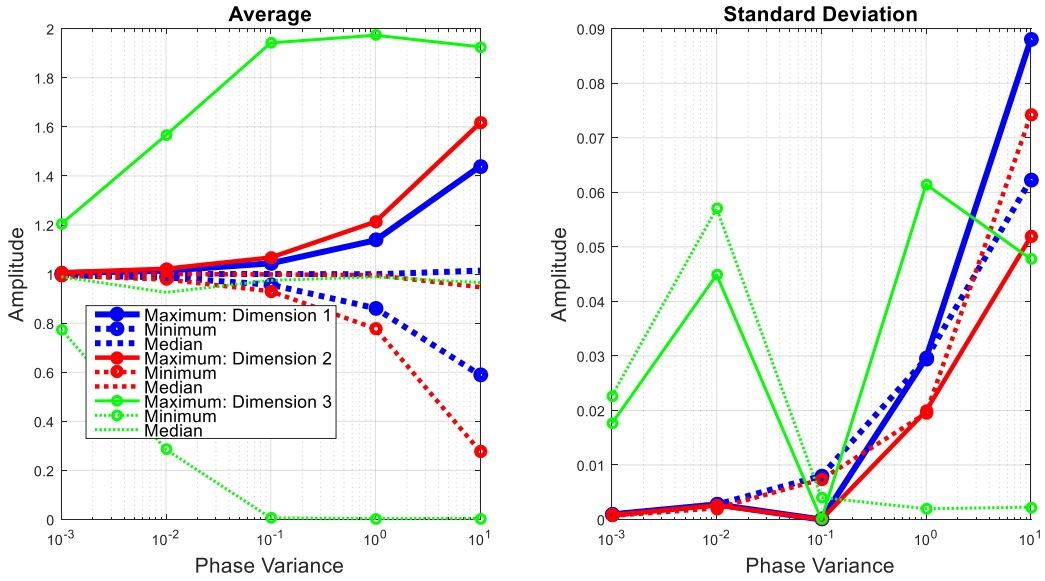

Figure 56. Amplitude Extrema of the Received Field

The three dimensional result shows a greater average amplitude due to the fact that the cube representation involves a gradual, cumulative phase change through a slab layer as opposed to the instantaneous phase effects of thin screens. However, unlike the one and two dimensional phase screens, it appears that the amplitude of the incident electric field scattered by the phase cube tends to saturate for phase variances greater than

0.1, or moderately weak scattering regimes. Therefore, there is no distinct relationship in the dispersion of the average amplitude with respect to an increase in the phase variance. A possible explanation is that the increased intensity of the gradual phase change through the cube causes more prominent cancellation effects from the superposition of phase shifts, thereby decreasing or maintaining the average amplitude around a peak intensity.

The following section examines a critical metric that generalizes the nature of the scattering in the form of an average scintillation index. Weak Scattering Theory is introduced for comparison to the phase screen results to verify agreement in the calculation of small scintillation index values. This process also validates the phase screen and propagation algorithm mechanism.

4.2 Weak Scattering Theory and Phase Screen Solution Comparisons

The implementation of phase screens in the wave propagation model accounts for random striations due to the fluctuating plasmas in the Earth's ionosphere. A metric to characterize the incident electric field amplitude fluctuations caused by this effect is the scintillation index. The phase screen based S_4 index solution is compared to the Salpeter formulation founded on the theory of Weak Scattering. The weak scintillation determined by these formula typically occur near the scattering region where most of the angular spectrum is in-phase. Under these conditions, it is simple to estimate the anisotropy. The scintillation formula given by (4.3) calculates the scintillation caused by elongated irregularities represented by the one dimensional Kolmogorov power spectral density. The scintillation formula given by (4.4) calculates the isotropic irregularities represented by the two dimensional Kolmogorov power spectral density.

$$S_4^2 = 4\int_{-\infty}^{\infty} S_\phi \sin^2\left(\left(K_x^2 z\right)/2k\right) dK_x \tag{4.3}$$

$$S_4^2 = 4\int_{-\infty}^{\infty}\left[\int_{-\infty}^{\infty} S_\phi \sin^2\left(\left(K_x^2 z\right)/2k\right) dK_x\right] \sin^2\left(\left(K_y^2 z\right)/2k\right) dK_y \tag{4.4}$$

These formulas are valid provided that the phase variance in the phase screens does exceed values in which the scintillation indices typically saturate to unity. For this reason, the S4 comparisons are made over relatively small phase variances to simulate small electron density fluctuations that occur under weak scattering conditions. The results in Figure 57 demonstrate excellent agreement as the error between the Salpeter theoretical formulation and the numerical phase screen based solutions of elongated and isotropic irregularities converges to zero as increasing frequency minimizes the scattering conditions while the phase screen maintains a constant phase variance of 10. The error bars represent the standard deviation of the error between the MPS and weak scattering approximations. The standard deviation is relatively consistent for each frequency increase, as expected for a constant phase variance in the phase screen.

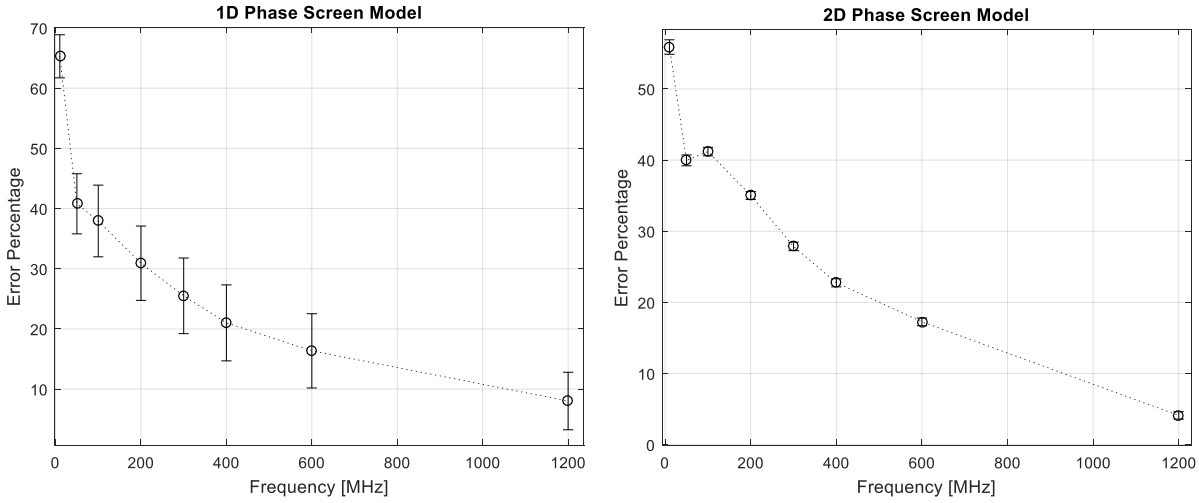

Figure 57. Error Difference of Phase Screen Solutions and Salpeter Weak Scattering Theory 1D (Left) and 2D (right)

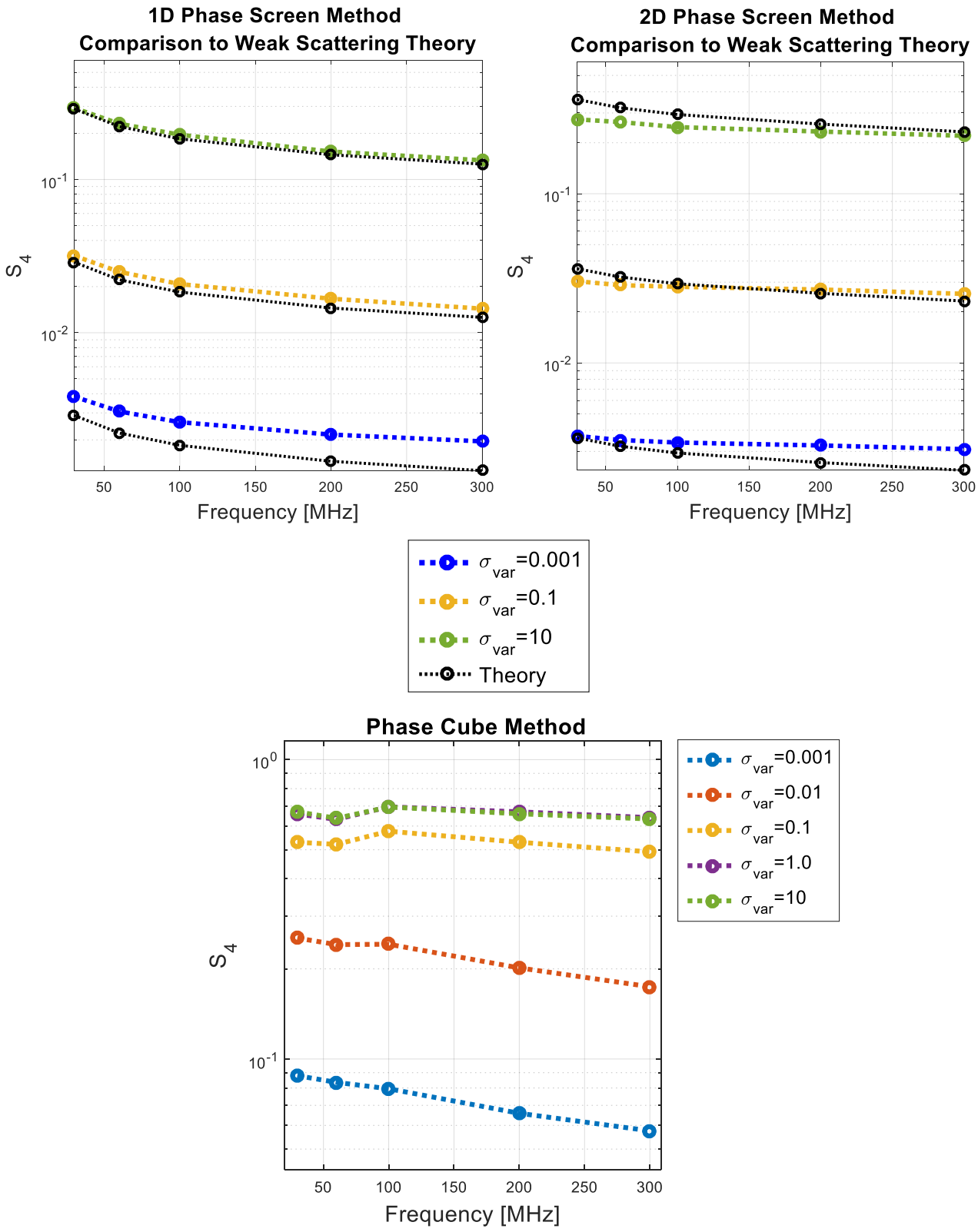

Figure 58. S4 Scintillation Indices Kolmogorov Screens/Cubes vs. Salpeter 1D and 2D Theory

A second test is applied to determine the weak scattering theory agreement with application of the phase cube under identical propagation parameters. In these cases, a variety of phase variance values are applied and demonstrate the finite agreement of the MPS and theoretical weak scattering cases. The S4 comparisons are made over relatively small phase variances to simulate small electron density fluctuations that occur under weak scattering conditions. The results in Figure 58 demonstrate excellent agreement between the Salpeter theoretical formulation for weak scattering and the numerical phase screen based solutions. The lowest of phase variations shows the most notable difference between the theory and numerical calculations of S4. It is believed that this is due to the numerical error accumulation being more dominant than the ambiguity of the physics being represented. As the phase variance increases, this difference seems to diminish. The curves show that at lower frequencies, the scintillation values increase. The increase is further driven by the increasing phase variance in the power spectrum. A larger phase variation over longer wavelengths in the incident field causes significant scattering. Additionally, greater scattering occurs with more persistent interactions between the incident field and the Kolmogorov power spectrum irregularities as observed with the phase cube results. In this case, at the minimum phase variance of 0.001, the scintillation index is comparable to a phase variance close to 1.0 for an instantaneous phase screen. Additionally, the increasing scintillation with respect to the increase in phase variance appears to saturate around 1.0 and 10. This result is likely relatable to the observation and explanation made previously with the amplitude extrema results in section 4.1.

The initial verification of the scintillation calculations and the weak scattering theory confirms that the propagation algorithm coupled with phase screens can provide

meaningful forward scatter solutions. Additionally, the smaller phase variances will be applied for the Kolmogorov phase cube structure implemented in the three dimensional propagation model presented as the end of the chapter when a random ionic background is desired. The following section examines the scattering mechanism of the three dimension ideal flute structure phase screen model.

4.3 Full Wave Model Backscatter Calculation Comparisons to the MPS Model

In this section, the phase screen based propagation model previously developed is compared to a full wave model that calculates the backscatter caused by the flute structure. The intent is to determine the differences in the pulse coherence calculations when considering the complete scattering phenomenology and without the slow varying envelope or paraxial approximations on the propagator. The size of the flute structure relative to the wavelength of the incident field should cause considerable backscatter that would otherwise not be measurable using the phase screen technique. A key disadvantage to the full wave model is the computational resources required to time step through the finite domain. For this reason, the propagation is strictly focused to one dimension. The finite difference method applied to solve Maxwell's equations is an explicit forward Euler scheme. The method is intuitive in terms of implementation but cumbersome to stabilize due to the limited choices for aspect ratio selection. Von Neumann stability analysis (see Appendix D) is applied to the finite difference scheme to determine the appropriate step sizes of the spatial and temporal derivatives. Figure 59 illustrates the discretization of the phase screen and finite difference domains.

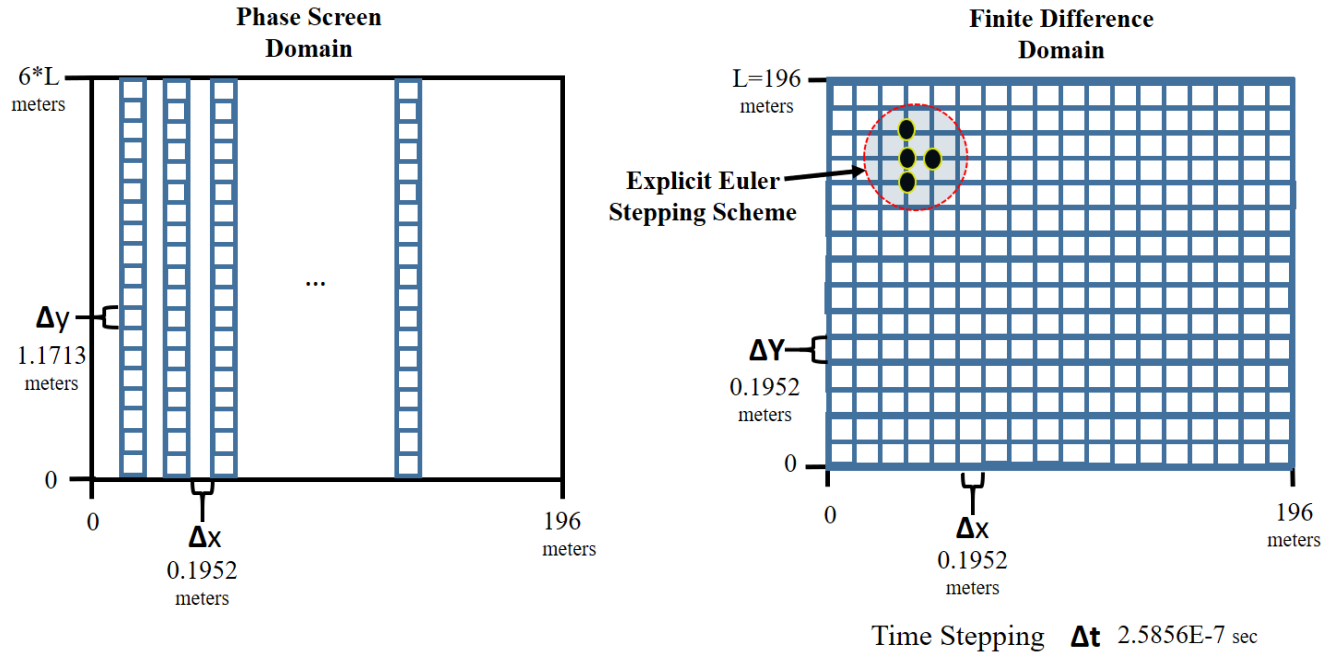

Figure 59. Comparisons between Phase Screen and Finite Difference Domain

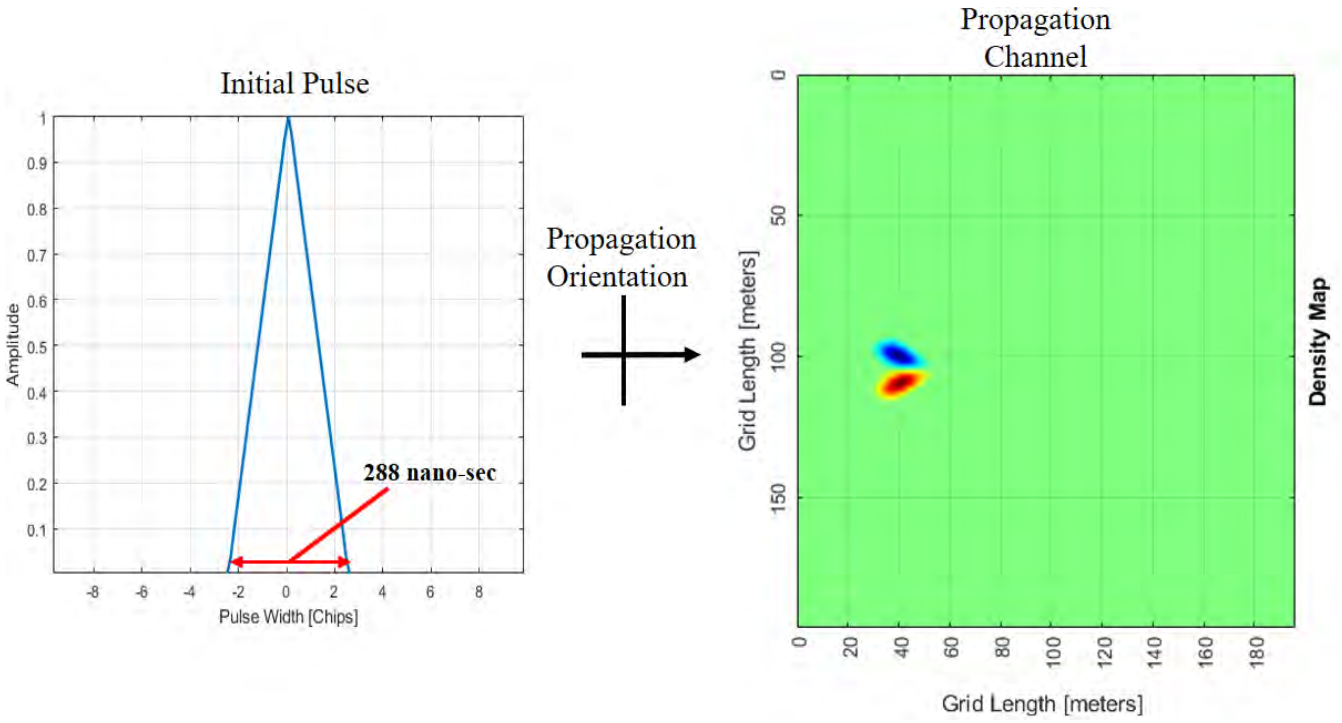

Figure 60. Full-wave Model Set-up

The initial triangular pulse modulates a carrier with a total time duration of 288 nanoseconds. Applying this pulse width, the carrier frequencies tested for each case are

10, 15, 20, 25, and 30 MHz to provide adequate coverage across the high frequency spectrum. The density propagation channel involves a single flute structure located at the 40 meter mark downrange in the *x* direction. The scattering caused by the single flute structure provides more concise observations when comparing the differences between the phase screen and full wave solutions. The incident field continues to propagate down range to approximately 196 meters, where the received field is analyzed.

The key observations addressed in the pulse time delay plots (see Figure 61) are directly related to the phase perturbations in the received wave caused by the flute structure. Focusing effects observed from the previous sections translate to amplitude growth whereas defocusing causes amplitude fading in the pulses. Time delay increases for more prominent diffraction around the edges of the flute structure. All of these effects are more pronounced at the lower frequencies where the wavelength size of 30 meters is comparable to the diameter of the flute structure of 44 meters. The higher frequencies of 15, 20, 25, and 30 MHz decrease the wavelengths to 20, 15, 12, and 10 meters, respectively. Under these conditions, the diffraction is minimized as the concentration of energy becomes more focused inward from the edges of the flute. The observation of the pulse time delay band becomes less prominent.

Similarly, the backscatter calculated from the full wave model becomes less prominent for higher frequencies as diffuse reflections off the flute structure are minimized. The time delay calculations tend to be greater in the full wave model for each incident wave carrier frequency tested. In the most significant scattering case, the phase screen model yields a time delay of 44 percent of the original pulse width at 10 MHz whereas the full wave model yields a delay that is 147 percent of the original pulse width.

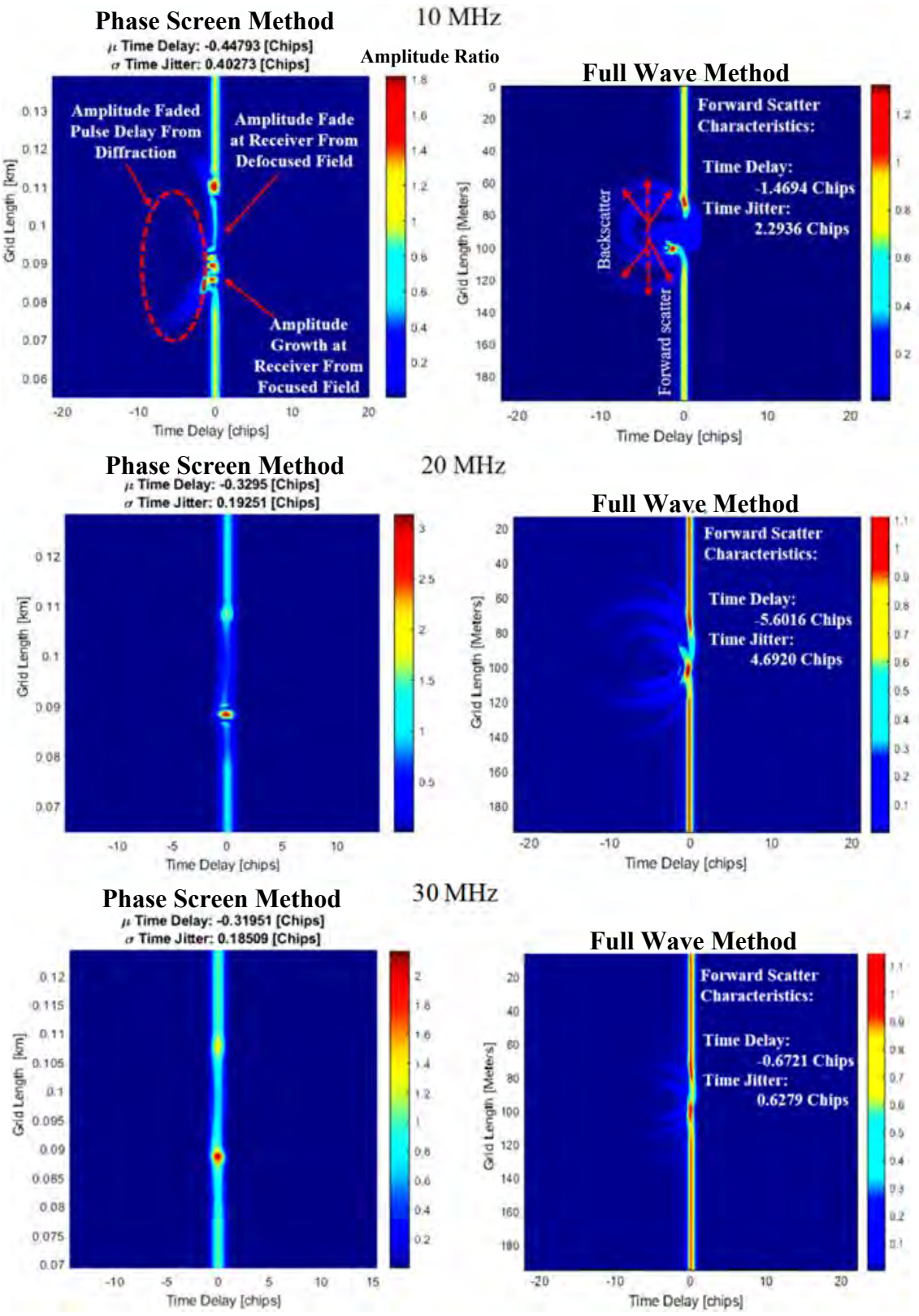

Figure 61. MPS vs. Full Wave Pulse Propagation Scatter Results

Both models observe the focus and defocusing effects that are characteristic of the dipole flute structure. Perhaps, the full wave model accounts for more domain sampling of the pulses in the two dimensional discretization as opposed to the one dimensional phase screen sample space. The additional scattered energy contributes to a greater temporal moment calculated along the receiver grid. This is also observable in the Figure 62 as more delay bands are present.

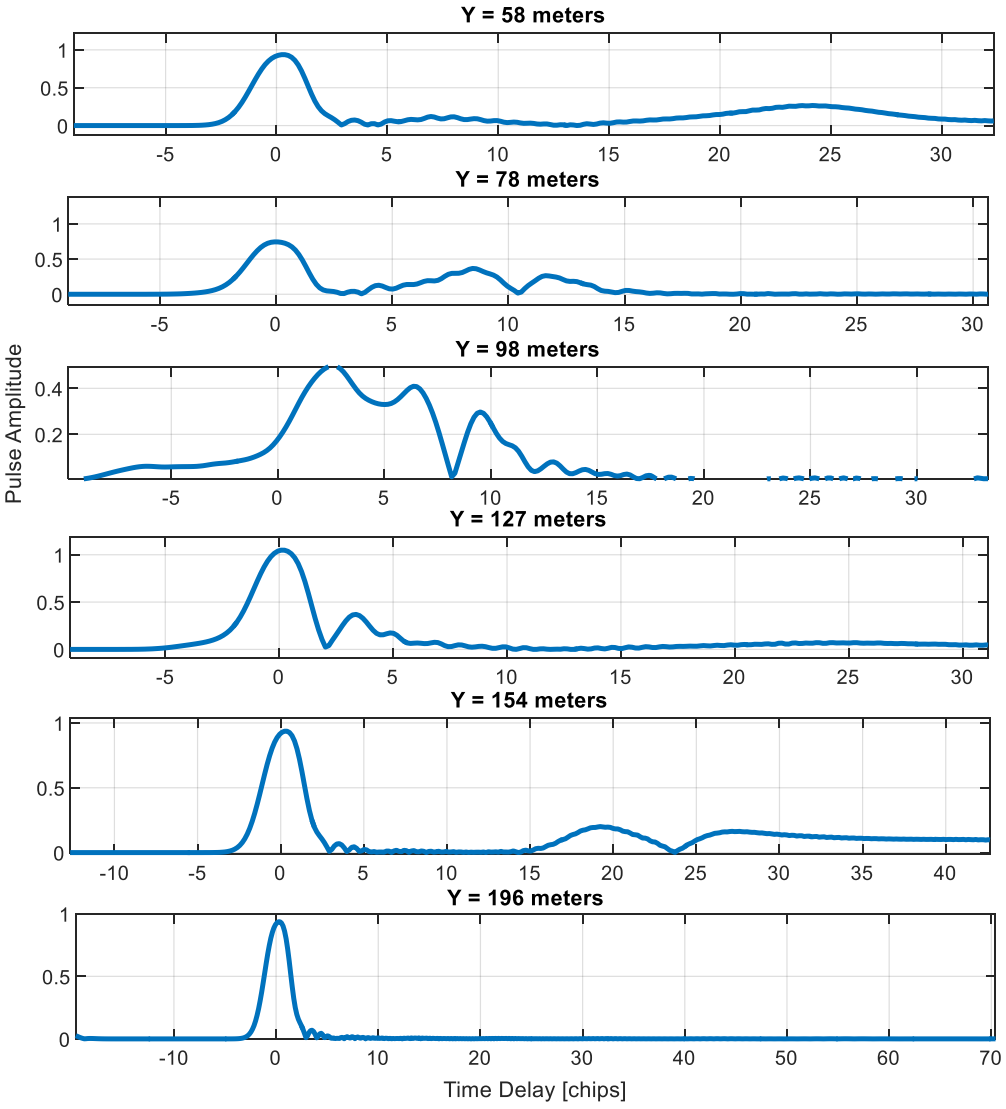

Figure 62. Full-Wave Model Amplitude Realizations along the Receiver Grid

Figure 63 provides a summary of the time delay and coherence bandwidth calculations comparisons between the forward scatter characteristics of each model. The coherence bandwidth is compared to the bandwidth of the transmitted pulses (14 MHz). The phase screen model generally yields a coherence bandwidth that exceeds the signal bandwidth, indicating a flat fading amplitude in which the pulses exhibit similar fading characteristics. Conversely, the full wave model results demonstrate that, in general, the pulses exhibit unique frequency selective fading characteristics as the coherence bandwidth of the propagation channel is lower than the pulse bandwidth.

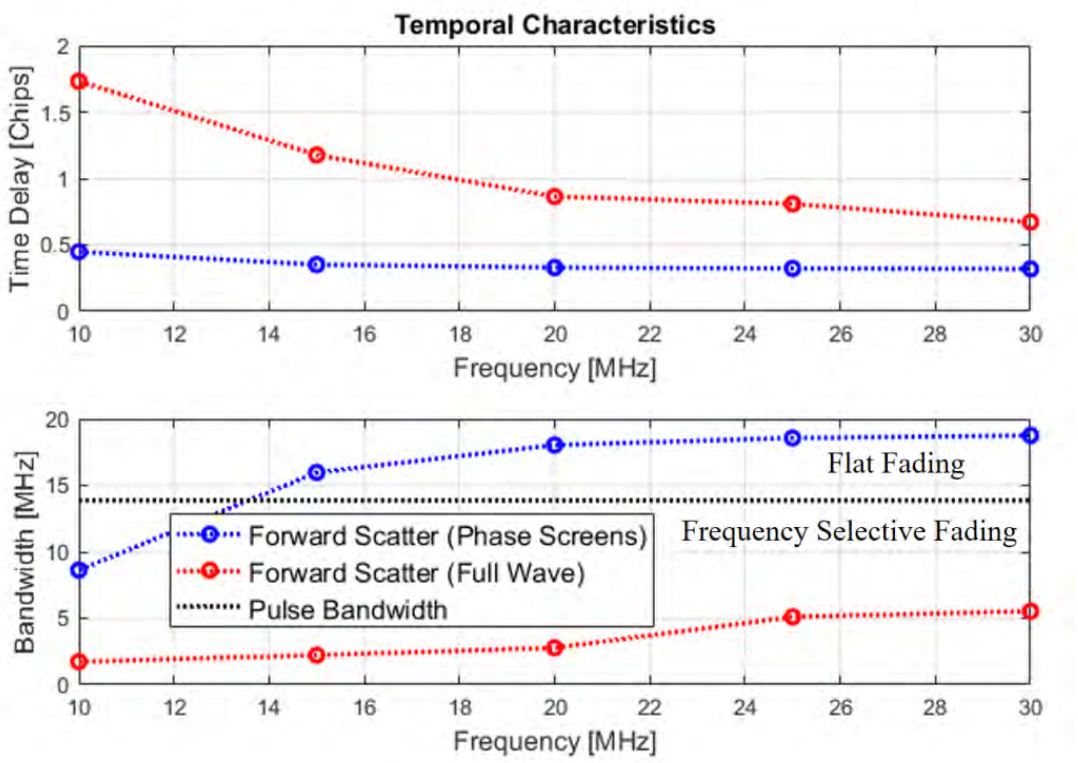

Figure 63. Time Delays and Coherence Bandwidths over the Carrier Frequencies

The second order moment of the received field is the root calculation for the coherence bandwidth. The second order moment accounts for the dispersion of the faded pulses which has greater prominence in the full wave calculations. The variation in the phase is

likely smaller in the phase screen approach because the slow varying envelope approximation applied in the propagator inherently relaxes the phase sampling requirements, thus making the cumulative phase changes in the intermediate free space regions between the screens less significant compared to amplitude variations. Generally, the slow varying envelope approximation is most valid for longer propagation distances relative to the wavelength of the propagating wave. Though more desirable, this comparison over longer propagation distances cannot be made due to the computational limitations and simulation time required to run the full-wave model.

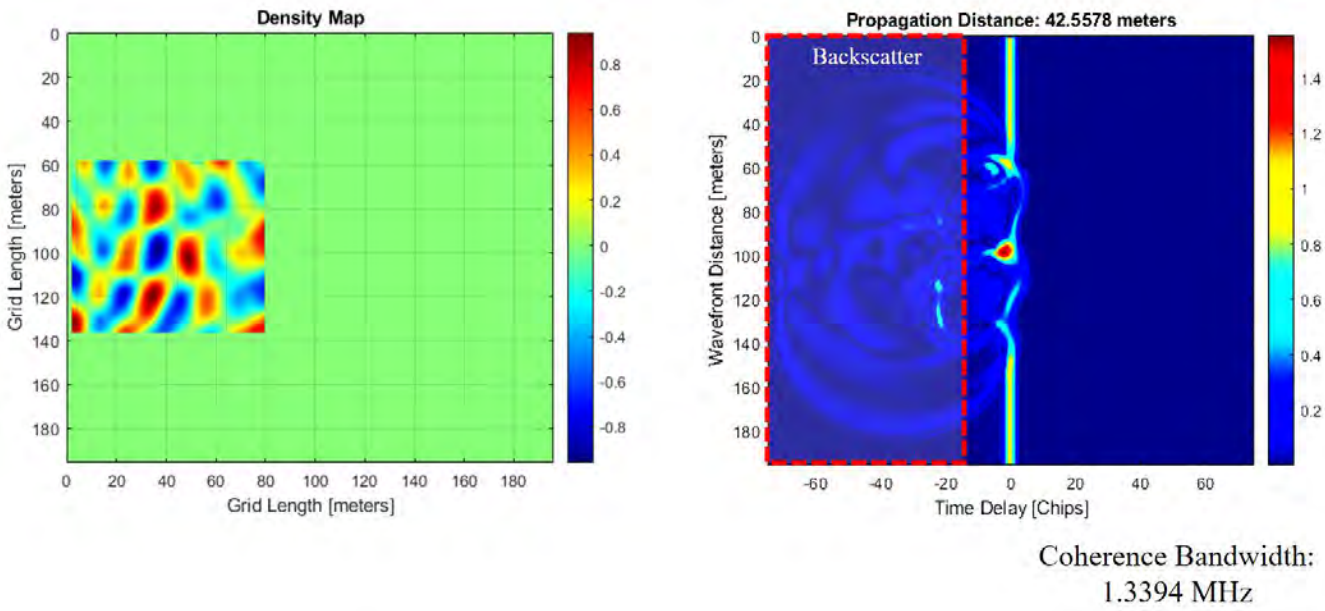

Figure 64. Stochastic Flute Map (Left) and corresponding Backscatter of pulses (Right)

Figure 64 illustrates the full wave model results of the pulse propagation through a density map in which multiple flute structures are present. In this case it is evident that the prominence of backscatter is greater than forward scatter over the propagation distance. This suggests that during the nonlinear stage of the interchange process, the prominence of bifurcating flutes may require more direct techniques to account for

propagation effects under conditions of strong scattering over shorter distances compared to the multiple phase screen technique. However, the multiple phase screen technique can at least provide a reasonable solution that reveals comparable amplitude characteristics of the received field, suitable for scintillation calculations.

4.4 FLUTE PHASE CUBE PROPAGATION TEST

The phase cube concept applied to the ideal flute structure is coupled with the propagation algorithms developed in the previous chapter. The objective is to observe the fundamental scattering characteristics of the ideal form of the flute structure over a two-dimensional receiver plane in the x , y, and z directions. The linear polarization concept is introduced in Figure 65.

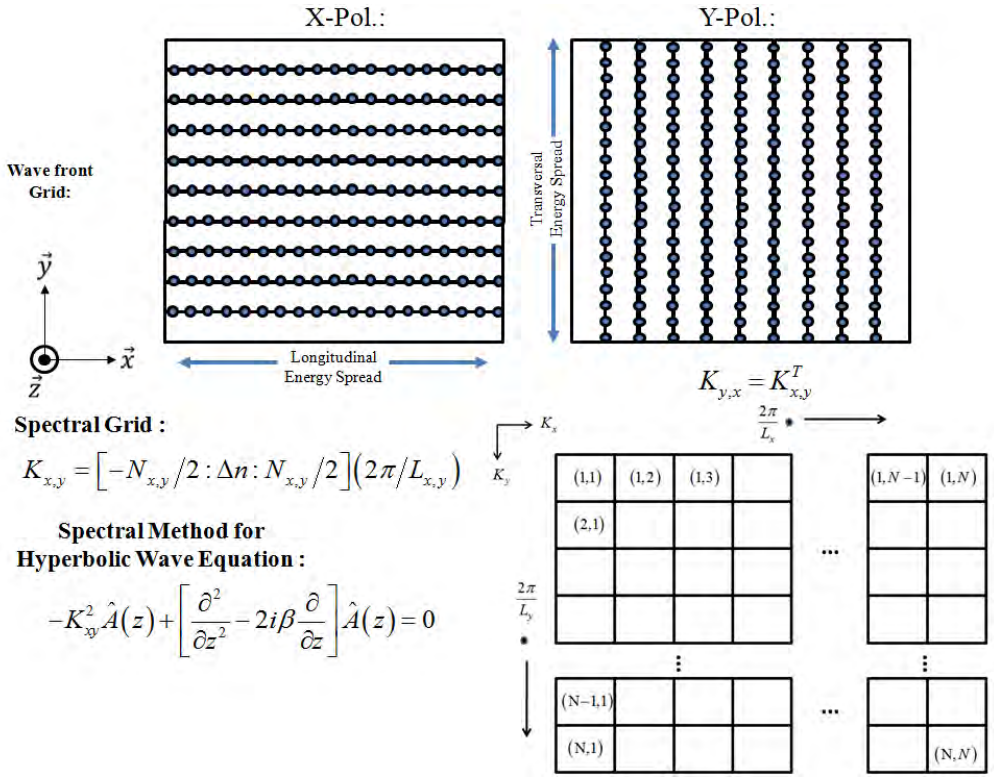

Figure 65. Linear Polarization Process in relation to Spectral Method

Varying the polarization orientation from horizontal to vertical requires transposing the spectral wavenumber grid that is used to discretize the spatial derivatives of the propagation algorithm in the fourier domain. This is a critical application of the phase cube flute structure model as it accounts for the scattering along the flute's elongated aspect where severe edge diffraction occurs. Figure 66 shows a demonstration of the scattering caused by a single flute structure in which the received plane is 500 kilometers downrange.

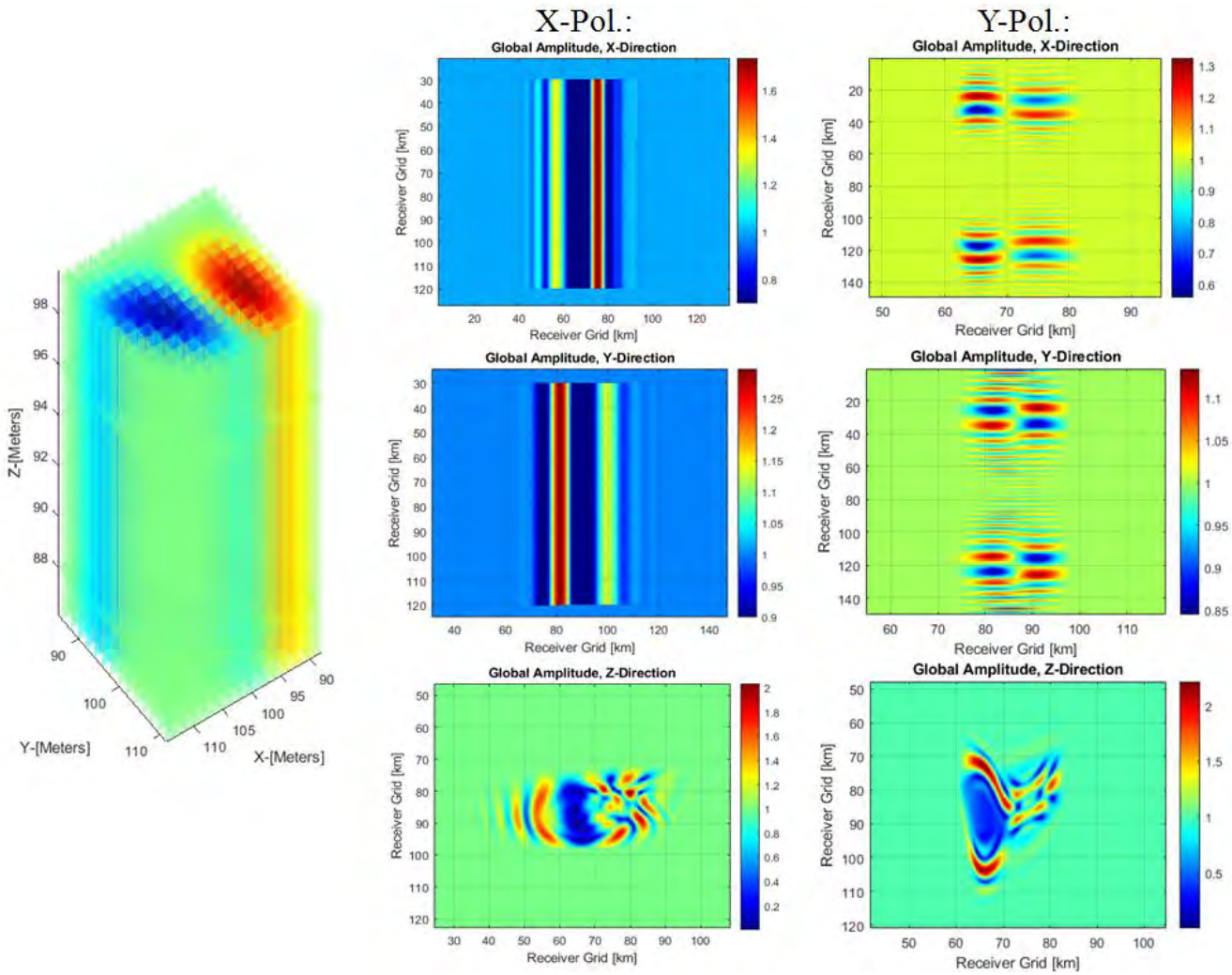

Figure 66. Single Flute Cube Scattering Orientations

The *x*- polarization broadside to the flute shows a wide horizontal diffraction pattern spanning the elongated portion of the structure in both the *x* and *y* propagation directions. The *y*-polarization broadside to the flute shows narrow vertical diffraction patterns along the elongated portion of the flute.

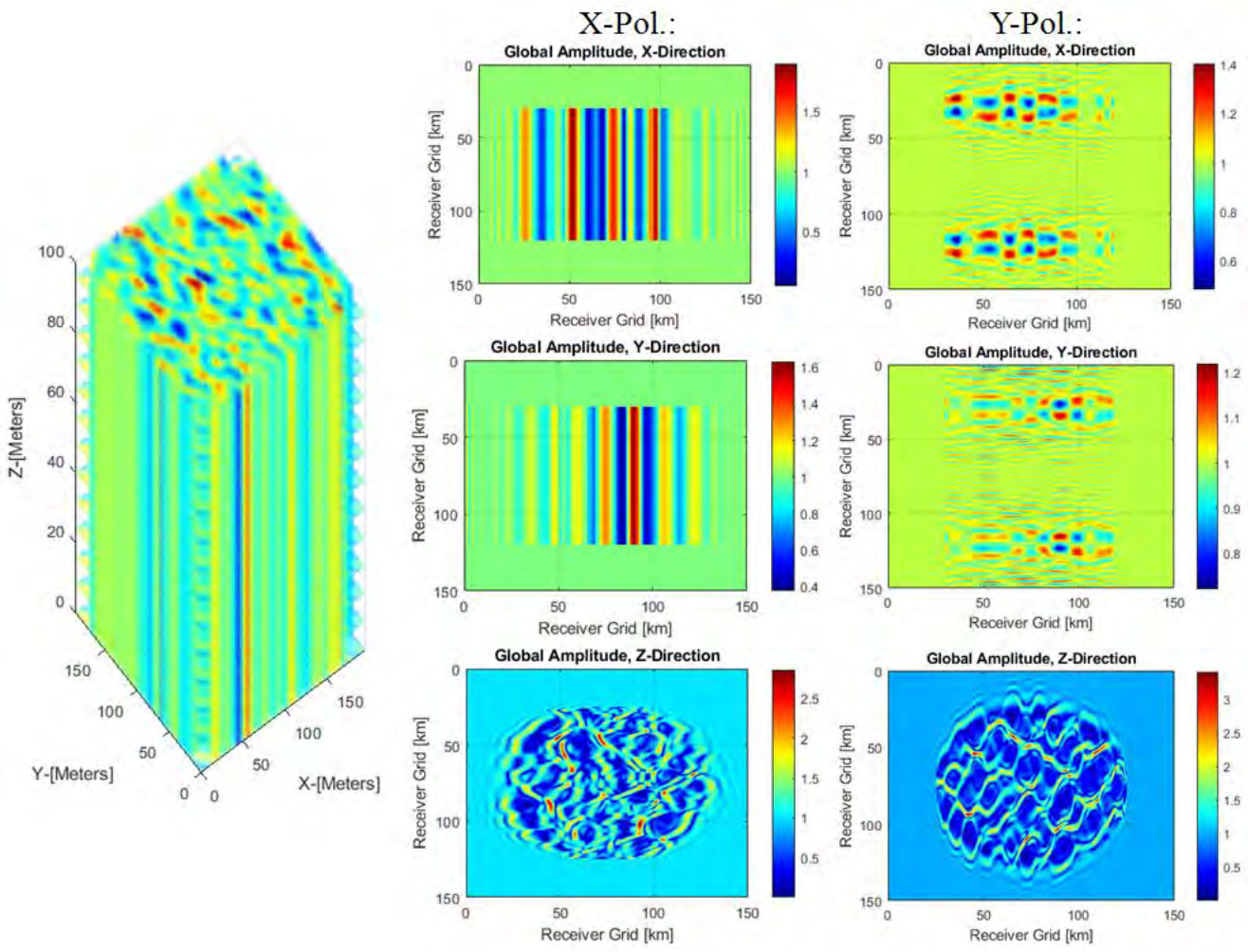

Figure 67. Stochastic Flute Cube Scattering Orientations

The top portion of the flute along the *z*-direction causes the field to exhibit significant focusing on the positive (red) portion of the perturbation and defocusing on the negative (blue) portion of the density perturbations. The interaction between the two regions cross interferes in the *x*-pol. case more significantly than in the y-pol. case, likely due to the

interior separatrix of the flute structure aligning perpendicular to the horizontal orientation. In this case, the stagnation points are aligned horizontally along this axis, the scattering line of sight, causing additional interference effects of the field. Figure 67 shows similar effects as well. The cases of diffraction are more frequent because the additional flutes within the phase cube cause extreme diffraction perpendicular to the elongation direction of the phase cube. The intensity extrema also appears to be more severe in these cases. This makes the propagation orientation along the z-direction more difficult to distinguish between the *x* and *y* polarization characteristics.

The two dimensional propagation algorithm demonstrates fundamental scattering phenomenon of the phase cube flute structure concept with respect to propagation direction and polarization. The following section will expand the phase cube model to implement the ray tracer and incorporate refractivity effects. An important feature is the inclusion of additional angles of incidence that will provide additional scattering features that are unique to the flute structure.

4.5 Ray Tracing Coupled with Phase Cube Structure

Calculating the azimuth and elevation angles of the incident wave vector involves converting the vector components from spherical to cartesian. The vector components propagate perpendicular to each two dimensional screen along its path. The vector components are recombined, yielding the total magnitude of the wave after propagating through the flute. This process is repeated similarly for the three dimensional Kolmogorov structures examined previously. The vector quantities of the electric field calculated from the angular components of the propagation vector.

$$\vec{E}_x = \hat{E}_r \cos(\theta_{Az})\cos(\theta_{El}) \tag{4.5a}$$

$$\vec{E}_y = \hat{E}_r \sin(\theta_{Az})\cos(\theta_{El}) \tag{4.5b}$$

$$\vec{E}_z = \hat{E}_r \sin(\theta_{El}) \tag{4.5c}$$

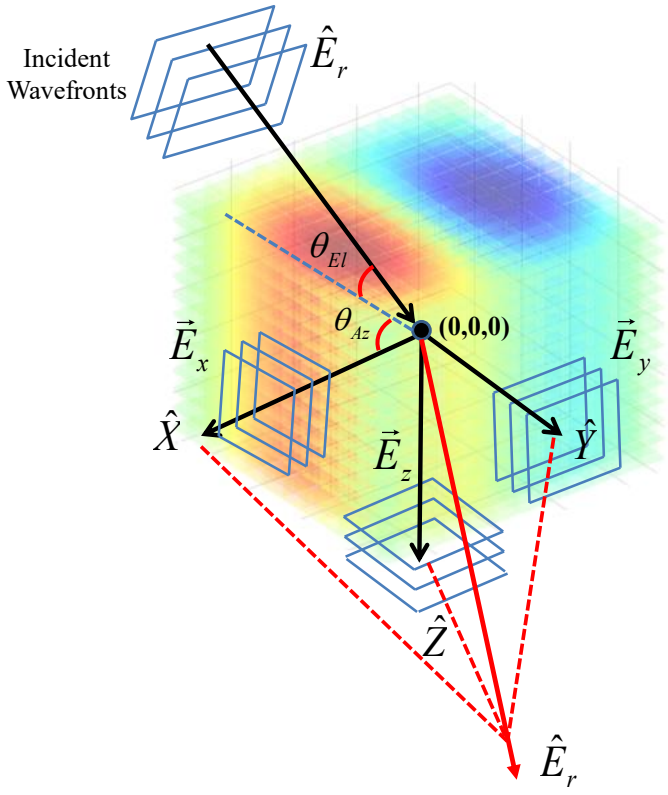

Figure 68. Electric Field Propagation Process

Recombining the components to acquire the total magnitude:

$$\hat{E}_r = \sqrt{\vec{E}_x^2 + \vec{E}_y^2 + \vec{E}_z^2} \tag{4.6a}$$

The phase components in each direction

$$\hat{\theta}_{x,y,z} = a\tan\left(imag\left(\vec{E}_{x,y,z}\right)/real\left(\vec{E}_{x,y,z}\right)\right) \tag{4.6b}$$

In order to determine the azimuthal and elevation angles for the field vector calculations, a ray tracer is implemented to account for the refractive variations between each phase screen. The ray tracer relies on gradient calculations of the velocity and position. Defining the position vector coordinates as follows:

$$\vec{r} = \cos\left(\theta_{Az}\right)\sin\left(\theta_{El}\right)\hat{i} + \sin\left(\theta_{Az}\right)\sin\left(\theta_{El}\right)\hat{j} + \cos\left(\theta_{El}\right)\hat{k} \tag{4.7}$$

The unit vector is formulated from the position vector:

$$\hat{u} = \vec{r}/|\vec{r}| = \vec{r}\Big/\sqrt{\left(\cos\left(\theta_{Az}\right)\sin\left(\theta_{El}\right)\right)^2 + \left(\sin\left(\theta_{Az}\right)\sin\left(\theta_{El}\right)\right)^2 + \cos\left(\theta_{El}\right)^2} \tag{4.8}$$

In Figure 69, a grid of discrete velocities are created from the cube arrangement of two dimensional phase screens.

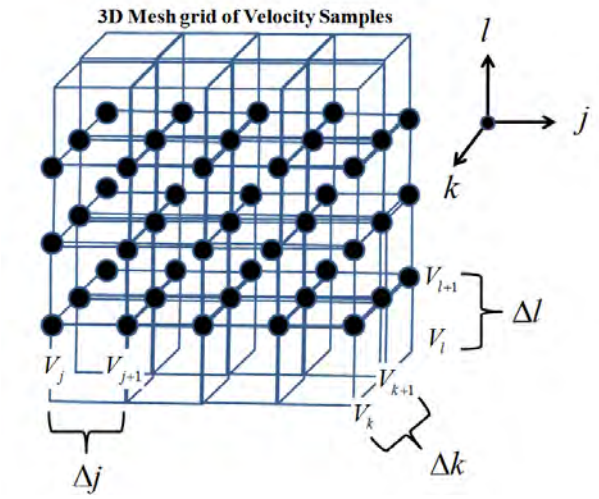

Figure 69. Velocity Gradient Sampling Cube

The velocity map indexing updates the velocity gradient. Calculating the change in velocity from the change in the refractive index, where *C* is the speed of light:

$$\Delta V_e = C/\Delta n \tag{4.9}$$

Creating velocity gradients from finite points on the three dimensional grid:

$$\frac{\partial V}{\partial x} \approx \frac{-V^{j} + V^{j+1}}{\Delta j} \quad (4.10a) \qquad \frac{\partial V}{\partial y} \approx \frac{-V^{k} + V^{k+1}}{\Delta k} \quad (4.10b) \qquad \frac{\partial V}{\partial z} \approx \frac{-V^{l} + V^{l+1}}{\Delta l} \quad (4.10c)$$

The velocity vector is calculated from the initial velocity divided from the unit vector:

$$\vec{V}_i = \hat{u} / V_i(j,k,l) \tag{4.10d}$$

The position advancement is achieved from multiplying the initial position by the sample index:

$$r_{j+1} = r_j(\Delta j) \quad (4.11a) \qquad r_{k+1} = r_k(\Delta k) \quad (4.11b) \qquad r_{l+1} = r_l(\Delta l) \quad (4.11c)$$

The corresponding indexing of the vector is determined by dividing the position by the sample index:

$$i_j = r_j / \Delta j \quad (4.11d) \qquad i_k = r_k / \Delta k \quad (4.11e) \qquad i_l = r_l / \Delta l \quad (4.11f)$$

Position gradient calculated from the velocity vector:

$$\left(\partial x / \partial s, \partial y / \partial s, \partial z / \partial s\right) = \left(V_f(\Delta j, \Delta k, \Delta l)\right)\vec{V}_i \tag{4.11g}$$

Updating the position vector using the position gradients:

$$\vec{r}_f(\Delta j, \Delta k, \Delta l) = \vec{r}_i(\Delta j, \Delta k, \Delta l) + \left(\partial x / \partial s, \partial y / \partial s, \partial z / \partial s\right) \tag{4.12}$$

Updating velocity vector using the velocity gradients:

$$\vec{V}_f(\Delta j, \Delta k, \Delta l) = \vec{V}_i(\Delta j, \Delta k, \Delta l) + \left(\partial V_x / \partial x, \partial V_y / \partial y, \partial V_z / \partial z\right) \tag{4.13}$$

The position gradient is determined with the initial velocity vector and the final velocity. The position vector is updated using the position gradient and the initial position while the velocity vector is updated concurrently as the unit vector and azimuth/elevation angles are recalculated. Both of these items work in tandem to approximate the ray trajectory. Approximation of the change in the index of refraction (n) from the change in the electron density is determined from the cold-collisionless plasma approximation of the Appleton-Hartree formulation:

$$n^2 = 1 - \frac{X}{1 - \frac{(1/2)Y^2 \sin^2(\theta)}{1-X} \pm \left(\frac{1}{1-X}\right)\left(\frac{1}{4}Y^4 \sin(\theta) + Y^2 \cos^2(\theta)(1-X)^2\right)^{1/2}} \tag{4.14}$$

where,

$X = \omega_o^2 / \omega^2$, $Y = \omega_H / \omega$, $Z = \nu / \omega$

ν = electron collision frequency

$\omega = 2\pi f$ is the angular frequency, and f is the ordinary frequency

$\omega_o = 2\pi f_o = \sqrt{N(e^2)/\varepsilon_o m}$ $\omega_H = 2\pi f_H = (B_o |e|)/m$ = gyro frequency

ε_o = permittivity of free space m = electron mass N= electron density

B_o = ambient magnetic field strength e = electron charge

θ = angle between the ambient magnetic field vector and the wave vector

It is important to note that the entry of the ray with respect to the flute structure will affect the arrangement of the phase screens that comprise the flute. This is due to the fact that the propagation algorithm always begins its spatial step iterations from the third

quadrant as the origin of the Cartesian coordinates is centered in the middle of the phase cube. Re-arrangement of the phase screen is also computationally efficient compared to recalculating the entire phase cube from re-orientation of the flute structure. Figure 70 shows the possible scenarios for correcting the entry of the ray trace by re-arranging the phase screens to maintain the quadrant three reference in the algorithm.

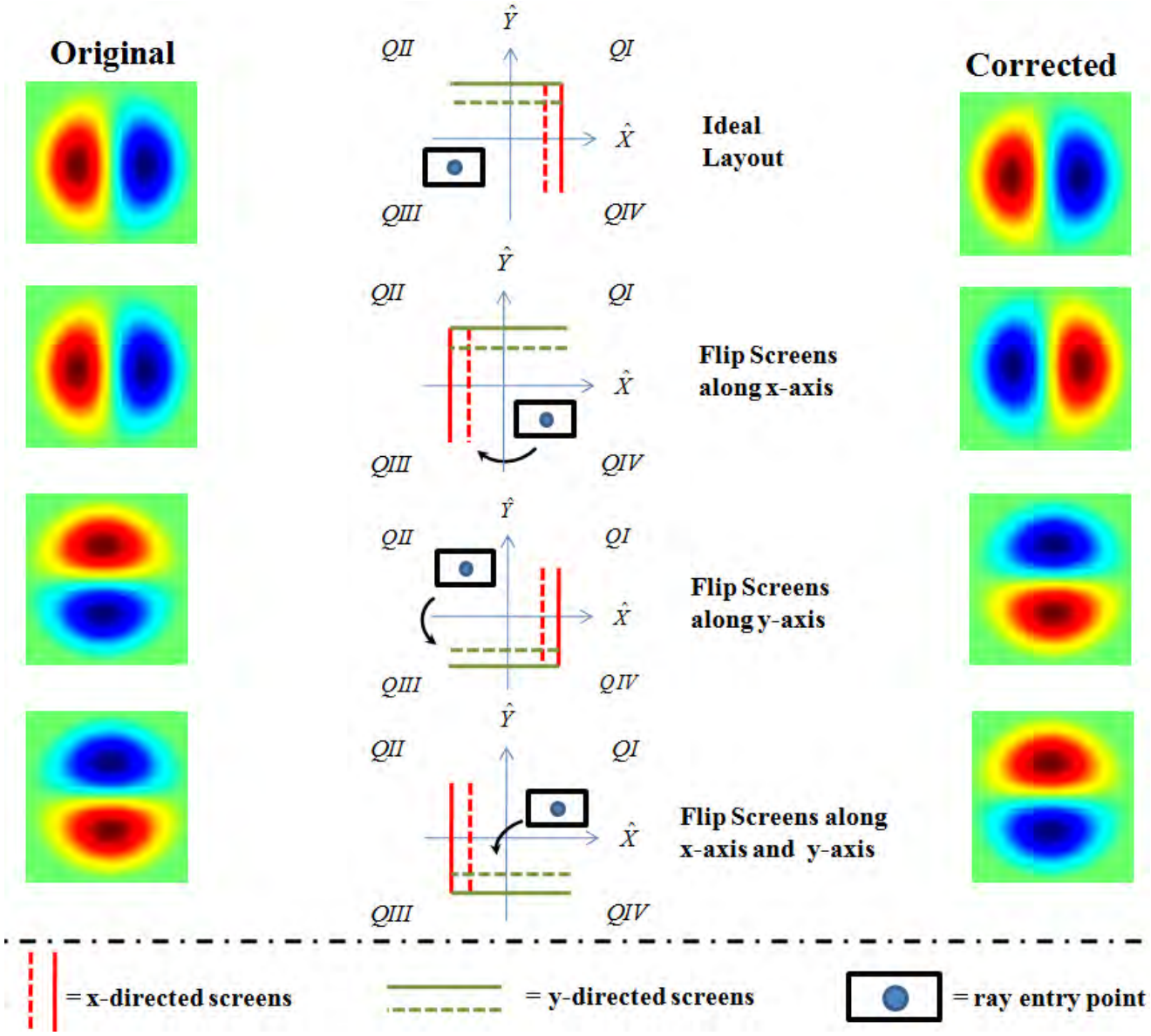

Figure 70. 2D Phase Screen Re-arrangements per Ray Entry

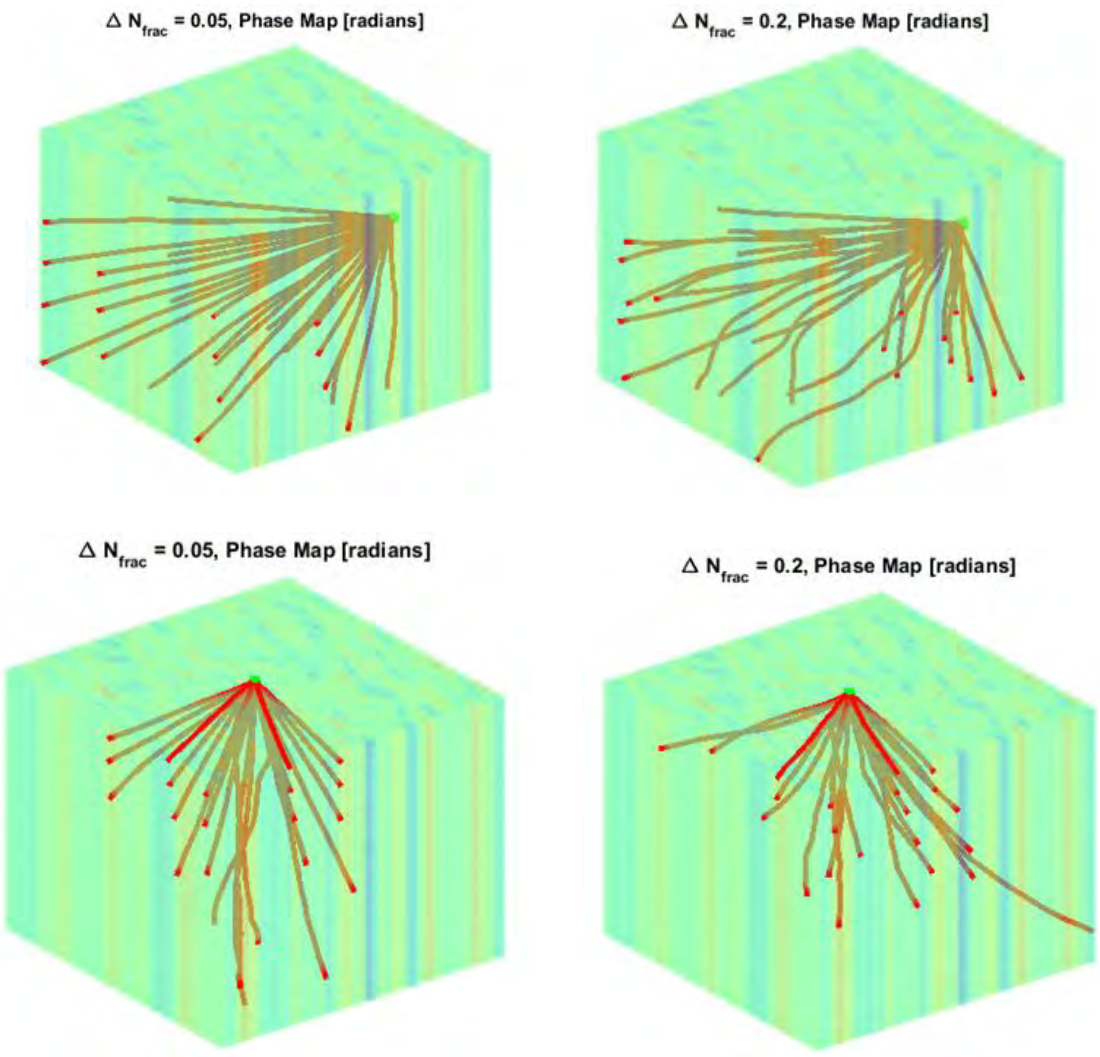

Figure 71. Flute Phase Cube Ray Refraction

A validation of the phase cube coupled ray trace model is shown in Appendix G. Figure 71 shows the variation in refraction as the ray passes through the flute structure at multiple angles through the broadside and topside entrance for weak and strong perturbation magnitudes. The ray entrance broadside to the flute structure exhibits the largest variation in azimuth and elevation angle deviations from the initial angles as the index of refraction has the greatest change in the *X*-*Y* plane. This is also shown in figure

72, where the final ray angles were calculated over a variety of azimuth and elevation incident angle samples.

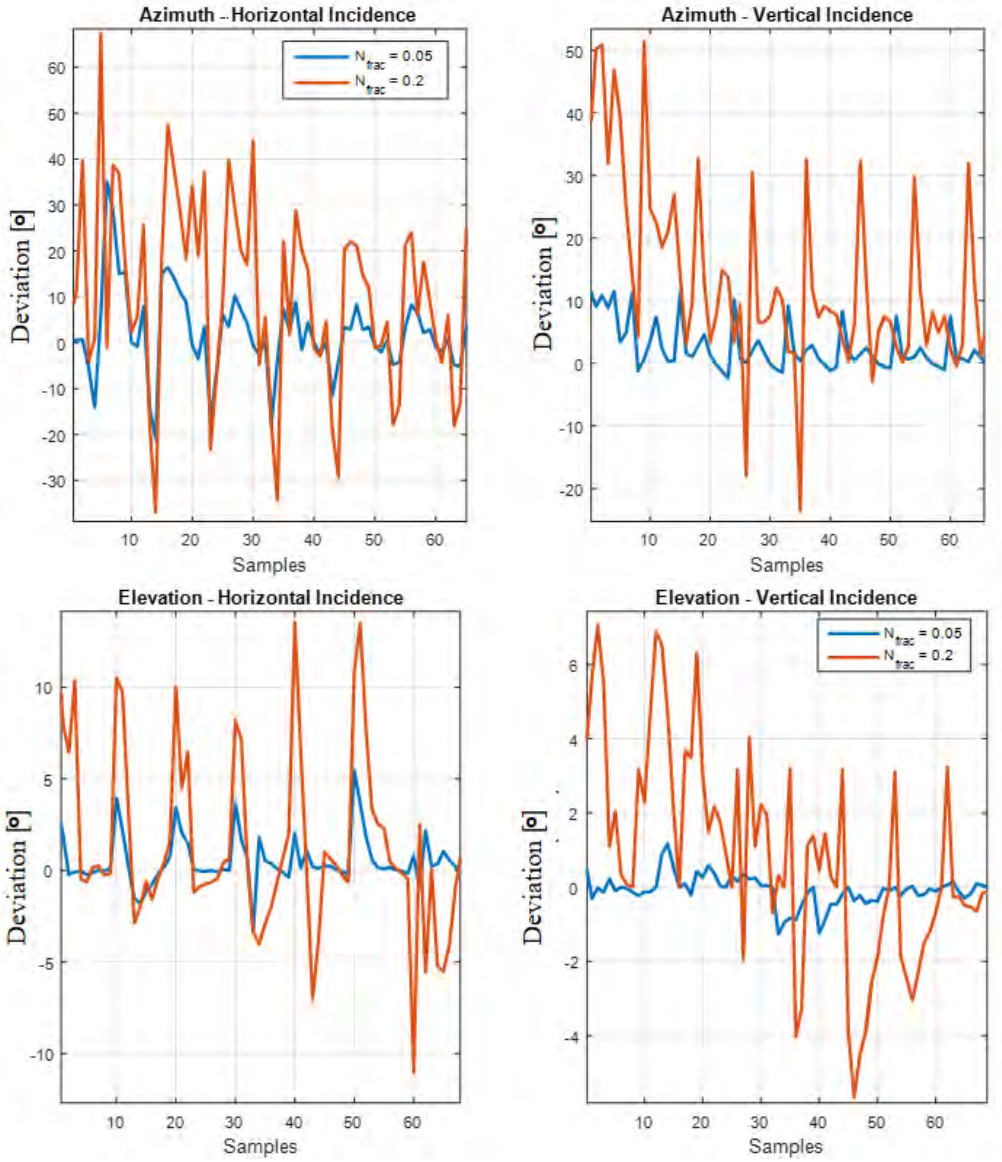

Figure 72. Azimuth and Elevation Refraction Angles for a variety of Ray Trace Samples

Application of the flute structure phase cube, Kolmogorov structure phase cube, ray tracer, and propagation algorithm is demonstrated in Figure 73 for a satellite communication system with a ground based receiver 500 kilometers downrange. Many of

the results presented in the following chapter are based on this configuration of the propagation model.

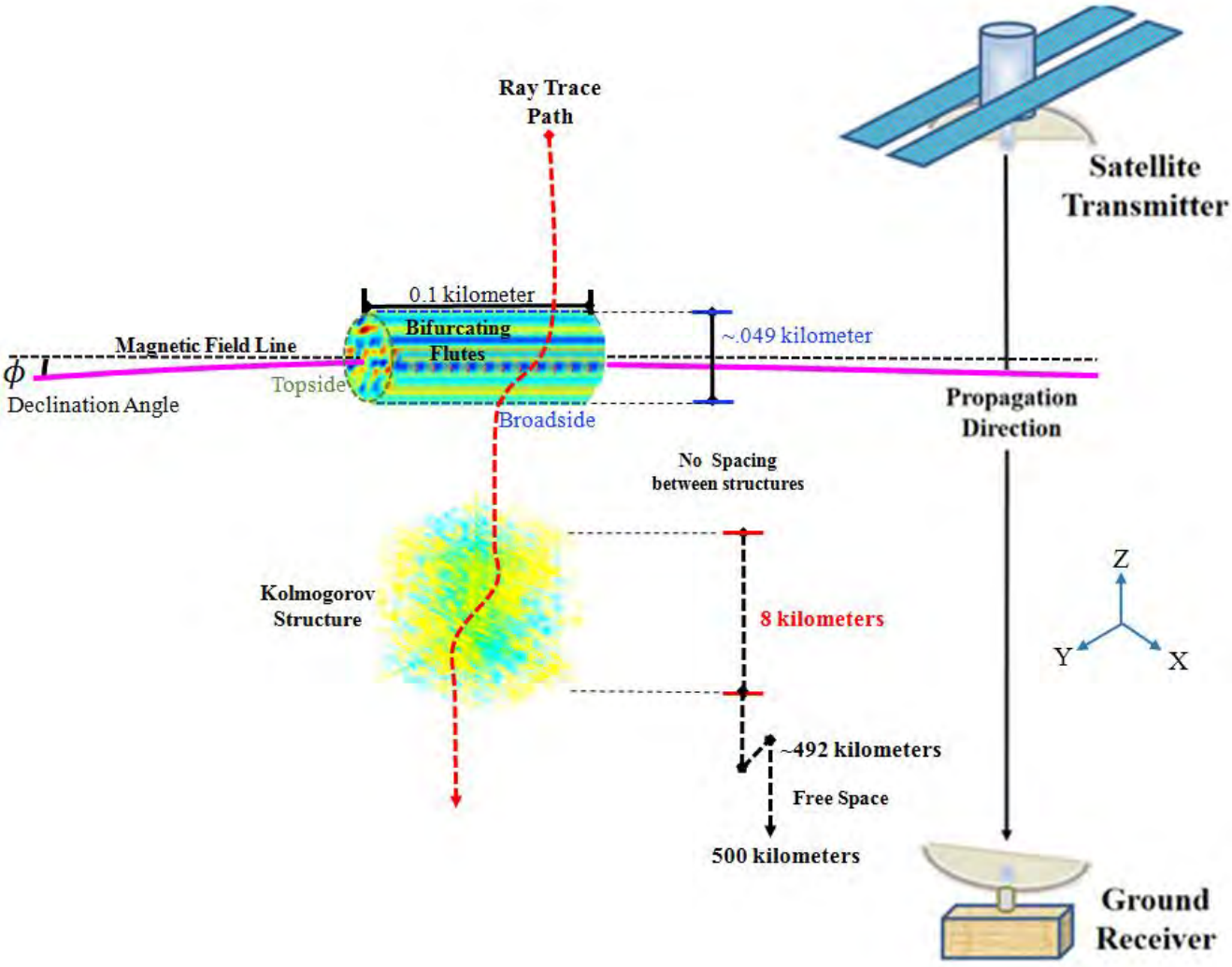

Figure 73. Forward Scatter Propagation Model Concept

The three dimensional propagation model presented in this section is utilized for a majority of the simulations and calculations presented in the following chapter. The immediate calculations from this model and the pulse coherence model introduced in chapter 2 involve the pulse delay/jitter and the scattering function to characterize the temporal effects and the spatial frequency domain parameters of the propagation channel.

The following section applies the moment method theory to validate the pulse coherence phase screen model.

4.6 Moment Method Theory Validation Results

The theoretical approach described in chapter 2 applies wave function coherence to a temporal moment. To summarize, these temporal moments are approximated using the mutual coherence of the complex field. The parabolic diffraction method that solves the mutual coherence function approximates the ionic irregularities of the medium as a phase structure function. This phase structure function is approximated as a series of Bessel functions that expand on the correlation spectrum of the random field. Applying these terms to the stochastic temporal moment integrals, the solutions for time delay (4.15) and time jitter (4.16) are:

$$\langle \tau \rangle = \beta \sigma_\phi^2 \left(2z - L\right) \left| A_2 \right| / 4\pi \omega_o \, A_o \tag{4.15}$$

$$\sigma_\tau^2 = t^2\left(0\right) + \sigma_\phi^2 / \omega_o^2 + \frac{\sigma_\phi^4 \lambda^2 A_2^2}{24\pi^2 \omega_o^2 A_0^2}\left(12z^2 - 16Lz + 6L^2\right) + \ldots \frac{\sigma_\phi^2 \lambda^2 A_4}{2\pi^2 \omega_o^2 A_0}\left(3z^2 - 3Lz + L^2\right) \tag{4.16}$$

where $t^2\left(0\right) = \int_0^\infty t^k \left| m\left(\tau\right)\right|^2 d\tau \Big/ \int_0^\infty \left| m\left(\tau\right)\right|^2 d\tau$, and m is the triangular pulse modulator.

The test matrix implemented for the method comparison is provided in table 1. Each frequency is evaluated over each down range distance and vice versa, creating a total of 25 combinations for holding the frequency values constant and an additional 25

combinations for holding the downrange distance constant. Figure 74 shows the comparisons the theory and numerical comparisons for holding frequency constant and varying distance. Figure 75 shows the comparisons holding distance constant and varying frequency. The pulse width of 288 nanoseconds is applied throughout the test matrix.

Frequency	10 MHz	12.5 MHz	15 MHz	17.5 MHz	20 MHz
Downrange Distance	100 km	200 km	300 km	400 km	500 km

Table 1. Moment Method Test Matrix

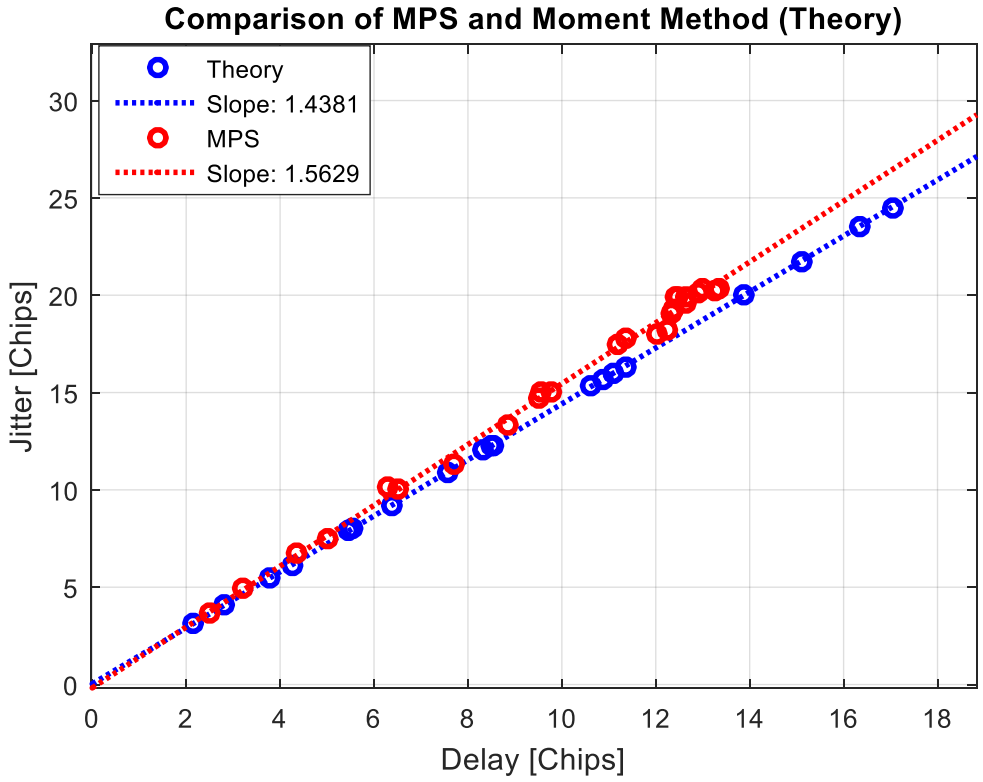

Figure 74. Time Delay-Jitter Ratio (Holding Frequency Constant and Varying Distance)

The relationship between the MPS and theoretical calculations appear to be consistent as indicated by the similar slopes they share with their respective time jitter to time delay slopes. At higher values of delay and jitter, there are deviations in which the theoretical

method tends to be somewhat larger compared to the MPS calculations. This lack of agreement could be the impact of using the narrow bandwidth approximation in the theoretical calculation which becomes less appropriate with increased strong scattering characteristics or increasing the bandwidth of the signal.

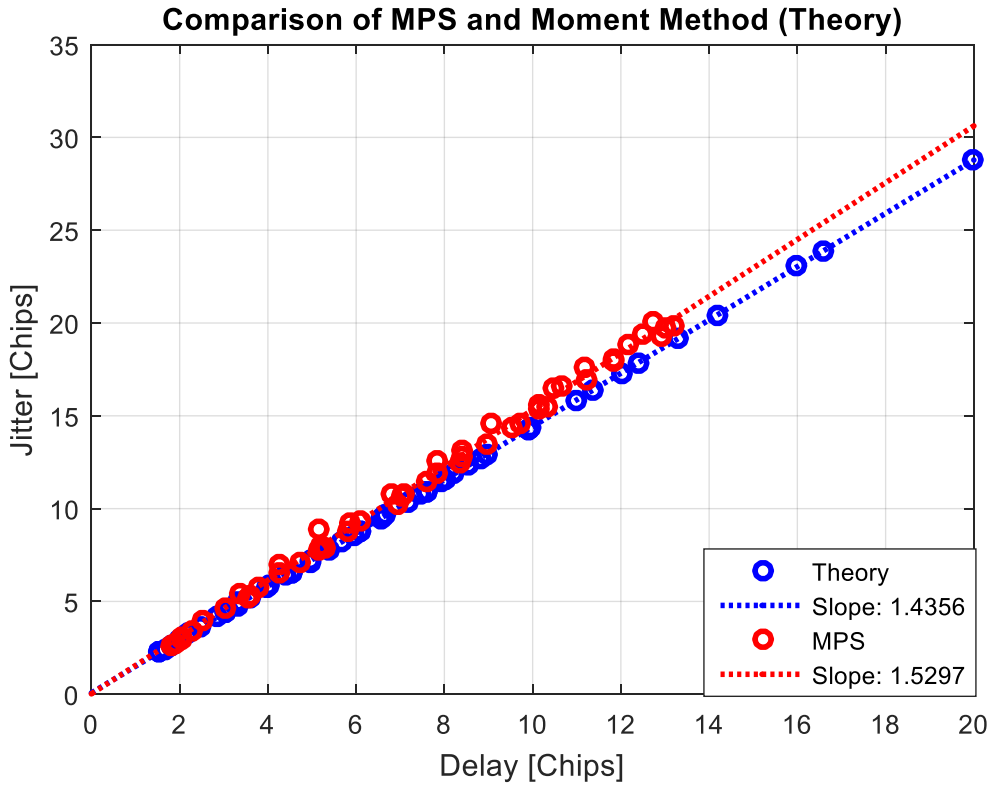

Figure 75. Time Delay-Jitter Ratio (Holding Distance Constant and Varying Frequency)

4.7 Scattering Function Characteristics and Validation

The scattering function is critical to characterizing the statistical features of the propagation channel. This section examines the scattering function of the multiple phase screen model by comparing the results of the Kolmogorov and Gaussian spectrums used in the phase screen calculation to determine any discernable features in the scattering function. The section concludes with a scattering function solution comparison between

the multiple phase screen method and the parabolic diffraction method introduced in chapter 2.

4.7.1 Kolmogorov vs. Gaussian Spectrum Scattering Function Comparisons

Initial observations of the scattering function involves examining the multiple phase screen propagation model electric field results for a 500 kilometer propagation distance through a series of phase screens along the propagation path. The results from the Kolmogorov and Gaussian Spectrum phase screens are compared to determine potential explanations for features observed in each spectrum. These observations will also provide a baseline expectation to aid the analysis of the flute spectrum phase screens presented in the following chapter, as strong scattering conditions are expected for high frequency transmissions in a flute perturbed channel.

Observations of multi-fringed scintillation arcs over a spatial doppler frequency spectrum are believed to be a result of strong scattering caused by rapid fluctuations in the electron density in the Ionosphere in which the anisotropy of the large scale gradients contributes to the distribution of energy over a time delay period. It has been demonstrated that a phase screen model can simulate this behavior provided that multiple screens are used to create multiple scattering planes for a prolonged anisotropy. In this demonstration, a phase variance of 10 is applied to these phase screens, separated by a distance of 50 kilometers. Figure 74 illustrates the delay-doppler maps of the scattering functions for both spectra after propagating the field at 10, 20, and 30 MHz at a pulse width of 288 nanoseconds. It is apparent that secondary arclets appear below the primary arc. As the frequency increases, these arcs become more shallow and pronounced, especially in the Gaussian spectrum. The scattering becomes more focused closer to the

origin of the doppler axis as the frequency increases, thereby making the discrete features of the secondary arcs more visible. It is apparent from the figures that anisotropy is a significant condition for these fine substructures. The Gaussian spectrum perhaps has less anisotropy compared to the Kolmogorov spectrum, thus broadening the Doppler-delay image. Additionally, the asymmetry of the primary arc is more notable in the 10 MHz case, where the strong scattering causes a prolonged and more intense energy spread for a narrower doppler shift q. As the frequency increases, the scattering broadens and the asymmetric features subside as the energy's time delay decreases over comparable doppler shifts.

The prominence of the arcs may also depend on the slope and inner scale of its wavenumber spectrum. As mentioned in Chapter 2, the Gaussian spectrum decays exponentially and only accounts for large scale anisotropy whereas the slope decay of the Kolmogorov spectrum is inclusive of the small scale structures as the energy spectrum cascades from low to high wave numbers. The low wave number spectrum with a high wavenumber roll-off in the Gaussian spectrum leads to an overall decrease in the propagating electric field intensity over identical propagation distance relative to the Kolmogorov spectrum. The Kolmogorov power law spectrum is much larger for the wave numbers that approach the smaller scale irregularities, thereby increasing the intensity of the field's fluctuations. This explains the general decline in the intensity of the energy spread observed in the Gaussian scattering function as the doppler frequency shifts away from the origin whereas the Kolmogorov scattering function energy spread appears to be globally more intense.

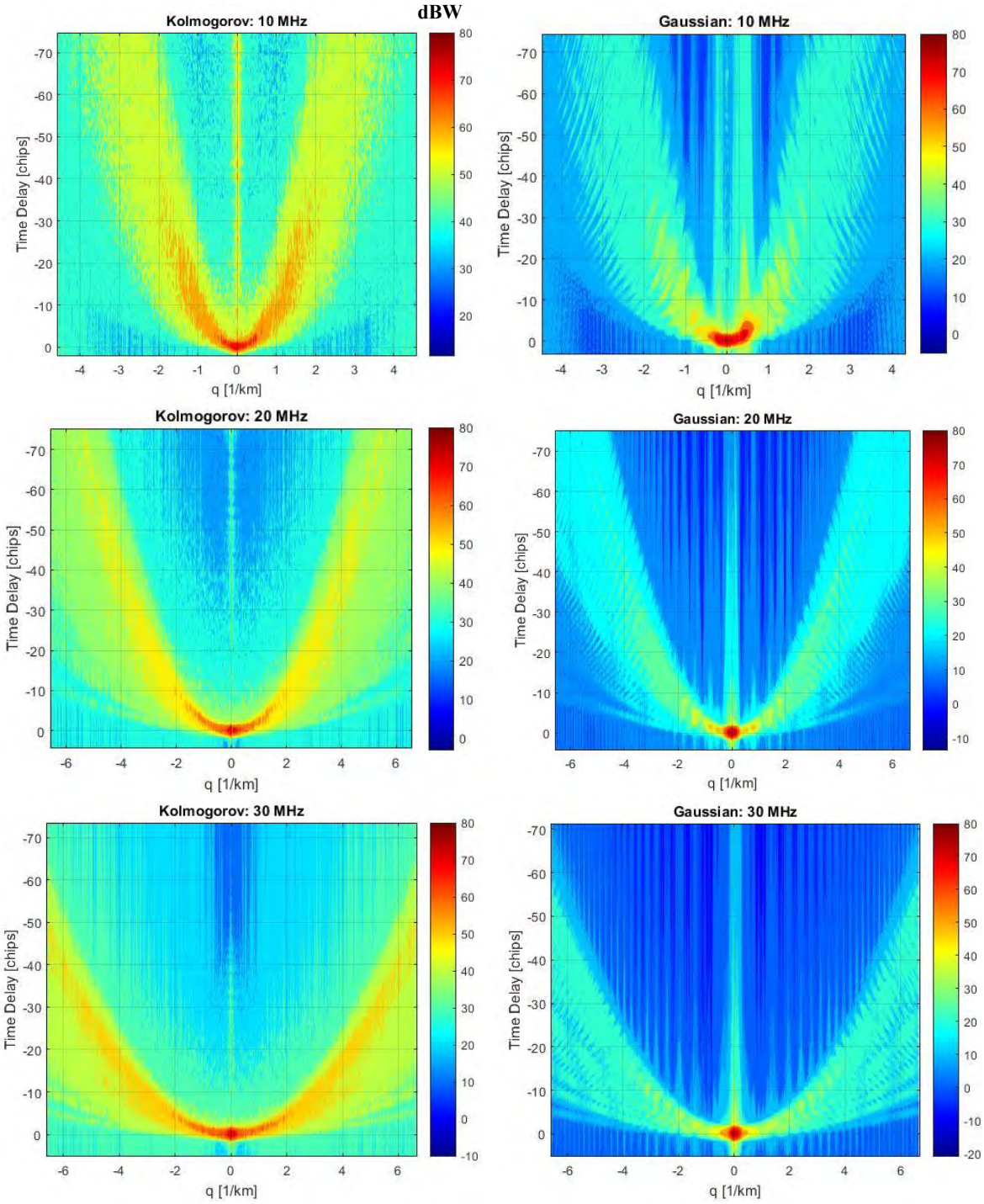

Figure 76. Scattering Functions for Kolmogorov (Left) and Gaussian (Right) Spectrum MPS Results at 500 kilometers propagation distance

Based on these results, an investigative aspect to consider for the stochastic flute maps presented in Chapter III is to examine the fluctuations in the power spectrum for the variety of linear, nonlinear, and quasi-linear flute structures. As presented previously, the slopes of each flute's phase power spectrum depends on the propagation direction of the incident field relative to the flute's stagnation points. Additionally, the uniformity and relationship of the stagnation points to the flute's interior separatrix also will affect the uniformity of the received field's scattering function. The following chapter will examine the nature of these factors on the scattering function calculations.

4.7.2 MPS Technique Comparison to PDM

The Parabolic Diffraction Method introduced in Chapter II yields the two-frequency, two-position mutual coherence function by directly solving a parabolic differential equation. It relies on the quadratic approximation of a phase structure function as the source term of the equation to model the phase effects from the ionospheric irregularities in the propagation channel. The resulting mutual coherence function is fourier transformed with respect to position and inverse fourier transformed with respect to frequency to yield the scattering function. PDM is considered a much more deterministic method in which no randomizations are required with respect to the calculations of the scattering function unlike the calculations in the MPS technique. It is limited in comparison to the MPS technique in that it cannot provide realizations of the propagating signal but rather the direct solution to the mutual coherence function. Additionally, the technique is only valid under strong scattering conditions and applying a relatively narrow band signal so that the scattering strength across the signal bandwidth is largely

dependent on the transmission carrier frequency. Despite these limitations, this alternative method is useful for comparisons of the scattering function in relation the MPS technique.

Solutions are compared for similarities in the doppler-delay distribution of the energy from an electric field propagating over a 500 kilometer distance. Figure 77 shows the delay-doppler maps acquired from both methods under the same propagation geometry for 10, 20, and 30 MHz transmissions with a pulse width of 288 nanoseconds. By inspection, the results appear to agree in terms of the energy extrema and doppler spread distribution with respect to time delay. This agreement is maintained as the scattering conditions weaken when frequency increases and the delay bands decrease. Visually, the stochastic nature of the phase screens translates to significant dispersion in the energy spread in the delay-doppler map, unlike in the PDM result. The MPS results could be smoothed if more trials are simulated and averaged, as accomplished in a Monte Carlo test. However, this is not practical given the computational expenses and the size of the test matrix scenarios detailed in the following chapter.

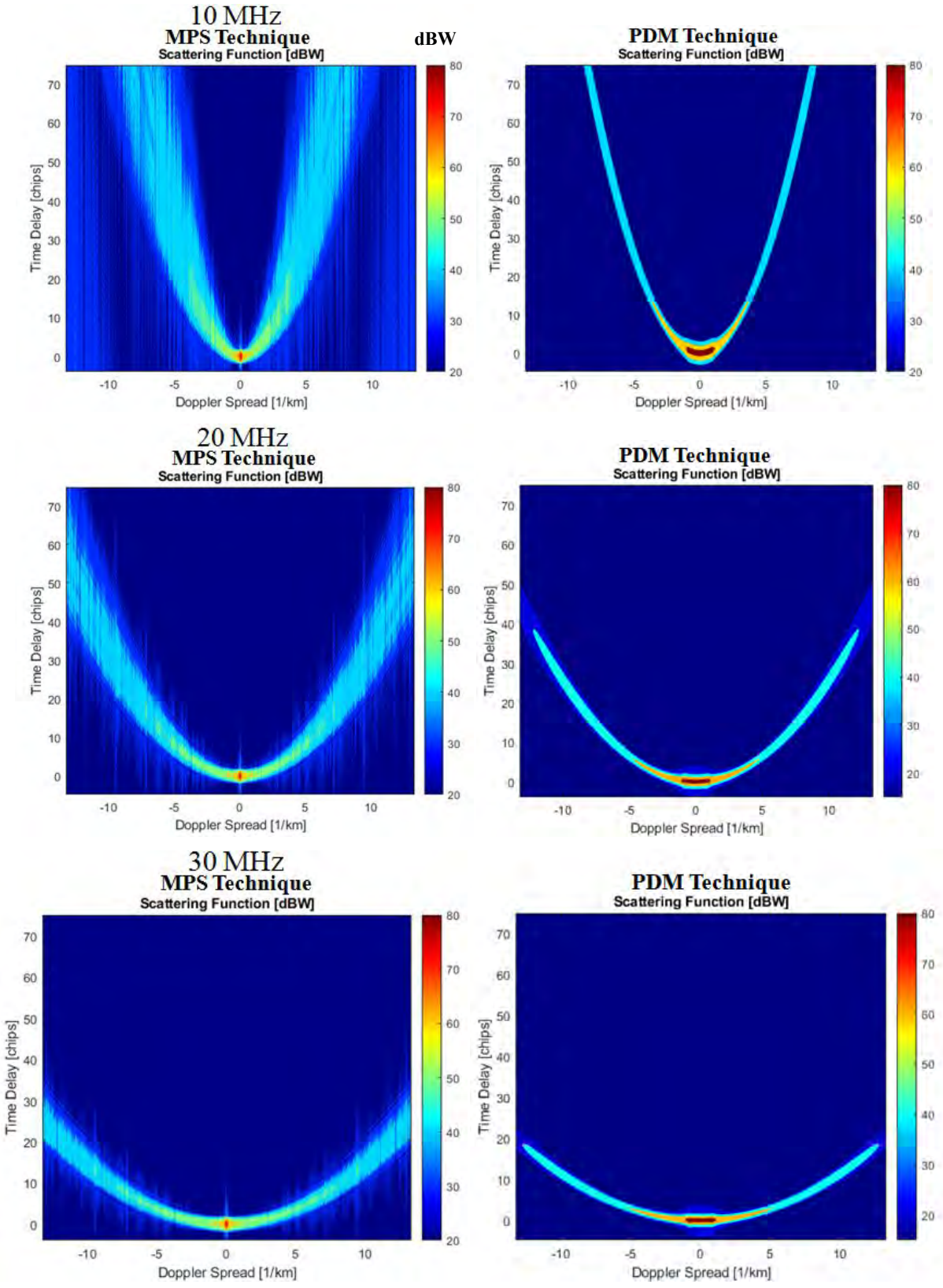

Figure 77. Scattering Functions for MPS (Left) and PDM (Right) Technique Comparison

4.5 Summary

The phase cube coupled ray tracer requires complex algorithms that arrange 2D phase screens sequentially along the propagation path within a three dimensional phase cube. The phase cube provides the additional geometry required to account for the radial and elongated profiles of the flute structure. As observed in the initial test of the phase cube model, the refractivity combined with polarization orientations provides added features of the scattering profile for a more complete model of the received field that would otherwise be unattainable using the conventional multiple phase screen model. The following chapter will demonstrate use of this phase cube model on a set of density map test cases for a variety of HF carriers to determine scintillation and delay-doppler characteristics. Conclusions about the observed scattering phenomenon will be determined from these results.

The carrier frequencies, polarizations, and propagation directions provide a variety of signal attributes that are evaluated from the scattering function determined at the receiver plane. The post analysis involves evaluating the scattering function's secondary calculations described in Chapter 2. These calculations include the signal time delay, time jitter, coherence bandwidth, doppler delay, doppler spread, doppler jitter, and spatial coherence. Additionally, the transfer function is calculated to observe the spatial and frequency coherence across the 2D receiver plane.

V. RESULTS AND ANALYSIS

This chapter analyzes the MPS simulations consisting of a variety of flute density perturbation maps that were initially derived and presented in Chapter's II and III. The objective of this analysis is to address the investigative questions posed in the beginning of this research to ascertain the scattering phenomenology associated with the flute structure's presence in a high frequency propagation channel. Important metrics to consider from the pulse coherence model are the S_4 and Phase Scintillation indices, the time delay and coherence bandwidth, followed by the observed scattering functions. Application of the 3D propagation model with ray tracing will focus exclusively on the behavior of the scattering function. Additionally, secondary calculations are applied to determine the power delay profile, frequency correlation, doppler delay, doppler spread, doppler jitter, spatial coherence, and mutual coherence. Observations from the variations in the scattering function and its associated parameters will provide valuable insight required to understand the characteristics of a flute structure.

5.1 Pulse Coherence Model

The pulse coherence model provides the temporal characteristics of a single-sideband, single carrier (SSC) modulated grid of pulses that span the width of the propagation channel. The scattering function solutions are a critical component of the frequency domain analysis complementing the temporal pulse calculations. Observations to consider when examining the scattering function include the uniformity and intensity of the energy distribution across the doppler-delay spread, the physical features of the

primary arcs corresponding to a particular flute density map, and possible substructures that occur from strong scattering conditions. Additionally, the arc curvature and broadening of the energy distribution is observed by varying the frequency of the propagating electric field. Interference patterns caused by the flute structures are revealed in the severity of the scattering and the fidelity of the scintillation arcs.

The pulse coherence model simulation test matrix is summarized in table 2. The test matrix includes a variety of stochastic flute maps with horizontal, vertical, and diagonal global orientations as determined by the random autocorrelation process corresponding to the ideal flute structures as presented in Chapter III. Each map represents a possible arrangement of flute structures that occur during the interchange instability process in the F-layer ionosphere. Isolated structures are also included in the test matrix to examine their unique contributions without the presence of other irregularities. An organized array of flutes is also examined to represent a scenario in which the zonal flows dominate the flute instabilities growth during the interchange process. Investigative aspects include the scintillation and pulse coherence characteristics to determine how they are altered in the corresponding flute density maps over select signal carrier frequencies in the high frequency spectrum. The propagation is examined in both x and y directions to capture the lateral profile features of the flute density maps. A time duration of 288 nanoseconds is applied to the initial triangular pulse width for most of these tests. This particular pulse width is sufficiently wide to cover a variety of frequencies within the signal's bandwidth but narrow enough to avoid mistakenly creating negative frequency values when subtracting half the bandwidth from the carrier on the left side of the triangular pulse. The exception to this value is when executing the tests

that examine multiple pulse width values for a single flute density map and a carrier frequency of 25 MHz.

<table>
<tr>
<td>Linear Flute Density Maps
 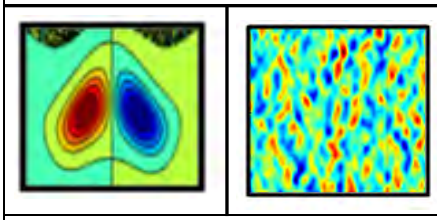
Quasi-I Flute Density Maps
 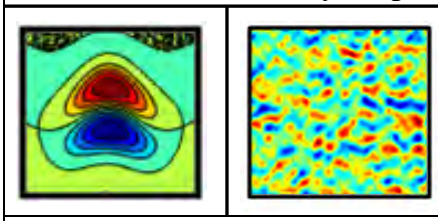 </td>
<td><u>Primary Test: Scintillation and Temporal Pulse Characterization</u>

▪ Transmission Frequencies: 10, 15, 20, 25, 30 MHz
▪ Pulse Width: 288 nanoseconds
▪ X and Y Propagation Directions
▪ 6 density maps – Stochastic Flute Map
▪ 4 density Maps – Single Flute Map
▪ 3 density Maps – Flute Array Map</td>
</tr>
<tr>
<td>Quasi-II Flute Density Maps
 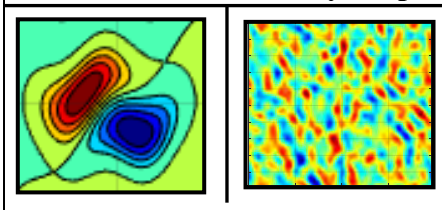
Quasi-III Flute Density Map
 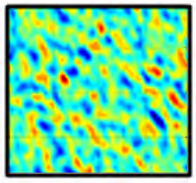 </td>
<td><u>Pulse Width Variations</u>

▪ Transmission Frequency: 25 MHz
▪ Pulse Width: 98, 118, 138, 158, 178, ...
198, 218, 238, 258, 278 nano-seconds

▪ X and Y Propagation Directions
▪ Density Map: Quasi-I</td>
</tr>
<tr>
<td>Nonlinear Flute Density Maps
 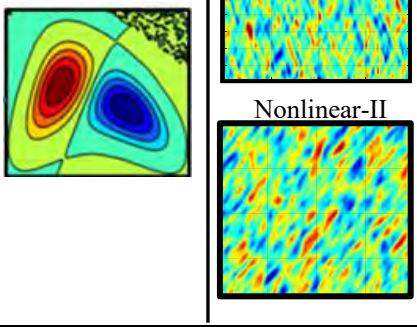
Nonlinear-I
Nonlinear-II</td>
<td> 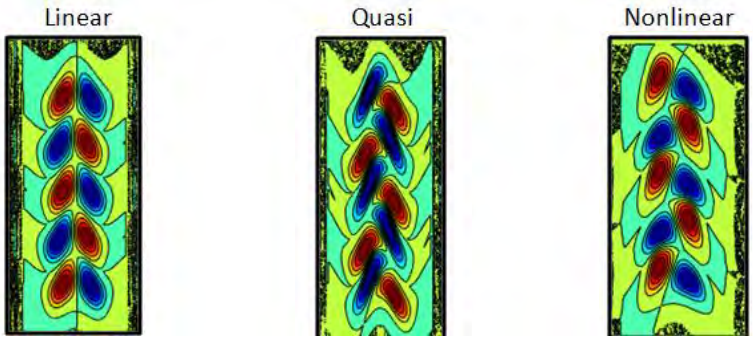
Linear
Quasi
Nonlinear

Total Simulations: 150</td>
</tr>
</table>

Table 2. Pulse Coherence Model Test Matrix

Applying a carrier frequency this high in the spectrum avoids an erroneous negative frequency on the left side of the triangular pulse baseband while also allowing for a greater variety of testable pulse widths. The main focus of the pulse widths are for the observations in the scattering function's doppler-delay spread for wide and narrow band signals in addition to the change in the bandwidth coherence of the propagation channel.

The key limitation of the pulse coherence model is primarily the one dimensional propagation direction and the one dimensional sampling grid of the received electric field. Additionally, the pulse coherence model utilizes MATLAB to execute the numerical algorithms required for the characterization. Iterating through 600 discrete frequencies along the bandwidth of the pulse is time consuming and is considered a limiting factor that restricts the test matrix. It is for this reason that the density maps in table 2 are applied to provide sufficient variety for the test as lieu of testing all twelve stochastic maps and an additional twelve single flute perturbations, as presented in Chapter 2.

The initial observation in the pulse coherence model are the received field realizations over the bandwidth of the signal. This is the primary calculation acquired from the MPS portion of the pulse coherence model, in which the ideal pulses are propagated at frequencies within the signal's bandwidth and over a 500 kilometer propagation distance beyond the flute density map. Figure 78 compares the field realizations for the Quasi-I flute and its corresponding stochastic map. Despite the identical power spectrum properties of each density map, the electric field’s diffraction patterns are notably unique. The presence of flutes in the density map causes expected interference patterns observed from repeated constructive and deconstructive interference

during the propagation process. Edge diffraction caused by the flute structure(s) dominates the electric field behavior at the receiver plane.

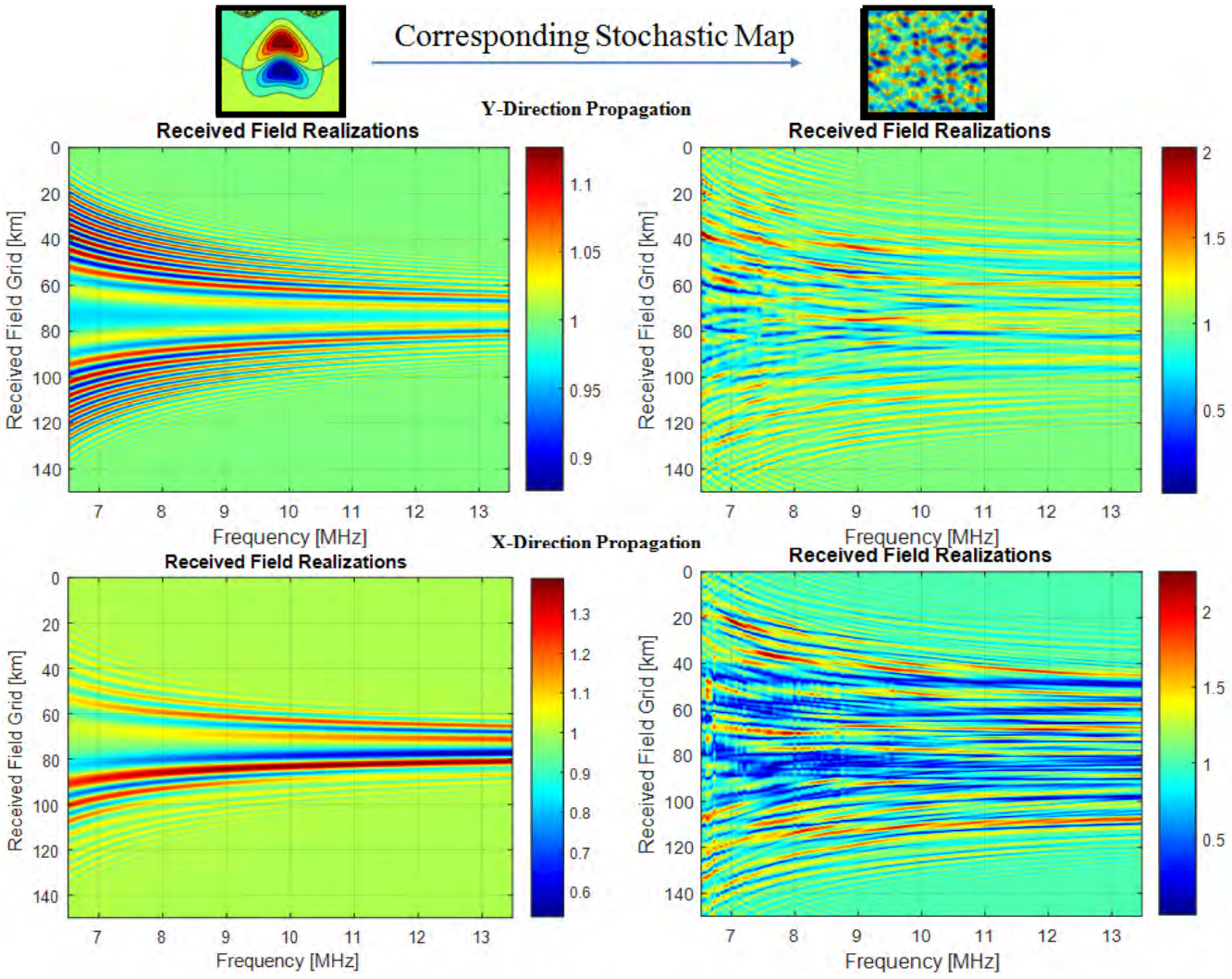

Figure 78. Dynamic Spectrum of propagation through the Single and Stochastic Flute Maps

Applying the stochastic map, diffraction is more prevalent in which each individual flute structure will create cross-interfering patterns. This leads to widespread losses and lack of coherence amongst the pulses along the receiver grid as shown in

Figure 79. In this figure, the time delay of the SSB-SC triangular pulses along the receiver grid is shown for the frequencies from the test matrix.

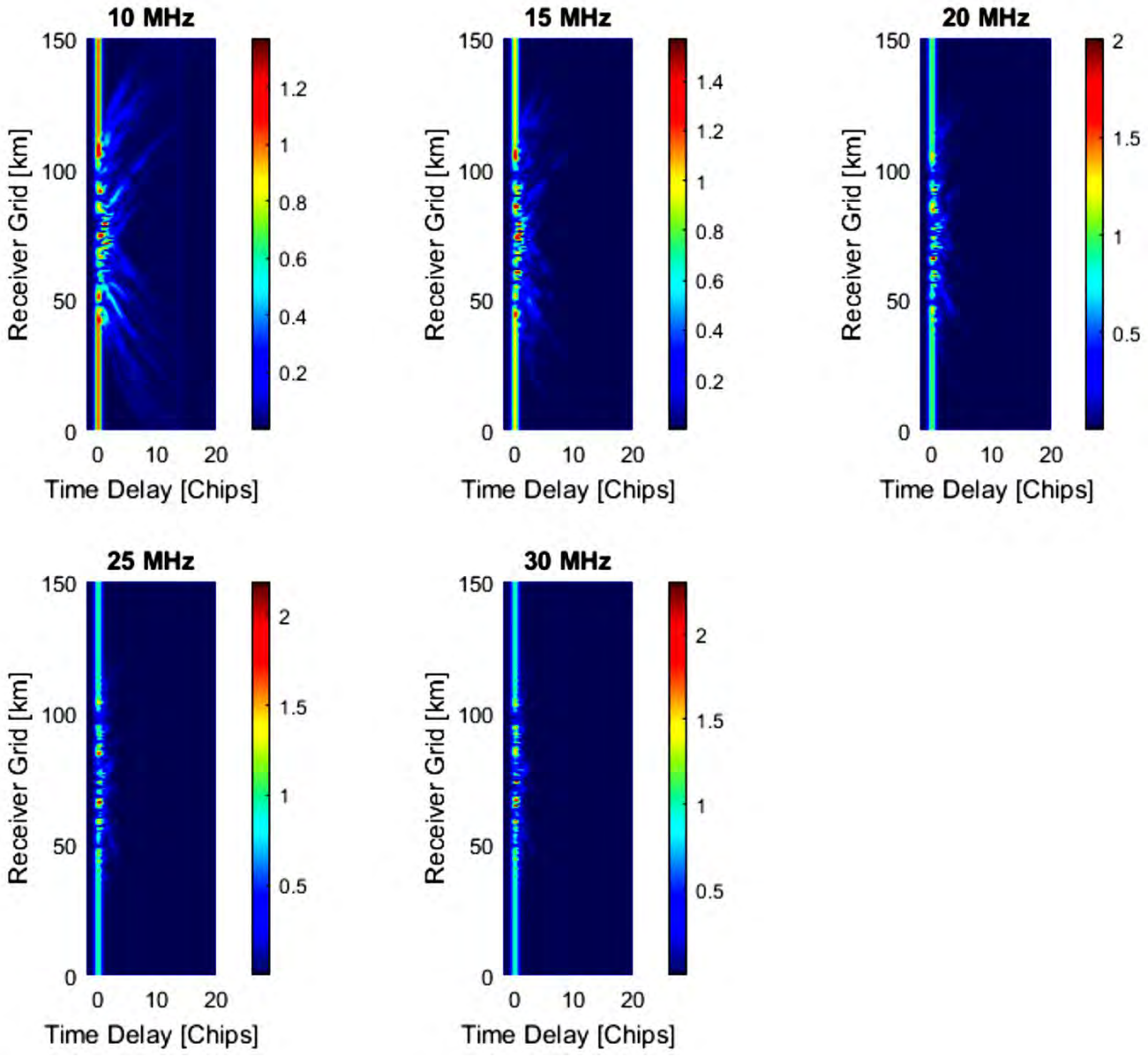

Figure 79. Global Amplitude Maps of Pulse Delays

As observed with the full wave model and phase screen method comparisons in chapter 4, the time delay and the amplitude fading in the pulses is more significant for the lower frequencies due to the comparable wavelengths to the physical sizes of the flutes. The

collective effect of the flute structures results in defocusing that causes the energy to scatter away from the center of the map, towards the edges. Towards the center of the map, there is a minimum in received power that's caused by this outward scattering of waves away from the center. The outward scattering increases with propagation distance between the transmitter and receiver. This is due to the overlapping of the scattering patterns from the individual striations that make up the stochastic flute map.

5.1.1 Pulse Coherence Temporal Moments

The initial analysis of the scattering parameters from the pulse coherence model is the temporal characteristics which includes the time delay and coherence bandwidth. Due to the dispersion in the data samples over the propagation distance, the box-and-whisker plots provide the average and relative ranges with respect to each flute density map tested. Based on observations of the collective results, the increase in carrier frequency contributes to smaller values observed in the time delay, scintillations, and higher coherence bandwidth.

As shown in chapter II, the mean time delay is calculated using the initial temporal moment of the pulses. Figure 80 shows the box-and-whisker plots of the total time delays averaged along the receiver grid as the 10MHz carrier field propagates towards the final distance of 500 kilometers. The time delay calculation is determined from the first order temporal moment. The highest delay is observed at approximately 0.85 chips when applying the Nonlinear-I map and propagating in the x-direction. In the y – propagation direction, the Quasi-I map contributed the greatest observed delay at approximately 0.62 chips. These observations correspond to phase changes of (15.38

radians for Nonlinear-I and 11.22 radians for Quasi-I) in the propagating field. The time delays generally appear to be at their highest for wave propagation in the y –direction for cases where the flute structure stagnation points have more spacing or have no direct overlaps with other flute structures in the propagation direction.

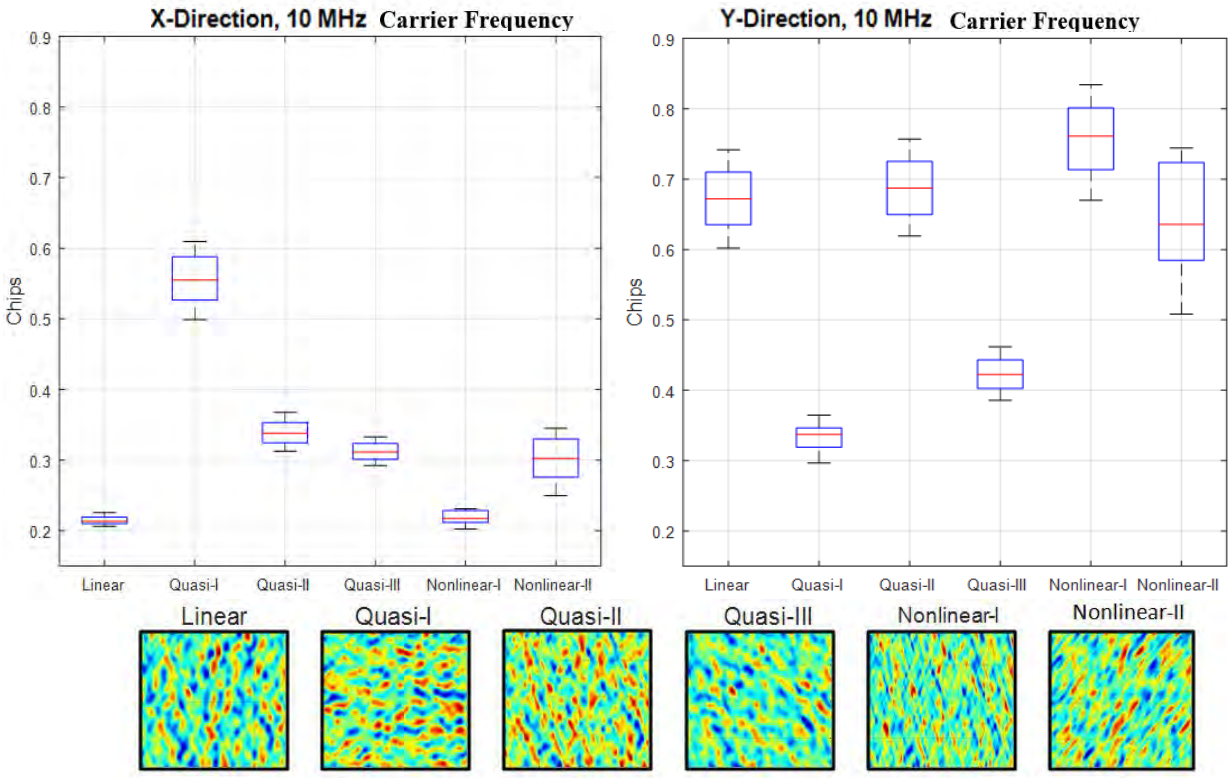

Figure 80. Time Delay data spread over distance caused by Stochastic Maps

As with the Quasi-I and Nonlinear-I maps, these conditions lead to higher total phase power spectral densities in each phase screen and greater cross interference patterns in the incident field perturbing a stochastic flute map. The single flute and flute array density maps do not produce comparable results to the stochastic flute maps in which the general the time delays are within 0.17 and 0.2 chips depending on the orientations of a particular flute structure with respect to propagation direction as seen in the stochastic maps. These results are shown in Appendix E.

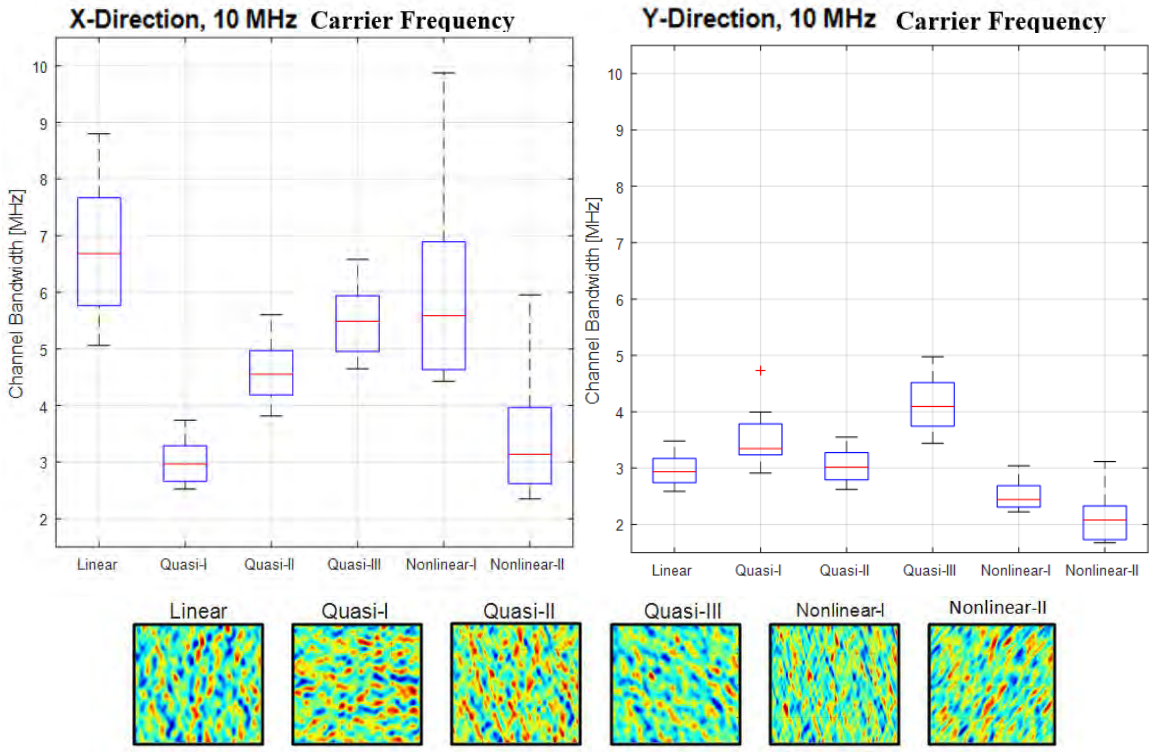

Figure 81. Channel Coherence Bandwidth data spread with respect to distance caused by Stochastic Maps

The coherence bandwidth of the channel is determined from the inverse of the time jitter or the second order temporal moment that describes the dispersion in the pulses observed along the receiver grid. Intuitively, the coherence bandwidth should be lower for the cases where the time delay was observed to be at its peak. In Figure 81, this is generally true with the exception of the Nonlinear-I and Quasi-II cases in the *y* propagation direction. The lowest coherence bandwidth (~1.7 MHz) is observed in the *y* propagation direction of the Nonlinear-II case. The highest coherence bandwidth of (~9.9 MHz) is observed in the *x* direction of the Nonlinear I case.

The 288 nanosecond pulse width corresponds to a signal bandwidth of 13.86 MHz. In all of the stochastic flute map cases, the channel bandwidth is less than the signal bandwidth, indicating that the fading characteristics are frequency-selective. Under

these conditions, different frequency components of the signal experience uncorrelated fading. The signal energy associated with each pulse is significantly spread out in time. This is also a consequence of the cross interference in which the adjacent transmitted pulses interfere with each other. These characteristics are more prevalent in the *y* – propagation direction in which the stagnation points within the stochastic flute map are aligned relatively perpendicular to the direction of propagation. Applying these conditions to a variation in the pulse width for a consistent carrier frequency reveals that the higher pulse widths will yield lower coherence bandwidths. This could suggest that wideband signals would in large part be incoherent with these type of flute stagnation orientations in a propagation channel. Figure 82 shows the relationship of the coherence bandwidth over the propagation distance in which the stagnations are aligned in the *y*-direction of the flute density map.

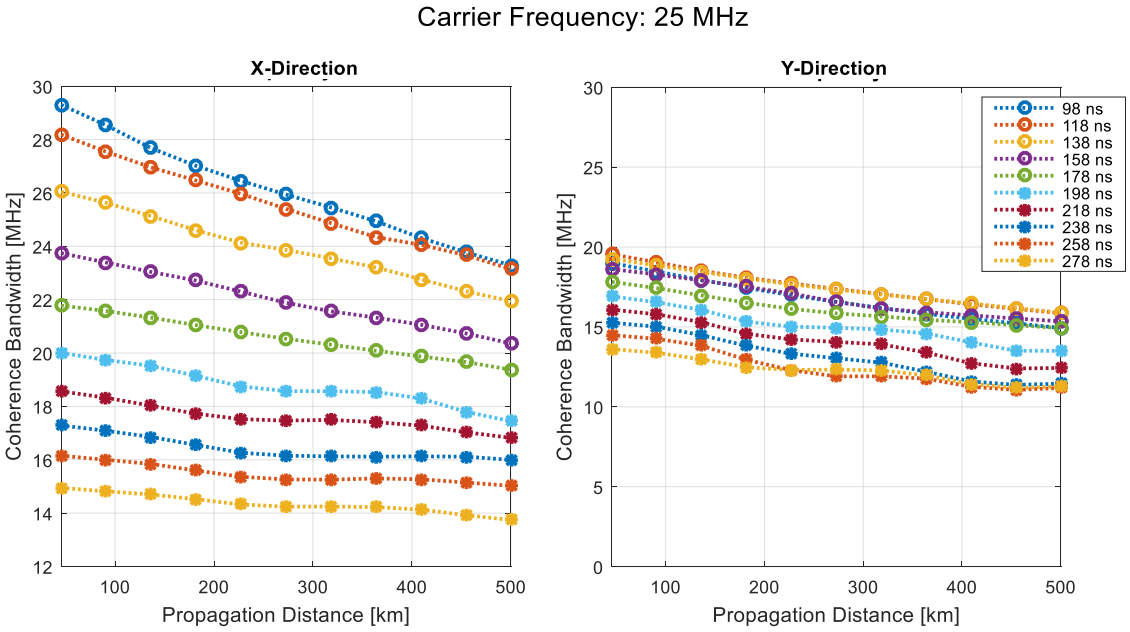

Figure 82. Coherence Bandwidth for a variety of pulse widths effected by the Quasi-I Flute Map propagation Channel

Figure 83 shows the coherence bandwidth for the Linear stochastic map. As the signal's carrier frequency increases, the coherence bandwidth increases and the incident electric field wavelength becomes smaller, focusing the energy. This effectively shortens the optical path length through the cascade of flute structures. In the high frequency range, the coherence bandwidth tends to approach the signal carrier frequency asymptotically in the *x* direction and increases linearly in the *y* direction. The channel remains frequency selective for all these cases.

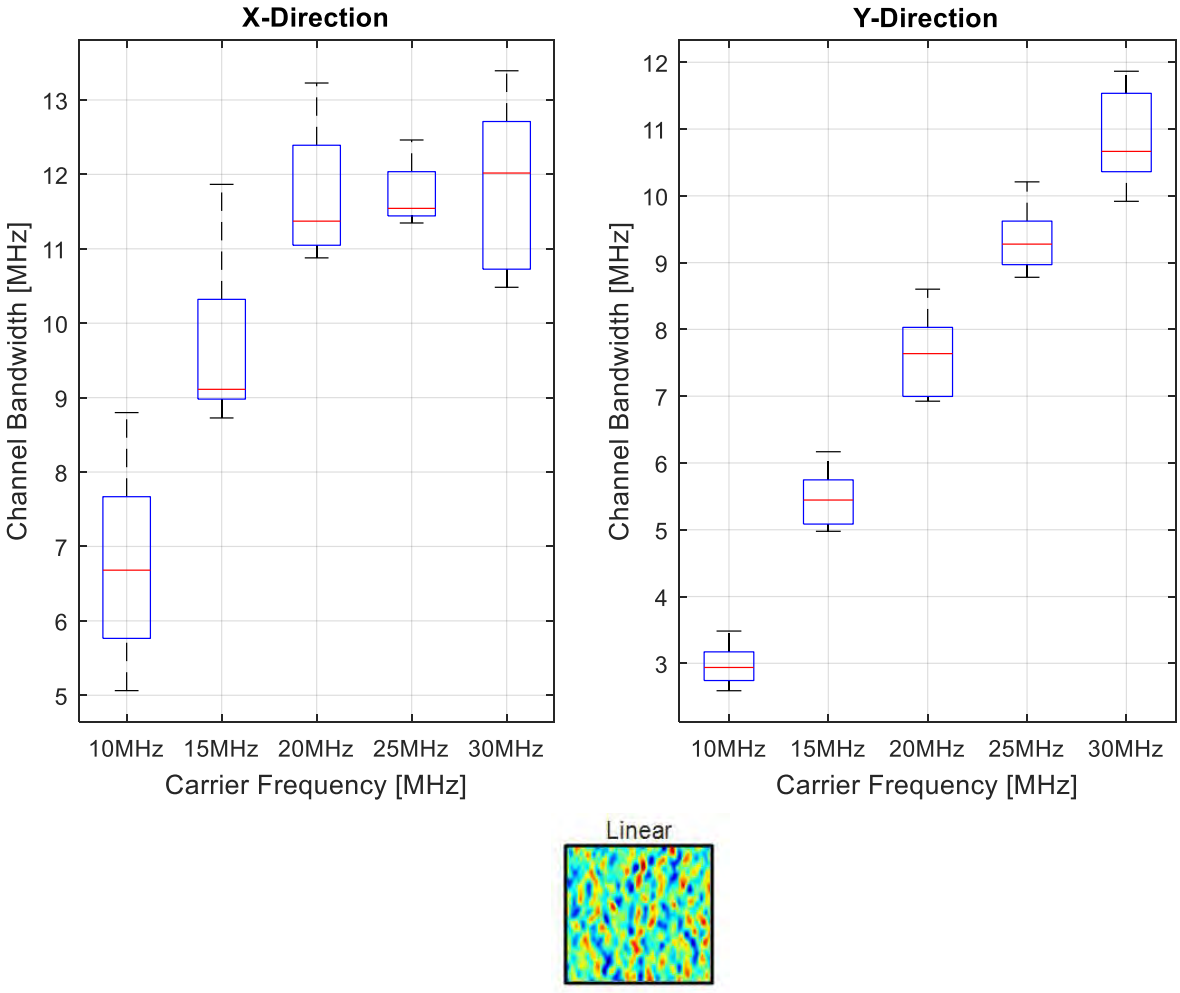

Figure 83. Coherence Bandwidth with varied carrier frequency - Linear stochastic map propagation Channel

Examining the increasing carrier frequency for the propagation scenarios involving the isolated Linear flute and Linear flute array channels, the phase dispersion is higher for the *y*-direction of the flute array map at lower carrier frequencies, causing a lower coherence bandwidth. At a carrier of 10 MHz in the y-direction, the average coherence bandwidth is approximately 5.5 MHz lower for flute array case in Figure 85 compared to the isolated flute case in Figure 84. The flute array case remains frequency selective in the *y*-direction at 15 MHz as the coherence bandwidth increases by an average of 4.5 MHz. The isolated flute structure has a frequency selective case at the 10 MHz carrier in the *y* - direction. All other carrier frequency scenarios are considered flat fading and appear to asymptotically approach a maximum coherence bandwidth around 15.5 MHz.

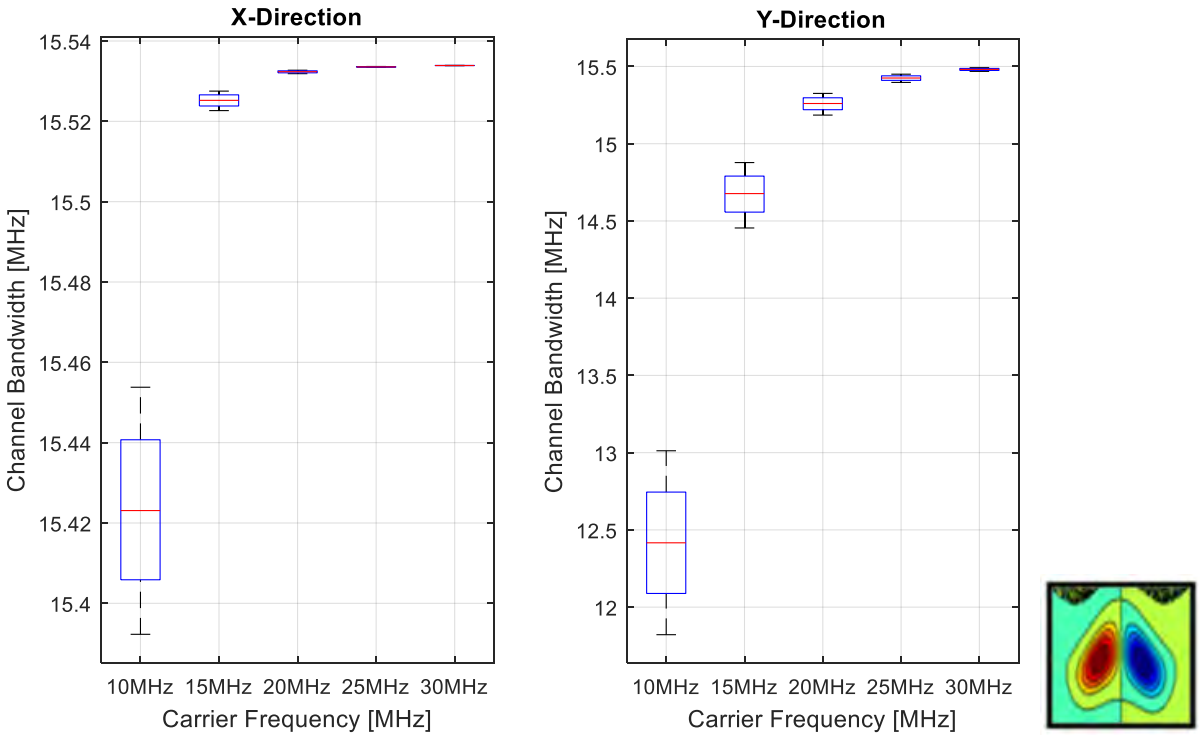

Figure 84. Coherence Bandwidth with varied carrier frequency - Single Flute map propagation Channel

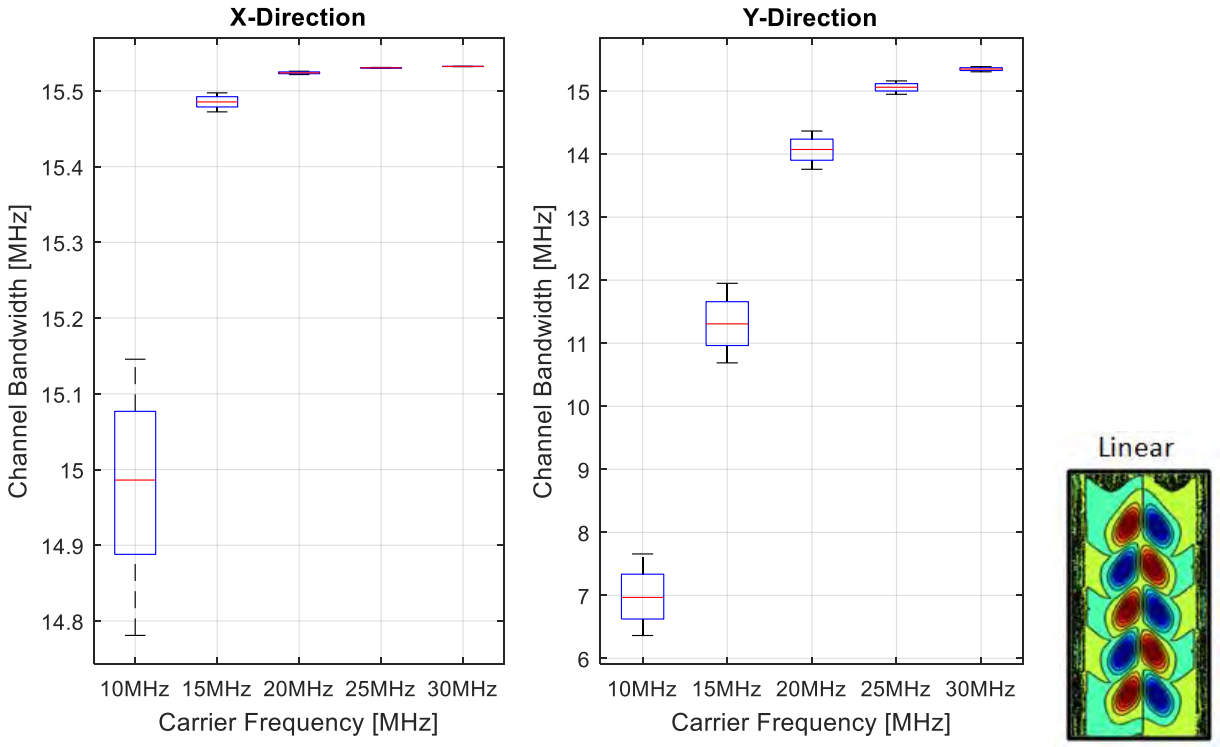

Figure 85. Coherence Bandwidth variation with respect to carrier frequency - Linear Flute Array map propagation Channel

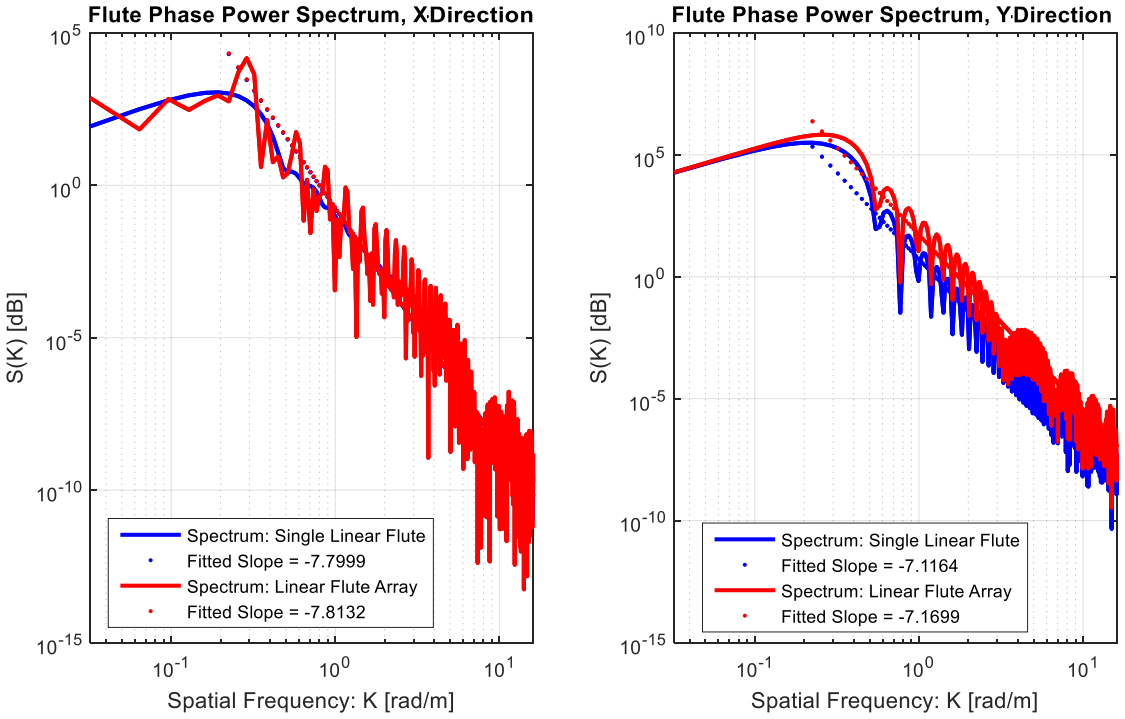

Figure 86. Power Spectrum Comparison for Linear Flute Array and Single Flutes

Revisiting the power spectral density plots in Figure 86, it is evident that the flute array along the propagation path creates a greater cumulative power spectrum in both the *x* and *y* directions compared to the single flute structure case even as the wave number of the spectra increases. Despite the similarities of the power spectrums that are compared in the *x*-direction, the total phase power spectrum tends to fluctuate due to the increase electron density perturbations along the autocorrelation sampling grid. The peak PSD intensity is also higher in the *y*-direction compared to the *x*-direction which supports the observations regarding greater phase dispersion.

In summary, the temporal results demonstrate that the quantity of flutes within the density map is not as significant as the orientation and position of the flutes with respect to their neighboring stagnation points. Initially, the magnitude of the phase power spectrum will determine the severity of the optical path length for an electric field incident on the isolated flute structure. The greater optical path length causes an increased phase variation and subsequent time delay as seen in the flute array maps *y* - direction. The time jitter, however, increases if a variety of phase variations are observed along the receiver grid, as caused by cross-interfering edge diffraction patterns most prominent when flute stagnation points positive and negative perturbations have minimal overlap. This condition is created when the flutes are staggered significantly within the density map and along the propagation path as is the case with the stochastic flute maps. The increased jitter causes a lower coherence bandwidth that has the potential to create frequency selective conditions in the high frequency regime.

5.1.2 Pulse Coherence Scintillation Characteristics

Variations in the S4 index are certainly aspect dependent on the electric field's incidence upon the flute structure and on the interaction of the field's amplitude interference patterns. The Quasi-I flute case has stagnation alignment that is predominantly horizontal in which the positive and negative perturbations are not overlapping with respect to the propagation direction, thereby minimizing the destructive interference that would occur in the *y*-direction. In this direction, focusing caused by the positive flute perturbation cancels the divergent negative flute perturbation. The Linear and Quasi-I cases have these features in the opposite direction as the stagnation points are oriented in the *y*-direction.

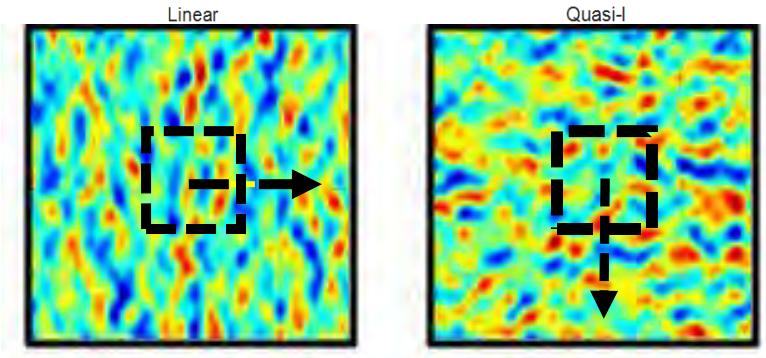

Figure 87. Global Flute Map Orientations

It was shown in chapter 2 that the total phase power spectrum has greater magnitude in these flute map cases in addition to steeper slope decay for higher wave numbers. The general orientation of the flutes in the density map contributes directly to these properties as seen in Figure 88. Figure 89 shows the spread in the S4 scintillation index calculation of the received field after propagating in the *x* and *y* directions. The Quasi-I and Linear cases had the weakest S4 index in the opposite maps, corresponding to lower phase power spectrums for comparable wave numbers. The Quasi-I case in the *x*- propagation direction exhibits strong scintillation (S4 > 0.6) whereas the other cases are considered

weak (S4 < 0.3). In the *x*-direction, the S4 index is generally mixed amongst the flute types but indicates weak to moderate scintillation.

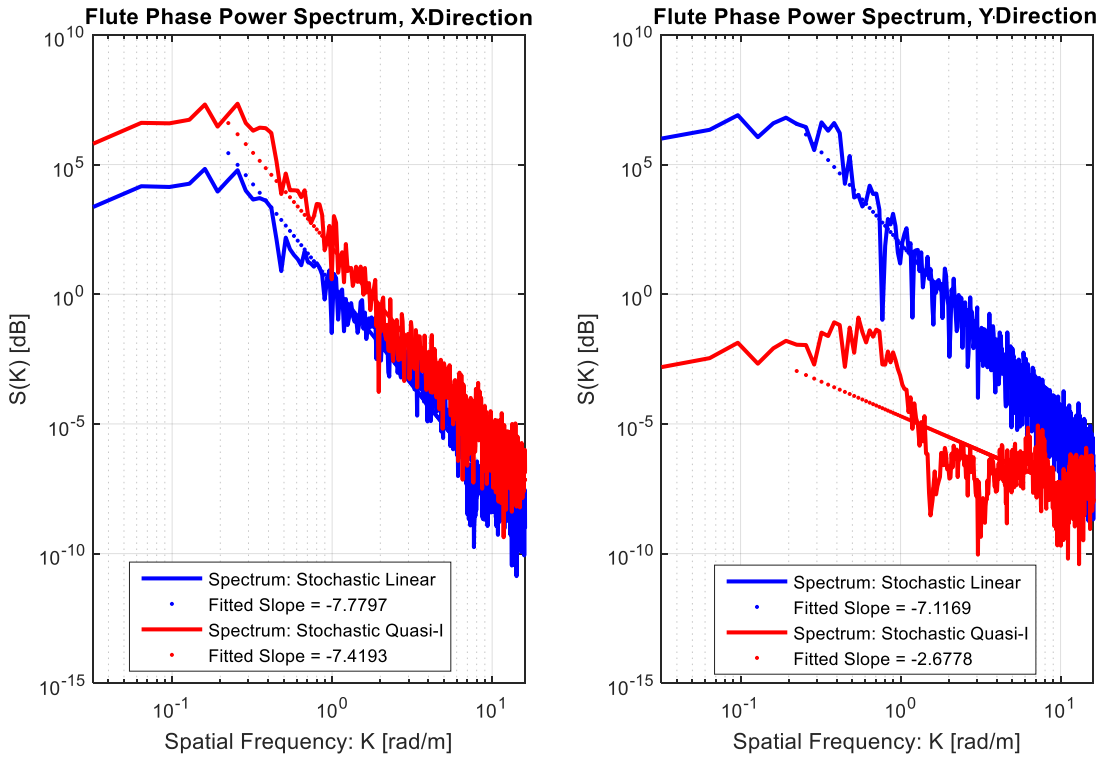

Figure 88. Power Spectrum comparison between Linear and Quasi-I stochastic Maps

These observations are also translated in the phase scintillation cases which can be observed in Appendix E. The phase scintillation often exceeds the amplitude scintillation, with the exception of the Quasi-I *y*-direction case. This is generally expected for the stochastic flute maps in which the density of flute structures changes rapidly over shorter propagation distances. At lower frequencies, there are more frequent phase variations per wavelength compared to higher frequencies. As explained in Chapter 2, these cases contributes to the observations of greater phase scintillation at lower wave numbers. In the Quasi-I *x*-direction case, the amplitude exhibits the most considerable scintillation caused by the density fluctuations. Recalling from Chapter 3 that the flutes spectra

appears to follow an asymptotic power law and referencing Figure 3 from Chapter 2, observations have shown that the phase scintillation is more prevalent for smaller wave number sizes in the spectral density of the plasma turbulence. As this wave number increases, the amplitude scintillation becomes dominant. These cumulative effects are perhaps more persistent in the Quasi-I map as the wave number increases during the propagation process.

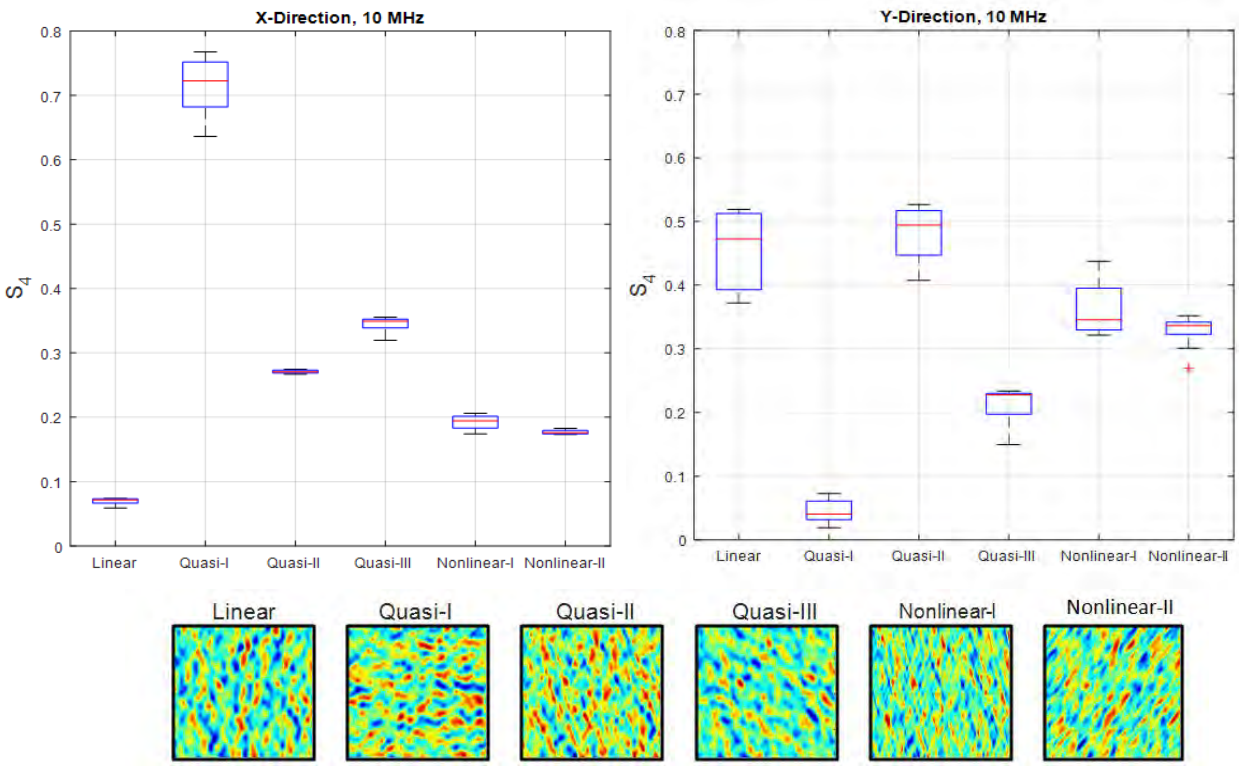

Figure 89. S4 Scintillation index data spread with respect to distance caused by Stochastic Maps

Figure 90 shows that for a variety of high frequency carriers, the scintillation index appears to be consistent in the y-direction. This is likely a result of the abundant variety of flute perturbation dimensions present in the stochastic flute map and the lack of overlap between identical flute stagnation points. Each size has direct correspondence to the wavelength of a particular carrier in the high frequency spectrum, causing comparable

scintillation characteristics. This is different from the x-direction or weak scattering cases in which the small scale sizes associated with the decline in the phase power spectrum exhibits a distinct relationship between scintillation index and carrier frequency.

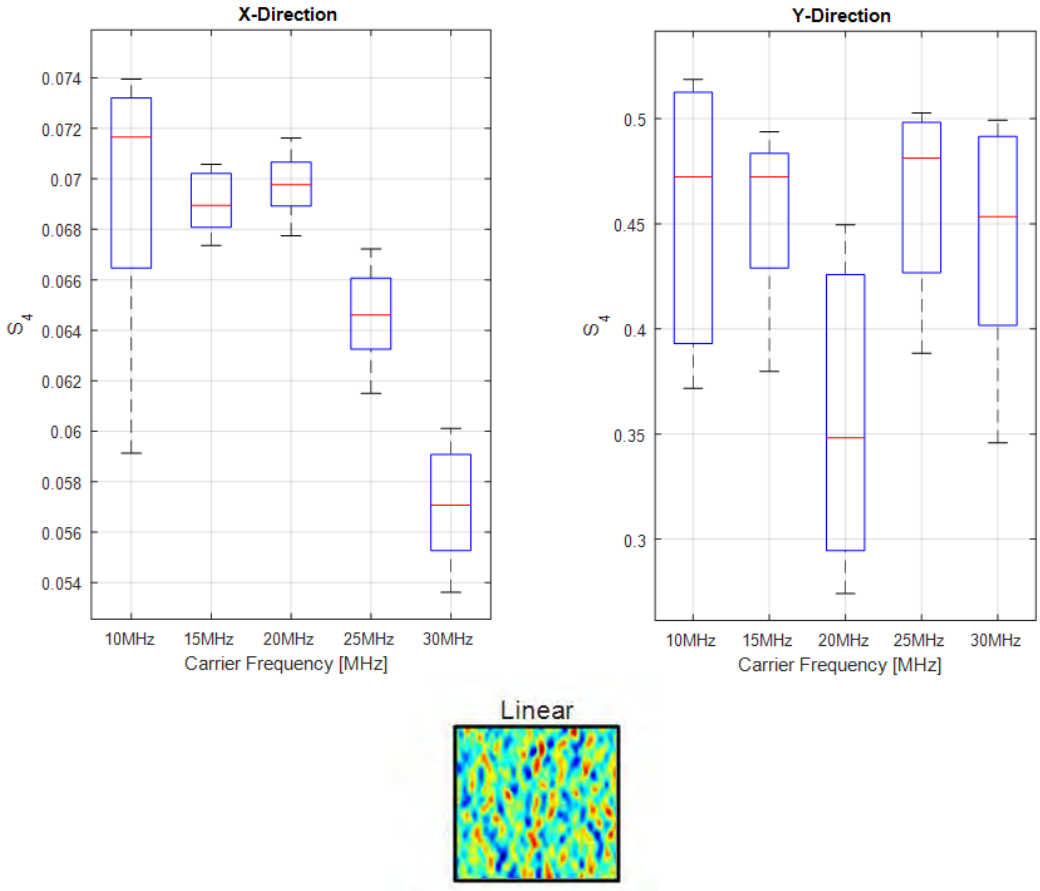

Figure 90. S4 Scintillation index variation with respect to carrier frequency- Linear Stochastic Flute Map

In comparison to the stochastic flute map results, the single flute and flute array cases exhibited comparable scintillations indices ($S_4 < 0.15$) as seen in Appendix E. These cases demonstrate weak scattering that could possibly occur during the initial stages of the interchange process. The added quantities of the flutes within the organized array does not appear to significantly increase the scintillation indices despite the increase in the optical path length in the y-direction. The total power spectrum comparisons in

Figure 91 shows that the total phase power spectrums of the Linear stochastic case and the Nonlinear flute array cases are comparable in the x -direction where the stagnation points have some overlap and the occurrence of weak scintillation. In the y-direction, the peak magnitude in the power spectrum for the Linear stochastic map exceeds the nonlinear array map by an order of magnitude. Despite the similar qualities in the orientation of the flute structures between each map, the imperfections and stagnated positioning of the flutes in the stochastic flute maps produce the most severe scattering.

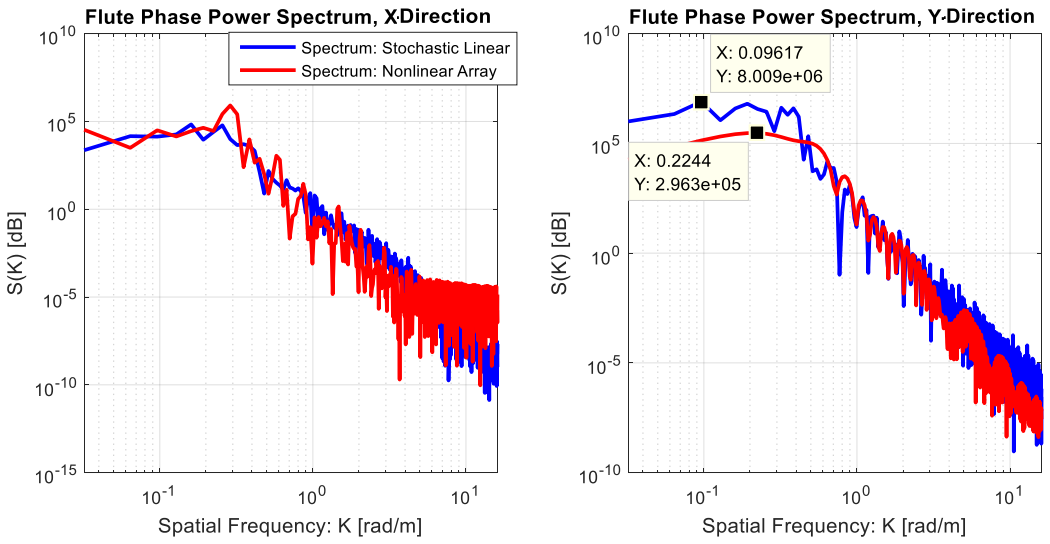

Figure 91. Power Spectrum Comparisons between Linear Stochastic flute map and Nonlinear Flute Array Map

These scintillation characteristics demonstrate that a variety of flute structure shapes and orientations with respect to propagation direction can cause a broad range of weak to strong scattering conditions effecting the scintillation of the high frequency incident electric field. Examining the stochastic flute maps and relating the temporal and scintillation results, strong scintillation does not necessarily indicate that the propagation channel will create frequency selective characteristics for the triangular pulses. For example, the Quasi-I flute case has an average scintillation index of approximately 0.73

in the *x*-propagation direction and its corresponding channel coherence bandwidth is close to 3 MHz. Likewise, the Nonlinear II flute map has an average scintillation index of 0.19, corresponding to a channel coherence bandwidth around 3.1 MHz. In the *y* direction the lowest average coherence bandwidth observed out of all the cases is approximately 2 MHz with a corresponding average scintillation index of 0.35. Similar traits can be observed in the phase scintillation. However, in many of the stochastic cases, the higher phase scintillation does correspond to a lower coherence bandwidth. In the isolated flute structure cases, the higher scintillation corresponds more clearly to lower coherence bandwidths as in the flute array cases when propagating in the *x* direction, the smallest optical path length. In the *y* direction, the relationship between scintillation and coherence bandwidth is more ambiguous such as the Quasi array case, having the least average scintillation but the smallest coherence bandwidth. The following section continues the analysis in the frequency domain to observe scattering function doppler-delay features that may be unique to each density map.

5.1.3 Pulse Coherence Scattering Function

In chapter 4, the previous observations of the scattering function between the Kolmogorov and Gaussian phase screens demonstrated the effects of slope and intensity within the phase power spectrum. Comparisons between the doppler-delay maps of their respective scattering functions showed that the fidelity of the scintillation arcs and energy spread were dependent on the phase power spectrum characteristics. In this section, these tests are repeated for a variety of flute maps to determine the evolution of their scattering function characteristics.

The Linear isolated flute map has a relatively uniform energy spread for the *y*-direction propagation of the electric field corresponding to the non-overlapping stagnation points along the optical path length. In such case, the total phase power spectrum has a greater magnitude and spectral slope for increasing wave numbers. This is translated in the delay-doppler map as Figure 92 shows a more intense doppler shift in the energy spread (+ or - 5 [1/km]) over a shorter amount of time delay (~15 chips) compared to the propagation in the *x* direction. In the x-direction, the stagnation points are askew and have overlap, increasing the optical path length. The total phase power spectrum magnitude declines significantly, thereby causing less intensity in the energy spread, and a more rapid doppler shift over a short time delay duration. There also appears to be some skew in this energy spread in relation to the *y*-axis. The portion of this energy spread with the greater magnitude over a greater delay corresponds to the portion of the flute structure in which the most significant overlap in the stagnation points occurring along the propagation axis.

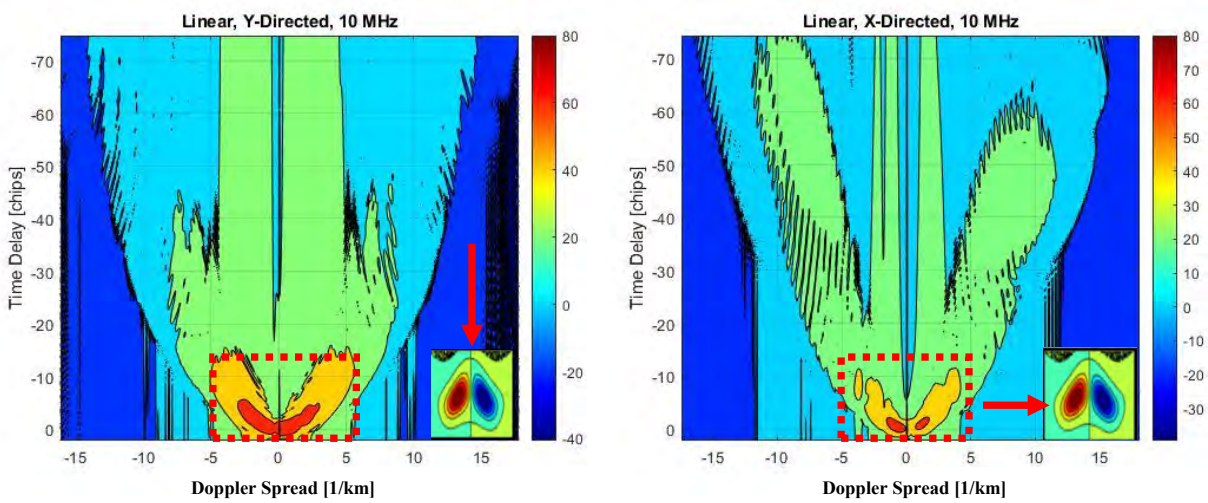

Figure 92. Linear Flute Delay-Doppler Power distributions from Received Field from propagation in *X* and *Y* direction

Figure 93 shows other examples of this skew in the doppler-delay profile.

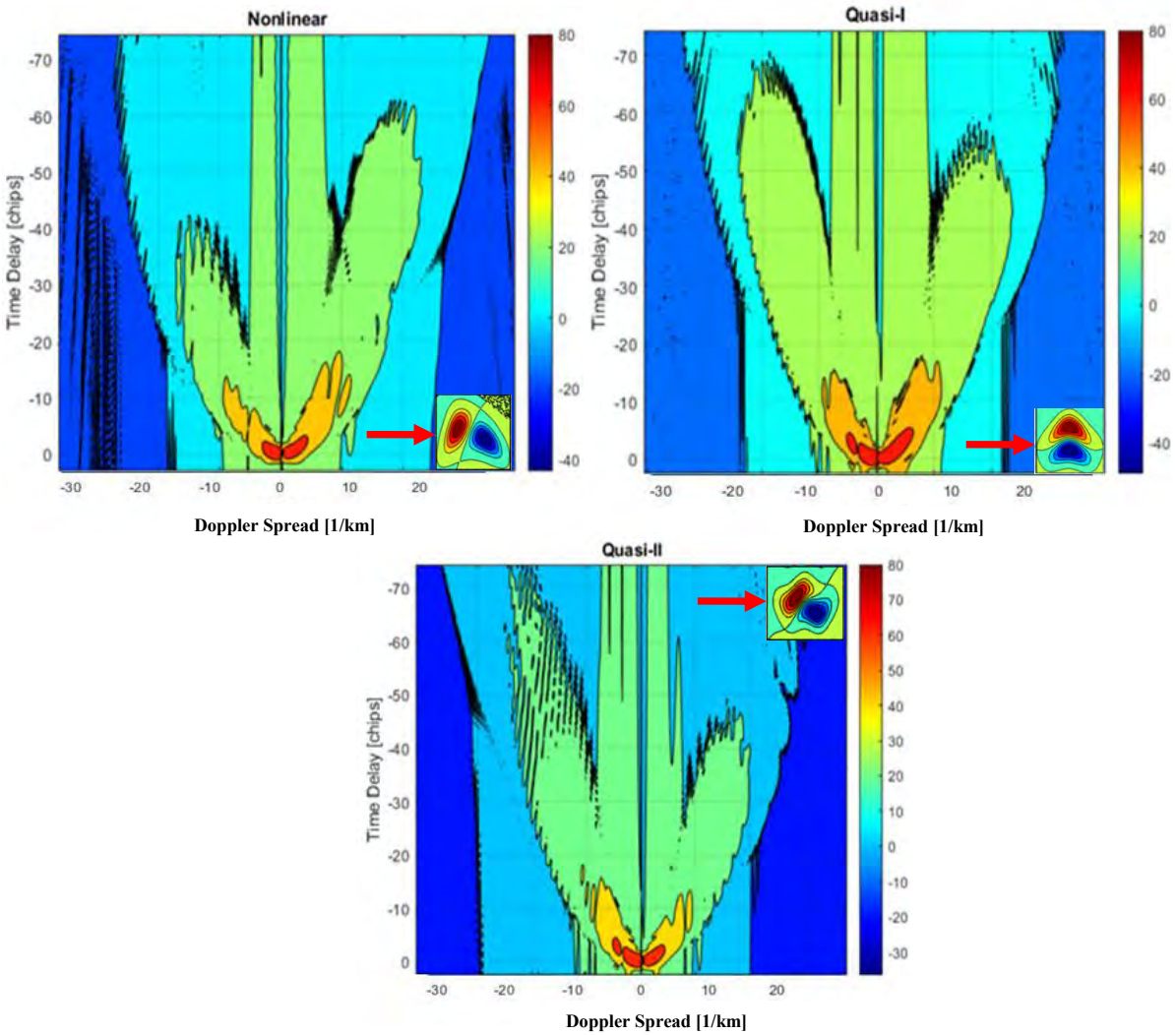

Figure 93. Asymmetric Delay-Doppler power distributions from Received Field of propagation in the *X* - direction

In Figure 94, the doppler-delay spread is shown for a higher carrier frequency of 30 MHz. The energy spread becomes much more concentrated compared to the lower frequency transmissions. This was also observed previously in chapter 4 with the Kolmogorov and Gaussian spectrum doppler-delay maps. The dispersion in the scattered field diminishes, causing a greater contrast in the scintillation arc profile, revealing the

presence of fringes. Figures 95 and 96 show similar behavior as the carrier frequency of the pulse transmission increases.

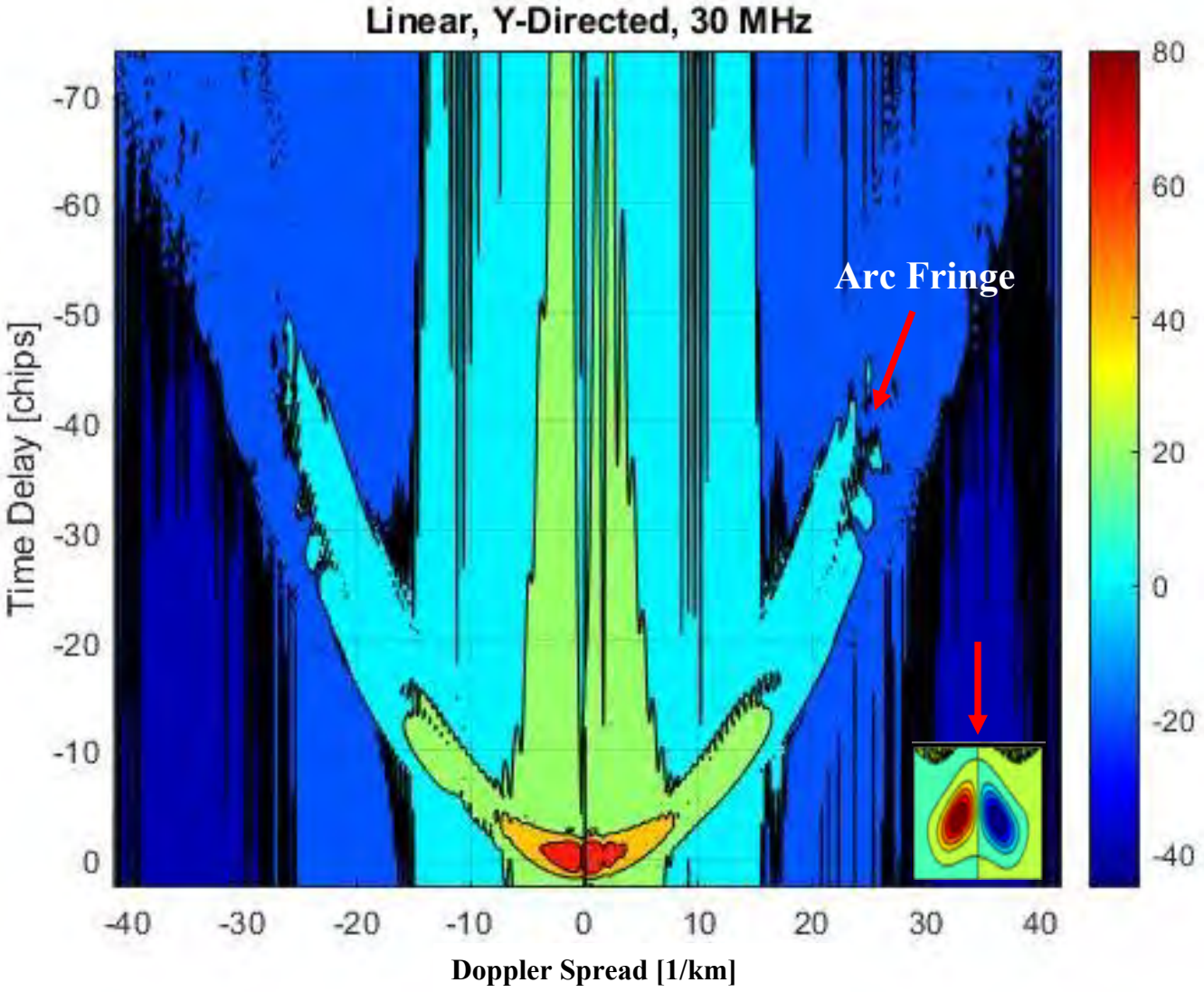

Figure 94. Delay-Doppler power distribution fringes from Received Field of propagation in the *Y*-direction

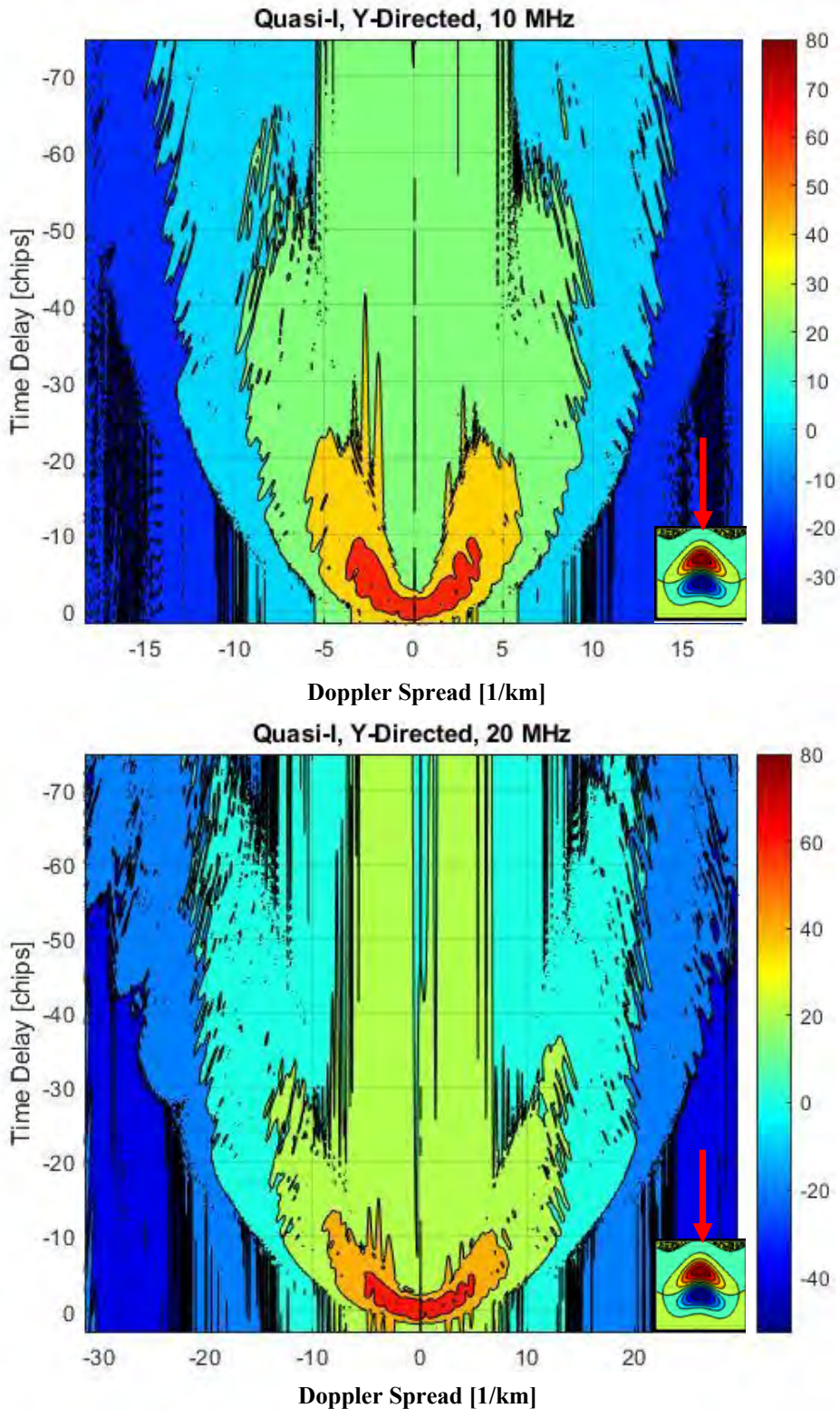

Figure 95. Delay-Doppler power distribution, Quasi-I, y-direction propagation, 10 MHz carrier (top) and 20 MHz carrier (bottom)

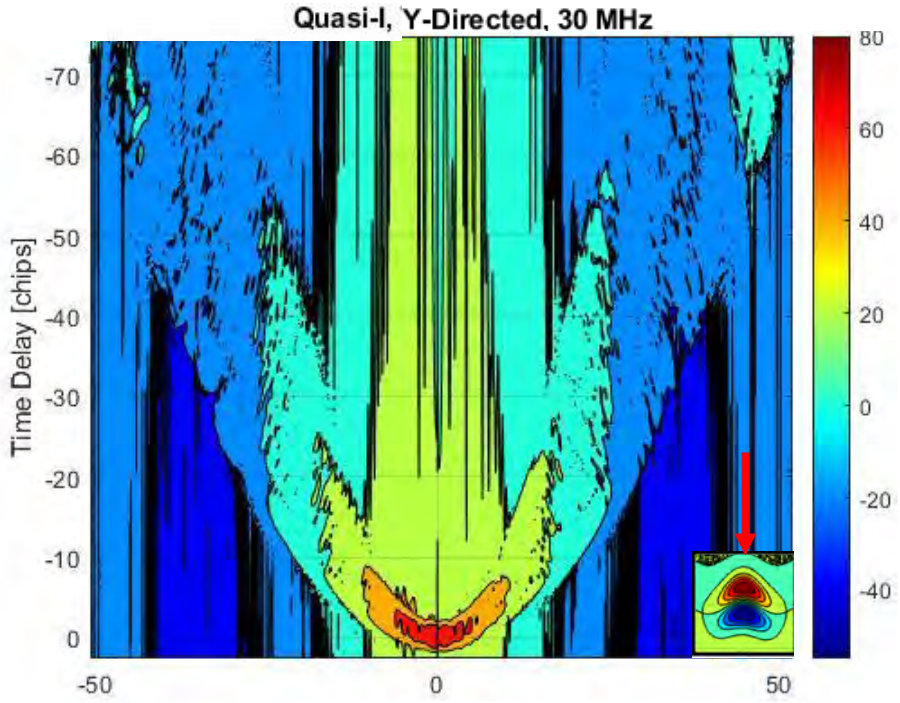

Figure 96. Delay-Doppler power distribution, Quasi-I, y-direction propagation, 30 MHz carrier

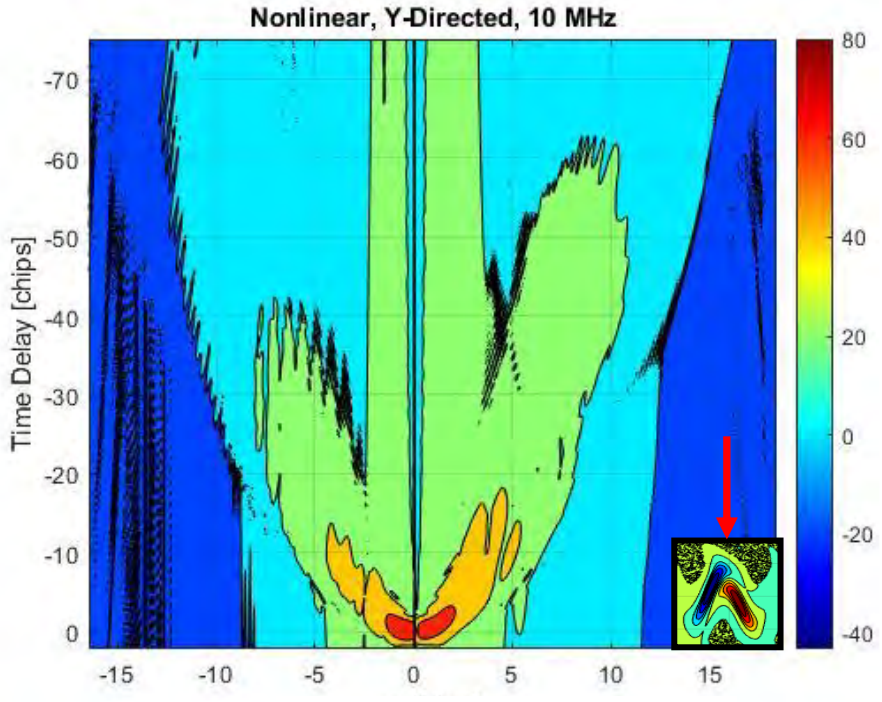

Figure 97. Delay-Doppler power distribution, Nonlinear-I, y-direction propagation, 10 MHz carrier

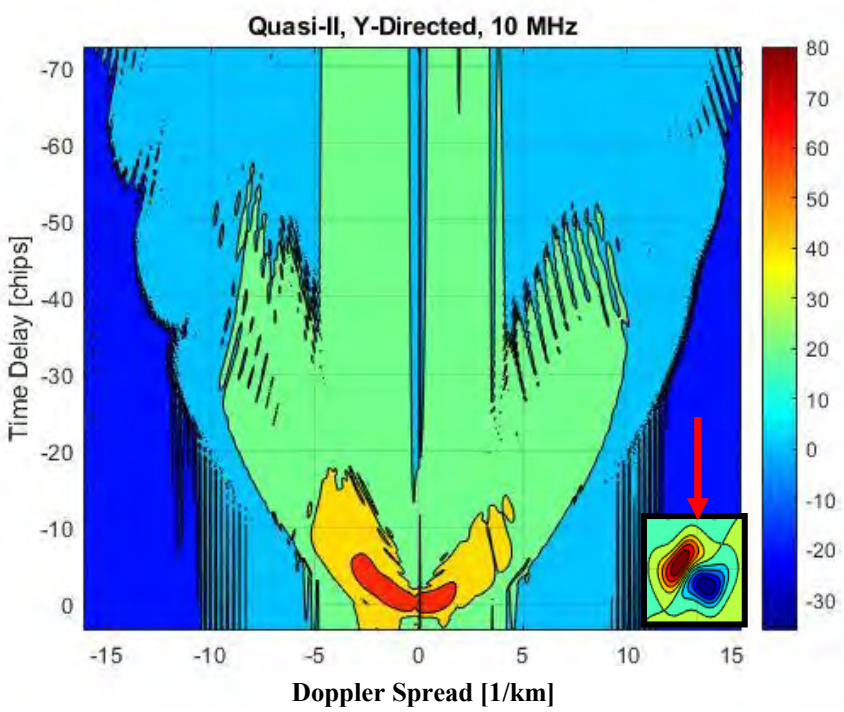

Figure 98. Delay-Doppler power distribution, Quasi-II, y-direction propagation, 10 MHz carrier

In the previous section, the stochastic flute maps have demonstrated greater time delays, greater scintillation, and lower coherence bandwidths compared to the single and array flute maps. These maps also create the most significant phenomenon observed in the doppler-delay spread of the received energy. Figures 99, 100, 101, and 102 show a variety of flute maps and propagation directions with respect to the orientation of the flute map. The variability of the stochastic flute maps can make the observable phenomenon of multiple fringe arcs more distinguishable at lower carrier frequencies for propagation in the *x* and *y* propagation directions in comparison to the isolated flute cases. Additionally, the fringes appear more prominent when the stagnation points are overlapping along the propagation direction, creating the weak scintillation conditions as observed in the previous section. The y-axis symmetry of the energy spread within a

doppler shift of + or - 5 [1/km] can be observed clearly in figures 101 and 102 . This skew is a result of the collective orientation effects of the flute structures within the density map as seen distinctly in the isolated flute cases.

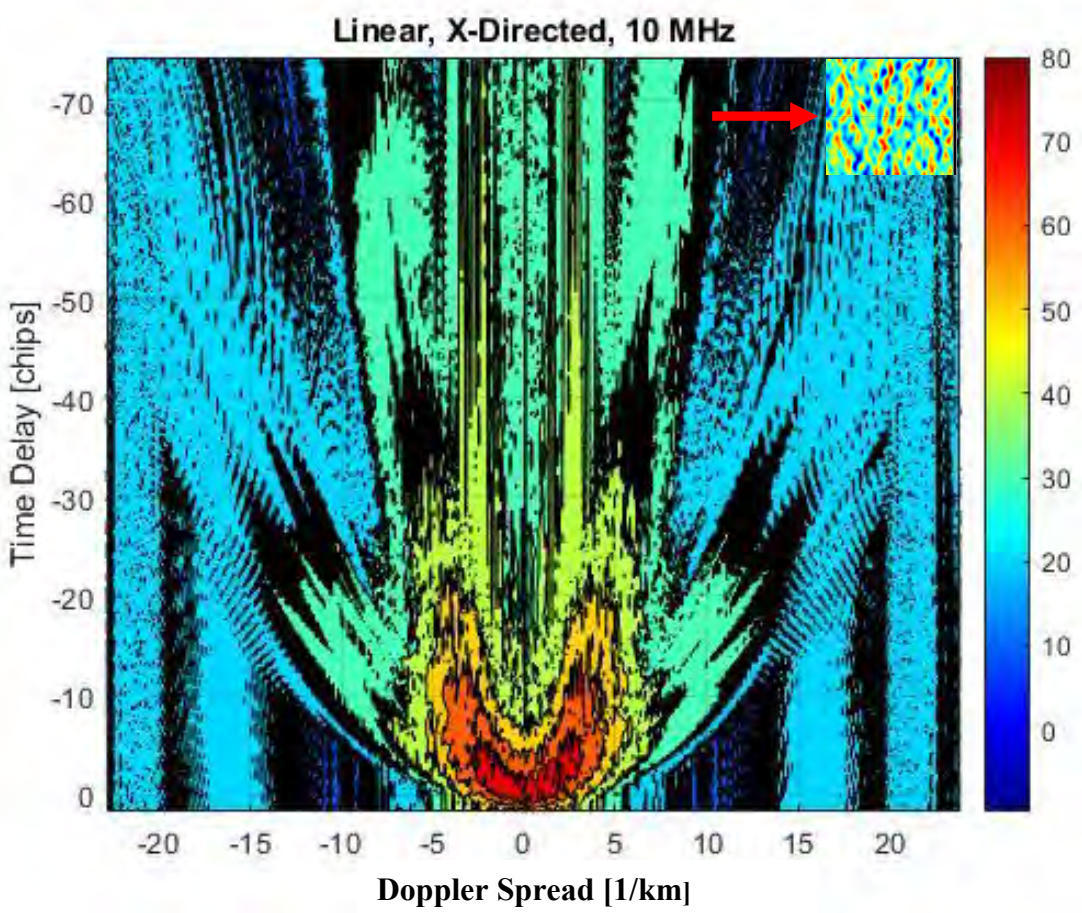

Figure 99. Delay-Doppler power distribution, Stochastic Linear, *x*-direction propagation, 10 MHz carrier

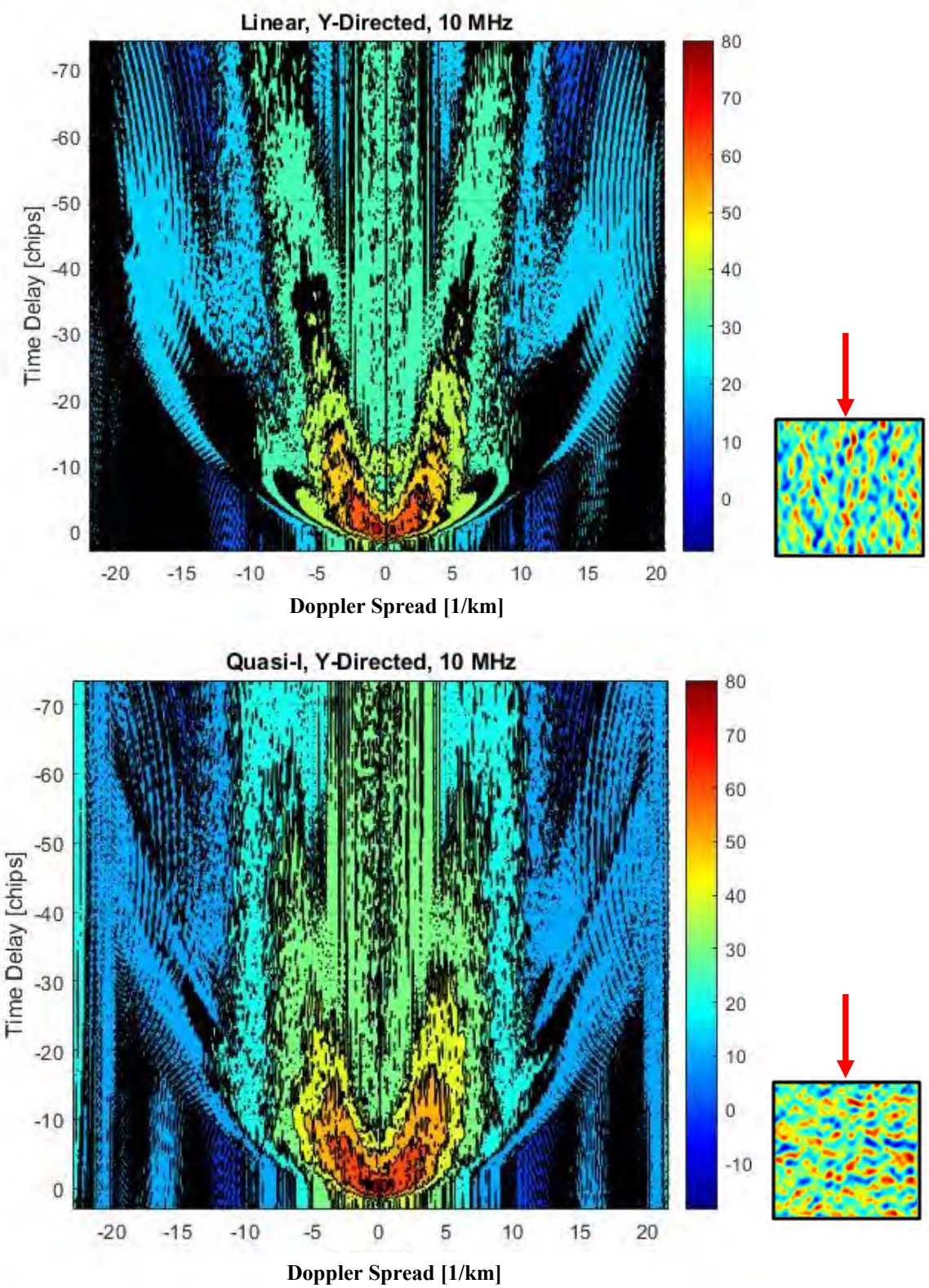

Figure 100. Delay-Doppler power distribution, Stochastic Quasi-I, *x*-direction propagation (top), y-direction (bottom)

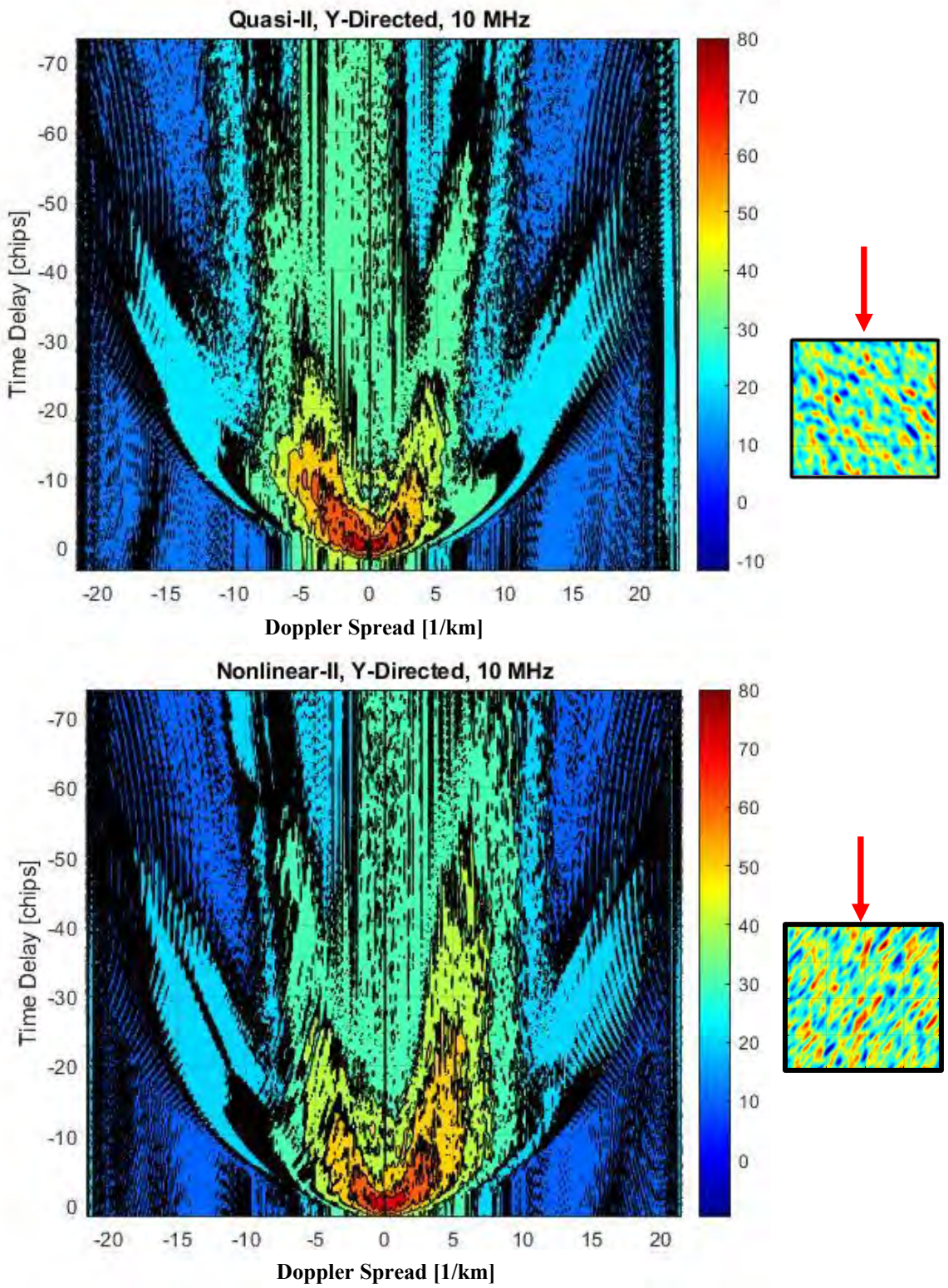

Figure 101. Delay-Doppler power distribution, Stochastic Nonlinear-II, *x*-direction propagation (top), *y*-direction (bottom)

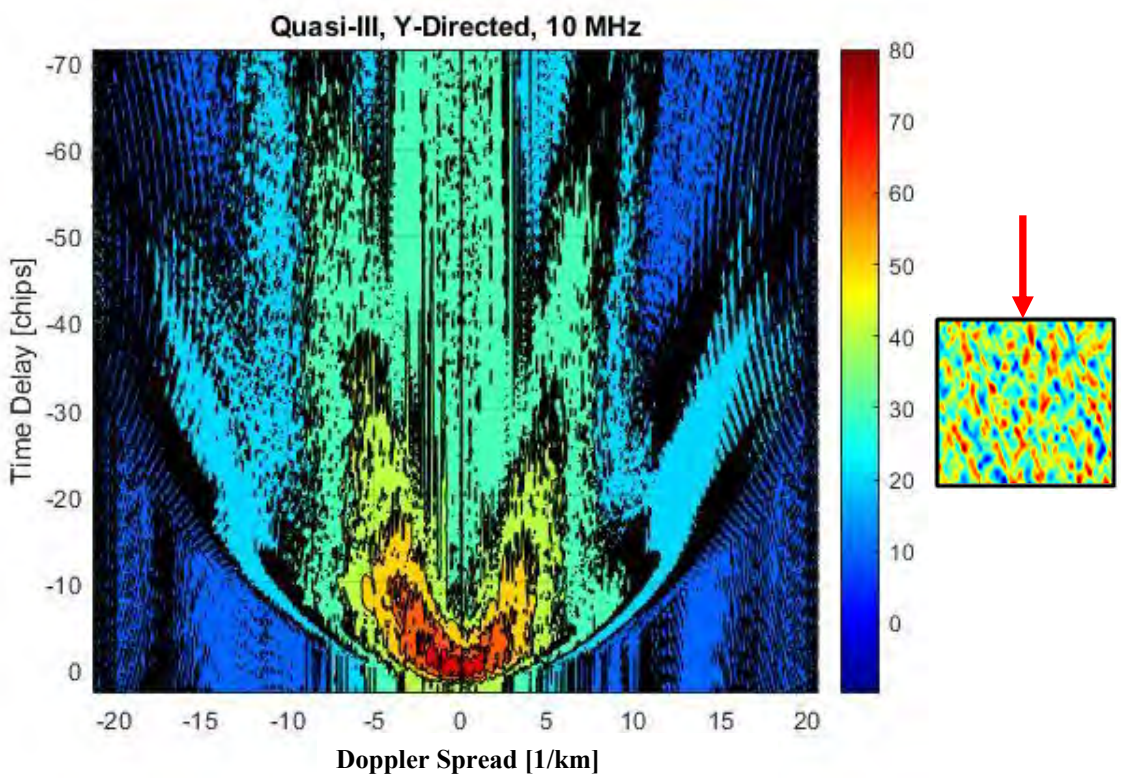

Figure 102. Delay-Doppler power distribution, Stochastic Quasi-III, *y*-direction propagation

Increasing the carrier frequency of the transmitted pulses, the doppler-delay map shows a reduction in the dispersion of scattered energy, allowing the energy to be more concentrated at the receiver as observed previously with the isolated flutes. However, the multiple fringe arcs appear to merge into the primary arc as the time delay decreases for all the parabolic arcs as a secondary arc appears with prominence. From 20 to 30 MHz, the time delay at the outer edges of the primary arc reduces by 10 chips, as it (along with the secondary arc) appears to shift outward along the doppler axis by 10 [1/km]. The energy spread broadens and dissipates substantially for high frequencies as the wave number increases as in the Gaussian and Kolmogorov doppler-delay maps in chapter 4.

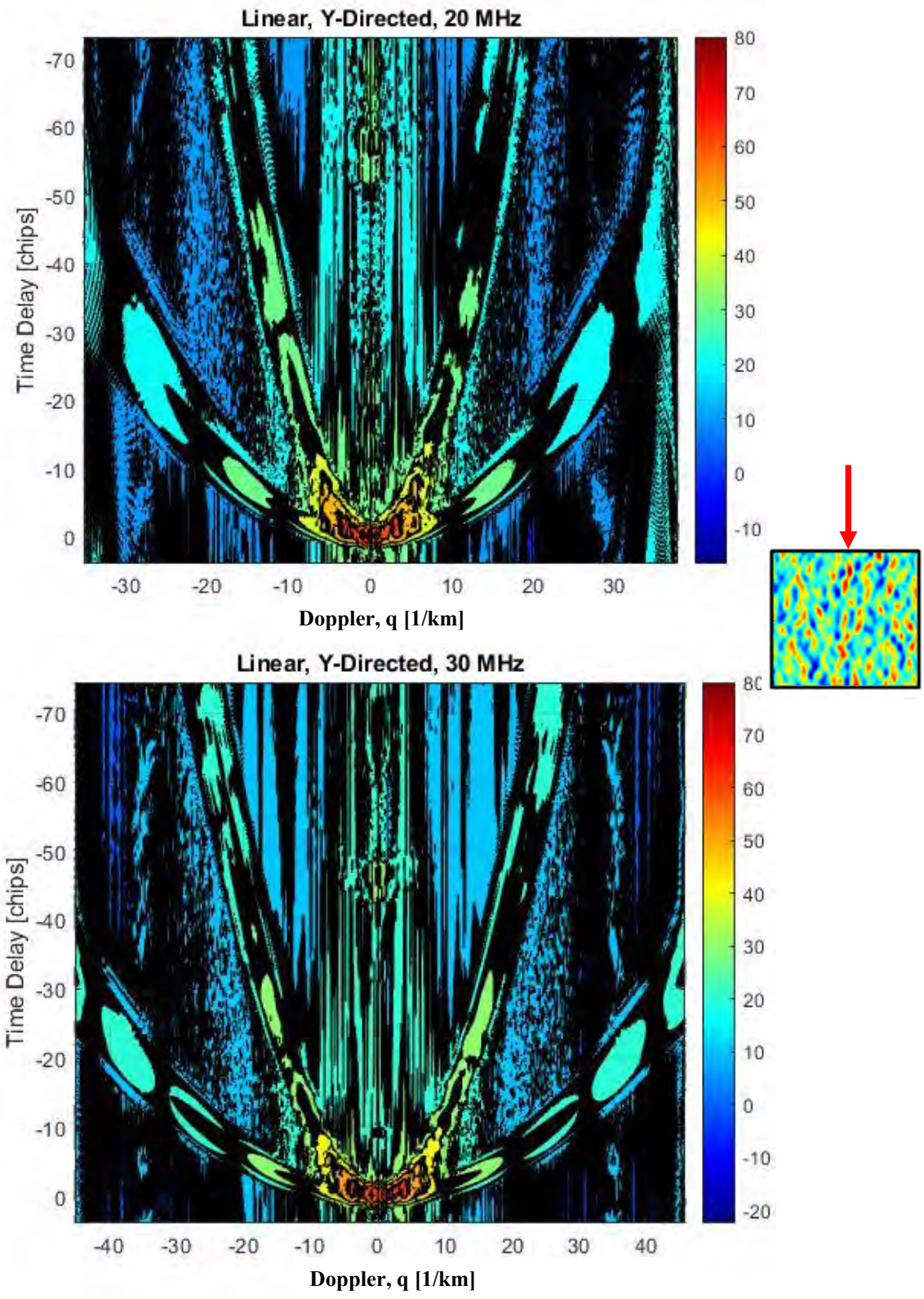

Figure 103. Delay-Doppler power distribution, Linear, *y*-direction propagation, 20 MHz carrier (top) and 30 MHz carrier (bottom)

Applying changes to the pulse width of the triangular pulses that modulate the incident electric field while maintaining a 25 MHz carrier frequency, the narrow pulses duration widens the bandwidth of the signal. A pulse duration of 98 nanoseconds corresponds to a pulse bandwidth of approximately 40 MHz. A 138 and 278 nanosecond pulse width results in a signal bandwidth of 29 MHz and 14 MHz , respectively. The wideband signal exhibits the greatest amount of dispersion that is comparable to the lower frequency phenomenon of narrow bandwidth pulses observed previously in this section. These conditions create severe frequency selectivity in the propagation channel perhaps by a greater margin compared to low carrier frequency cases in which the amplitude fading is uncorrelated amongst the received pulses. As the signal bandwidth narrows, the primary arcs tend to broaden and time delay decreases as observed in figures 104 and 105.

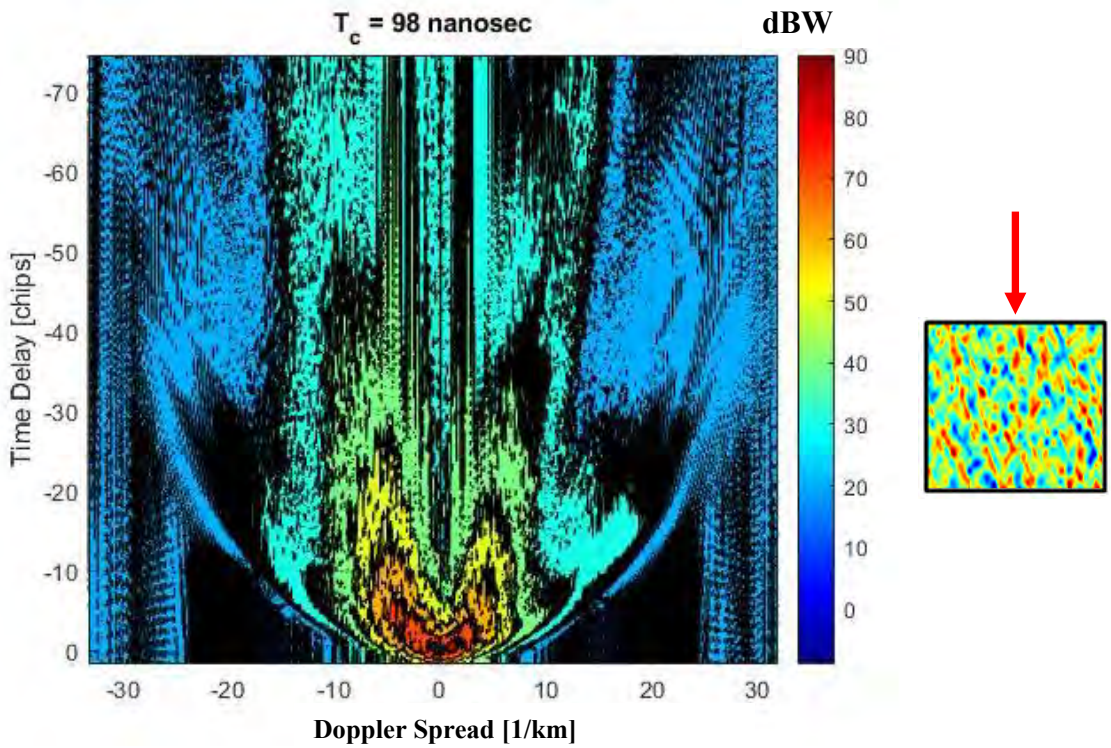

Figure 104. Delay-Doppler power distribution, Stochastic Quasi-I, *y*-direction propagation

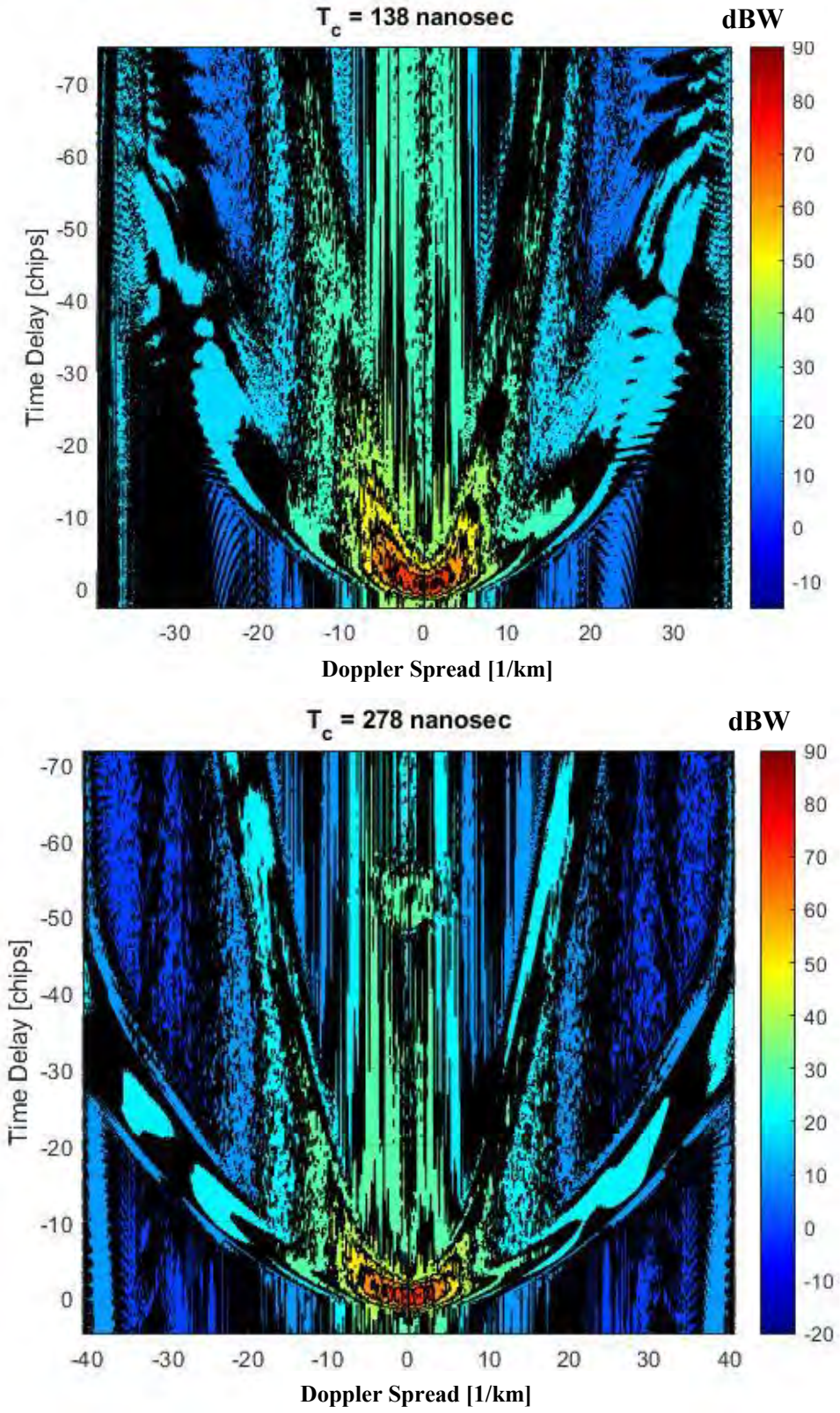

Figure 105. Delay-Doppler power distribution, Linear, *y*-direction propagation, Pulse Width increase

The pulse coherence model results certainly demonstrate that the presence of flute structures can disturb the propagation of an electric field transmitted in the high frequency range. Given that the amplitude and phase scintillation can be weak for isolated flute structures and strong in the presence of dense flute channels, the scintillation index does not appear to be an adequate metric to determine the presence of flutes. However, the frequency domain analysis of the received field scattering function does provide features that could possibly differentiate the flutes from other existing irregularities in the F-layer ionosphere. Upon inspection of the doppler-delay maps derived from the stochastic flute map propagation channel, multiple distinct fringe patterns were observed at low frequency. This is a contrast to the Kolmogorov and Gaussian spectra cases examined in Chapter 4 in which the distinction of the fringe patterns were not apparent until the carrier frequency of the signal increased towards the higher end of the HF spectrum. In chapter 3, it was shown that in many of the flute cases, the total phase power spectrum had a steeper spectral decay compared to the Kolmogorov spectrum as the wave numbers increased.

Two factors to consider are that the large scale size of the flute irregularities are an order of magnitude smaller than the large scale size of the Kolmogorov irregularities, and the peak magnitude of the flute PSD occurs at a much higher wavenumber before the spectral decay occurs. Therefore, in a wide range of spatial frequencies, the higher energy corresponding to large scale structure in the power spectrum is sustained. Additionally, the large scale sizes of the irregularities corresponding to the smaller wave numbers in the flute spectrum is comparable to the wavelengths of the incident field. The wave numbers generally have to increase in the Kolmogorov and Gaussian spectrums to

observe irregularity sizes comparable to the incident field's wavelength, therefore revealing the distinct scattering characteristics such as the multiple scintillation arcs in the delay-doppler map. These characteristics identified in the frequency domain are likely the most crucial observations required to differentiate flute structures from other ionospheric instabilities.

5.2 Flute Phase Cube Scattering Function Characteristics

This section introduces the phase cube implementation of the stochastic flute structures in which the scattering function is analyzed across the central grids along the 2D receiver plane. These regions will exhibit the most notable diffraction patterns caused by the flute structures, as horizontal and vertical polarizations are applied to the propagation algorithm. Figure 106 shows the propagation orientations of the 2D planar wavefronts to be analyzed at 500 kilometers beyond the phase cube in each direction.

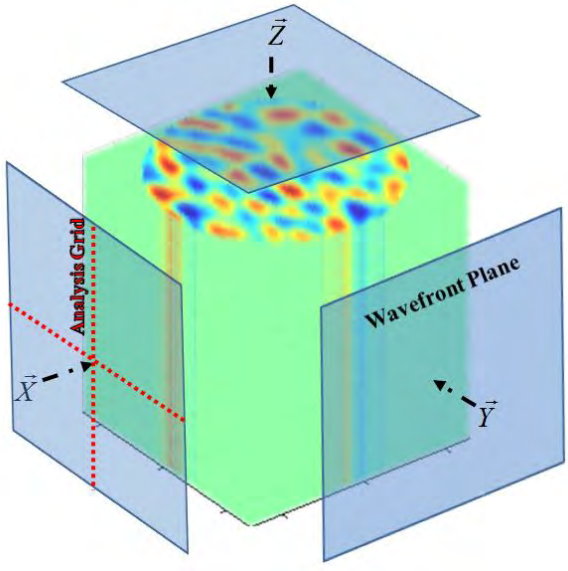

Figure 106. Planar Wavefront Interface with Phase Cube

The matrix applied to test the phase cube concept in shown in table 3.

Flute Density Cubes		
Nonlinear Flute	**Stochastic Flutes**	**Scattering Function Parameter Characterization**
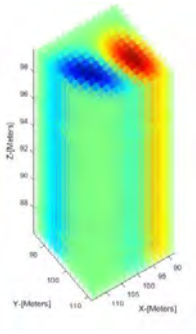	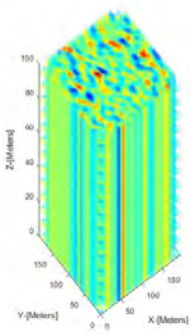	▪ Carrier Frequencies: 10, 15, 20, 25, 30 MHz ▪ Pulse Width: 288 nanoseconds ▪ *X*, *Y,* and *Z* Propagation Directions ▪ Horizontal and Vertical Polarizations ▪ 1 density map – Stochastic Flute Map ▪ 1 density Map – Single Flute Map

Total Simulations: 36

Table 3. Phase Cube Test Matrix

The carrier frequencies, polarizations, and propagation directions provide a variety of signal attributes that are evaluated from the scattering function determined at the receiver plane. The post analysis involves evaluating the scattering function's secondary calculations described in Chapter 2. These calculations include the signal time delay, time jitter, coherence bandwidth, doppler delay, doppler spread, doppler jitter, and spatial coherence. Additionally, the transfer function is calculated to observe the spatial and frequency coherence across the 2D receiver plane.

5.2.1 Scattering Function Observations and Secondary Calculations

The scattering function evaluated for all cases required additional processing due to issues with arc wrapping beyond the left and right boundaries of the receiver grid. This issue was mitigated by doubling the length of the finite domain. The negative trade-off is that the solution is repeated for the corresponding periodic wave numbers. The regions

from the center to the boundaries of the spectral grid were extracted and placed on opposite ends of the original array in an attempt to unwrap the excess doppler-delay portions of the scattering function. The result was the full parabolic arc pattern with extra features that could interfere with the secondary calculations. The cross-over and extra peaks caused by the unwrapping algorithm required removal from the total image of the scattering function. This required precise extraction in which the scintillation arc curvature was approximated using three-point parabola fittings for the interior and exterior arc regions. The region above the outer arc and below the inner arc was replaced with the minimum value of the exterior region (non-inclusive of the extra features removed). The entire process is shown in Figure 107.

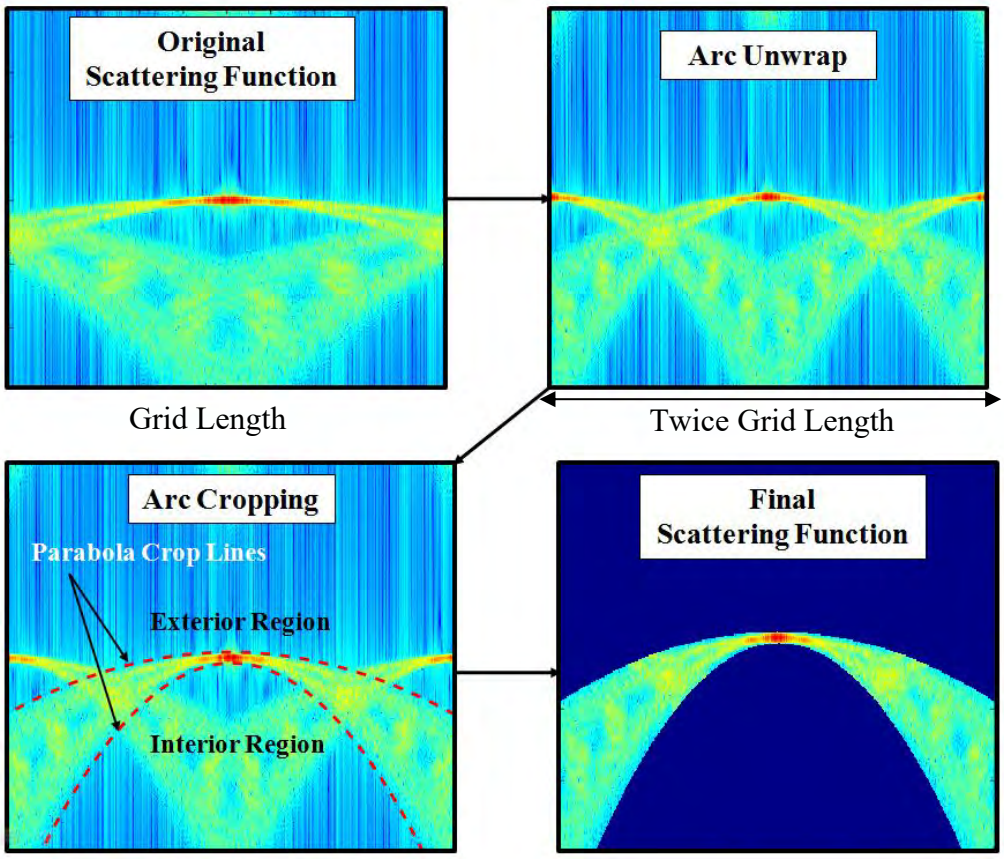

Figure 107. Scattering Function, Arc Processing

The doppler-delay maps of the scattering functions are shown in Figure 108 for a propagation 500 km beyond a stochastic flute map at a carrier frequency of 10 MHz. The *x*-pol. represents horizontal polarization and the y-pol. represents the vertical polarization. The polarization has significant differences observed for the *x* and *y* propagation directions. The alignment of the *x*-polarization will exhibit greater variations in the electric field as there is more non-homogeneity across the density map in this orientation. This translates to a greater energy spread (~45 dBW, +/- 10 [1/km] over a delay of 60 chips) as shown in the corresponding delay-doppler maps. In terms of the *y*-polarization, there is more homogeneity associated with the elongation portion of the flute structures, and therefore the scattering is considerably weaker (generally ~20 dBW over a comparable delay-doppler range). In the case of the *z*-propagation direction, the homogeneity varies along the lateral portion of the sampling grids, with little indifference between the *x* or *y* polarizations. These variations along the grid remain consistent over a greater propagation distance, as the length of the 3D phase cube flute structure is greater than the width. Generally, the greatest magnitude of the energy spread in the *z* -direction is observed in the y-polarization case, an overall global difference of 10 dBW compared to the *x*-polarization. In the y-pol. case, each of the stochastic flute stagnation points are roughly horizontally aligned perpendicular to the sampling grids, thereby reducing phase cancelation effects as observed in the total phase power spectrums calculated in Chapter 3. Each of the orientations and polarizations show a variety of fringes whose prominence is largely dependent on the polarization and direction relative to the flute phase cube. In comparisons to the delay-doppler maps observed in the pulse coherence model, these fringes are not as distinctive for transmission frequencies at the low end of the HF

spectrum. As the frequency increases, a primary and secondary arc becomes visible over a wider range of doppler shifts as doppler delay decreases (see Figure 109).

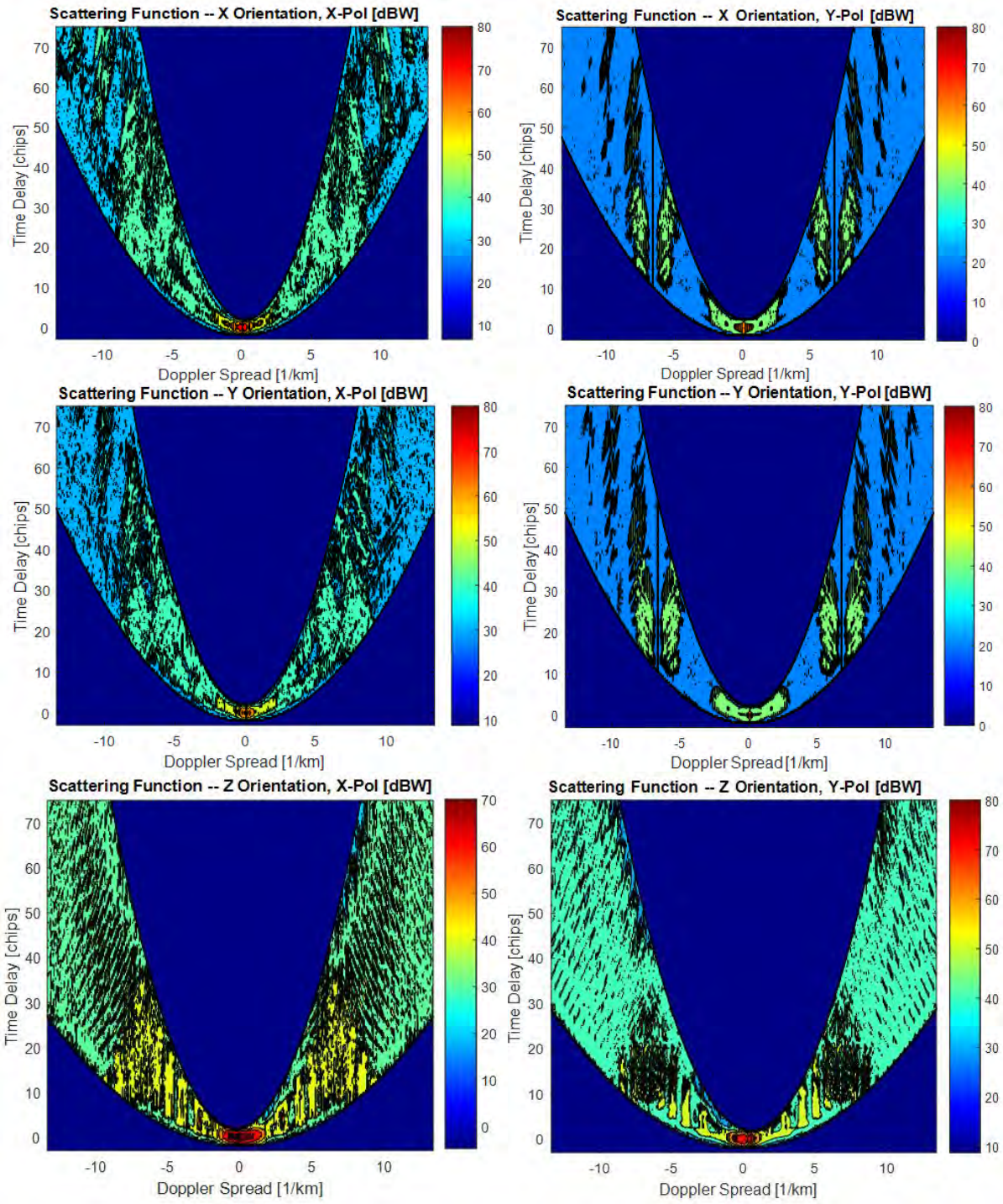

Figure 108. Stochastic Phase Cube, Doppler-Delays *X*, *Y*, and *Z* Orientation and *X* and *Y* Polarizations, Carrier: 10 MHz

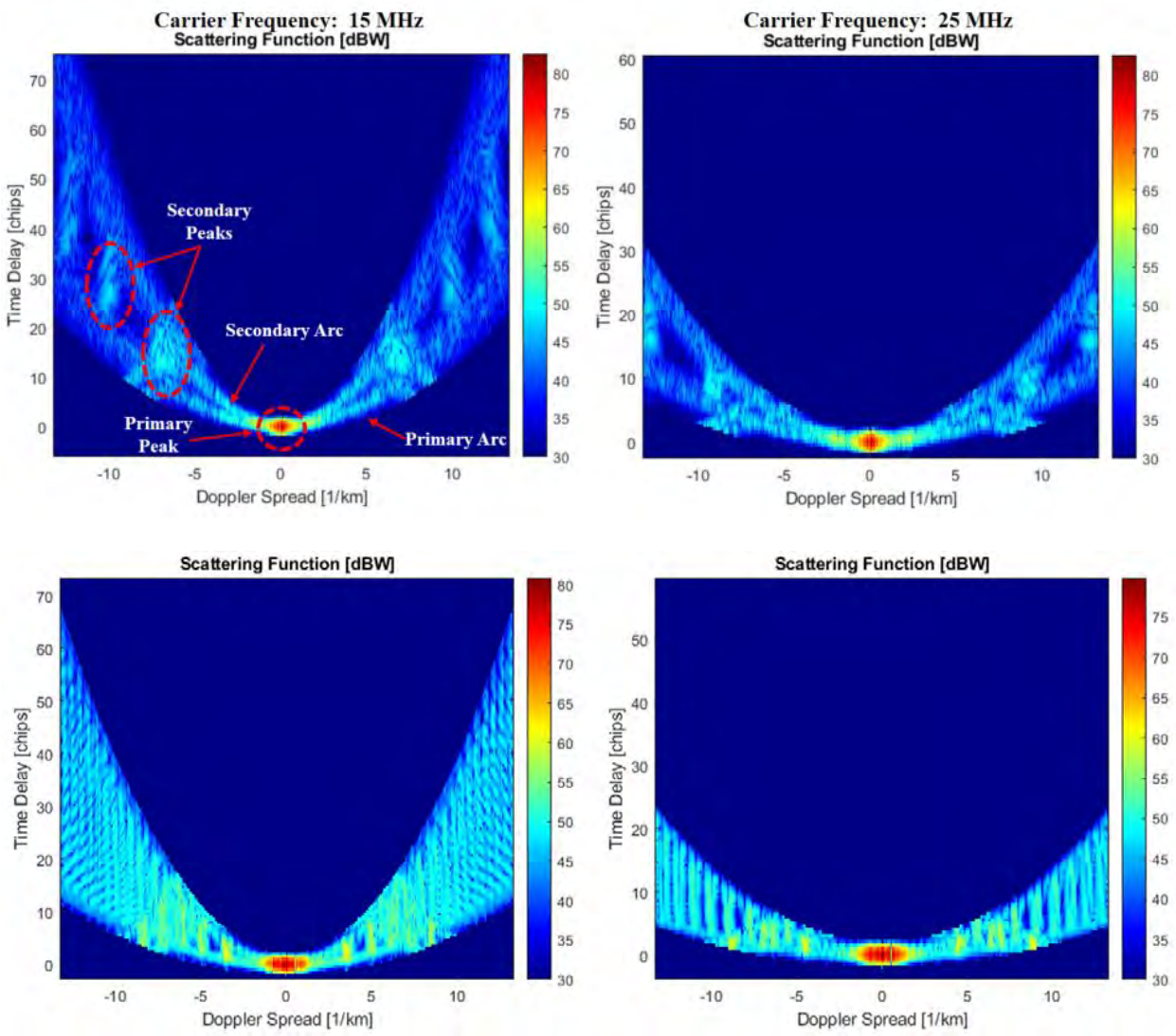

Figure 109. *X*-propagation Direction, *X*-pol. (top) and *Z*-propagation Direction, *Y*-pol. (bottom)

Additional phenomenon includes secondary energy peaks in between the primary and secondary scintillation arcs. These peaks tend to be distinctive in the *x* and *y*-propagation directions but very ambiguous in the *z*-direction, in which the energy ripples between the arcs as seen in the bottom delay-doppler maps of Figure 109. These observations might be an indication of additional dispersion or cross interference patterns along the second dimension of the 2D plane that would not be captured in the 1D model. Appendix F

shows a simplified version of this 1D-2D effect on the received field using a Gaussian lens to compare the diffraction pattern differences over the same propagation distance. These type of observations in the received field exist between the 3D propagation model and the 1D pulse coherence model over a comparable propagation distance of 500 kilometers. An additional understanding of these differences includes examining the source of the scattering, the 2D phase power spectrums of each phase cube at each orientation along the propagation path.

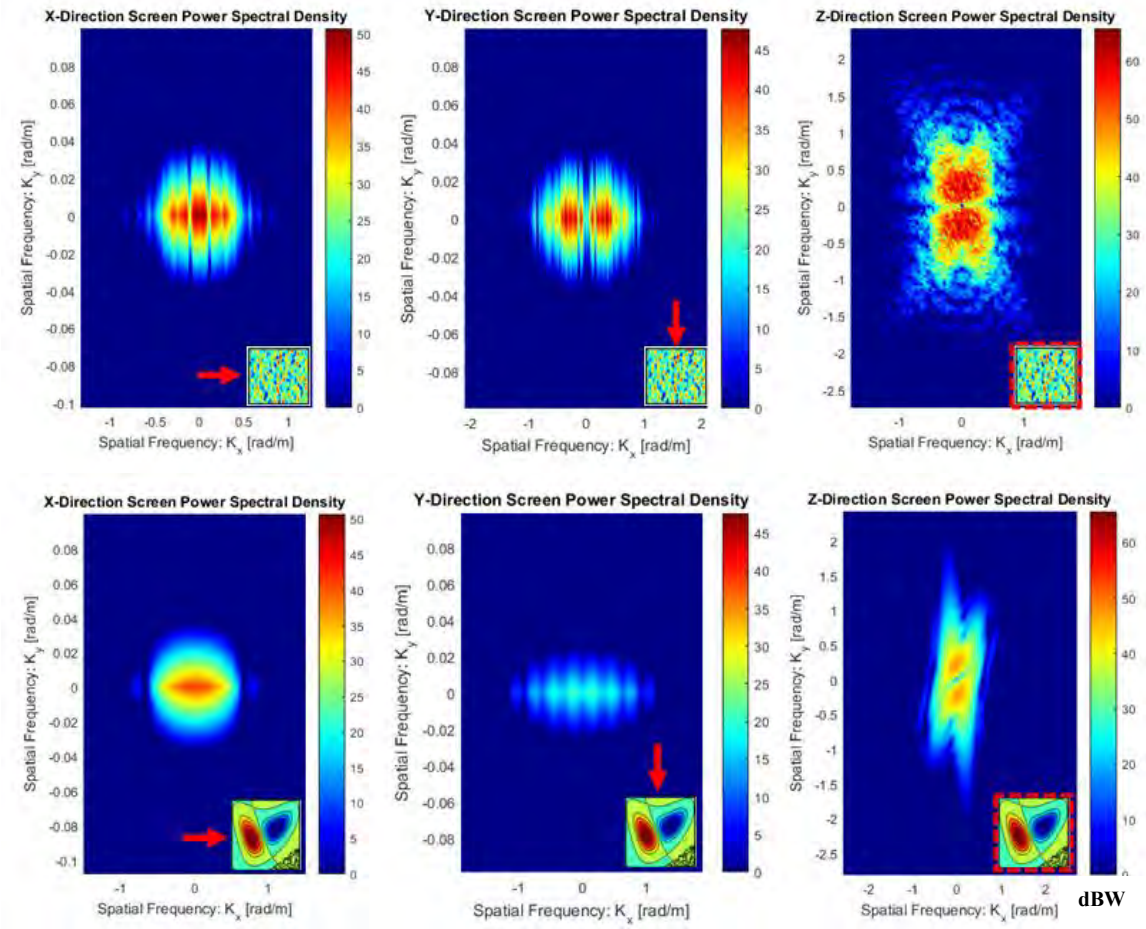

Figure 110. Stochastic Flute Phase Cube (top) and Single Flute Phase Cube (bottom) PSD Distributions for *X*, *Y*, and *Z* Directions

Figure 110 shows the 2D power spectrums corresponding to each flute density map in the *x, y,* and *z* directions. In comparison to the single nonlinear flute map, key observations in the PSD of the stochastic map include the approximate differential in PSD peaks; +10 dBW greater in the *x*-direction, +25 dBW greater in the *y* - direction, and +20 dBW greater in the *z*-direction. The power distribution has a greater widespread magnitude in the *y* and *z* directions of the stochastic flute map and comparable in the *x* -directions of both maps. The widespread distribution of the power spectrum in the phase cube appears to broaden the energy spread over a greater number of doppler shifts and time delay in comparison to the phase screens applied in the pulse coherence model. In the pulse coherence cases, for a given realization of the received field analyzed, the entire diffraction pattern of the received field caused by a phase screen was entirely accounted in the scattering function calculation. However, in the phase cube method, only a 1D section along the central (most intense) portion of the diffraction pattern over the 2D received field plane is accounted in the scattering function calculation. This, in essence, is not inclusive of the entire total phase power spectrum effect on the field, and therefore offers another explanation for differences in the scattering functions calculated previously.

The Mutual Coherence Functions (MCFs) corresponding to the Figure 108 scattering functions via fourier transforms are shown in Figure 111. The MCF is used to derive the spatial and frequency correlations of the received field. The Δx or Δy is the sample points along the axis in which the electric field is evaluated from the original 2D receiver plane at the 500 kilometer propagation distance.

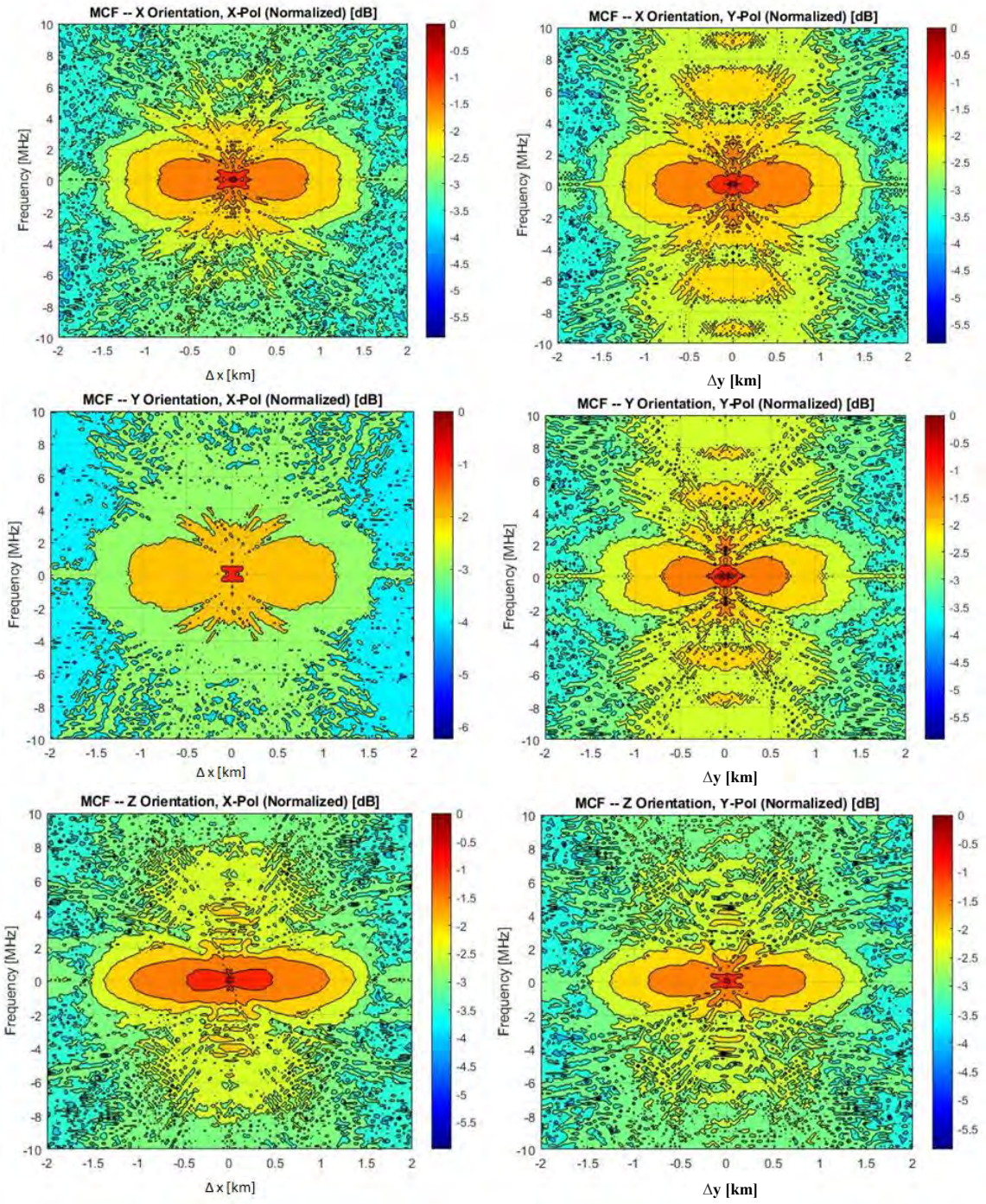

Figure 111. Stochastic Phase Cube, Mutual Coherence *X*, *Y*, and *Z* Orientation and X and Y Polarizations, Carrier: 10 MHz

The Δf is the change in frequency over the bandwidth of the signal. The greater MCF value (in dBs) corresponds to a greater correlation along the spatial and frequency

samples of the received field. This appears to be the case for the propagation in the x – direction with polarization along the y-axis (the elongation portion of the flute structure in which the density gradients are mostly homogenous). This was observed with the scattering functions that had fringing and secondary peaks of doppler-delay shifted energy. The propagation in the y – direction with polarization along the x axis has the lowest overall MCF. This corresponds to less homogeneity along the propagation path. The secondary calculations initially presented in chapter 2 are applied to the scattering function to determine the power delay profile, doppler power spectrum, and the mutual coherence function. The power delay profile involves comparing the signal paths received at different moments by calculating the mean time delay and time jitter. The doppler power spectrum provides the broadening, or the widening of a narrow band signal propagating through the channel. Additionally, the mean doppler delay and jitter is calculated over the power delay spectrum profile. The mutual coherence function can yield the spatial correlation function and the frequency correlation function, providing the spatial coherence and coherence bandwidth of the channel, respectively.

The example in Figure 112 demonstrates the foundational functions required for these calculations and their relationships. This example is the 10 MHz, x-direction, x-pol. phase cube model of a received field after propagating 500 km beyond the flute structure. The mean time delay and jitter are calculated from the power delay profile using the temporal moment technique referenced in Chapter 2. Likewise, the doppler delay and jitter are calculated in the same manner while referencing the profile of the doppler power spectrum.

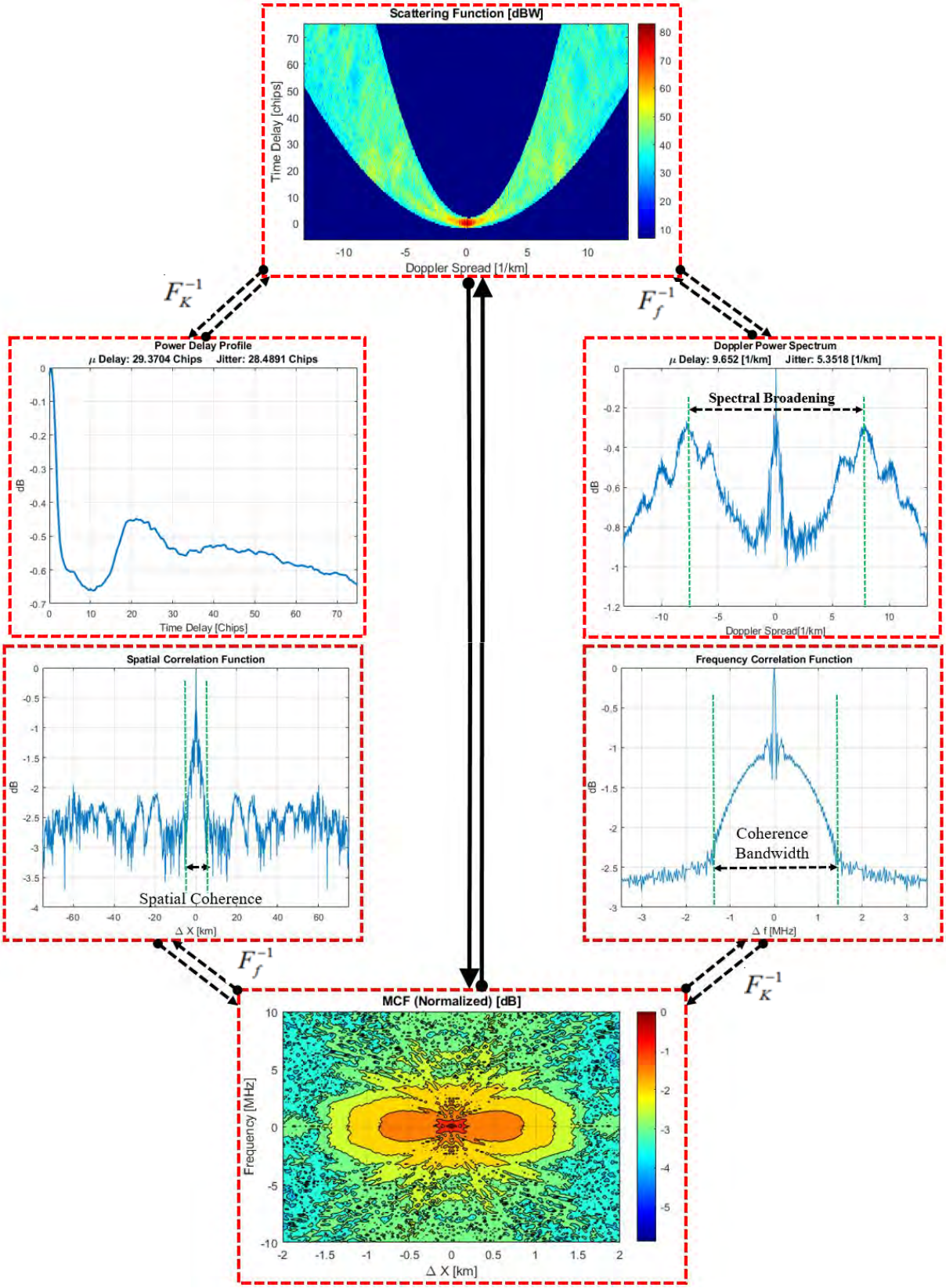

Figure 112. Scattering Function Secondary Calculations

The doppler spread is measured from the origin of the doppler axis to the spatial frequency where the peak of the spectral broadening is observed along the doppler power spectrum. The nature of the doppler spread indicates that the phase changing medium of a flute structure causes the signals traveling along different paths to exhibit different rates of change in phase as observed in Figure 110 in which the doppler spread is approximately 7.5 [1/km].

The spatial and bandwidth coherence measurements are observed at the central grids along the 2D mutual coherence function plane, as the spatial correlation plot is analyzed for $\Delta f = 0$ and the frequency correlation plot is analyzed for $\Delta x = 0$. These regions on the MCF plane are where the most extreme peaks and variations of coherence occur. Measuring the spatial and bandwidth coherence is accomplished in a similar manner in which the region where the power levels begin to become indistinguishable indicates that the signal will experience uncorrelated fading characteristics. From Figure 112, the spatial correlation observed to be approximately 14 kilometers wide. This indicates that out of the total width of 150 kilometers along the receiver grid, approximately 9.3% of this region is where the electric field experiences similar fading characteristics along the physical space of the grid. The coherence bandwidth is 3.16 MHz, well below the signal bandwidth indicating a frequency selective channel as observed in the previous section. The significance of these metrics is further understood through comparisons of two different propagation channels; the stochastic flute map and the isolated flute map.

In Figure 113, each metric is presented as the average observed over the propagation distance and corresponds to a particular carrier frequency. The objective is to

identify relationships or trends between the carrier frequency and the metric in focus. The temporal results are significantly greater than in the pulse coherence model, likely due not only to the 2D plane analysis (added dimension) of the propagating electric field, but also the method of calculating these metrics directly from the power delay profile. In the previous section, temporal moments of the pulses were taken along the receiver grid. In this case, temporal moments are not applied and the analysis is taken directly from the scattering function.

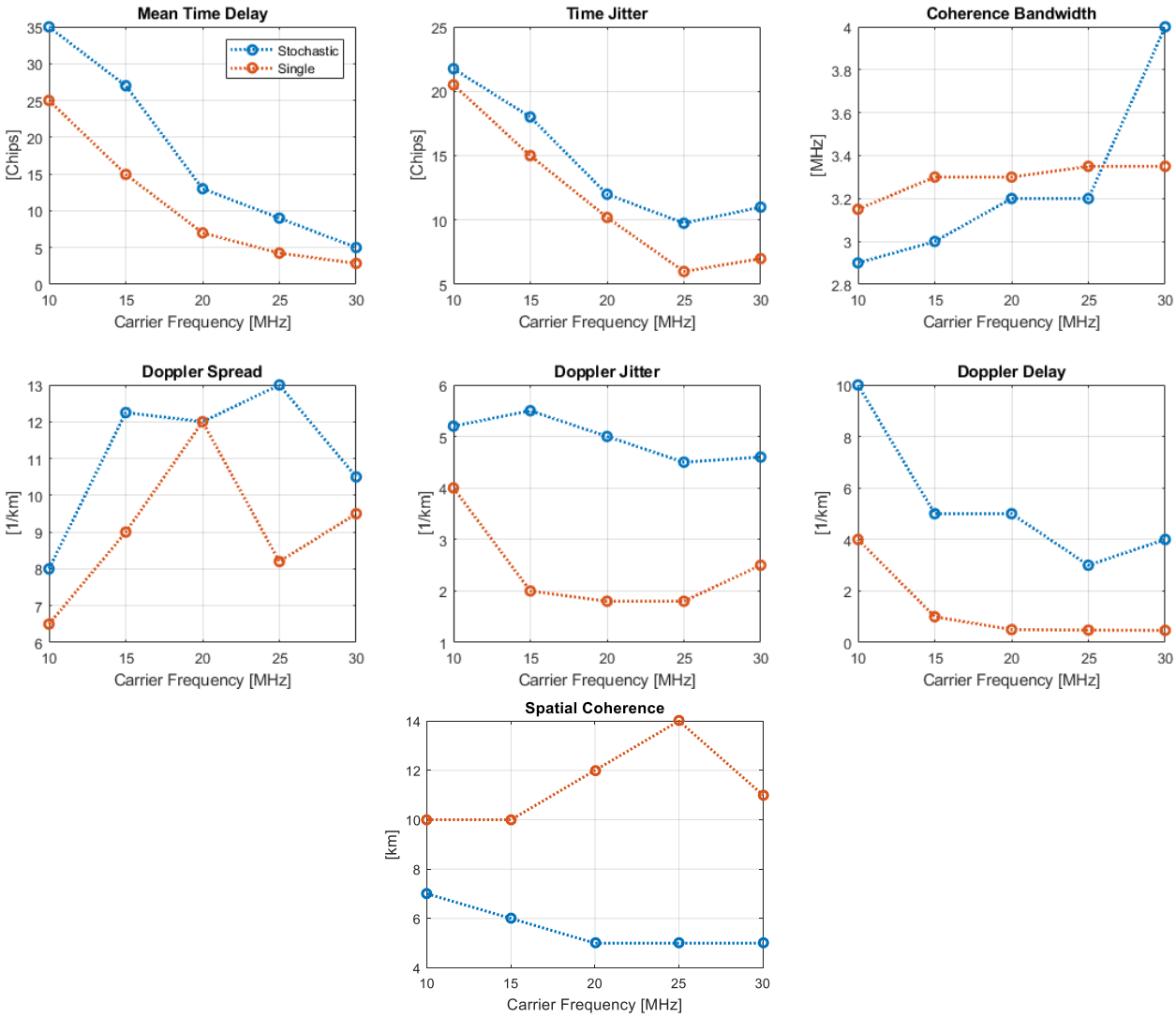

Figure 113. Scattering Function Secondary Calculations comparing Stochastic and Single Flute Phase Cubes, Averaged results over propagation distances

For the lower frequencies, the time delays appear significantly high even for the presence of an isolated flute structure (~25 chips) and generally decay gradually with increasing frequency. Subsequently, the coherence bandwidth is lower than reported in the previous section's pulse coherence results by 5 to 10 MHz. At a 10 MHz carrier, a single flute structure in this phase cube model can cause ~3.2 MHz coherence bandwidth compared to ~2.9 MHz from the stochastic map, indicating that either channel has high frequency selectivity. This remains true at the 30 MHz carrier, which was previously a flat fading channel in the 1D pulse coherence results. The relationship between the carrier frequency and doppler spread does not appear to be distinguishable, but rather relatively comparable between the single and stochastic flute maps in which the extreme cases of spectral broadening are 49% to 98% of the spectral grid for both flute cases. The doppler power spectrum profiles are greater for the stochastic flute results and therefore generally yield a greater mean delay and jitter. Spatial coherence is clearly greater and likely corresponds to the severity of the flute structure's inhomogeneity. Approximately 6.67% of the spatial grid is considered coherent in the worst case scenario of single flute maps at 10 and 15 MHz carrier, twice more than in the stochastic map cases.

The results in Figure 114, show box and whisker plots corresponding to the single and stochastic flute maps for x -pol. and x-direction, continuing the preceding analysis. Each box and whisker plot is inclusive of the data spread observed over the 500 kilometer propagation distance along with the averages and extrema of these results. While it remains difficult to obtain a distinguishable relationship between an isolated flute and stochastic flute map, the stochastic map on average causes the most severe case for each metric, an expectation based on the observations made from the power spectrums of each

phase cube examined previously in Figure 110. However, in many cases, the isolated flute causes the greatest spread in the simulation results over the 500 kilometer propagation distance.

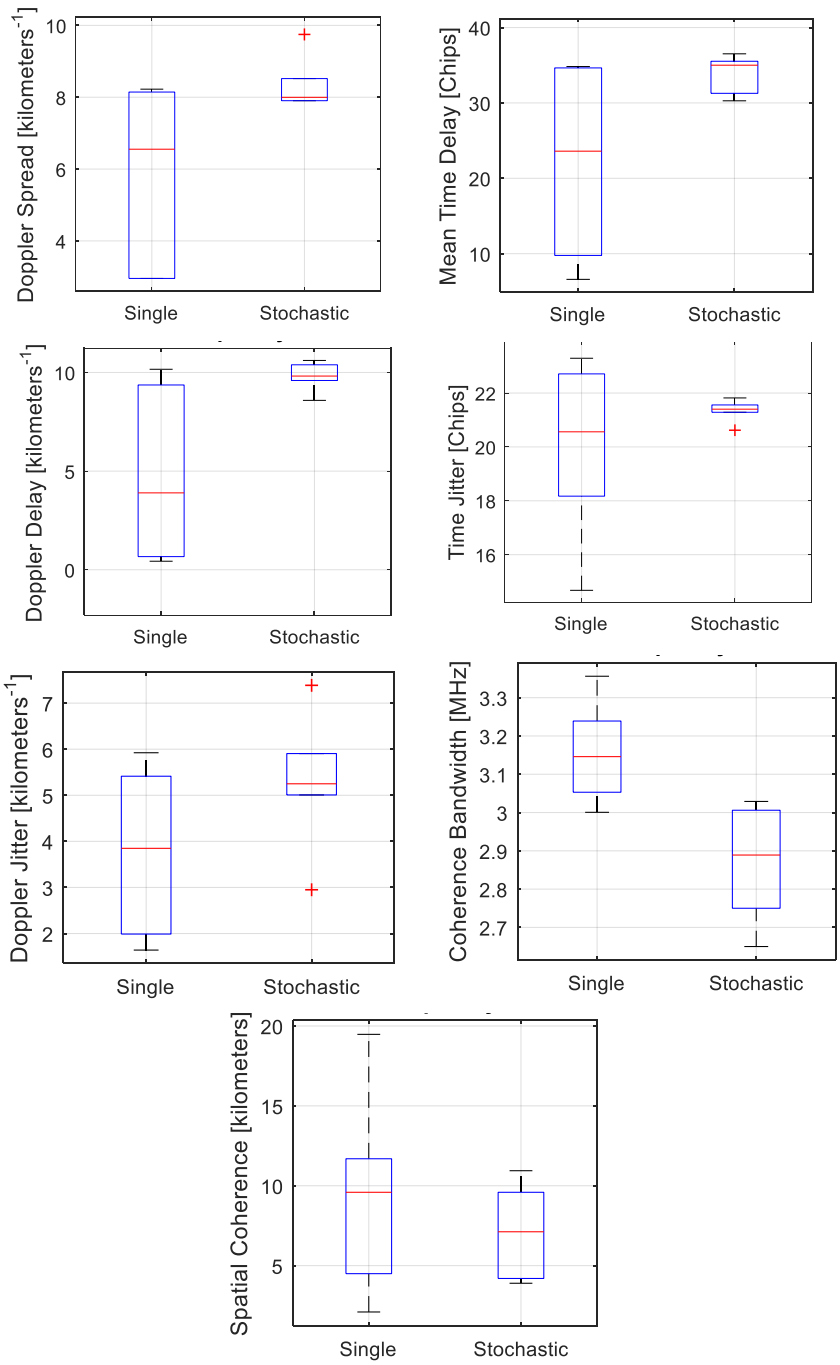

Figure 114. Scattering Function Secondary Calculations comparing Stochastic and Single Flute Phase Cubes, Spread of results over propagation distances

Additionally, the maximum extrema in the single flute map may exceed the maximum extrema or average of the stochastic cases. The spread of the stochastic map results are much closer to the average, over the entire propagation distance. This demonstrates that the most intense propagation effects occur early on and throughout the process, whereas the single flute map effects are much more gradual and cumulative.

Some observations to note are the significantly low spatial coherences achieved in the single flute case. The lowest value indicates that 1.3% of the received signal at the carrier frequency is coherent. In the single flute case, the lower extrema of the coherence bandwidth is comparable to the upper extrema of the stochastic flute case at ~3 MHz. This observation can also be made in the doppler delay at around 9 [1/km]. The opposite extrema relationship between the stochastic and single flute maps is observed for the time delay at around 32 chips. An expected result is the low values of doppler spread that occurs in the single flute case, a minimum of 1.5 [1/km] versus the minimum of 8 [1/km] in the stochastic map case.

Additional box and whisker plots that show the results for increases in the carrier frequency for a variety of polarizations are shown in Appendix E. Figure 115 summarizes the averages of these metrics with respect to the polarization and direction of propagation at the distance of 500 kilometers and at a carrier of 10 MHz. For each polarization and direction on average, the stochastic map generally causes the more extreme cases such as higher time delay, doppler spread, doppler delay, lower spatial coherence, and lower coherence bandwidth. In some cases, these values are comparable between the flute maps depending on the propagation direction and polarization (see *Y*-pol., *X*-direction for time

delay and spatial coherence and *X* pol., *Y*-direction in the spatial coherence and coherence bandwidth cases).

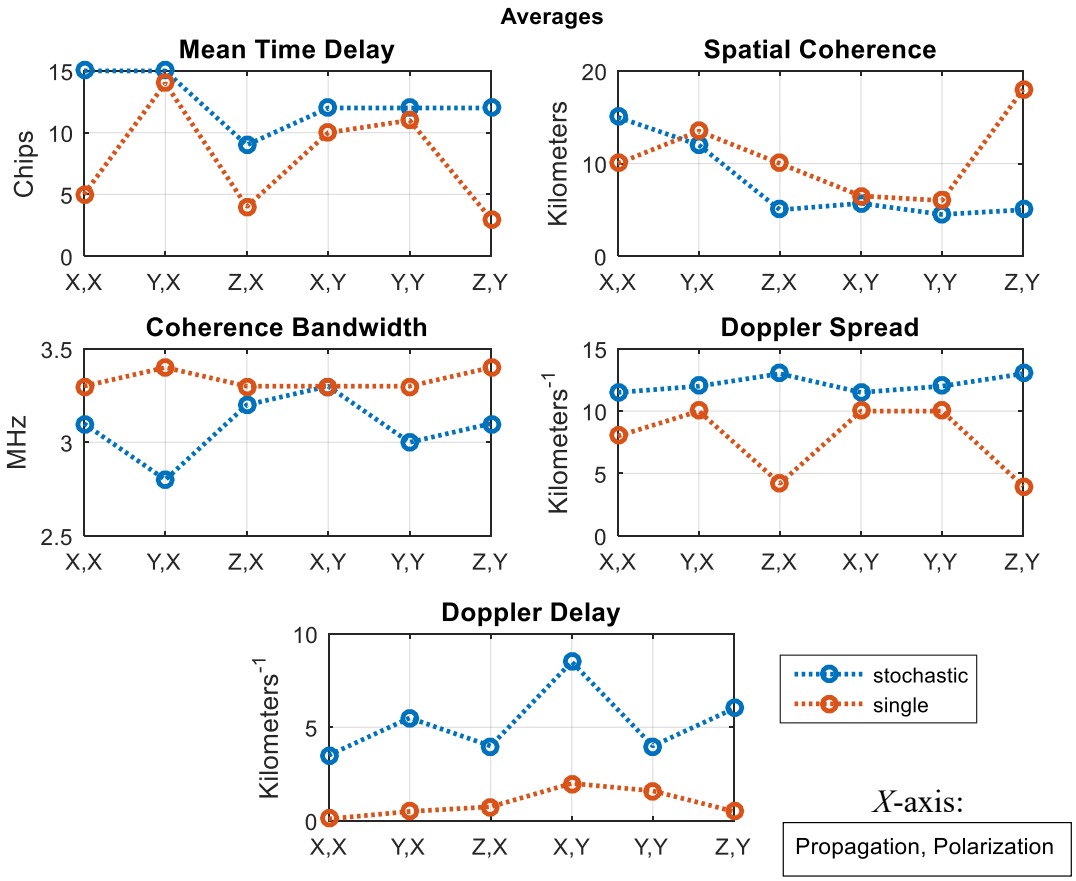

Figure 115. Scattering Function Secondary Calculations comparing Stochastic and Single Flute Phase Cubes, Spread of results over propagation distances, *x*-axis = (Propagation, Polarization)

To summarize, the observations with respect to the stochastic and single flute map cases demonstrate that the combination of polarization and propagation direction of the electric field greatly effects these secondary calculations from the scattering function more significantly than the carrier frequency. This was not an expectation based on the results observed in the pulse coherence model when it came to scintillation indices and initial observations of the doppler-delay maps. A key difference mentioned earlier in this section is the difference in the scattering profile caused by the 1D and 2D phase screens

as the field evolves with propagation distance. The scattering profile will also change from the inclusion of the elongated portion of the flute structure with respect to the lateral propagation direction and the radial flute geometry along the *z* axis. A more complete profile of the flutes from the sequence of 2D screens causes the features of the power spectrum to change as well. These changes make the differences between the single and stochastic flute maps less distinguishable. Therefore, despite the fact that the stochastic map produces the greater power spectrums in all directions, the variety of polarization and propagation directions in the incident field revealed that the single flute map is still capable of causing a cumulative impact on the secondary parameters. The following section extends the analysis by applying ray tracing to the phase cubes in order to determine the impact of the refractive characteristics on the scattering functions and secondary calculations.

5.2.2 Ray-Trace and Polarization Effects on the Scattering Function Calculations

In this section, two stochastic flute map ray trace demonstrations are analyzed to examine the severe refractive effects caused by multiple flutes and coupled phase cube calculations to acquire additional scattering aspects of the flute structure. Each example demonstrates the effects of varying the azimuthal and elevation angles relative to the entry point of the ray through the flute structure. The final ray trace demonstration is applied to a single flute map to determine how the scattering function changes with respect to minor refractive changes along the propagation path. A Kolmogorov phase cube is also incorporated into the model to determine if the background irregularities of various scale sizes create enhancements in the scattering function initially produced by

the flute structure. Secondary calculations from the scattering function are re-examined for comparison over the various scattering conditions.

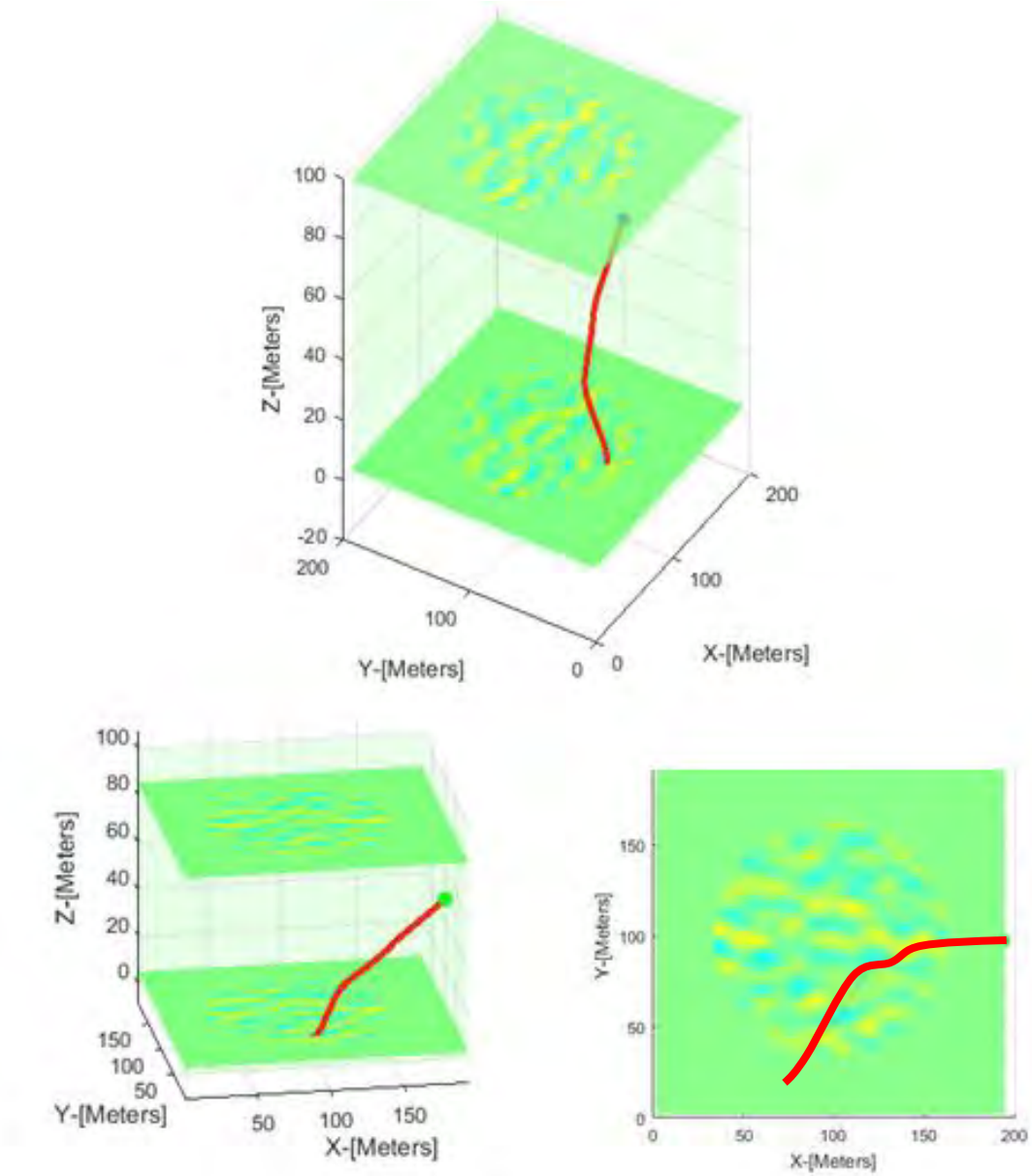

Figure 116. Ray Trace Plots for 0° azimuth and 155° elevation case

The first ray trace case involves a 0° azimuth and 155° elevation angle of a ray entering the flute structure. The N_{frac} value is assumed to be 0.2, or 20% of the peak

background electron density. The ray entry point is biased towards the topside of the flute to examine the elongated gradient effects of the flute structure. Figure 116 shows the 3D ray trace map generated from this set-up. The ray deviates along the x-axis by 40.31°, the y-axis by 49.68°, and the z-axis by 23.3°.

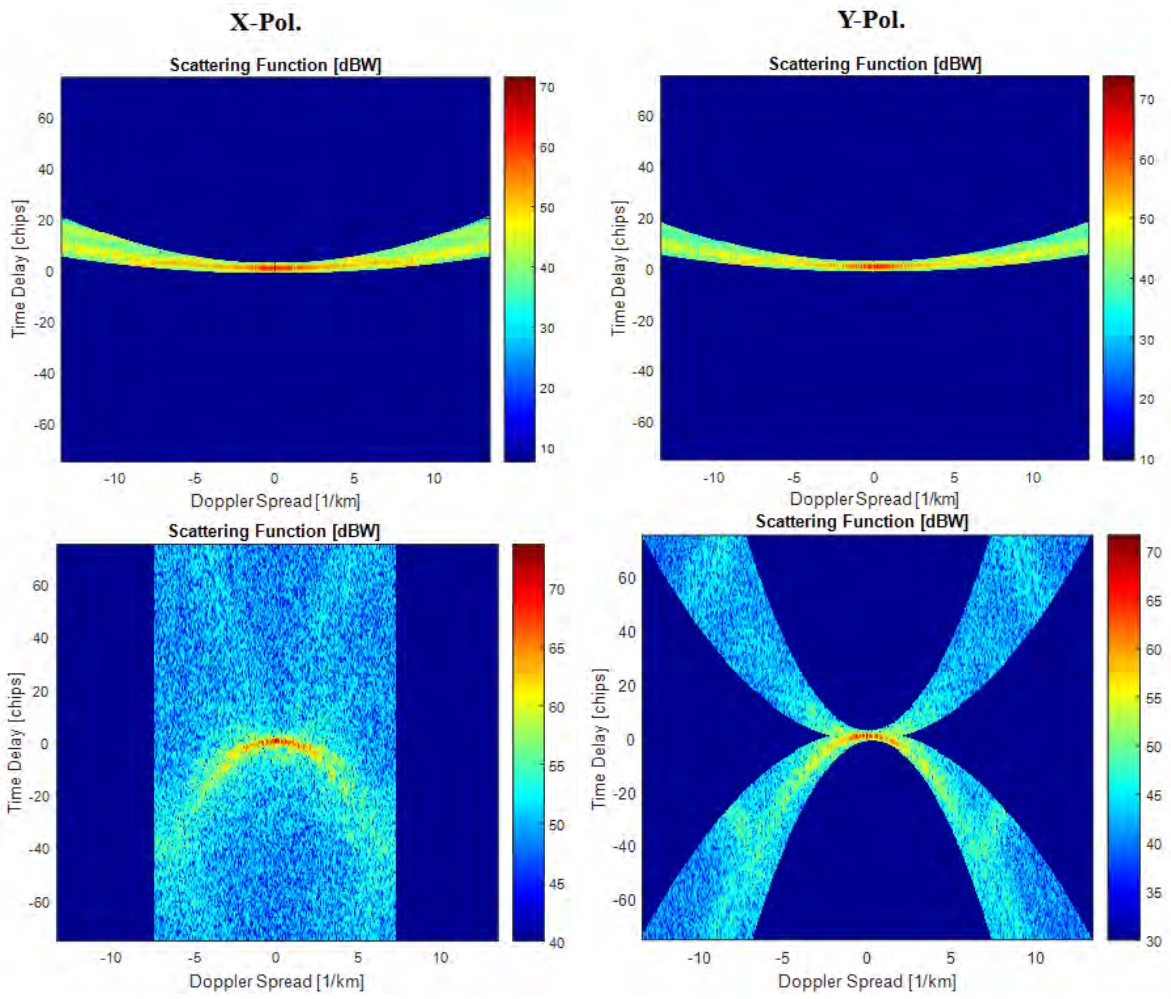

Figure 117. Scattering Functions for 0° azimuth and 155° elevation case, Flute Only presence (top), Flute and Kolmogorov presence (bottom)

Figure 117 shows the scattering functions corresponding to the polarizations. The scattering is considerably weaker through the elongated portion of the flute structure as indicated by the low time delays and consistency in the energy distribution over the doppler spread in both the *X*-pol. and *Y*-pol. cases. Furthermore, the addition of the

Kolmogorov phase cube structure significantly narrows the doppler spread and increases the time delay in both polarization cases. A clear reverse parabolic arc is present in the y-pol. case between a doppler of +/- 5 [1/km], not previously present when scattering occurred independently from the flute structure. The *x*-pol. case appears to have a faint reverse arc that fades out beyond 20 chips.

The plots in Figure 118 shows two distinct profiles of the doppler power spectrum between the flute phase cubes and the Kolmogorov phase cubes. In the flute cases, the doppler spread follows a Gaussian-like ("inverted-V" or "bell-shape") distribution in the amplitude of the spectra. The Kolmogorov case follows a Rayleigh or Rican distribution at the left and right edges of the total distribution creating an "upward-V" – shape at the center indicating significant broadening in the spread of the signal carrier. This demonstrates that the Kolmogorov structure causes more fading from its dense phase variations in comparison to the elongated portion of the flute structure. The V-shape in doppler spread is typically observed when scattered waves arrive at unique angles along the receiver. The two peaks in power occur at the observed maximum doppler frequency spread. As the anisotropy of the scattering medium increases, the spectral broadening grows and the severity in the fading increases, causing the "upward V-shape". Since the flute has a consistent density for each sample point along the elongated portion of the structure, the anisotropy is very low, and therefore does not broaden the power spectrum. The bell-shape in doppler spread is typical of the fading characteristics for scattering angles that do not substantially differ from one point to the next along the plane of the receiver.

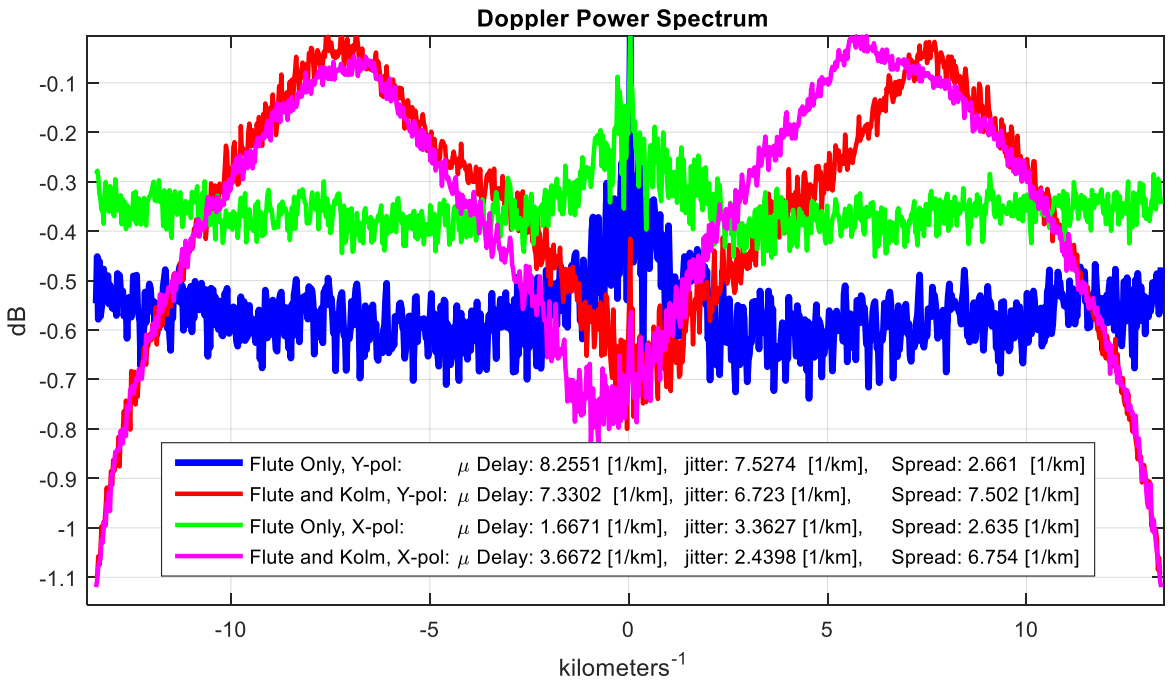

Figure 118. Doppler Power Spectrums for 0° azimuth and 155° elevation case

Despite the indifference of the density gradients along the elongation of the flute structure, the y-pol. case exhibits the most gradient changes as seen with the ray trace refraction of about 10° more in the y-direction compared to the x-direction. This translates to a 1.05 kilometer decline in the spatial coherence for the y-pol. in comparison to x-pol., as seen in Figure 119. The spatial coherence declines by 1 to 1.5 kilometers with the addition of the Kolmogorov phase cube for either polarizations. The frequency correlation in Figure 120 appears to be smooth and symmetric with additional distinct side lobes and nulls leaking out from the carrier at a shallow roll-off rate. The coherence bandwidth declines by ~1.2 MHz with the inclusion of the Kolmogorov phase cube. As the spectral resolution declines, spikes dominate the power level roll-off from the peak.

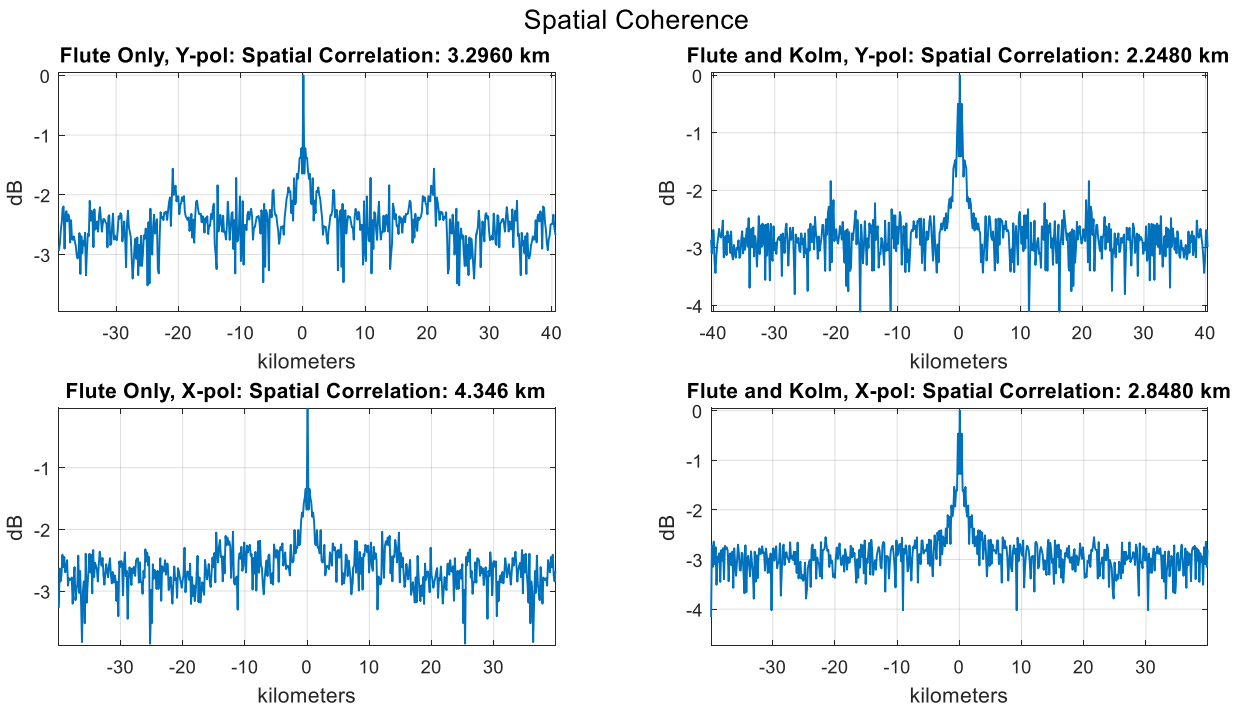

Figure 119. Spatial Correlation Distributions for 0° azimuth and 155° elevation case

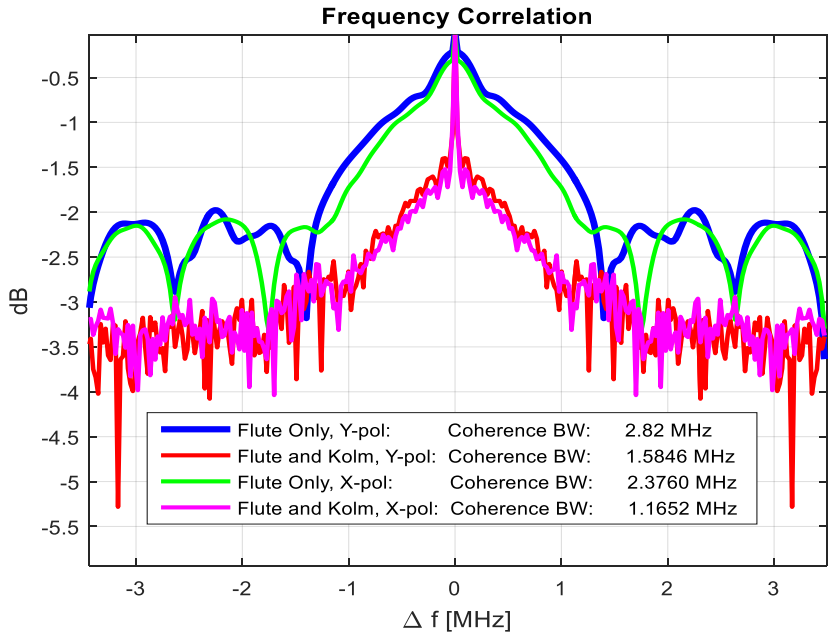

Figure 120. Frequency Correlation Distributions for 0° azimuth and 155° elevation case

These initial ray trace results reveal that the additional Kolmogorov structure can cause enhancement in the scattering conditions and its corresponding secondary calculations. The intriguing observation is the reverse parabolic arc over the doppler axis mirroring the primary arc. The additional phase contributions of the Kolmogorov structure increases the angular spread at the receiver, a possible cause for this phenomenon. The next ray trace example will further examine how these observations change with a more lateral ray trace propagation through the broadside of the flute structure where a bulk of the refractivity exists.

The second ray trace case involves a 0° azimuth and 105° elevation angle of a ray entering the flute structure as seen in the ray trace map of Figure 121. The ray deviates along the y-axis by 12.94° after initially entering normal to this axis. Figure 122 shows the scattering functions corresponding to the polarizations for flute structures and the cases of combined Kolmogorov structures.

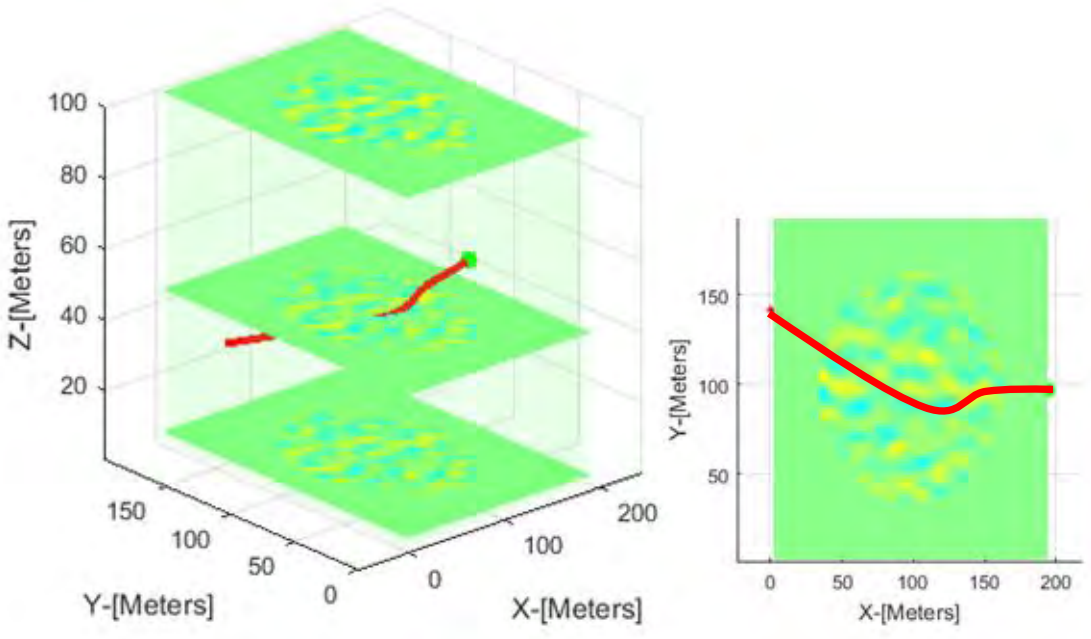

Figure 121. Ray Trace plots for 0° azimuth and 105° elevation case

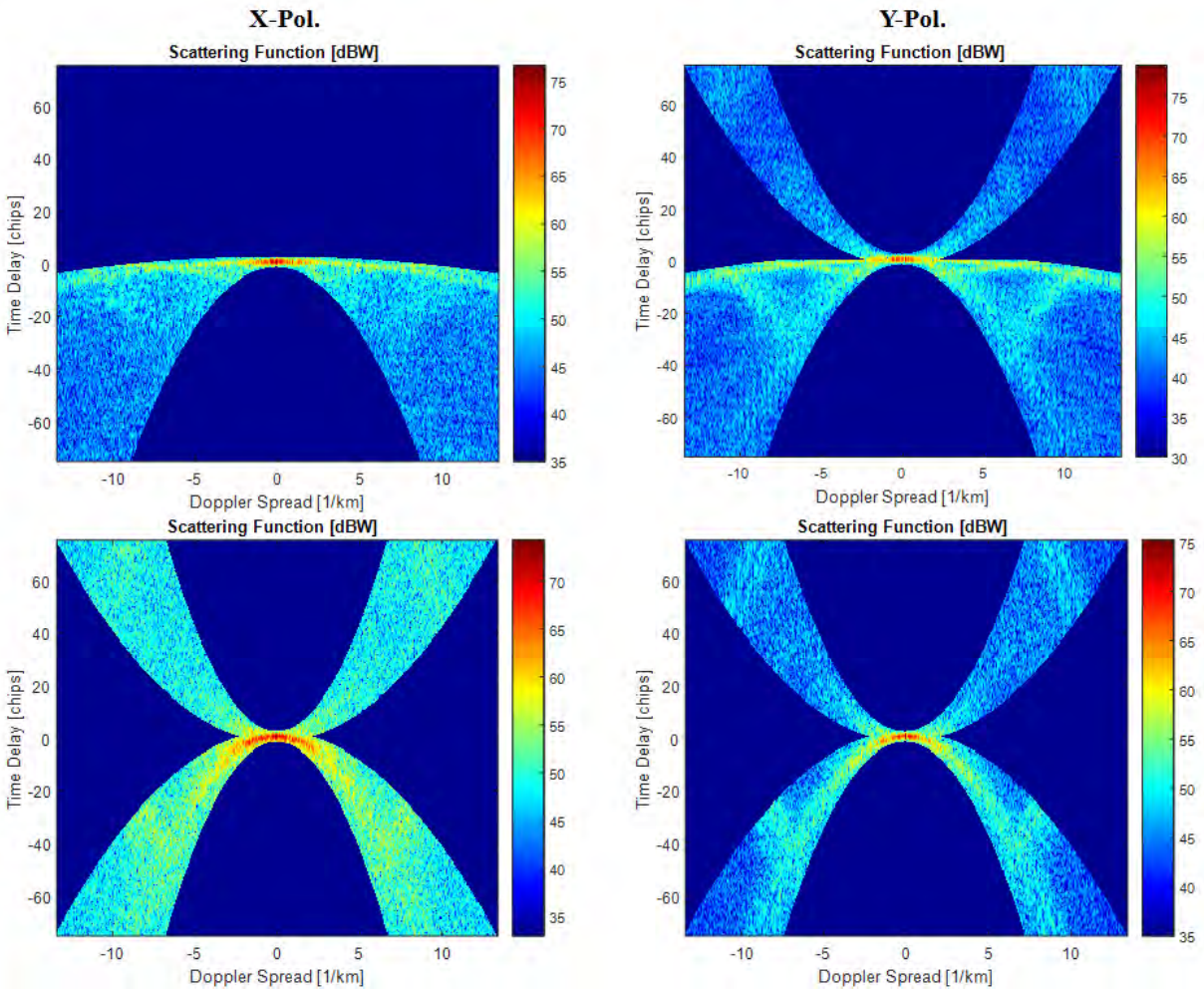

Figure 122. Scattering Functions for 0˚ azimuth and 105˚ elevation case, Flute Only presence (top), Flute and Kolmogorov presence (bottom)

The *x*-pol. scattering function delay-doppler map has a primary and a faint secondary arc over a large time delay, similar to the observations from the previous section. The energy is faintly dispersed in the region between these arcs. The *y*-pol. case has a clear, multi-fringe secondary arc and an additional faint arc mirrored over the doppler axis between +/- 7 [1/km] over a delay of 40 chips. This phenomenon has not been observed in previous simulations. In both polarizations, the addition of the Kolmogorov phase cube narrows the doppler spread of the energy (within +/- 10 [1/km]) over the time delay of 80 chips. The primary arc in the *x*-pol. case becomes enhanced

along with the narrowing doppler spread and a wider peak intensity between +/- 5 [1/km]. In the y-pol. case, the fringe patterns enhance by approximately 5 dBW. The reverse arc in the *y*-pol. case has a very minor energy spread enhancement while maintaining a similar doppler width and curvature to the primary arc.

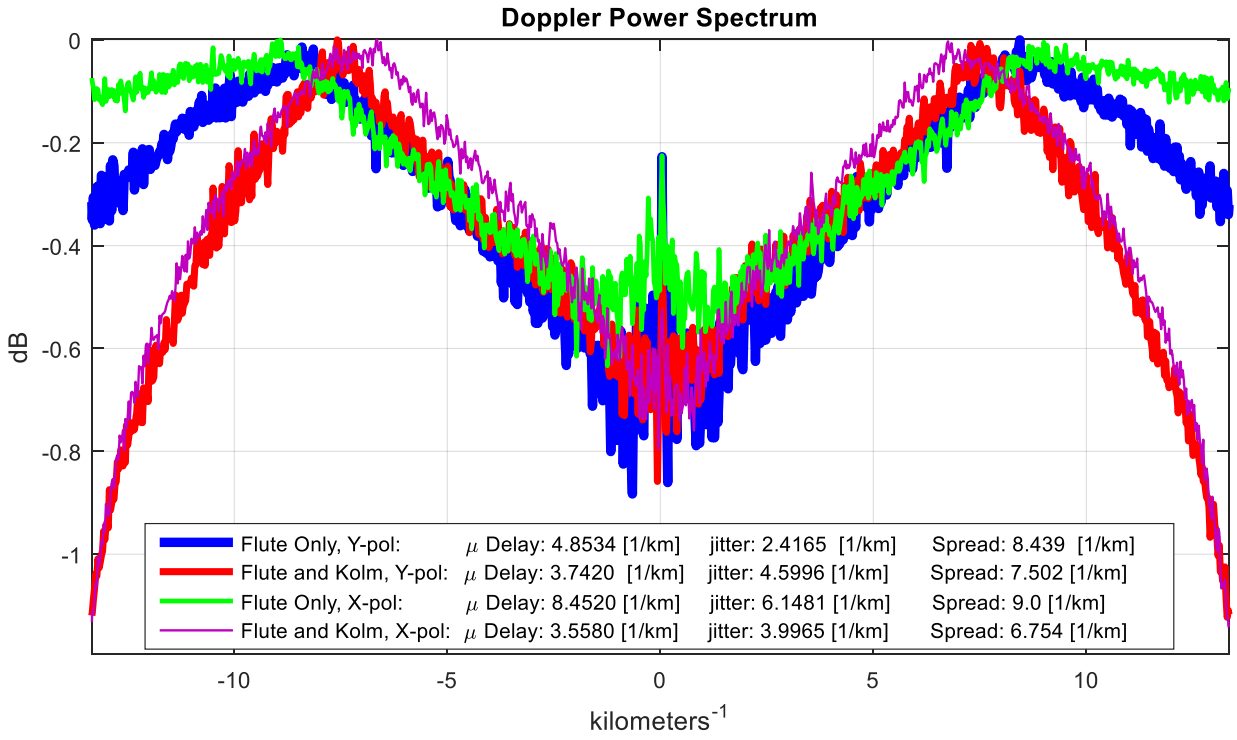

Figure 123. Doppler Power Spectrums for 0° azimuth and 105° elevation case

Examining the characteristics of the secondary calculations, Figure 123 shows the broadening of the doppler power spectrum. The *x* - pol. experiences the most doppler delay, jitter, and spread caused by the flute structure in the direction that experiences the most gradient density variations. The additional Kolmogorov phase cube narrows the doppler spread but causes greater decay rate in the doppler power beyond the peak. In Figure 124, the spatial coherence is the smallest in the *y*-pol. cases as observed previously, in which the 2.698 km corresponds to 1.8% of the total grid length of the

received field. Second order peaks in the power levels appear in the y-pol. case with the combination of flute and Kolmogorov structures.

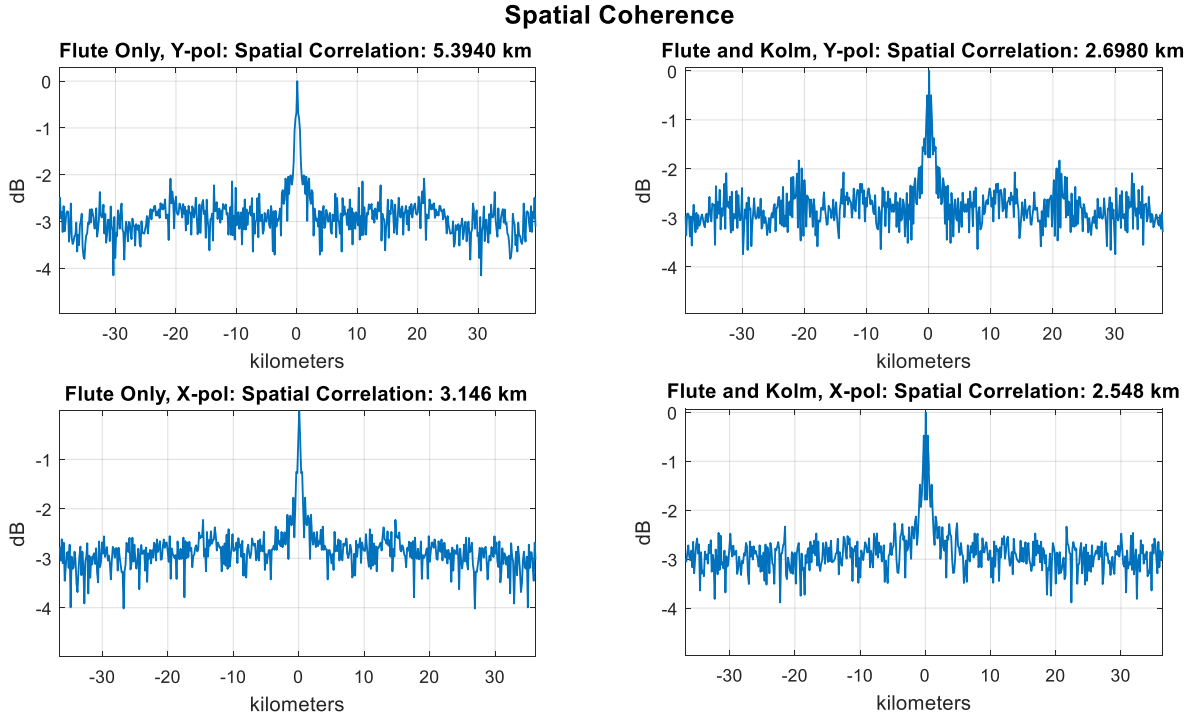

Figure 124. Spatial Correlation Distributions for 0° azimuth and 105° elevation case

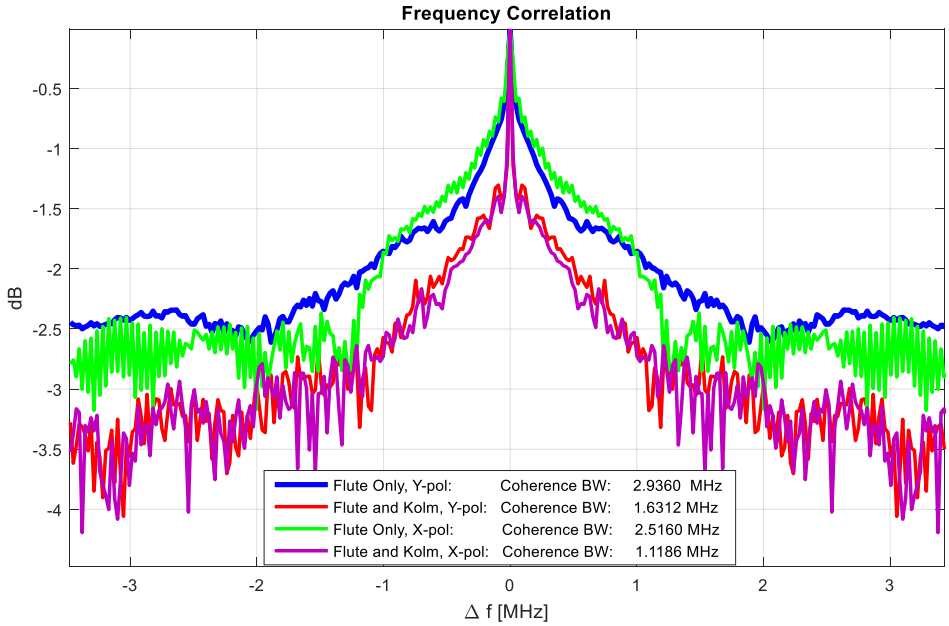

Figure 125. Frequency Correlation Distributions for 0° azimuth and 105° elevation case

The addition of the Kolmogorov phase cube causes the spatial coherence to decline further by 2.25 km in the *x*-pol. case and 0.15 km in the *y*-pol. case. In Figure 125, the frequency correlations reveal bandwidths less than 3 MHz, well within the criteria for a frequency selective channel. The Kolmogorov phase structure reduces the coherence bandwidth by around 1.3 MHz, very similar to the observation in the first ray trace example. The x-pol. cases exhibit the lowest coherence bandwidth as well. Spikes dominate the power roll-off at a greater decay slope in comparison to the initial ray trace example. Based on both ray trace results, it is evident that the flute structure creates the most influence on the slope decay rate of the frequency correlation spectrum. The addition of the Kolmogorov structure causes a ~1 dB decline in the power levels away from the peak.

The most intriguing observation is the continued presence of the reverse parabolic arc mirrored over the doppler axis. In this example, the arc was present without the addition of a Kolmogorov structure, indicating that the rapid phase variations along the lateral portion of the flute density map could be a major influence as they were in general for the Kolmogorov structure. The following ray trace example reduces the gradients of the density map by applying a single flute structure at the same incident azimuth and elevation angles as the previous example. Figure 126 shows the ray bending along the y-axis at an angle of 18.03°, as it passes through the positive and negative density perturbation gradients.

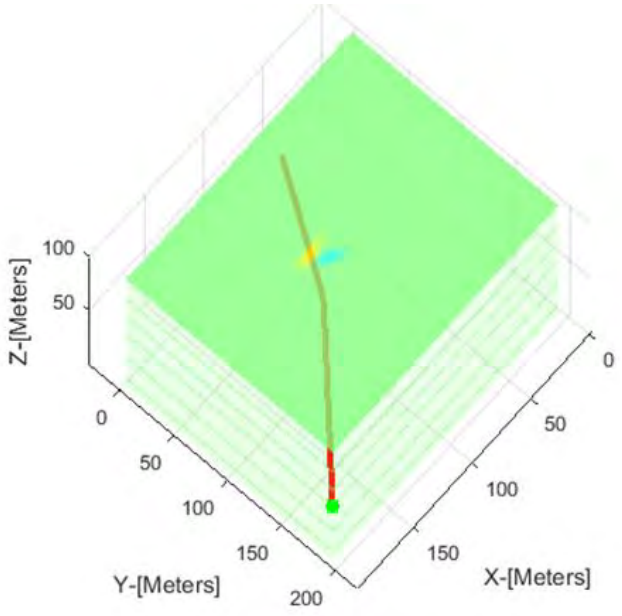

Figure 126. Ray Trace plots for 0° azimuth and 18.03° elevation case

An addition to this analysis is to examine various regions of the 2D plane of the received field to determine how regions of the diffraction profile can alter the scattering function and its secondary calculations. The y-pol. case is of most interest because it has a greater variety of intensity variations occurring at the top and bottom edges of the flute at broadside as shown in Figure 127.

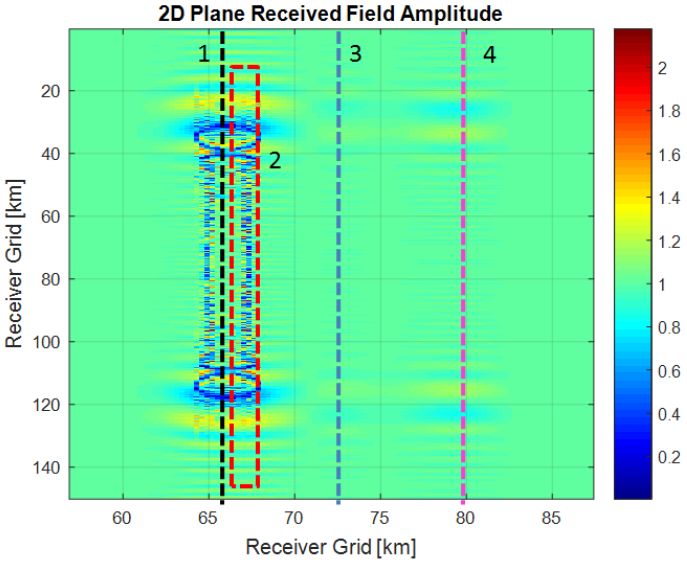

Figure 127. Four Evaluation Regions of the Y-Pol., 2D Amplitude Realizations

There are four regions evaluated along the vertical axis of the receiver grid. The first region accounts for the peak intensity fluctuations caused by the edge diffraction without cross interference. The second region includes an intense cross interference pattern with sharp fluctuations over a widespread portion of the receiver grid. This is created from the positive portion of the flute density perturbation. The third region is at the center of the grid and in between the two regions of diffraction caused by the positive and negative portions of the flute density perturbation. The fourth and final region is the central portion of the edge diffraction caused by the negative perturbation in the flute density. The global amplitudes of the received field over the bandwidth of the signal is shown in figure 128.

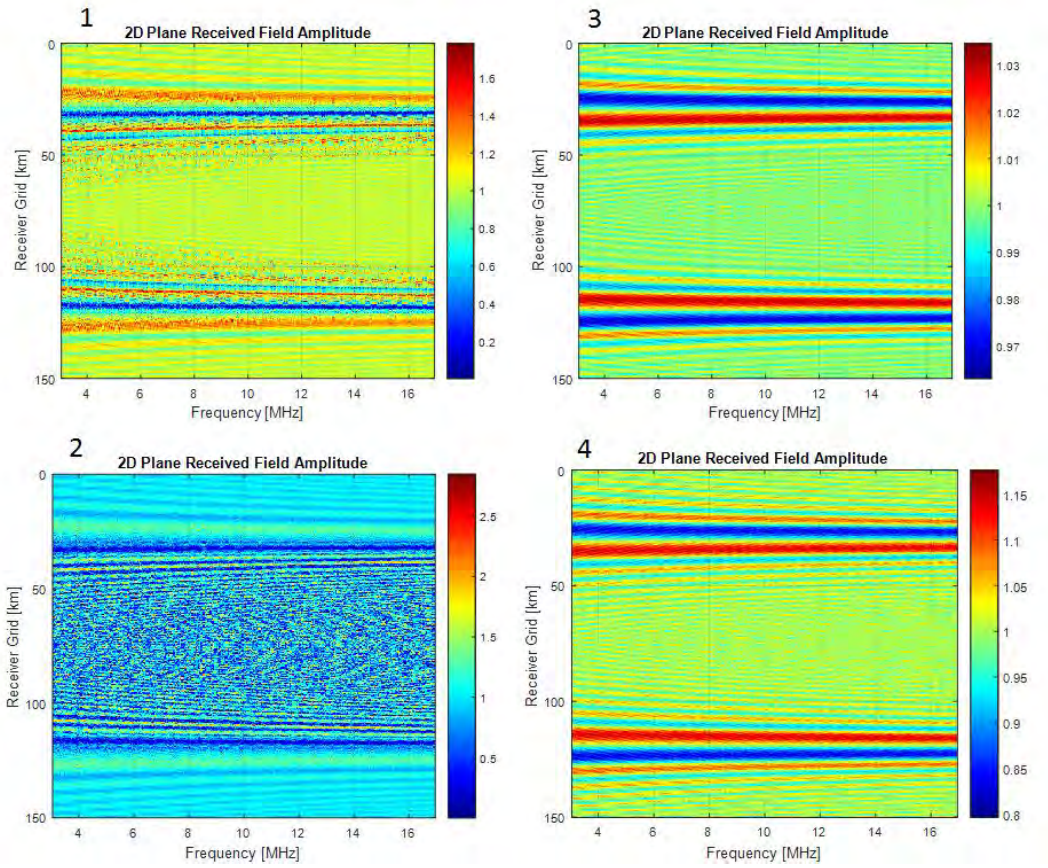

Figure 128. Dynamic Spectrum of each of the four Evaluation Regions

The dynamic spectrum of regions 1 and 2 reveal that the diffraction pattern growth originating from the top and bottom edges of the flute eventually achieves a peak intensity across the entire spectrum. As the frequency of the band increases, the secondary amplitude patterns appear to bow outward with continuity at the central region between the primary diffraction pattern at the edges. Regions 3 and 4 are similar in diffraction patterns over the spectrum, with region 4 having a slightly greater intensity. The corresponding scattering functions and mutual coherence functions are shown in figures 129 and 130.

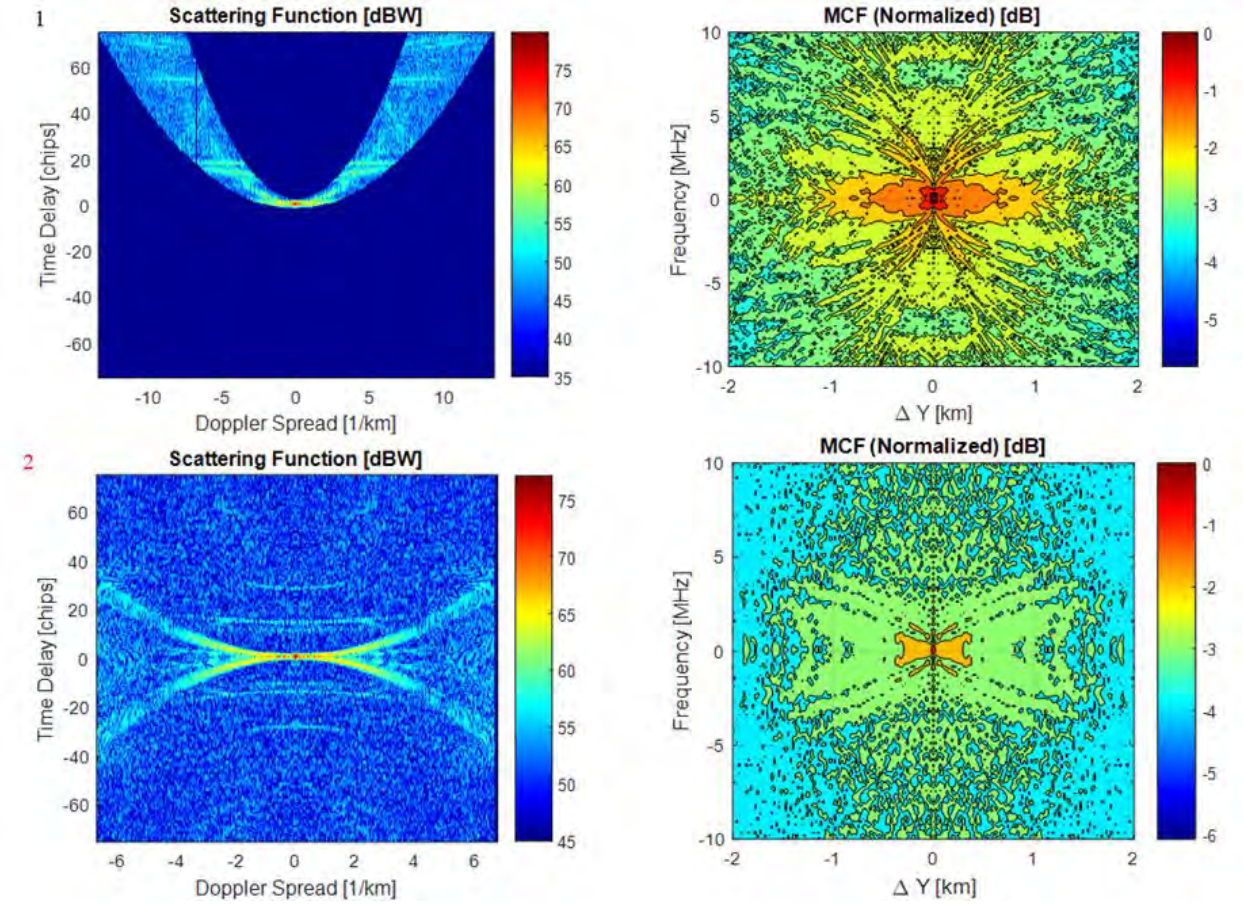

Figure 129. Scattering Functions (left) and Corresponding Mutual Coherence Functions (Right) Regions 1 and 2

In region 1, two parabolic arcs are observed distinctly between +/- 5 [1/km] and continue to disperse over an 80 chip time delay. In region 2, a clear identical parabolic arc is mirrored across the doppler axis. Very faint small second order arcs appear to be mirrored over the doppler axis as well. The mutual coherence plot shows considerable degradation in the power levels with respect to frequency and spatial resolution in comparison to the region 1 mutual coherence function. Region 4 has a more intense power spectrum over the parabolic arc compared to region 3. This greater intensity is accompanied by narrower spatial and frequency correlations.

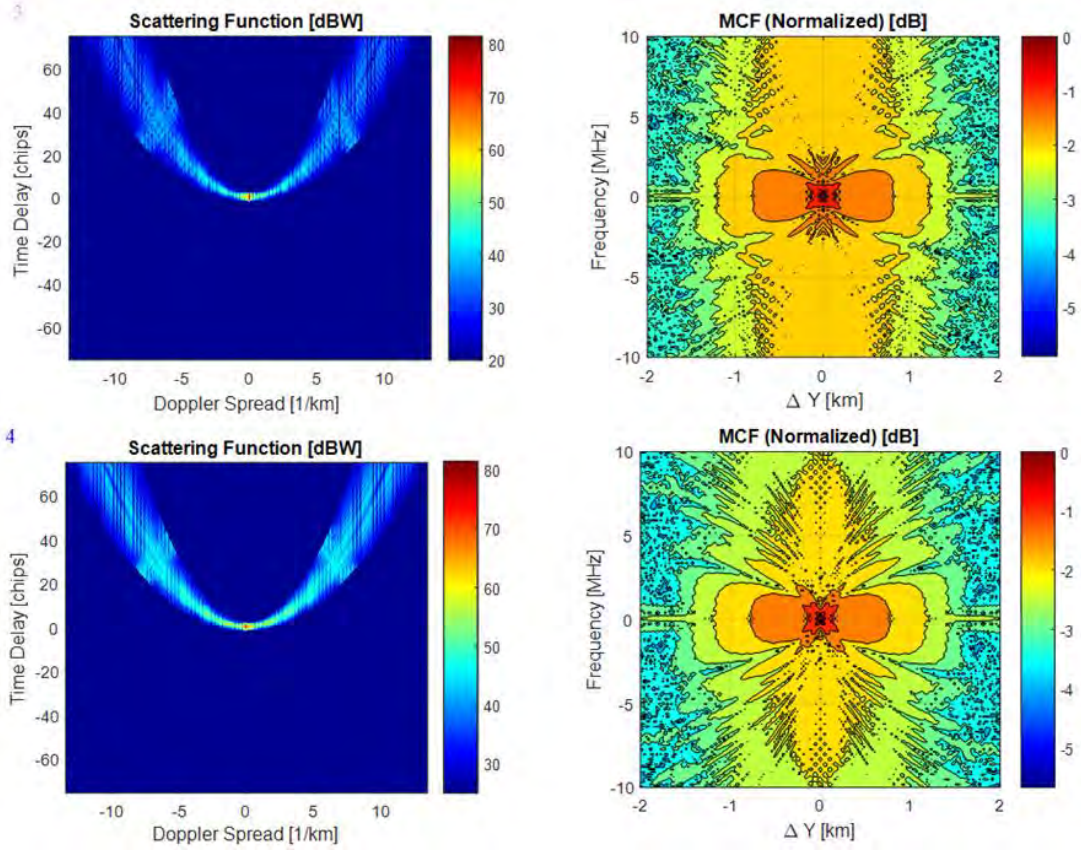

Figure 130. Scattering Functions (left) and Corresponding Mutual Coherence Functions (Right) Regions 3 and 4

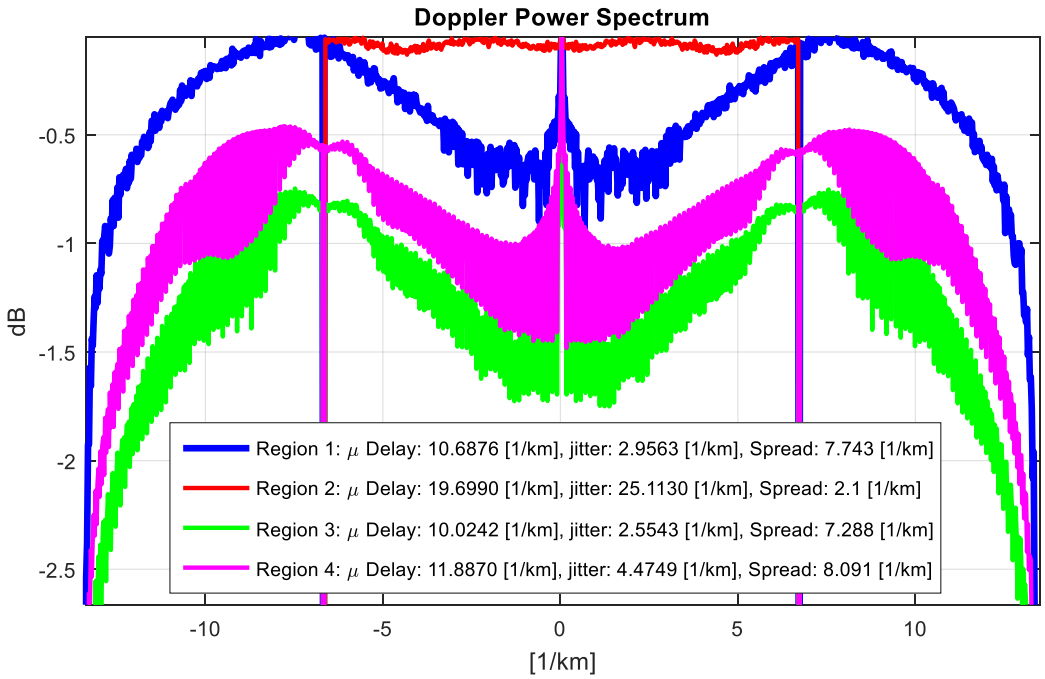

Figure 131. Doppler Power Spectrums corresponding to each region

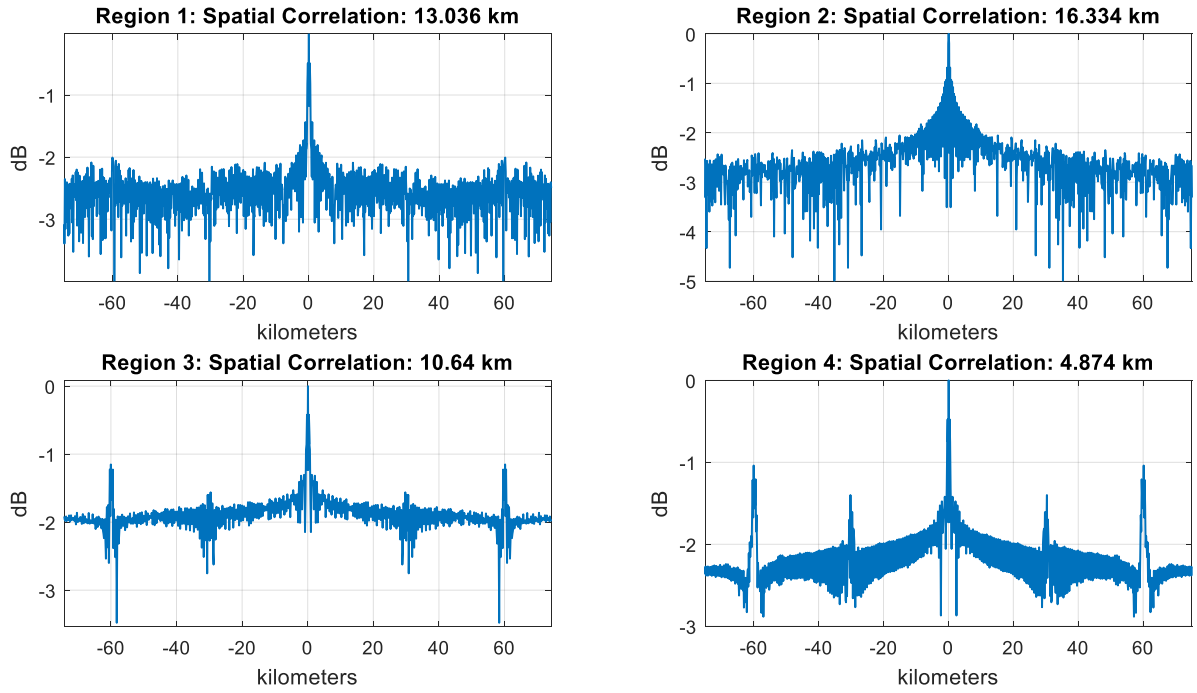

Figure 132. Spatial Correlation Distributions corresponding to each region

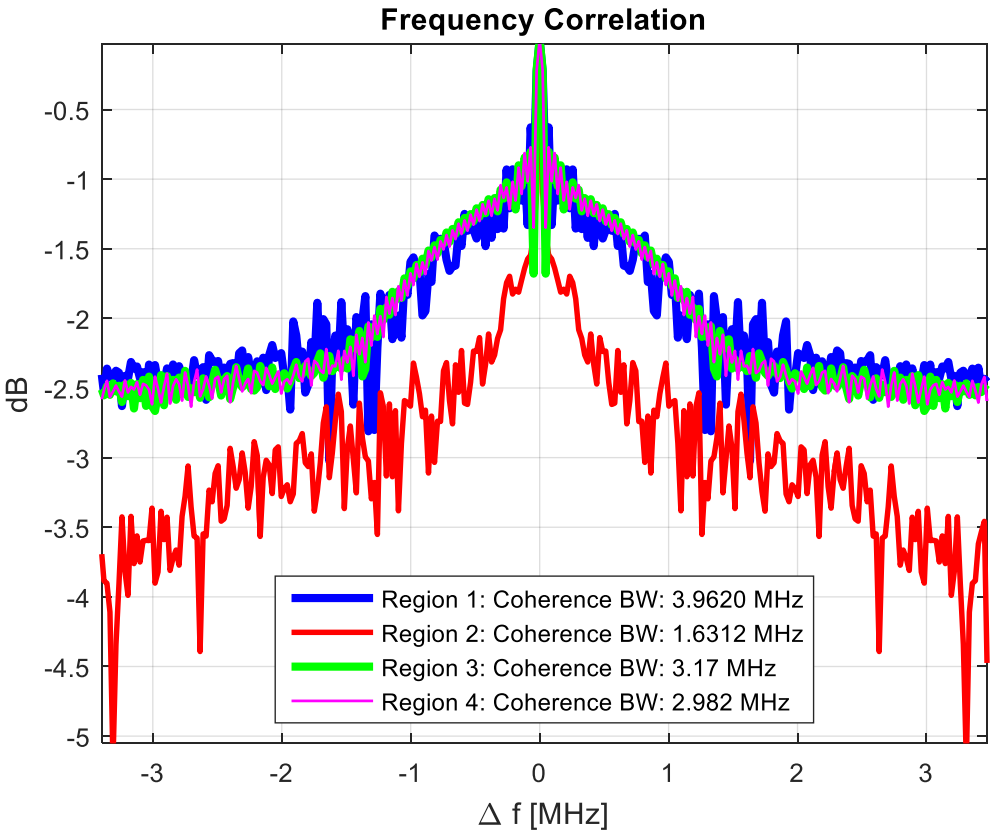

Figure 133. Frequency Correlation Distributions corresponding to each region

Figure 131 shows the doppler power spectrums for each region. Region 2 has the smallest doppler spread and the largest doppler delay and jitter. The spectral broadening is not as significant in comparison to the other results. The spread can be described as sinusoidal whereas the other doppler power amplitudes follow the Rayleigh distribution at the left and right edges. The other regions have relatively comparable doppler spread, delay, and jitter. Another feature of region 2 is that the spatial coherence is the largest. Regions 3 and 4 have second order peaks with nearly identical spatial coherence widths as the first order peaks. In the frequency correlation plots of Figure 133, the region 2 power spectrum exhibits the steepest decay in the peak power, in addition to the lowest

coherence bandwidth while the other regions, comparably, have a broader spectrum.

Additional results are presented in the following figure sequence:

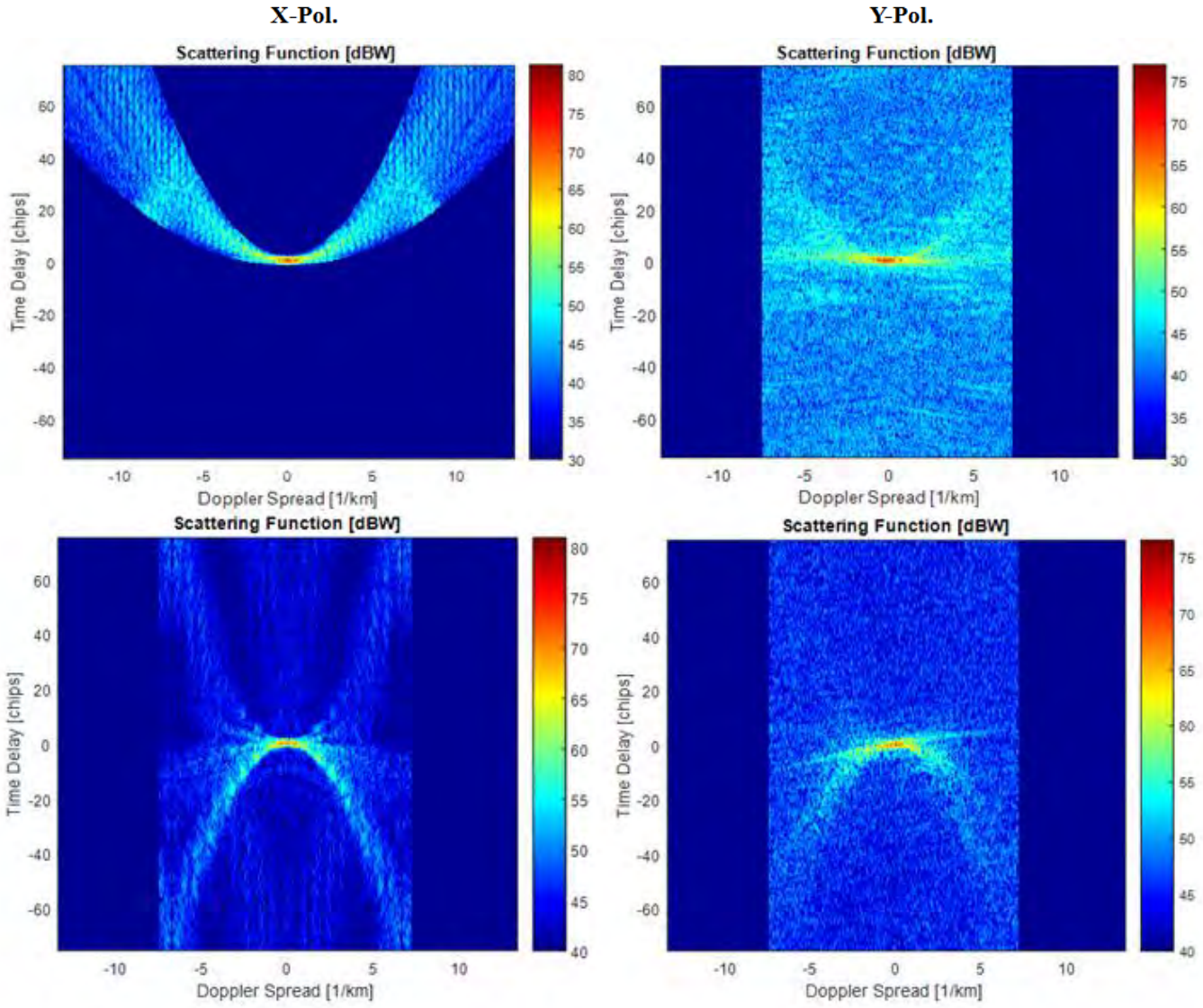

Figure 134. Scattering Functions for 10 MHz Carrier, 180° azimuth and 90° elevation case, Flute Only presence (top), Flute and Kolmogorov presence (bottom)

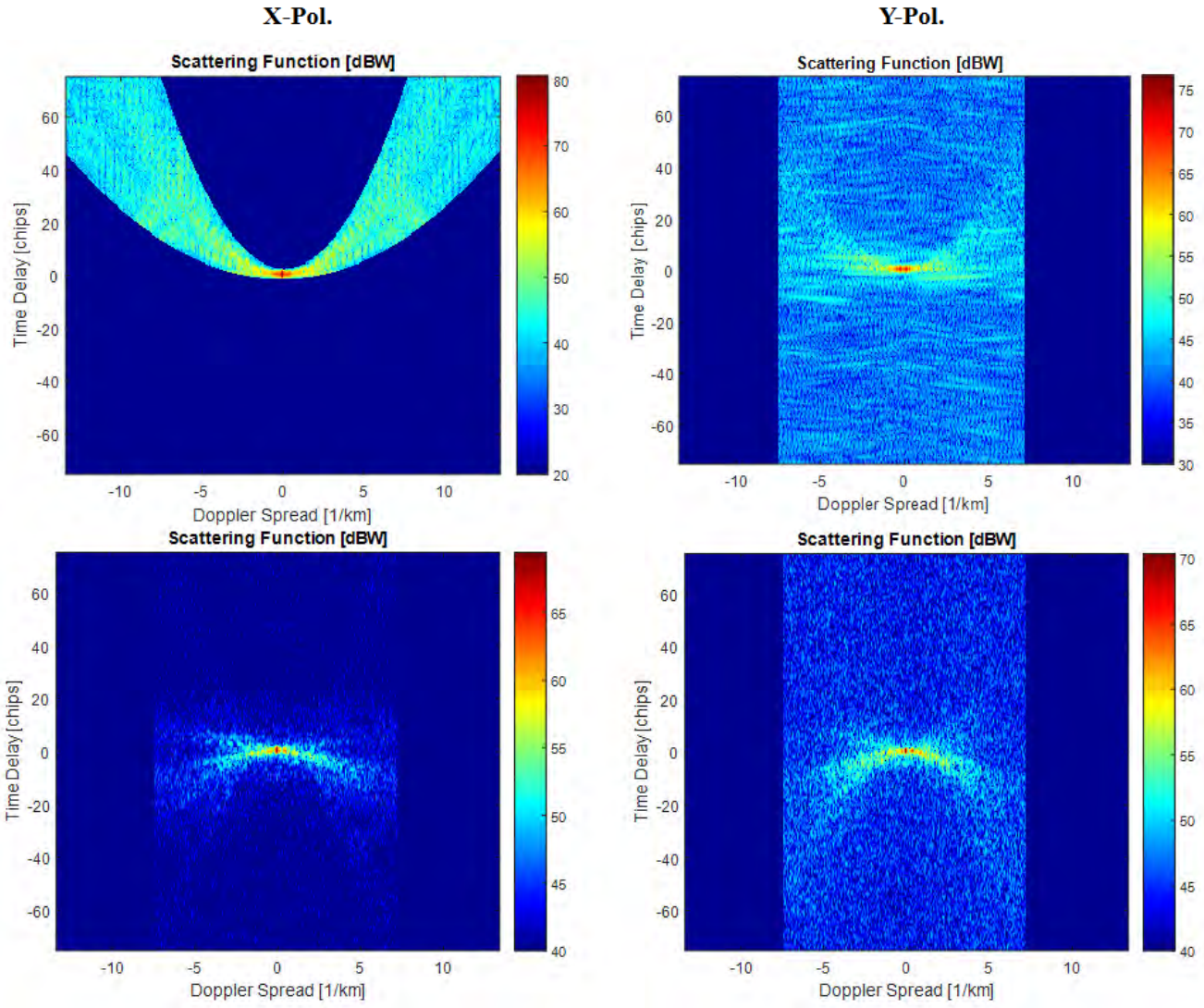

Figure 135. Scattering Functions for 10 MHz Carrier, 90° azimuth and 90° elevation case, Flute Only presence (top), Flute and Kolmogorov presence (bottom)

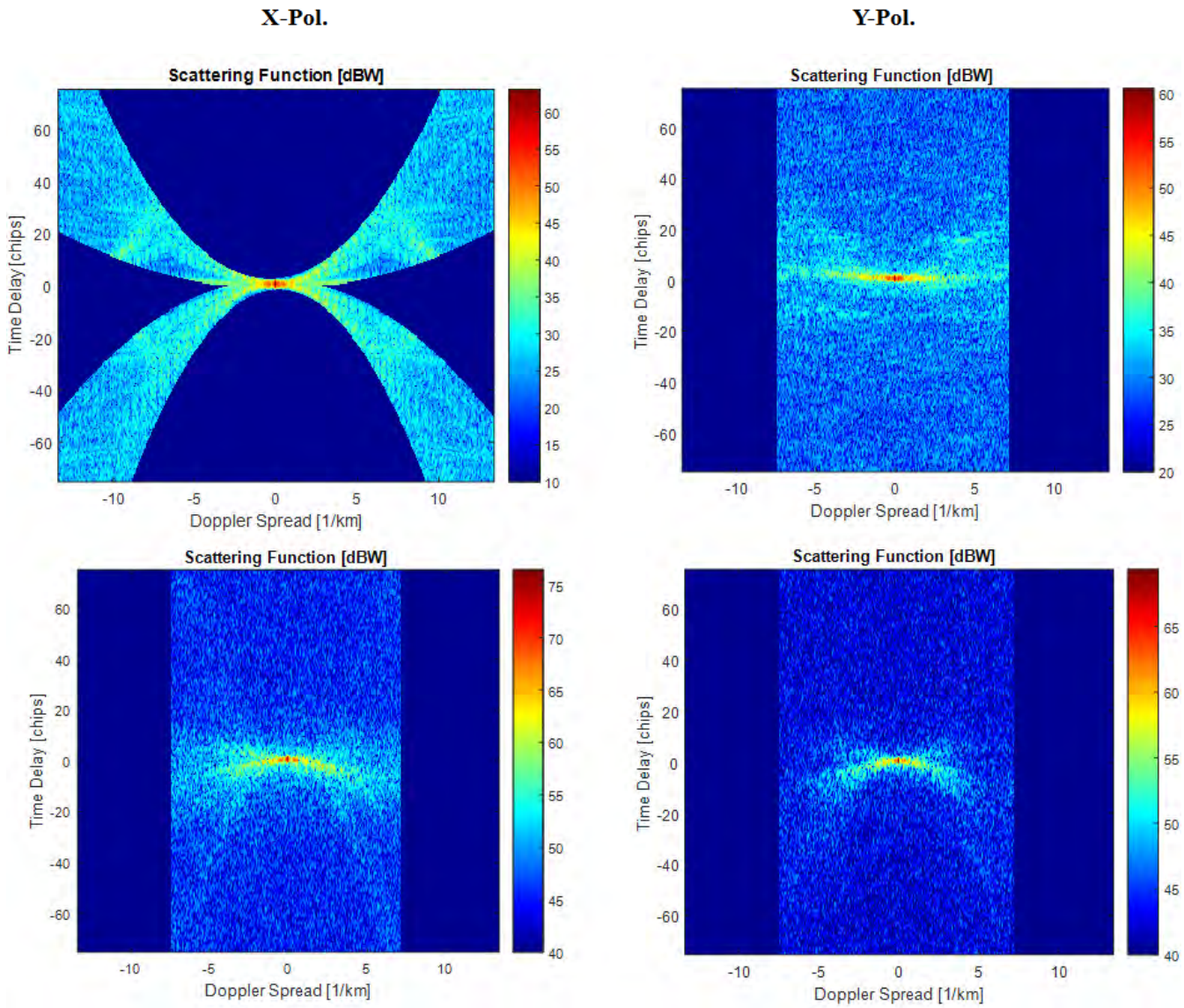

Figure 136. Scattering Functions for 10 MHz Carrier, 45˚ azimuth and 90˚ elevation case, Flute Only presence (top), Flute and Kolmogorov presence (bottom)

5.3 Summary

In summary, the results from all these ray trace tests demonstrated that the propagation orientation with respect to the density gradients of the flute can cause significant differences in the scattering functions in a similar manner as the scintillation

indices observed in the pulse coherence results. The intensity of the parabolic arcs in the scattering function is a decent indicator of the spectral broadening in the doppler power spectrum. The spatial coherence and frequency correlation will narrow for high power levels in the energy distribution across the scattering function delay-doppler. The density gradients of the flute perturbation will impact the decay rates of the power spectrum. Gradual phase changes caused by the elongation portion of the density perturbations can broaden the power spectrum and create distinct side lobes with small decay rates. The rapid phase changes along the lateral portion of the flute structure leads to a rapid decay rate from the peak intensity and the coherence bandwidth reduces as well. The addition of a Kolmogorov structure generally narrows the coherence bandwidth and spatial coherence, and steepens the decay rate of the doppler spectrum.

The additional analysis of the dynamic spectrum of the 2D field realization plane demonstrated that in the y-pol., the top and bottom edges of the flute structure creates a cross interference pattern that propagates with an increase in the frequency band. This is the key phenomenon that reveals a definitive reverse parabolic arc over the doppler spectrum. In other cases, the reverse arc is not present as the edge diffraction does not cross-interfere over the frequency spectrum. Further review of literature related to the parabolic arc phenomenon, [28] addresses the phenomenon by initially determining the angular spectrum of plane waves or scattered brightness distribution. They conclude that the narrow thin arc structures imply that this brightness distribution is highly anisotropic (elongated) and that some of these scintillation arcs arise from 1D features of the deflecting structures as seen in projections. Evidence of this phenomenon can be observed in Figure 137, showing an interstellar scintillation observed at the Arecibo

Observatory pulsar B1133+16 from the first half of 2015: left at 1450 MHz, middle at 432 MHz, and right at 327 MHz.

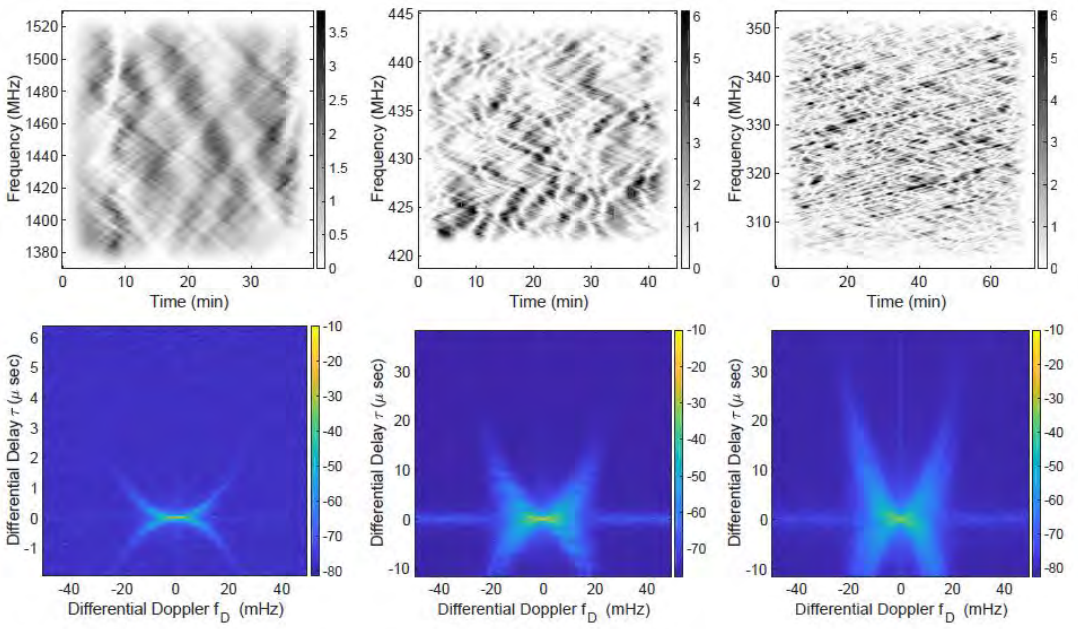

Figure 137. [29] Dynamic Spectrums and Scattering Functions from pulsar B1133+16, 1450 MHz (left), 432 MHz (middle), and 327 MHz (right).

The top portion are the dynamic spectrums corresponding to the scattering functions below. The forward arc occurs as the angular brightness decreases away from its maximum near the origin where the relatively unscattered wave interferes with the scattered waves. The narrow arcs correspond to a very anisotropic brightness distribution. The reverse arcs are caused by isolated peaks in the brightness offset from the origin that interfere with the waves scattered from the core. Another source, [29], mentions that the existence of discrete reverse arcs as due to the discrete peaks in the scattered brightness interfering with an extended halo. These isolated peaks are expected due to speckle in the scattered image. This speckle pattern is apparent in the 2D plane field realization (region 2) of Figure 128 and explains the phenomenon observed.

VI. CONCLUSION AND FUTURE WORK

6.1 Conclusion

The critical ionospheric F-layer flute instability effects on electromagnetic wave propagation has been characterized from a unique phase cube coupled ray tracing approach to efficiently propagate an incident field over a variety of aspect angles and polarizations. Applying an MHD approach to create zonal and shear flows and macroscopically modify the ideal flute structure generated a subset of unique flute structures required to observe the broad effects that the interchange process may have on the scattering characteristics of an incident electric field.

The phase power spectrum of these flute structures were calculated numerically through autocorrelation and fourier transform techniques. Unique Gaussian realizations of their power spectrums were averaged and inverse fourier transformed to yield distinct two dimensional phase screen realizations of the flute perturbations. The phase screen representation of each flute revealed the unique influence that each sampled flute structure has on the stochastic flute map characteristics such as curvature and global orientation. A variety of these stochastic maps were selected for testing based on their unique density gradient characteristics and power spectrum features.

The phase cube concept was introduced to include the elongated geometry portion of the flute structure that exists in nature when the growth of the perturbation occurs along the geomagnetic field lines during drift instability. Using the application of two-dimensional phase screens, the phase cube was constructed by sampling the 3D flute perturbation in the *X*-*Y*, *X*-*Z*, and *Y*-*Z* planes. This phase cube geometry allowed for a

characterization of horizontal and vertical polarizations effects on the electromagnetic scattering calculated from a modified form of the 2D slow varying envelope propagation algorithm. Pseudo spectral methods were implemented to numerically solve the parabolic and hyperbolic forms of this second order homogenous differential equation. Coupling the ray tracer and the phase cube technique involved conditional algorithms to orient the 2D phase screens according to the ray entry point. The gradient descent concept was applied to calculate the ray vector trajectory along the propagation path as influenced by the refractive properties of the density perturbation gradients within the phase cube. The azimuth and elevation angles update the vector components of the electric field magnitude distributed along the x, y, and z propagation directions, and recombined using vector analysis after propagation through the phase cube is complete.

A one-dimensional pulse coherence model was developed to examine the temporal characteristics of a SSB-SC modulated carrier passing through a 2D flute density map. Observations were made from comparison to a full wave model that applied Maxwell's equations and accounted for the flute structure's material parameters. It was determined in the high frequency spectrum that significant backscatter occurs in the incident field due to the comparable wavelengths to the physical size of the flute, effecting the phase and coherence of the received field. Results from the pulse coherence model demonstrated a vast range of scintillation indices can occur depending on the stochastic flute map applied and the direction of propagation. These variety of scintillation indices indicated weak and strong scattering regimes. Weaker scattering regimes corresponded to isolated flute structure density maps or organized arrays of flute structures that could primarily exist during the linear stages of the interchange process.

The stochastic flute maps, representing the nonlinear interchange process, caused moderate and severe cases of scattering, demonstrating that it is not practical to conclude a particular scattering regime for the presence of flute structures based on primary ionospheric measurements such as the S4 metric. The stochastic flute maps also demonstrated that pulse time delays can be observed up to a full pulse width shift and the corresponding coherence bandwidths are predominantly indicative of a frequency selective channel. In fact, the channel did not show any distinct relationship in results for the variety of frequencies tested in the HF spectrum. The cases of single flutes or flute array maps observed much more notable relationships between the increase in carrier frequency and the corresponding scintillation and temporal results. In these cases, often, the coherence bandwidths were above the signal bandwidth, indicating a flat fading channel.

The scintillation and temporal results demonstrated that the important features to consider are the alignment of the flute's positive and negative perturbed stagnation points with respect to the direction of propagation, and the quantities of flute structures within a given density map. The flute array maps revealed results comparable to the isolated flute maps despite the fact that there were significantly more flute structures present. Based on the variety of flutes examined, the most significant scattering occurs where the interior separatrix had minimal overlap between the stagnation points in the direction of propagation. If these flutes interact with neighboring flutes that are not aligned along the optical path of the preceding flute structure, the staggered arrangement causes the edge diffraction to cross interfere, creating the most significant amplitude and phase

fluctuations in the incident field, translating to higher scintillation, time delay, and decreased coherence bandwidth.

Re-examining the total phase power spectrum calculations revealed that the unique, staggered flute structures in the stochastic flute map produced the highest magnitude at the plateau of the spectrum prior to decay over higher wave numbers. Under these conditions, the phase changes are more cumulative and constructive. As the slope steepens in the decay of the power spectrum, the small scale structures have less contribution to the phase change of the incident field. This is not only dictated by the slope of the decay in the strength of the phase variations, but also the location of the maximum wavenumber where the peak of the plateau begins to roll-off. If the slope is relatively shallow, the flute structure perturbations maintain relative consistency in the phase effect amongst all the irregularity scale sizes within the density map.

The scattering functions observed in the pulse coherence results revealed multi-fringe doppler-delays at low frequencies that merged into primary and secondary arcs at the higher frequencies. A direct relationship between the increase in frequency and decrease in the time delay of the doppler shifted energy was observed. The orientation of the stagnation points within the flute structure translated to the energy doppler-delay symmetry at the receiver. Applying the stochastic maps created the most significant fringe patterns. The attributes of the fringe patterns include rapid phase changes or increased refractivity along the propagation path. An additional revelation is that the wider band pulses exhibited the most severe cases of scattering, even for a carrier frequency at the high end of the HF spectrum, re-enforcing the frequency selective characteristics of the stochastic flute map channel.

In the application of the phase cube coupled ray trace model, the secondary calculations from the scattering functions revealed similarities in the stochastic and single flute maps. Initial testing involved propagation in the x, y, and z directions without application of the ray tracer. On average, the stochastic flute map cause the most extreme cases of time delay, jitter, coherence bandwidth, doppler spread, doppler delay, doppler jitter, and spatial coherence. However, examining the spread in the data over the propagation distance reveals that in the isolated flute cases, some of the extrema of these metrics may exceed the results from the stochastic flute map cases. These observations are dependent on polarization and propagation direction. The extra dimension creates a more complete profile of the flute structure that was not previously present in the pulse coherence model. The propagation through the phase cube involves a 2D wavefront plane that exhibits additional scattering features that were not accounted in the 1D propagation model.

The incorporation of the ray tracer allowed for angular incidence on the phase cube. A couple ray trace examples demonstrated incidence into the topside or broadside portions of the flute structure. The Kolmogorov phase cube was also included in these simulations to observe the changes in the scattering function characteristics. Results demonstrated the spectral broadening of the doppler spectrum along the propagation path with the most significant gradient changes in the density perturbation, causing Rayleigh shapes on the left and right edges of the doppler power spectrum. The spatial and frequency correlations narrow with inclusion of the Kolmogorov phase cubes, increasing the phase variations that causes stronger scattering along the propagation path. An interesting observation in these simulations was the observation of reverse parabolic arcs

mirrored over the doppler spectrum, especially in the y-polarization cases. This was examined further using a simplified single flute phase cube to distinguish the scattering phenomenon observed at the 2D receiver plane. The y-pol. has created the most intriguing scattering phenomenon with respect to the flute structure geometry and was therefore applied in the analysis. The results showed that these reverse arcs are likely caused by the propagation of cross interference or overlapping amplitudes in the dynamic spectrum across the entire bandwidth of the carrier signal.

6.2 Future Work

This dissertation has provided a foundation in the computational modeling of flute structures and the application of propagation algorithms to characterize the scattering phenomenon. As mentioned previously, the results are of qualitative value more so than quantitative due to the lack of comparison to real world measurements. The next step in this research is to perform real world data collections in ionospheric measurements of high frequency scattering caused by the presence of flute structures at available observatories around the world. A variety of geographic locations can possibly provide more measurable features of the flute structure as its declination angle will vary along the geomagnetic field line. Additional measurements shall include pulsar radiation, incoherent scatter radar (ISR), radio occultation (RO), and SATCOM to measure a variety of incidence aspects. Taking multiple forms of measurements is especially crucial as this research has revealed when examining a variety propagation orientations with respect to the gradients of the flutes. A key challenge to this is accounting for other instabilities that might be present during the data collection. In fact, the complexity of the

interchange process may trigger other instabilities that involve the gravity driven Rayleigh Taylor or velocity shear driven Kevin Helmholtz. The dynamic nature of the ionosphere makes this a difficult task. Alternatively, the interchange instability can possibly be controlled in a lab setting if conditions for this instability can be created on a smaller scale.

Many aspects of this research should be further explored to improve the results from the pulse coherence and phase cube models. Efficient and abundant computational memory and processing would improve the fidelity of the phase screens and phase cubes by increasing the sample points along the flute structure. A severe limitation was the time it takes for simulations to execute, thus limiting the test matrix in terms of the variety of density maps that could be evaluated. This was also a limitation for the full wave model and the propagation distances covered. The backscatter phenomenon should be further investigated and evaluated to determine scattering functions and their associated secondary characteristics. Improved computational performance can also allow for more multiple phase screen simulations at shorter propagation distances when applying the hyperbolic wave equation that is absent of the paraxial approximation (valid for sufficiently long propagation distances). This was a key reason for conducting the test matrices over hundreds of kilometers beyond the propagation channel.

The creation of flute density maps could involve treating the plasma behavior as two-fluid if macroscopic behavior is desired. If observatory data results demonstrate some correlation to the model results, a kinetic behavior method such as particle-in-cell (PIC) should be considered to further the precision of the plasma's evolution during the interchange instability. The pulse coherence model was limited to investigating amplitude

modulation of the received field realizations. Other analog modulation schemes should be investigated such as phase (PM) and frequency (FM), followed by digital schemes such as QAM, BPSK, and QPSK. The phase cube - ray trace coupling should be optimized by perhaps applying alternative ray trace techniques and phase screen sampling along the propagation path. Polarization techniques should also be further explored as the propagation algorithm interacts with the phase screen. This could reveal other types of scattering function doppler-delay features that are otherwise not apparent in the current models.

The key beneficiary of this research effort is the Air Force Research Lab (AFRL/RYMF) Plasma Physics Lab. Through continued computational model enhancements and observatory data collections, the AFRL team can further their objectives to characterize critical instability mechanisms in the ionosphere and develop environmentally assured Electronic Warfare systems that rely on transionospheric propagation.

APPENDIX A. Plasma Parameters and Single Fluid MHD Calculations

A.1 NRL Plasma Formulary

Table 4 displays the plasma parameters are applied to model the plasma conditions of the flute as referenced in the NRL Plasma Formulary [27].

Flute Velocity		0.65	cm/sec
Magnetic Field		0.3	Gauss
Gravitational Acceleration		500	cm/sec^2
Electron Number Density	n_e	6×10^6	1/cm^3
Ion Number Density	n_i	6×10^6	1/cm^3
Electron Temperature	T_e	0.026	eV
Ion Temperature	T_i	0.026	eV
Average Atomic Weight (ion)		16	
Density Scale Length	λ_D	1/(3e4)	cm
Total Density	$d_n = n_e + n_i$	1	Fractional Magnitude
Decay Factor:		0.8	
Cold Ar - Ar + Cross Section		1×10^{-14}	cm^2
Neutral Density	$D_n = \frac{2.6868\times10^{19} P_n}{760}$	3.5353×10^{16}	1/cm^3
Electron Plasma Frequency	$\omega_{pe} = 5.64\times10^4\sqrt{n_e}$	1.3815×10^8	rad/sec
Ion Plasma Frequency	$\omega_{pi} = 1.32\times10^3 Z\sqrt{n_i/\mu}$	8.0833×10^5	rad/sec
Electron Gyroradius	$r_e = 2.38\sqrt{T_e}B$	1.2792	cm
Ion Gyroradius	$r_i = 1.02\times10^2\sqrt{\mu T_i/BZ}$	219.2934	cm

Debye Length	$\lambda_D = 7.43\times10^2\sqrt{T_e/n_e}$	0.0489	cm
Electron Trapping Rate:	$V_{Te} = 4.19\times10^7\sqrt{T_e}$	6.7562×10^6	sec^{-1}
Ion Trapping Rate	$V_{Ti} = 9.79\times10^5\sqrt{T_i/\mu}$	3.9465×10^4	sec^{-1}
Electron Gyrofrequency	$\omega_{ce} = 1.76\times10^7 B$	5280000	rad/sec
Electron Plasma/Gyrofrequency Ratio	$\frac{\omega_{pe}}{\omega_{ce}}$	26.1650	ratio
Ion Cyclotron Frequency	$\omega_{ci} = 9.58\times10^3\frac{B}{\mu}$	179.6250	rad/sec
Sound Speed:	$C_s = 9.79\times10^5\sqrt{T_e/\mu}$	3.9465×10^4	cm/sec
Lower Hybrid	$\omega_{LH} = \sqrt{\frac{\omega_{pi}^2}{1+\omega_{pe}^2/\omega_{ce}^2}}$	3.0871×10^4	rad/sec
Alfven Velocity	$V_{Alf} = 2.18\times10^{11}\left(\frac{B}{\sqrt{\mu n_i}}\right)$	6.6749×10^6	cm/sec
Ion-Neutral Collisional Frequency for Ar+	$\eta_{AR} = n_o\rho_{AR}V_{ti}$	1.3952×10^7	sec^{-1}
Plasma Beta (electrons)	$\beta_e = 4.03\times10^{-11}\left(\frac{n_eT_e}{B^2}\right)$	6.9853×10^{-5}	ratio
Plasma Beta (ions):	$\beta_i = 4.03\times10^{-11}\left(\frac{n_iT_i}{B^2}\right)$	6.9853×10^{-5}	ratio

Table 4. NRL Plasma Formulary

A.2 Single Fluid Magnetohydrodynamic Model for Flute Structure Turbulence

The formulary referenced in this section yields the updated velocity terms. Starting with the momentum equation:

$$\left[{}^{\partial u}\!/_{\partial t} + U \bullet \nabla U \right] = -\frac{1}{\rho} \nabla P - g\hat{y} \tag{A.1}$$

Integration of velocity with respect to time will yield the spatial changes of the density with respect to time.

$$\rho\left(\vec{\mathrm{x}}, t\right) = \rho\left(\vec{\mathrm{x}} - \int_0^t \vec{v}\left(x(\tau), \tau\right) d\tau \right) \tag{A.2}$$

Similarly, the relation to the advection velocity is given by:

$$\vec{v}\left(\vec{\mathrm{x}}, t\right) = \vec{v}\left(\vec{\mathrm{x}} - \int_0^t \vec{v}\left(x(\tau), \tau\right) d\tau \right) \tag{A.3}$$

The equation of motion in the $\hat{x}$ direction can be described as:

$$\left[{}^{\partial U_x}\!/_{\partial t} \right] = \frac{1}{\rho} \left[\nabla P_x \right] \tag{A.4a}$$

Applying finite differences, the discretization of the momentum equation becomes:

$$\frac{\vec{U}_{x1} - \vec{U}_{xo}}{\Delta t} = \frac{1}{\rho} \left[\frac{\vec{P}_{x1} - \vec{P}_{xo}}{\Delta x} \right] \tag{A.4b}$$

Solving for the velocity term:

$$\vec{U}_{x1} = \frac{1}{\rho} \left[\frac{\vec{P}_{x1} - \vec{P}_{xo}}{\Delta x} \right] \Delta t + \vec{U}_{xo} \tag{A.4c}$$

From the force balance equation, the equation of motion in the $\hat{y}$ direction is given by:

$$\left[\partial U_y \big/ \partial t\right] = \frac{1}{\rho}\left[\nabla P_y\right] - g\hat{y} \tag{A.5a}$$

Discretization of the equation using finite differences:

$$\frac{\vec{U}_{y1} - \vec{U}_{yo}}{\Delta t} = \frac{1}{\rho}\left[\frac{\vec{P}_{y1} - \vec{P}_{yo}}{\Delta y}\right] - g\hat{y} \tag{A.5b}$$

Solving for the velocity term in the $\hat{y}$ direction:

$$\vec{U}_{y1} = \left(\frac{1}{\rho}\left[\frac{\vec{P}_{y1} - \vec{P}_{yo}}{\Delta y}\right] - g\hat{y}\right)\Delta t + \vec{U}_{yo} \tag{A.5c}$$

$$\left.\begin{aligned} \vec{U}_{x1} &= \vec{U}_{x0}^{k+1} + \nabla\phi^{k+1} \\ \vec{U}_{y1} &= \vec{U}_{y0}^{k+1} + \nabla\phi^{k+1} \end{aligned}\right\}$$

ϕ is scalar field called Helmholtz potential and $\vec{U}^{k+1}$ is the divergence free component of $\vec{U}_x$ (or $\vec{U}_y$). The continuity property (Divergence Free) component is $\nabla\bullet\vec{U}^{k+1} = 0$.

The orthogonality property is applied to the decomposition:

$$\nabla\bullet\vec{U}_{x,y} = \nabla\bullet U^{k+1} + \nabla\bullet\nabla\phi^{k+1} \tag{A.6a}$$

Substitution of the continuity property:

$$\nabla\bullet\vec{U}_{x,y} = 0 + \nabla\bullet\nabla\phi^{k+1} \tag{A.6b}$$

The simplification results in the Poisson equation for the Helmholtz potential:

$$\nabla \bullet \vec{U}_{x,y} = \nabla^2 \phi^{k+1} \tag{A.6c}$$

Solving the equation numerically using the spectral method:

$$\nabla \bullet \vec{U}_{x,y} = \frac{U_{i+1,j} - U_{i-1,j}}{2\Delta x} + \frac{U_{i,j+1} - U_{i,j-1}}{2\Delta y} \tag{A.6d}$$

Let $f = \nabla \bullet U$ and converting the input to the fourier domain: $\hat{f} = fft(f)$

Apply the spectral grid in two dimension: $K^2 = \left(\frac{2\pi}{L} \left[\left(0 : \left(N/2 - 1 \right) \right), -N/2 : -1 \right] i \right)^2$

The second order derivative (Laplacian) is approximated as $\nabla^2 = K_x^2 + K_y^2$

Inverse Fourier transform back to the spatial domain: $\phi = ifft\left(\hat{f} / \left[K_x + K_y \right] \right)$

Substitution of the scalar field into the decomposition equations:

$$\vec{U}_x^{k+1} = \vec{U}_{x1} - \left(\frac{\phi_{x1} - \phi_{x0}}{2\Delta x} \right) \tag{A.7a}$$

$$\vec{U}_y^{k+1} = \vec{U}_{y1} - \nabla \phi_y \tag{A.7b}$$

B Two-Fluid Magnetohydrodynamic Derivation of Flute Structure Behavior

The research conducted in [4] elaborates further on the two-fluid MHD process for deriving dipole flute structures. The following equations are the sum total density, magnetic field, and pressure and their perturbed components.

$$n = n_o(x) + \delta n(x, y, t) \tag{B.1a}$$

$$B_z = B_{0z}(x)\hat{z} + \delta B_z(x, \mathrm{y}, \mathrm{t}) \tag{B.1b}$$

$$P = P_o(x) + \delta P(x, \mathrm{y}, \mathrm{t}) \tag{B.1c}$$

$$P_j = n_j T_j \tag{B.1d}$$

$$g = g\hat{x} \tag{B.1e}$$

The two-fluid model equations to describe the behavior of the flute perturbed plasma are generalized in the following formulary:

Continuity: $$\partial n_j / \partial t + \nabla \bullet (n_j \vec{\upsilon}_j) = 0 \tag{B.2a}$$

Momentum: $$\frac{q_j}{m_j}\left[\frac{1}{C}\vec{\upsilon}_j \times \vec{B} + \vec{E}\right] = \frac{-\nabla P_j}{m_j n_j} + \vec{g} = \left(\frac{\partial}{\partial t} + \vec{\upsilon}_j \bullet \nabla\right)\vec{\upsilon}_j \tag{B.2b}$$

where q_j = charge, m_j = mass, n_j = density, ∇P_j is the gradient pressure, j is the species for which $j=e$(electrons), and $j = I$ (ions). A key assumption is that the plasma follows a quasi-neutrality condition in which the quantity of electrons is equivalent to the quantity

of ions in the two-fluid plasma. This quasi-neutrality condition also translates to the density perturbation for both the electrons, ions, and the total density:

$$\delta n_e = \delta n_i = \delta n \tag{B.3a}$$

Another assumption is that these flute modes derived only have a tangential velocity component and no vector components perpendicular to the tangential forces applied.

$$\hat{z} \bullet \vec{\upsilon}_j = 0 \tag{B.4a}$$

$$\hat{z} \bullet \nabla_{\perp} = 0 \tag{B.4b}$$

The objective is to apply these MHD equations and assumptions to yield nonlinear equations representing the electrostatic potential and density fluctuations as defined by variables φ and δn, respectively. Redefining the continuity equation by it respective species:

$$\frac{\partial n_{i,e}}{\partial t} + \nabla \bullet \left(n_{i,e} \vec{\upsilon}_{i,e} \right) = 0 \tag{B.5}$$

The ion and electron species parameters are specifically defined for the ion momentum equation (B.6a) and the electron momentum equation in (B.6b).

$$\left(Ze/m_i \right) \left[\left(1/c \right) \vec{\upsilon}_i \times \vec{B} + \vec{E} \right] - \nabla P_i / m_i n_i + \vec{g} = \left(\frac{\partial}{\partial t} + \vec{\upsilon}_i \bullet \nabla \right) \vec{\upsilon}_i \tag{B.6a}$$

$$\left(-e/m_e \right) \left[\left(1/c \right) \vec{\upsilon}_e \times \vec{B} + \vec{E} \right] - \nabla P_e / m_e n_e + \vec{g} = \left(\frac{\partial}{\partial t} + \vec{\upsilon}_e \bullet \nabla \right) \vec{\upsilon}_e \tag{B.6b}$$

with $\vec{E}$ electric field, *Z* ion charge number, $\vec{\upsilon}_i$ ion velocity, $\vec{\upsilon}_e$ electron velocity, m_i ion mass, and m_e electron mass. Additionally, $\vec{B} = B_o(x)\hat{z}$ is the external magnetic field that is homogenous along the *x*-direction and points towards the *z*-direction, and the fictitious gravitational acceleration constant is applied in the *x* direction as $\vec{g} = g\hat{x}$. The, particle pressure components $P_j = n_j T_j$ are the particle temperature, T_j multiplied with the species density n_j. The electron charge is $q_e = -e$ and the ion charge is defined as $q_i = Ze$, where the *e* is the electron charge number.

The momentum equations are used to determine the diamagnetic drift velocities to be applied in the continuity equations. Initially the cross product of the momentum equation is taken with the magnetic field $\vec{B}$ to create a double cross product with the property: $\vec{a}\times(\vec{b}\times\vec{c}) = (\vec{a}\cdot\vec{c})\vec{b} - (\vec{a}\cdot\vec{b})\vec{c}$. Applying this property and the flute mode assumptions from (4a) and (4b), equations (6a) and (6b) can be simplified to acquire the drift velocities from each species momentum equations:

$$\vec{v}_{e_D} = \left(-cT_e/(eB_o)\right)K_n\hat{y} \tag{B.7a}$$

$$\vec{v}_{i_D} = \left(-cT_i/(ZeB_o)\right)K_n\hat{y} \tag{B.7b}$$

where the differential operators for the magnetic field and density are defined as:

$$K_B = \frac{1}{B_o}\frac{\partial B_o}{\partial x} \tag{B.8a}$$

$$K_n = \frac{1}{n_o}\frac{\partial n_o}{\partial x} \tag{B.8b}$$

It is observed that the particle motion is $\hat{y}$ directed, and therefore the equilibrium particles motion then constitutes an electric current along the $\hat{y}$ - axis. To this notion, the current density calculations are determined from the parameters of charge, density, and velocity of each species:

$$j = q_i n_{oi} \vec{\upsilon}_i + q_e n_{oe} \vec{\upsilon}_e \tag{B.9}$$

Substituting the parameters defined previously for charge, density, and the diamagnetic drift velocity determined from the momentum equations:

$$j_y = (eZ) n_{oi} \left(\frac{cT_i}{(eZ) B_o} K_n \right) - (eZ) n_{oi} \left(\frac{g(m_i)c}{(eZ) B_o} \right) + \frac{cT_e}{(e) B_o} K_n \tag{B.10}$$

The current density is found with respect to the Alfven velocity, the velocity of the ions oscillation in the magnetic field:

$$j_y = \left(\frac{cB_o}{4\pi} \right) \left(\frac{\beta}{2} K_n - \frac{g}{\upsilon_A^2} \right) \tag{B.11}$$

Using this current density and Ampere's Law to derive the equilibrium condition:

$$\left(\nabla \times \vec{B} \right)_y = (4\pi/c) j_y \tag{B.12}$$

Substituting the previously determined components into:

$$-K_B = (4\pi/c)(cB_o/4\pi) \left(\frac{\beta}{2} K_n - \frac{g}{\upsilon_A^2} \right) \tag{B.13}$$

Simplifying:

$$-K_B - \frac{\beta}{2}K_n - \frac{g}{\upsilon_A^2} = 0$$

(B.14)

A second approximation is applied to expand the series on the velocity terms for low ion cyclotron frequency conditions. The series expansion of the velocity terms leads to:

$$\vec{\upsilon}_e = \vec{\upsilon}_{oe} + \vec{\upsilon}_{ie} \quad \text{(B.15a)} \qquad \vec{\upsilon}_i = \vec{\upsilon}_{1i} + \vec{\upsilon}_{2i} \quad \text{(B.15b)}$$

Substitution of these terms into the momentum equations:

$$\frac{\partial \vec{\upsilon}_e}{\partial t} + \left(\vec{\upsilon}_e \bullet \nabla\right)\vec{\upsilon}_e = \frac{-e}{c\left(m_e\right)}\vec{\upsilon}_e \times \vec{B} + \frac{-e}{\left(m_e\right)}\vec{E} - \frac{\nabla \vec{P}_e}{m_e n_e}$$

(B.16a)

$$\frac{\partial \vec{\upsilon}_i}{\partial t} + \left(\vec{\upsilon}_{1i} \bullet \nabla\right)\vec{\upsilon}_{1i} = \frac{Ze}{c\left(m_i\right)}\left(\vec{\upsilon}_{1i} + \vec{\upsilon}_{2i}\right) \times \vec{B}_o + \frac{Ze}{\left(m_i\right)}\vec{E} - \frac{\nabla \vec{P}_i}{m_i n_i}$$

(B.16b)

Taking the cross product with $\vec{B}$ to isolate the drift velocities and applying the flute mode conditions from (4a) and (4b), the electron drift velocity becomes:

$$\vec{\upsilon}_{oe} = \vec{\upsilon}_e = \frac{c\vec{E} \times \hat{z}}{B_z} - \left(\frac{zT_e}{m_i \omega_{ci} n_e}\right)\frac{B_o}{B_z}\left(\hat{z} \times \vec{\nabla} n_e\right)$$

(B.17)

$\vec{\upsilon}_e = \vec{\upsilon}_E + \vec{\upsilon}_{eD}$, where $\vec{\upsilon}_E$ is the gradient drift velocity, $\vec{\upsilon}_{1e} = \vec{\upsilon}_{eD}$ is the diamagnetic drift velocity. The total velocity is defined as $\vec{\upsilon}_e = \vec{\upsilon}_E + \vec{\upsilon}_{eD}$. In the case of the ion drift velocity, the same process is applied, but with the addition of the ion gravitational drift

velocity term and polarization components. The second approximation of the ion drift velocity begins with the solution of the first order drift term:

$$\vec{\upsilon}_{1i} = \frac{c\vec{E}\times\hat{z}}{B_z} - \left(\frac{T_i}{m_i\omega_{ci}n_i}\right)\frac{B_o}{B_z}\left(\hat{z}\times\vec{\nabla}n_i\right) + \frac{\vec{g}\times\hat{z}}{\omega_{ci}} \tag{B.18a}$$

The first order term is expanded to:

$$\vec{\upsilon}_{1i} = \vec{\upsilon}_E + \vec{\upsilon}_{iD} + \vec{\upsilon}_g \tag{B.18b}$$

where $\vec{\upsilon}_{iD}$ is ion diamagnetic drift velocity

$\vec{\upsilon}_g = \dfrac{\vec{g}\times\vec{z}}{\omega_{ci}}$, where $\vec{\upsilon}_g$ is the ion diamagnetic drift velocity

The second order approximation is determined as (B.19) after substitution of (B.18b) and taking the cross product with $\vec{B}$ as before with the first order approximation and applying flute mode conditions:

$$\vec{\upsilon}_{2i} = -\vec{\upsilon}_{1i} + \vec{\upsilon}_E + \vec{\upsilon}_{iD} + \vec{\upsilon}_g + \frac{\hat{z}\times\left(\partial/\partial t + \vec{\upsilon}_E\cdot\nabla\right)\vec{\upsilon}_E}{\omega_{ci}} + \frac{\hat{z}\times\left(\partial/\partial t + \vec{\upsilon}_E\cdot\nabla\right)\vec{\upsilon}_{iD}}{\omega_{ci}} \tag{B.19}$$

At this point, the polarization components of the second order ion drift are introduced and defined below:

$\vec{\upsilon}_{2i} = \vec{\upsilon}_E^{\rho} + \vec{\upsilon}_{iD}^{\rho}$, the polarization components of the ion drift velocity

$$\vec{\upsilon}_E^{\rho} = \frac{\hat{z}\times\left(\partial/\partial t + \vec{\upsilon}_E\cdot\nabla\right)\vec{\upsilon}_E}{\omega_{ci}} = \frac{c}{\omega_{ci}}B_o\left(\partial/\partial t + \vec{\upsilon}_E\cdot\nabla\right)\vec{E} \tag{B.20}$$

$$\vec{\upsilon}_{iD}^{\rho} = \frac{\hat{z} \times \left(\partial/\partial t + \vec{\upsilon}_E \cdot \nabla\right)\vec{\upsilon}_{iD}}{\omega_{ci}} = \frac{-\mathrm{P}_i^2}{n_{oi}}\left(\partial/\partial t + \vec{\upsilon}_E \cdot \nabla\right)\nabla\vec{n}_i$$

(B.21)

The total ion velocity drift becomes:

$$\vec{\upsilon}_i = \vec{\upsilon}_e + \vec{\upsilon}_{iD} + \vec{\upsilon}_g + \vec{\upsilon}_E^{\rho} + \vec{\upsilon}_{iD}^{\rho}$$

(B.22)

The relationship between the normalized perturbation in the magnetic field and the normalized perturbation in the number density is found using Ampere's law in the *x*-direction and is determined to be:

$$\frac{\delta B}{B_o} = -\frac{\beta}{2}\frac{\tilde{n}}{n_o} \quad \text{(B.23a)} \qquad \frac{\tilde{n}_i}{\tilde{n}_{oi}} = \frac{\tilde{n}_e}{\tilde{n}_{oe}} = \frac{\tilde{n}}{\tilde{n}_o} \quad \text{(B.23b)}$$

Apply continuity equation using the velocities from the momentum equation to determine density:

$$\frac{\partial\vec{n}_e}{\partial t} + \left(\vec{\nabla}\vec{n}_e\right)\bullet\vec{\upsilon}_e + \vec{n}_e\vec{\nabla}\bullet\vec{\upsilon}_e + \vec{\nabla}\bullet\left(\vec{n}_e\vec{\upsilon}_{eD}\right) = 0$$

(B.24a)

$$\frac{\partial\vec{n}_i}{\partial t} + \vec{\nabla}\bullet\left(\vec{n}_i\vec{\upsilon}_E\right) + \vec{\nabla}\bullet\left(\vec{n}_i\vec{\upsilon}_{iD}\right) + \vec{\nabla}\bullet\left(\vec{n}_i\vec{\upsilon}_E^{\rho}\right) + \vec{\nabla}\bullet\left(\vec{n}_i\vec{\upsilon}_{iD}^{\rho}\right) = 0$$

(B.24b)

Substitution of velocity terms for the electron continuity equation and simplifying:

$$\frac{\partial \vec{n}_e}{\partial t} + \left(\vec{\upsilon}_e \bullet \vec{\nabla}\right)\vec{n}_e + \frac{cE_y \vec{n}_{oe}}{B_o}\mathrm{K}_n - \frac{cE_y \vec{n}_{oe}}{B_o}\mathrm{K}_B - \vec{n}_{oe}\left(\partial/\partial t + \vec{\upsilon}_E \cdot \nabla\right)\frac{\delta B}{B_o} + \ldots$$
$$\frac{cT_e}{eB_o^2}\left\{\tilde{n}_e, \delta B\right\} - \frac{cT_e}{eB_o}\left[\mathrm{K}_B \frac{\partial \vec{n}_e}{\partial y} - \left(\frac{\mathrm{K}_n n_{oe}}{B_o}\right)\frac{\partial \delta B}{\partial y}\right] = 0$$

(B.25a)

Substitution of velocity terms for the ion continuity equation and simplifying:

$$\frac{\partial \vec{n}_i}{\partial t} + \left(\vec{\upsilon}_E \bullet \vec{\nabla}\right)\vec{n}_i + \frac{cE_y \vec{n}_{oi}}{B_o}\mathrm{K}_n - \frac{cE_y \vec{n}_{oi}}{B_o}\mathrm{K}_B - \vec{n}_{oi}\left(\partial/\partial t + \vec{\upsilon}_E \cdot \vec{\nabla}\right)\frac{\delta B}{B_o} + \frac{cT_i}{ZeB_o}\left(\mathrm{K}_B + \frac{\beta}{2}\mathrm{K}_n\right)\frac{\partial \vec{n}_i}{\partial y} - \ldots$$
$$\left(\frac{g}{\omega_{ci}}\right)\left(1 + \frac{\beta}{2}\right)\frac{\partial \vec{n}_i}{\partial y} + \left(\partial/\partial t + \vec{\upsilon}_E \cdot \nabla\right)\vec{E} - \rho_i^2\left[\left(\partial/\partial t + \vec{\upsilon}_E \cdot \vec{\nabla}\right)\vec{\nabla}\tilde{n}_i - \left\{\hat{E}_j, \vec{\nabla}\vec{n}_i\right\}\right] = 0$$

(B.25b)

Equilibrium condition from Ampere's law allows for the reduction of the electron and ion continuity equations:

$$\left(1 + \frac{\beta}{2}\right)\left(\partial/\partial t + \vec{\upsilon}_E \cdot \vec{\nabla}\right)\delta n + \left(\mathrm{K}_n - \mathrm{K}_B\right)\hat{E}_y - \frac{\beta_e}{2\omega_{ci}}\left(\mathrm{K}_B + \frac{\beta}{2}\mathrm{K}_n\right)\frac{\partial \delta n}{\partial y} = 0$$

(B.26)

$$\left(\partial/\partial t + \vec{\upsilon}_E \cdot \vec{\nabla}\right)\left(1 + \frac{\beta}{2} - \rho_1^2 \nabla_\perp^2\right)\delta n + \left(\mathrm{K}_n - \mathrm{K}_B\right)\hat{E}_y - \left(1 + \frac{\beta}{2}\right)\frac{g}{\omega_{ci}}\frac{\partial \delta n}{\partial y} + \ldots$$
$$\frac{1}{\omega_{ci}}\nabla_\perp^2 \bullet \left(\partial/\partial t + \vec{\upsilon}_E \cdot \vec{\nabla}\right)\hat{E}_\perp + \frac{\rho_i^2}{n_{oi}}\left\{\hat{E}_j, \vec{\nabla}\vec{n}_i\right\} = 0$$

(B.27)

where β is the species plasma beta term.

The following are the resulting nonlinear two-fluid differential equations that represent the electrostatic potential and density perturbations of the dipole flute structures:

$$\frac{\partial \Delta_\perp \Phi}{\partial t} - \frac{V_{Ti}^2}{\omega_{ci}} \left[\frac{\left(-\frac{1}{n_o}\frac{dn_o}{dx} \right) + \frac{\beta}{2}\left(-\frac{1}{n_o}\frac{dn_o}{dx} \right) + \frac{g\beta_i}{2V_{Ti}^2}}{1+\frac{\beta}{2}} \right] \frac{\partial \Delta_\perp \Phi}{\partial y} + \frac{gB_{0z}}{n_{i0}c} \left(1 + \frac{\rho_i^2 \frac{\beta_e}{2}}{1+\frac{\beta}{2}} \Delta_\perp \right) \frac{\partial \delta n}{\partial y}$$

$$- \frac{V_{Ti}^2}{\omega_{ci} c} \left(\frac{\partial \Delta_\perp \delta B_z}{\partial t} + \frac{g}{\omega_{ci}} \frac{\partial \delta B_z}{\partial y} \right) - \frac{g}{\omega_{ci}} \left(\frac{\partial \Delta_\perp \Phi}{\partial y} + \frac{V_{Ti}^2}{\omega_{ci} c} \frac{B_{0z}}{n_{io}} \frac{\partial \Delta_\perp \delta n}{\partial y} \right)$$

$$= \frac{V_{Ti}^2}{\omega_{ci} n_{0i}} \vec{\nabla}_\perp \bullet \left(\frac{\partial \vec{\nabla}_\perp \Phi}{\partial x} \left[\frac{\partial \delta n}{\partial y} \right] - \frac{\partial \vec{\nabla}_\perp \Phi}{\partial y} \left[\frac{\partial \delta n}{\partial x} \right] \right) + \frac{c}{B_{0z}} \left(\frac{\partial \Delta_\perp \Phi}{\partial x} \left[\frac{\partial \Phi}{\partial y} \right] - \frac{\partial \Delta_\perp \Phi}{\partial y} \left[\frac{\partial \Phi}{\partial x} \right] \right) \tag{B.28a}$$

$$\frac{\partial \delta n}{\partial t} + \frac{c}{B_{oz}} \frac{-\frac{1}{n_0}\frac{dn_0}{dx} + \frac{1}{B_{0z}}\frac{dB_{0z}}{dx}}{1+\frac{\beta}{2}} \frac{\partial \Phi}{\partial y} - \frac{\beta_e}{\beta_i} \frac{V_{Ti}^2}{\omega_{ci}} \left[\frac{\frac{1}{B_{0z}}\frac{dB_{0z}}{dx} - \frac{\beta}{2}\frac{1}{n_0}\frac{dn_0}{dx}}{1+\frac{\beta}{2}} \right] \frac{\partial \delta n}{\partial y} = \frac{c}{B_{0z}} \left[\frac{\partial \delta n}{\partial x}\frac{\partial \Phi}{\partial y} - \frac{\partial \delta n}{\partial y}\frac{\partial \Phi}{\partial x} \right] \tag{B.28b}$$

$$\delta B_z = \frac{\beta}{2} \delta n \tag{B.28c}$$

APPENDIX C. Derivations of the Backscatter (Full Wave) Propagation Model

The model presented in this chapter intends to determine the full wave solution of a SSB-SC pulse interaction with flute structures on a density map in order to characterize the total scattering effects that are otherwise unaccounted in the multiple phase screen model. The disadvantage of the full wave model is the computational limitations that inhibit the solving of a large scale (kilometer range) propagation problem. The time steps must be sampled at a fine mesh to achieve a conditionally stable propagation algorithm. Additionally, due to the computation limitations, only the one dimensional cross sections of the flute perturbations along the density maps will be analyzed with this full wave propagation model across the range of the density map.

Maxwell's equations are considered to be first order partial differential equations that must be coupled to solve for more than one unknown. The electric field $\vec{E}$ and the magnetic field $\vec{H}$ are both unknowns that appear in each equation. This research focuses on the analyzing the behavior of the electric field. Therefore, the $\vec{E}$ component will be solved to uncouple Maxwell's equations at the sacrifice of forming a second order differential equation that will be solved numerically. Starting with Maxwell's Equations (1), (2), (3), and (4).

$$(1) \quad \nabla \times \vec{E} = -\frac{\partial \vec{H}}{\partial t} \qquad (C.1) \qquad (2) \quad \nabla \times \vec{H} = \mu_o \vec{J} + \mu_o \varepsilon \frac{\partial \vec{E}}{\partial t} \qquad (C.2)$$

$$(3) \quad \nabla \bullet \vec{D} = q_{ev} \qquad (C.3) \qquad (4) \quad \nabla \bullet \vec{B} = q_{mv} \qquad (C.4)$$

where,

E = electric field intensity (V/m) q_{ev} = electric charge density ($Coulombs/m^3$)

H = magnetic field intensity (A/m) q_{mv} = magnetic charge density (Wb/m^3)

D = electric flux density ($Coulombs/m^2$) J = electric current density (A/m^2)

B = magnetic flux density (Wb/m^2)

The following steps are taken to solve Maxwell's equations for the vector wave equation:

1.) Use the identity: $$\nabla\times\left(\nabla\times\vec{A}\right)=\nabla\left(\nabla\bullet\vec{A}\right)-\nabla^2\vec{A}$$ (C.5a)

2.) Apply Identity on both sides of (1): $$\nabla\times\left(\nabla\times\vec{E}\right)=-\nabla\times\frac{\partial\vec{H}}{\partial t}$$ (C.5b)

3.) Simplification: $$\nabla\times\left(\nabla\times\vec{E}\right)=-\frac{\partial}{\partial t}\left(\nabla\times\vec{H}\right)$$ (C.5c)

4.) Simplification of (2): $$\nabla\left(\nabla\bullet\vec{E}\right)-\nabla^2\vec{E}=-\frac{\partial}{\partial t}\left(\mu_o\vec{J}+\mu_o\varepsilon\frac{\partial\vec{E}}{\partial t}\right)$$ (C.5d)

5.) Distribution of $\frac{\partial}{\partial t}$: $$\nabla\left(\nabla\bullet\vec{E}\right)-\nabla^2\vec{E}=-\frac{\partial}{\partial t}\mu_o\vec{J}+\mu_o\varepsilon\frac{\partial^2\vec{E}}{\partial t^2}$$ (C.5e)

6.) from (3): $$\nabla\bullet\vec{D}=\varepsilon\nabla\bullet\vec{E}=q_{ev}$$ (C.5f)

Isolate $\nabla\bullet\vec{E}$ $$\nabla\bullet\vec{E}=q_{ev}/\varepsilon$$ (C.5g)

The pulse propagation is considered to be in a source free region. Therefore, the charge density: $q_{ev} = 0$

7.) Substitution of the result from (6) into (5):

$$\nabla(0) - \nabla^2 \vec{E} = -\frac{\partial}{\partial t}\mu_o \vec{J} + \mu_o \varepsilon \frac{\partial^2 \vec{E}}{\partial t^2} \tag{C.5h}$$

8.) Simplification of (7):

$$-\nabla^2 \vec{E} = -\frac{\partial}{\partial t}\mu_o \vec{J} - \mu_o \varepsilon \frac{\partial^2 \vec{E}}{\partial t^2} \tag{C.5i}$$

9.) Isolate the Laplacian term:

$$\nabla^2 \vec{E} = \frac{\partial}{\partial t}\mu_o \vec{J} + \mu_o \varepsilon \frac{\partial^2 \vec{E}}{\partial t^2} \tag{C.5j}$$

The electric behavior of the plasma is characterized by the constitutive parameters σ, ε, and μ. These constitutive parameters are considered linear, as they are not functions of the applied field. The density perturbation caused by the flute structure results in a nonhomogenous medium in which the constitutive parameters for conduction and charge current density is a function of position within the density map. The permittivity is a function of frequency and therefore, the plasma is considered dispersive. The electron mobility parameter is a function of the direction of the applied field. Therefore, the plasma can be considered anisotropic. The following steps develop the relationship between the flute density perturbations and the material parameters.
The formulation for the conduction current density is (C.6).

$$J_c = q_{ev}(-\mu_e E) = \sigma_e E \tag{C.6}$$

where, J_c = Conduction Current Density, q_{ev} =electric charge density, μ_e = electron mobility. The electric conductivity is defined as:

$$\sigma_e = -q_{ev}\mu_e = -N_e q_e \mu_e = N_e |q_e| \mu_e \tag{C.7}$$

where, $N_e(r)$ = free electron density, $|q_e|$ = charge of an electron (magnitude) = 1.6×10^{-19} Coulombs. The electric charge density is defined as $q_{ev} = -N_e(r)|q_e|$, in which the negatively charged particles (electrons) travel opposite to the E-field. Substitution of the conductivity parameters into the relation for (C.6), the following formulation for the conduction current density becomes:

$$\vec{J}_c = \ddot{\sigma}_e \vec{E} = \left(N_e |q_e| \ddot{\mu}_e\right)\vec{E} \tag{C.8}$$

Substitution of the relation into the Time Domain Vector Wave Equation:

$$\nabla^2 \vec{E} = \frac{\partial}{\partial t}\mu_o \left(N_e(r)|q_e|\ddot{\mu}_e\right)\vec{E} + \mu_o \varepsilon \frac{\partial^2 \vec{E}}{\partial t^2} \tag{C.9}$$

where the electron mobility tensor for a cold plasma is defined as:

$$\ddot{\mu}_e = \begin{bmatrix} \left(ie/m\right)\left(\frac{\omega_i}{\omega_i^2-\omega_c^2}\right) & \left(-e/m\right)\left(\frac{\omega_c}{\omega_i^2-\omega_c^2}\right) & 0 \\ \left(e/m\right)\left(\frac{\omega_c}{\omega_i^2-\omega_c^2}\right) & \left(ie/m\right)\left(\frac{\omega_i}{\omega_i^2-\omega_c^2}\right) & 0 \\ 0 & 0 & \left(ie/m\omega_i\right) \end{bmatrix} \tag{C.10}$$

where, ω_i = incident wave frequency ω_c = cyclotron frequency

The conditions upon which the cold plasma assumption is valid are:

$$\omega_i >> \omega_{pe} \qquad\qquad \omega_i >> \omega_{ce}$$

ω_{pe} = electron plasma frequency $\qquad\qquad$ ω_{ce} = electron gyro frequency

The total permittivity for the plasma is defined as:

$$\varepsilon = \varepsilon_o \varepsilon' \tag{C.11}$$

where, ε = Total Permittivity, where ε_o = free space permittivity = $8.854\times10^{-12}\ F/m$, and the permittivity of the unmagnetized cold plasma is related to the frequency in the following:

$$\varepsilon' = 1 - \omega_p^2 / \omega^2 \tag{C.12}$$

where, $\omega_p = \sqrt{N_e^2 / m\varepsilon_o}$,critical plasma frequency, e = $1.6\times10^{-19}\ Coulombs$,

mass (m) = $9.1\times10^{-31}\ kg$, and N = density per m^3.

The following results demonstrate the flute structure constitutive parameter characteristics for a variety of frequencies, flute intensities, and sizes. The complexity of deriving solutions from a second order differential equation makes it more practical to consider solving for the numerical solution. The numerical scheme applied to the vector wave equation derived in the previous section is finite difference method.

$$\frac{\partial^2 \vec{E}}{\partial t^2} = \frac{1}{\mu_o \varepsilon} \nabla^2 \vec{E} - \left(\frac{N_e(r) |q_e| \vec{\mu}_e}{\varepsilon} \right) \frac{\partial \vec{E}}{\partial t} \tag{C.13}$$

Create the following variable declarations:

$$A = \frac{1}{\mu_o \varepsilon} \qquad B = \left(\frac{N_e(r)|q_e|\vec{\mu}_e}{\varepsilon} \right) \qquad \nabla^2 \vec{E} = \partial^2 \vec{E} \Big/ \partial x^2 + \partial^2 \vec{E} \Big/ \partial y^2$$

Explicit Numerical Scheme:

$$\frac{E_{j,k}^{n+1} - 2E_{j,k}^{n+1} + E_{j,k}^{n-1}}{\Delta t^2} = A\left[\frac{E_{j+1,k}^{n} - 2E_{j,k}^{n} + E_{j-1,k}^{n}}{\Delta x^2} + \frac{E_{j,k+1}^{n} - 2E_{j,k}^{n} + E_{j,k-1}^{n}}{\Delta y^2} \right] + B\left[\frac{E_{j,k}^{n+1} - E_{j,k}^{n-1}}{2\Delta t} \right] \tag{C.14a}$$

let $\Delta x^2 = \Delta y^2 = \Delta s^2$

Simplification:

$$E_{j,k}^{n+1} - 2E_{j,k}^{n+1} + E_{j,k}^{n-1} = \frac{A\Delta t^2}{\Delta s^2}\left[E_{j+1,k}^{n} - 2E_{j,k}^{n} + E_{j-1,k}^{n} + E_{j,k+1}^{n} - 2E_{j,k}^{n} + E_{j,k-1}^{n} \right] + \frac{B\Delta t}{2}\left[E_{j,k}^{n+1} - E_{j,k}^{n-1} \right] \tag{C.14b}$$

Simplification:

$$E_{j,k}^{n+1} = \frac{1}{\left(1 - \frac{B\Delta t}{2}\right)}\left(\frac{A\Delta t^2}{\Delta s^2}\left[E_{j+1,k}^{n} - 2E_{j,k}^{n} + E_{j-1,k}^{n} + E_{j,k+1}^{n} - 2E_{j,k}^{n} + E_{j,k-1}^{n} \right] - \left(\frac{B\Delta t}{2} - 1 \right) E_{j,k}^{n-1} - 2E_{j,k}^{n} \right) \tag{C.14c}$$

APPENDIX D. Consistency and Stability of Numerical Propagation Algorithms

The notion of convergence in any numerical scheme is based on the fundamental theorem of Numerical Analysis, known as Lax Equivalence Theorem. In essence, the theorem states that the convergence of a numerical scheme is implied when consistency and stability are achieved. The following descriptors will pertain to derivative based numerical approximations that are applied in finite difference approximations. Consistency refers to the following:

$$\lim_{\Delta z \to \infty} \left(\tau_{\Delta z} \right) \to 0$$

where "τ" refers to the truncation error of the system per spatial step "Δz", the cut-off approximation of the numerical scheme relative to the analytic solution. The computation of the truncation error will be explained in further in the section on Finite Difference Method. As the spatial step size of the numerical scheme becomes smaller (meaning more samples on the finite grid are collected) the truncation error should become smaller, meaning that the numerical solution agrees more with the analytic solution. A function can be approximated by a finite number of terms of its Taylor series. Taylor's Theorem gives quantitative estimates on the error introduced by the use of such an approximation. Analytic functions are equal to their Taylor series on an open interval.

Applying the consistency check to the hyperbolic wave equation:

$$\left[\frac{\hat{A}^{n+1} - 2\hat{A}^{n} + \hat{A}^{n-1}}{\Delta z^{2}} \right] - 2i\beta \left[\frac{\hat{A}^{n+1} - \hat{A}^{n}}{\Delta z} \right] + K_{xy}^{2} \hat{A}^{n+1} = 0 \tag{D.1}$$

Taylor Series expand each term on the left side of the equation:

For the term $\frac{\hat{A}^{n+1} - 2\hat{A}^{n} + \hat{A}^{n-1}}{\Delta z^2}$:

$$\begin{aligned} A_j^{n+1} &\simeq A_j^n + dz\left(A_j^n\right)_z + \frac{1}{2}(dz)^2\left(A_j^n\right)_{zz} + \ldots \\ -2A_j^n &= -2A_j^n \\ A_j^{n-1} &\simeq A_j^n - dz\left(A_j^n\right)_z + \frac{1}{2}(dz)^2\left(A_j^n\right)_{zz} + \ldots \end{aligned}$$

$$\frac{}{\Delta z^2} \tag{D.2}$$

For the term: $-2i\beta\left(\frac{\hat{A}^{n+1} - \hat{A}^{n}}{\Delta z}\right)$:

$$-2i\beta\left(\begin{array}{r} A_j^{n+1} \simeq A_j^n + \Delta z\left(A_j^n\right)_z + \frac{1}{2}(\Delta z)^2\left(A_j^n\right)_{zz} + \frac{1}{6}(\Delta z)^3\left(A_j^n\right)_{zzz} + \ldots \\ -A_j^n = -A_j^n \\ \hline \Delta z \end{array}\right) \tag{D.3}$$

For the term: $K_{xy}^2 A_j^{n+1}$:

$$K_{xy}^2\left(A_j^n + \Delta z\left(A_j^n\right)_z + \frac{1}{2}(\Delta z)^2\left(A_j^n\right)_{zz} + \frac{1}{6}(\Delta z)^3\left(A_j^n\right)_{zzz} + \frac{1}{24}(\Delta z)^4\left(A_j^n\right)_{zzzz} \ldots\right) \tag{D.4}$$

Combining the terms for cancellation, the remaining terms become:

$$\left[\left(A^n\right)_{zz}+\frac{1}{12}\left(\Delta z^2\right)\left(A^n\right)_{zzzz}+....\right]-2i\beta\left[\left(A^n\right)_z+\frac{1}{2}\left(\Delta z\right)\left(A^n\right)_{zz}+....\right]$$
$$+K_{xy}^2\left(A^n+\Delta z\left(A^n\right)_z+\frac{1}{2}\left(\Delta z^2\right)\left(A^n\right)_{zz}+...\right)=0 \tag{D.5}$$

Re-arrange the terms to for comparison to the analytic representation of the equation:

$$\tau_n=\left[\left(A^n\right)_{zz}-2i\beta\left(A^n\right)_z+K_{xy}^2A^n\right]+\left[-i\beta\Delta z\left(A^n\right)_{zz}+\frac{1}{12}\left(\Delta z\right)^2\left(A^n\right)_{zzzz}+...\right]$$
$$+K_{xy}^2\Delta z\left(A^n\right)_z+...=0 \tag{D.6}$$

The truncation error is calculated by taking the difference between the analytic form of the hyperbolic wave equation and the Taylor series expansion of the numerical form:

$$\tau=Analytic-\tau_n$$
$$\tau=\left[-i\beta\Delta z\left(A^n\right)_{zz}+\frac{1}{12}\left(\Delta z\right)^2\left(A^n\right)_{zzzz}+O\left(z^3\right)\right]$$
$$+K_{xy}^2\Delta z\left(A^n\right)_z+O\left(\Delta z^2\right)=0 \tag{D.7}$$

It appears that the discretization is of first order accuracy, $\tau=O\left(z\right)$.

The Taylor Series expansion result is supported by the Cauchy error calculation, as the infinity norm error of the solution with respect to finer step sizes converges at a slope of unity. The input function is a vector of arbitrary complex values.

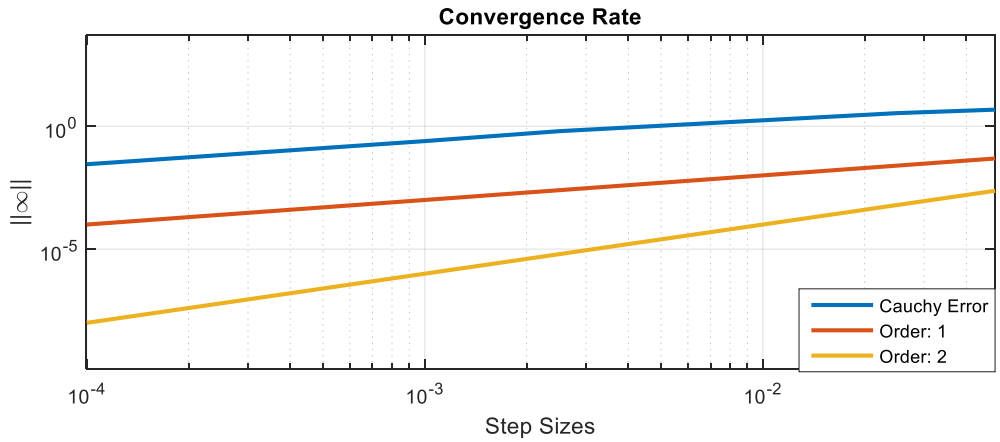

Figure 138. Cauchy Error Convergence Rate for Pseudo Spectral Method

Stability of a numerical scheme is arguably the most important trait that the scheme should be designed upon. The steps sizes must be chosen to ensure that the error bounds between the numerical and analytic solutions do not grow uncontrollably. Choice of the aspect ratio, the ratio between the spatial steps can be determined using Von Neumann stability analysis. In order to understand stability in a numerical system, it is crucial to interpret how the error propagates in a linear function:

$$x^n = \hat{x}^n + \delta W^n \tag{D.8}$$

δ is the smallness parameter, $\hat{x}^n$ is the exact trajectory, and W^n is the perturbed trajectory. The smallness parameter represents a perturbation size that must be bounded in finite space and absolutely stable if perturbations shrink over time. Using the smallness of δW^n, the necessary conditions for stability are derived to achieve the optimal trajectory $\hat{x}^n$.

$$\hat{x}^{n+1} = \mathrm{H}(x^n) \tag{D.9a}$$

Where "H" describes a numerical system.

Substitution of $x^n = \hat{x}^n + \delta W^n$:

$$\hat{x}^{n+1} + \delta W^{n+1} = \mathrm{H}(\hat{x}^n + \delta W^n) \tag{D.9b}$$

If the smallness parameter $\delta \to 0$, the approximation will be in the radius of its Taylor series expansion, therefore, approximate to the Taylor Series and neglect its higher order terms to focus on linear stability:

$$\hat{x}^{n+1} + \delta W^{n+1} = H(\hat{x}^n) + \frac{\partial H}{\partial x}(\hat{x}^n)(\delta W^n) + \cdots \tag{D.9c}$$

By simplification, the following remains:

$$\hat{x}^{n+1} = H(\hat{x}^n) \text{ will cancel}$$

The remaining term is:

$$W^{n+1} = \frac{\partial H}{\partial x}(\hat{x}^n)(W^n) \tag{D.9d}$$

The term, $\frac{\partial H}{\partial x}(\hat{x}^n)$ is a non-constant coefficient. A solution cannot be written for this term, therefore, it is approximated by a constant: σ. Now the term is no longer linear stability but it is spectral stability. The linear constant coefficient differential equation solutions are exponentials:

$$W^{n+1} = \sigma W^n \to \frac{W^{n+1}}{W^n} = \sigma \tag{D.9e}$$

The stability criteria for this approximation is as follow:

$$\lim_{n\to 0}|w^n| = A\lim_{n\to 0}|\sigma^n| = \begin{cases} \infty & |\sigma|>1 \quad \text{unstable} \\ A\bullet 1 & |\sigma|=1 \quad \text{marginal} \\ 0 & |\sigma|<1 \quad \text{A-stable} \end{cases}$$

Applying Von Neumann Stability Analysis to the numerical scheme:

$$\left[\frac{\hat{A}^{n+1}-2\hat{A}^{n}+\hat{A}^{n-1}}{\Delta z^2}\right]-2i\beta\left[\frac{\hat{A}^{n+1}-\hat{A}^{n}}{\Delta z}\right]+K_{xy}^2\hat{A}^{n+1}=0$$

(D.10a)

Substitute: $A^{n+1}=\sigma^{n+2}e^{i\xi j}$, $A^{n}=\sigma^{n+1}e^{i\xi j}$, and $A^{n-1}=1$ into the numerical scheme.

$$\left[\frac{\sigma^{n+2}e^{i\xi j}-2\sigma^{n+1}e^{i\xi j}+e^{i\xi j}}{\Delta z^2}\right]-2i\beta\left[\frac{\sigma^{n+2}e^{i\xi j}-\sigma^{n+1}e^{i\xi j}}{\Delta z}\right]+K_{xy}^2\sigma^{n+2}e^{i\xi j}=0$$

(D.10b)

Arrange the like-terms:

$$\sigma^{n+2}e^{i\xi j}-2\sigma^{n+1}e^{i\xi j}+e^{i\xi j}-2i\beta\Delta z\left[\sigma^{n+2}-\sigma^{n+1}\right]e^{i\xi j}+\Delta z^2K_{xy}^2\sigma^{n+2}e^{i\xi j}=0$$

(D.10c)

$$\sigma^{n+2}\left(1-2i\beta\Delta z+\Delta z^2K_{xy}^2\right)+\sigma^{n+1}\left(-2-2i\beta\Delta z\right)+1=0$$

(D.10d)

The equation above is solved using the quadratic formula.

$$\sigma = \left| \frac{(-B) \pm \sqrt{(B)^2 - 4(A)(C)}}{2(A)} \right|$$

(D.10e)

Where,

$$A = \left(1 - 2i\beta\Delta z + (\Delta z)^2 K_{xy}^2\right)$$

$$B = -2 - 2i\beta\Delta z$$

$$C = 1$$

Substitute the parameters into the quadratic formula and simplify:

$$\left|\sigma^n\right| = \left| \frac{(2 + 2i\beta\Delta z) \pm \sqrt{(-2 - 2i\beta\Delta z)^2 - 4\left(1 - 2i\beta\Delta z + (\Delta z)^2 K_{xy}^2\right)(1)}}{2\left(\left(1 - 2i\beta\Delta z + (\Delta z)^2 K_{xy}^2\right)\right)} \right|$$

(D.11f)

$$\left|\sigma^n\right| = \left| \frac{(2 + 2i\beta\Delta z) \pm \sqrt{-4\left((\Delta z)^2 K_{xy}^2\right)}}{\left(2 - 4i\beta\Delta z + 2(\Delta z)^2 K_{xy}^2\right)} \right|$$

(D.11g)

Introduce the stability condition:

$$\left|\sigma^n\right| = \left| \frac{(2 + 2i\beta\Delta z) \pm 2\left((\Delta z) K_{xy}\right) i}{\left(2 - 4i\beta\Delta z + 2(\Delta z)^2 K_{xy}^2\right)} \right| \leq 1$$

(D.11h)

Since β and Δz are constants, let these variables equal 1 to ease the simplification.

$$\left|\sigma^n\right| = \left| \frac{(2 + 2i) \pm 2\left(K_{xy}\right) i}{\left(2 - 4i + 2K_{xy}^2\right)} \right| \leq 1$$

(D.11i)

Multiply the denominator of the inequality to the other side of the equation and calculate the magnitudes:

$$\left|\left(2+2i\right)\pm 2\left(K_{xy}\right)i\right|\le\left|\left(2-4i+2K_{xy}^{2}\right)\right|$$

$$\sqrt{(2)^{2}+\left(2\pm 2\left(K_{xy}\right)\right)^{2}}\le\sqrt{\left(2+2K_{xy}^{2}\right)^{2}+(-4)^{2}}$$

The condition is always satisfied no matter the selection of step sizes, and is therefore, absolutely stable.

The results from this section demonstrate that the implicit numerical finite difference scheme used to solve the solution of the hyperbolic wave equation is consistent with a rate of order 1, and by Von Neumann stability analysis, absolutely stable. Therefore, by the Lax equivalence theorem, the consistency and stability implies convergence in the numerical scheme.

Von Neumann Stability Analysis:

$$\frac{U_{i,j}^{n+1}2(1-B\Delta t)-4U_{i,j}^{n}+U_{i,j}^{n-1}2(1+B\Delta t)}{2\Delta t^{2}}=A\left(\frac{\sigma^{n}e^{i\xi(j+1+k)}-2\sigma^{n}e^{i\xi(j+k)}+\sigma^{n}e^{i\xi(j+k-1)}}{\Delta s^{2}}+\frac{\sigma^{n}e^{i\xi(j+1+k)}-2\sigma^{n}e^{i\xi(j+k)}+\sigma^{n}e^{i\xi(j+k-1)}}{\Delta s^{2}}\right)$$

(D.12)

$$U_{j+1}=\sigma^{n}e^{i\xi(j+1)}\qquad U_{j}=\sigma^{n}e^{i\xi(j)}\qquad U_{j-1}=\sigma^{n}e^{i\xi(j-1)}$$

Check the right side:

$$f\left(U\right)=A\left(\frac{U_{i+1,j}^{n}-2U_{i,j}^{n}+U_{i-1,j}^{n}}{\Delta x^{2}}+\frac{U_{i,j+1}^{n}-2U_{i,j}^{n}+U_{i,j-1,}^{n}}{\Delta y^{2}}\right)$$

(D.13a)

$$f(U) = A\left(\frac{\sigma^n e^{i\xi(j+1+k)} - 2\sigma^n e^{i\xi(j+k)} + \sigma^n e^{i\xi(j+k-1)}}{\Delta s^2} + \frac{\sigma^n e^{i\xi(j+1+k)} - 2\sigma^n e^{i\xi(j+k)} + \sigma^n e^{i\xi(j+k-1)}}{\Delta s^2} \right)$$

(D.13b)

Introduction of left side eigenvalue:

$$\lambda = A\left(\frac{e^{i\xi} - 2 + e^{-i\xi}}{\Delta s^2} + \frac{e^{i\xi} - 2 + e^{-i\xi}}{\Delta s^2} \right)$$

(D.14a)

$$\lambda = A\left(\frac{4}{\Delta s^2}\cos(\xi) - \frac{4}{\Delta s^2} \right)$$

(D.14b)

Let:

$$\lambda = \pi \qquad \lambda = A\left(-\frac{8}{\Delta s^2} \right)$$

Introduce the time step:

$$\lambda \Delta t = A\left(-\frac{8}{\Delta s^2} \right)$$

Solve the left hand side for the stability condition:

$$\frac{U_{i,j}^{n+1} 2(1 - B\Delta t) - 4U_{i,j}^{n} + U_{i,j}^{n-1} 2(1 + B\Delta t)}{2\Delta t^2} = f(U)$$

(D.15a)

Variable change for eigenvalue:

$$\frac{W^{n+1} 2(1 - B\Delta t) - 4W^{n} + W^{n-1} 2(1 + B\Delta t)}{2\Delta t^2} = \lambda W^{n}$$

(D.15b)

$$W^{n+1} 2(1 - B\Delta t) - 4W^{n} + W^{n-1} 2(1 + B\Delta t) = 2\Delta t^2 \lambda W^{n}$$

(D.15c)

$$W^{n+1}2(1-B\Delta t)-\left(4+2\Delta t\lambda\right)W^{n}+W^{n-1}2(1+B\Delta t)=0$$

(D.15d)

Stability Ratio: $\sigma=\dfrac{W^{n+1}}{W^{n}}=\dfrac{W^{n}}{W^{n-1}}$

$$2(1-B\Delta t)\sigma^{2}-\left(4+2\Delta t\lambda\right)\sigma+2(1+B\Delta t)=0$$

(D.15e)

Substitute the aspect ratio:

$$2(1-B\Delta t)\sigma^{2}-\left(4+2\Delta t\left(\frac{-8A}{\Delta s^{2}}\right)\right)\sigma+2(1+B\Delta t)=0$$

(D.15f)

Let $\Delta s=L/N$

$$\sigma^{2}-\left(\frac{4+2\Delta t\left(-8A/\left(L/N\right)^{2}\right)}{2\left(1-B\Delta t\right)}\right)\sigma+\frac{2(1+B\Delta t)}{2(1-B\Delta t)}=0$$

(D.15g)

Using the quadratic equation to solve the polynomial:

$$|\sigma|=\left|\left[\left(\frac{4+2\Delta t\left(-8A/\left(L/N\right)^{2}\right)}{2\left(1-B\Delta t\right)}\right)\pm\sqrt{\left(\frac{4+2\Delta t\left(-8A/\left(L/N\right)^{2}\right)}{2\left(1-B\Delta t\right)}\right)^{2}-4(1)\left(\frac{2(1+B\Delta t)}{2(1-B\Delta t)}\right)}\right]\Big/2\right|\leq 1$$

(D.15h)

$$|\sigma|=\left|\left[\left(\frac{4+2\Delta t\left(-8A/\left(L/N\right)^{2}\right)}{2\left(1-B\Delta t\right)}\right)\pm\sqrt{\left(\frac{4+2\Delta t\left(-8A/\left(L/N\right)^{2}\right)}{2\left(1-B\Delta t\right)}\right)^{2}-4(1)\left(\frac{2(1+B\Delta t)}{2(1-B\Delta t)}\right)}\right]\right|\leq 2$$

(D.15i)

Select the time step Δt to satisfy this condition.

Examine the truncation error of the numerical scheme:

Taylor Series expansion of each term:

$$E_{j,k}^{n+1} \approx E_{j,k}^{n} + \Delta t\left(E_{j,k}^{n}\right)_{t} + \frac{1}{2}\Delta t^{2}\left(E_{j,k}^{n}\right)_{tt} + \cdots \qquad E_{j-1,k}^{n} \approx E_{j,k}^{n} - \Delta x\left(E_{j,k}^{n}\right)_{x} + \frac{1}{2}\Delta x^{2}\left(E_{j,k}^{n}\right)_{xx} + \cdots$$

$$E_{j,k}^{n-1} \approx E_{j,k}^{n} - \Delta t\left(E_{j,k}^{n}\right)_{t} + \frac{1}{2}\Delta t^{2}\left(E_{j,k}^{n}\right)_{tt} + \cdots \qquad E_{j,k+1}^{n} \approx E_{j,k}^{n} - \Delta y\left(E_{j,k}^{n}\right)_{y} + \frac{1}{2}\Delta y^{2}\left(E_{j,k}^{n}\right)_{yy} + \cdots$$

$$E_{j+1,k}^{n} \approx E_{j,k}^{n} + \Delta x\left(E_{j,k}^{n}\right)_{x} + \frac{1}{2}\Delta x^{2}\left(E_{j,k}^{n}\right)_{xx} + \cdots \qquad E_{j,k-1}^{n} \approx E_{j,k}^{n} - \Delta y\left(E_{j,k}^{n}\right)_{y} + \frac{1}{2}\Delta y^{2}\left(E_{j,k}^{n}\right)_{yy} + \cdots$$

Substitution into the numerical scheme:

$$\frac{\begin{array}{l}\left[E_{j,k}^{n} + \Delta t\left(E_{j,k}^{n}\right)_{t} + \frac{1}{2}\Delta t^{2}\left(E_{j,k}^{n}\right)_{tt} + \frac{1}{6}\Delta t^{3}\left(E_{j,k}^{n}\right)_{ttt} + \frac{1}{24}\Delta t^{4}\left(E_{j,k}^{n}\right)_{tttt}\cdots\right] - 2E_{j,k}^{n} \\ \quad + \left[E_{j,k}^{n} - \Delta t\left(E_{j,k}^{n}\right)_{t} + \frac{1}{2}\Delta t^{2}\left(E_{j,k}^{n}\right)_{tt} - \frac{1}{6}\Delta t^{3}\left(E_{j,k}^{n}\right)_{ttt} + \frac{1}{24}\Delta t^{4}\left(E_{j,k}^{n}\right)_{tttt}\cdots\right]\end{array}}{\Delta t^{2}}$$

$$= \frac{\begin{array}{l}A\left(\left[E_{j,k}^{n} + \Delta x\left(E_{j,k}^{n}\right)_{x} + \frac{1}{2}\Delta x^{2}\left(E_{j,k}^{n}\right)_{xx} + \frac{1}{6}\Delta x^{3}\left(E_{j,k}^{n}\right)_{xxx} + \frac{1}{24}\Delta x^{4}\left(E_{j,k}^{n}\right)_{xxxx}\cdots\right] - 2E_{j,k}^{n}\right. \\ \left. \quad + \left[E_{j,k}^{n} - \Delta x\left(E_{j,k}^{n}\right)_{x} + \frac{1}{2}\Delta x^{2}\left(E_{j,k}^{n}\right)_{xx} - \frac{1}{6}\Delta x^{3}\left(E_{j,k}^{n}\right)_{xxx} + \frac{1}{24}\Delta x^{4}\left(E_{j,k}^{n}\right)_{xxxx}\cdots\right]\right)\end{array}}{\Delta x^{2}}$$

$$+ \frac{\begin{array}{l}A\left(\left[E_{j,k}^{n} + \Delta y\left(E_{j,k}^{n}\right)_{y} + \frac{1}{2}\Delta y^{2}\left(E_{j,k}^{n}\right)_{yy} + \frac{1}{6}\Delta y^{3}\left(E_{j,k}^{n}\right)_{yyy} + \frac{1}{24}\Delta y^{4}\left(E_{j,k}^{n}\right)_{yyyy}\cdots\right] - 2E_{j,k}^{n}\right. \\ \left. \quad + \left[E_{j,k}^{n} - \Delta y\left(E_{j,k}^{n}\right)_{y} + \frac{1}{2}\Delta y^{2}\left(E_{j,k}^{n}\right)_{xx} - \frac{1}{6}\Delta y^{3}\left(E_{j,k}^{n}\right)_{yyy} + \frac{1}{24}\Delta y^{4}\left(E_{j,k}^{n}\right)_{yyyy}\cdots\right]\right)\end{array}}{\Delta y^{2}}$$

$$+ B\left(\frac{\begin{array}{l}E_{j,k}^{n} + \Delta t\left(E_{j,k}^{n}\right)_{t} + \frac{1}{2}\Delta t^{2}\left(E_{j,k}^{n}\right)_{tt} + \frac{1}{6}\Delta t^{3}\left(E_{j,k}^{n}\right)_{ttt} + \frac{1}{24}\Delta t^{4}\left(E_{j,k}^{n}\right)_{tttt}\cdots \\ -E_{j,k}^{n} + \Delta t\left(E_{j,k}^{n}\right)_{t} - \frac{1}{2}\Delta t^{2}\left(E_{j,k}^{n}\right)_{tt} + \frac{1}{6}\Delta t^{3}\left(E_{j,k}^{n}\right)_{ttt} - \frac{1}{24}\Delta t^{4}\left(E_{j,k}^{n}\right)_{tttt}\cdots\end{array}}{2\Delta t}\right)$$

(D.15j)

Simplification:

$$\frac{\left[\frac{1}{2}\Delta t^2\left(E_{j,k}^n\right)_{tt}+\frac{1}{24}\Delta t^4\left(E_{j,k}^n\right)_{tttt}\cdots\right]+\left[\frac{1}{2}\Delta t^2\left(E_{j,k}^n\right)_{tt}+\frac{1}{24}\Delta t^4\left(E_{j,k}^n\right)_{tttt}\cdots\right]}{\Delta t^2}$$

$$=\frac{A\left(\left[\Delta x^2\left(E_{j,k}^n\right)_{xx}+\frac{1}{24}\Delta x^4\left(E_{j,k}^n\right)_{xxxx}\cdots\right]+\left[\Delta x^2\left(E_{j,k}^n\right)_{xx}+\frac{1}{24}\Delta x^4\left(E_{j,k}^n\right)_{xxxx}\cdots\right]\right)}{\Delta x^2}$$

$$+\frac{A\left(\left[\Delta y^2\left(E_{j,k}^n\right)_{yy}+\frac{1}{24}\Delta y^4\left(E_{j,k}^n\right)_{xxxx}\cdots\right]+\left[\Delta y^2\left(E_{j,k}^n\right)_{y}+\frac{1}{24}\Delta y^4\left(E_{j,k}^n\right)_{yyyy}\cdots\right]\right)}{\Delta y^2}$$

$$+B\left(\frac{\frac{1}{2}\Delta t^2\left(E_{j,k}^n\right)_{tt}+\frac{1}{24}\Delta t^4\left(E_{j,k}^n\right)_{tttt}\cdots+\frac{1}{2}\Delta t^2\left(E_{j,k}^n\right)_{tt}+\frac{1}{24}\Delta t^4\left(E_{j,k}^n\right)_{tttt}\cdots}{2\Delta t}\right)$$

(D.15K)

Simplification:

$$\left(E_{j,k}^n\right)_{tt}+\frac{1}{12}\Delta t^2\left(E_{j,k}^n\right)_{tttt}+O\left(\Delta t^3\right)$$

$$=A\left(\left(E_{j,k}^n\right)_{xx}+\frac{1}{12}\Delta x^2\left(E_{j,k}^n\right)_{xxxx}+\left(E_{j,k}^n\right)_{yy}+\frac{1}{12}\Delta y^2\left(E_{j,k}^n\right)_{yyyy}+O(\Delta x^3,\Delta y^3)\right)$$

$$+B\left(\left(E_{j,k}^n\right)_{t}+\frac{1}{6}\Delta t^2\left(E_{j,k}^n\right)_{ttt}+O\left(\Delta t^3\right)\right)$$

(D.15L)

Isolate the PDE terms to the left side of the equation:

$$\left(E_{j,k}^{n}\right)_{tt} - A\left[\left(E_{j,k}^{n}\right)_{xx} + \left(E_{j,k}^{n}\right)_{yy}\right] - B\left(E_{j,k}^{n}\right)_{t} = \frac{1}{12}\Delta t^{2}\left(E_{j,k}^{n}\right)_{tttt} + O\left(\Delta t^{3}\right)$$

$$A\left(\frac{1}{12}\Delta x^{2}\left(E_{j,k}^{n}\right)_{xxxx} + \frac{1}{12}\Delta y^{2}\left(E_{j,k}^{n}\right)_{yyyy} + O(\Delta x^{3}, \Delta y^{3})\right)$$

$$+B\left(\frac{1}{6}\Delta t^{2}\left(E_{j,k}^{n}\right)_{ttt} + O\left(\Delta t^{3}\right)\right) \quad \text{(D.15M)}$$

The Truncated terms remain on the right side of the equation:

$$\tau = \left[-\frac{1}{12}\left(E_{j,k}^{n}\right)_{tttt} + B\left(\frac{1}{6}\right)\Delta t^{2}\left(E_{j,k}^{n}\right)_{ttt}\right]\Delta t^{2}$$

$$+\left(\frac{A}{12}\Delta x^{2}\left(E_{j,k}^{n}\right)_{xxxx} + \frac{A}{12}\Delta y^{2}\left(E_{j,k}^{n}\right)_{yyyy}\right) + O(\Delta t^{3}, \Delta x^{3}, \Delta y^{3})$$

(D.15N)

$\therefore$ First Order Accurate Scheme

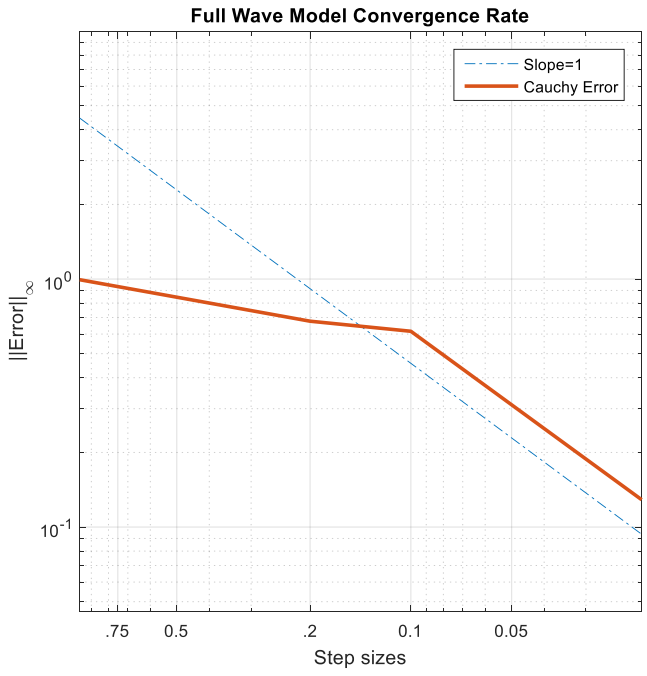

L = 210 meters

N = 512 samples

$\Delta t = 0.1$

Figure 139. Cauchy Error Convergence Rate for Full Wave Explicit Scheme

APPENDIX E. Pulse Coherence Model Comprehensive Results

The following results are focused on observing the power distributions for changes in direction, polarization, and frequency. This analysis intends to be primarily qualitative to determine the conditions that causes the most significant changes in the scattering function's secondary calculations. These results were also considered when attempting to minimize the test matrix presented in chapter 4.

Figure 140. Power Delay Profiles in relation to Propagation Direction

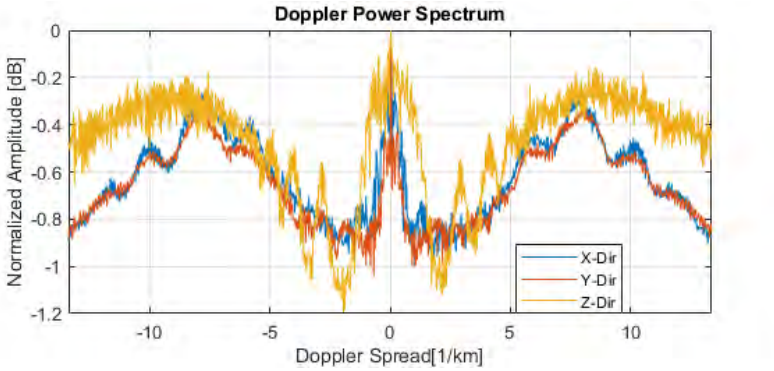

Figure 141. Doppler Power Spectrum in relation to Propagation Direction

Figure 140 shows the lowest power delay profile occurring along the z-propagation path, the elongated portion of the flute structure. In the *z*-direction, the doppler power spectrum decay is more gradual with a wider doppler spread across the peak amplitude. The frequency correlation power distribution tends to be higher with a

slightly wider coherence bandwidth. Examining the spatial coherence, second order peaks in magnitude occur in the z-direction and appear non-periodic in the *x*-pol. case. In the y-direction, y-pol. case, the second order peaks appear to be periodic (occurring every 30 km) with inconsistent spatial coherence relative to the first order peak.

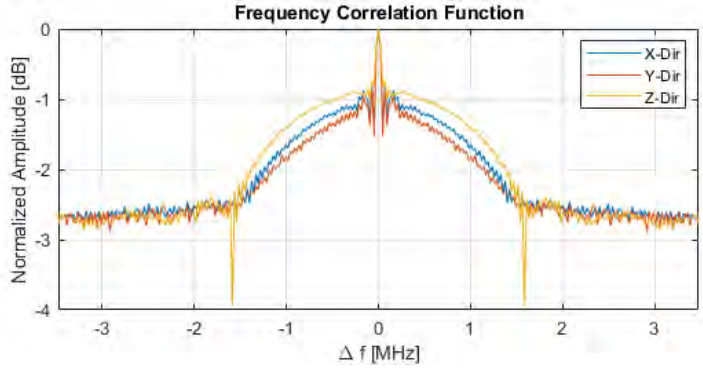

Figure 142. Frequency Correlation Function in relation to Propagation Distances

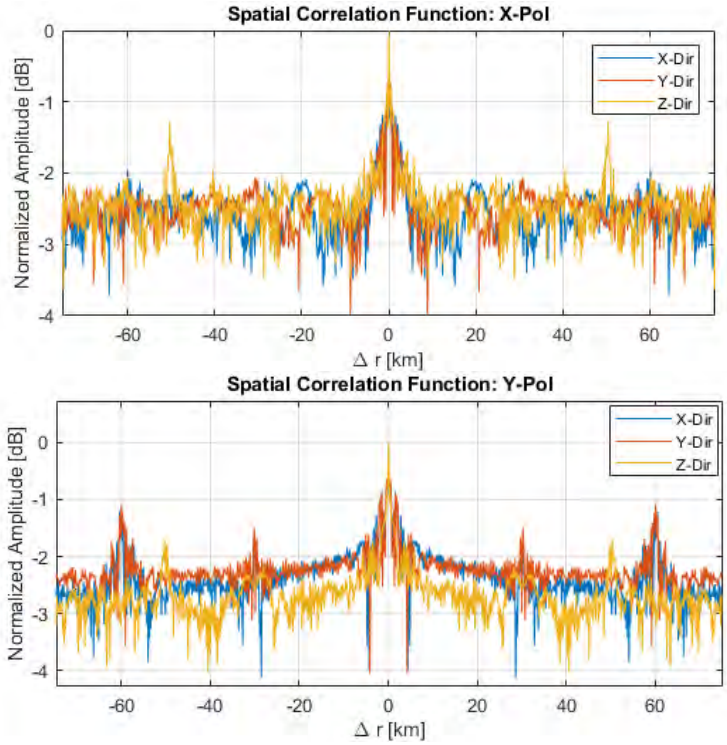

Figure 143. Frequency Correlation Function in relation to Propagation Distances

In terms of propagation distance, the power distributions tend to be more consistent, with very subtle differences primarily observed in the doppler power spectrum. The power

roll-off has a tendency to decline more rapidly as the scattered energy spreads more outward over propagation distance. However, the doppler spread, coherence bandwidth, and spatial coherence tend to remain consistent.

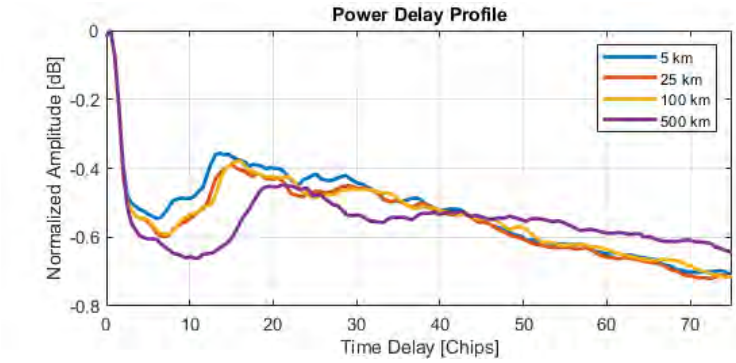

Figure 144. Power Delay Profiles in relation to Propagation Distances

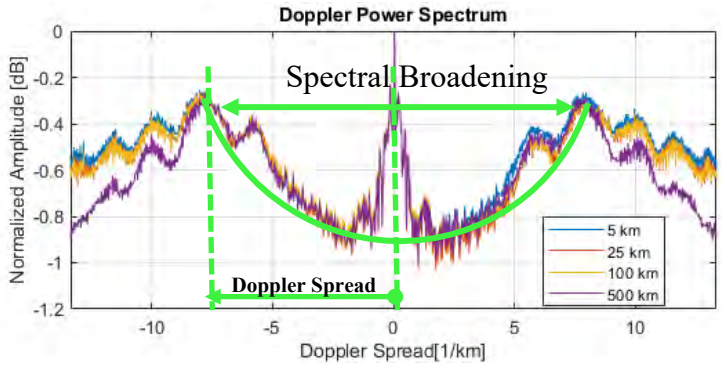

Figure 145. Doppler Power Spectrum in relation to Propagation Distances

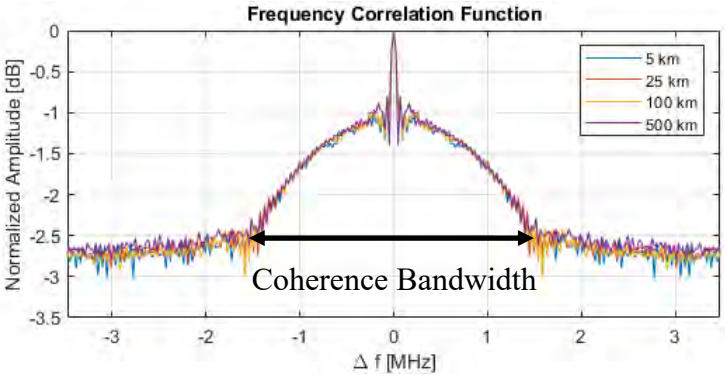

Figure 146. Power Delay Profiles in relation to Propagation Distances

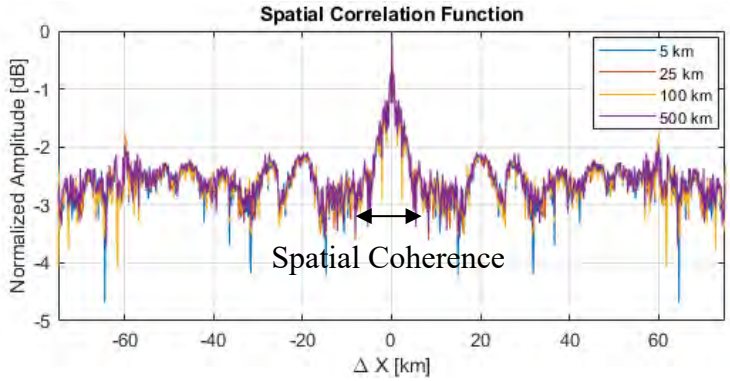

Figure 147. Spatial Correlation Function in relation to Propagation Distances

The variability in the results caused by increasing the carrier frequency are notably distinguishable in large part due to the reduction in scattering features. Higher frequency causes the power delay profile to decline, increases the spectral broadening, spatial coherence of the signal, and coherence bandwidth of the propagation channel.

Figure 148. Power Delay Profiles in relation to Carrier Frequency

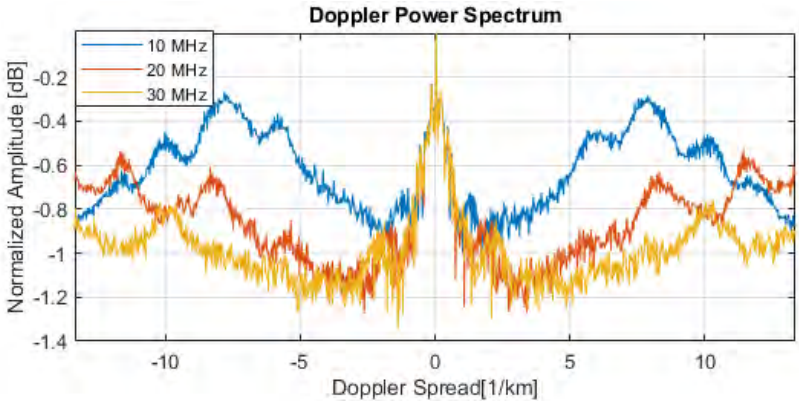

Figure 149. Doppler Power Spectrums in relation to Carrier Frequency

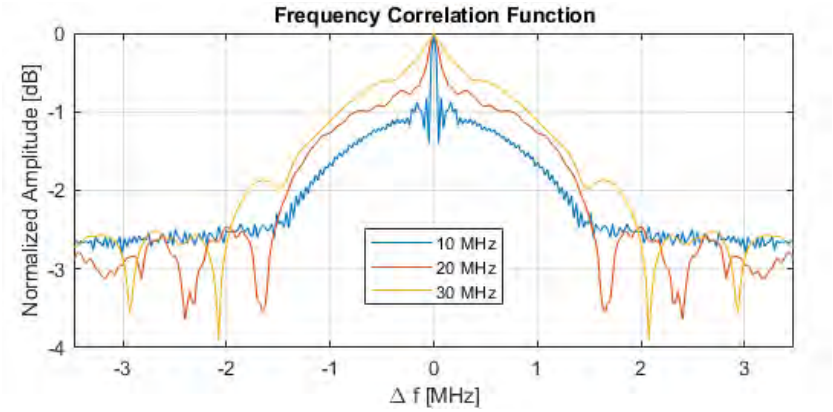

Figure 150. Frequency Correlation Function in relation to Carrier Frequency

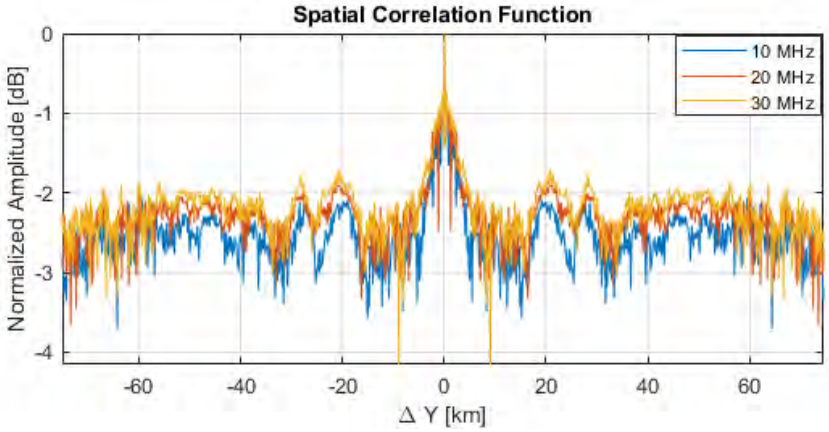

Figure 151. Spatial Correlation Function in relation to Carrier Frequency

The linear polarization orientation also has notable differences, primarily in the amplitude levels of the power distributions. Cross-interference caused by edge diffraction tends to be more prevalent in the y-pol. case, causing significant lobbing in the doppler power spectrum, and second order peaks in the spatial correlation function.

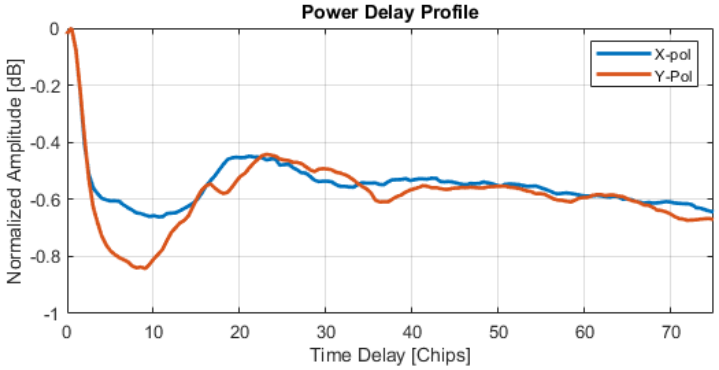

Figure 152. Power Delay Profiles in relation to Polarization

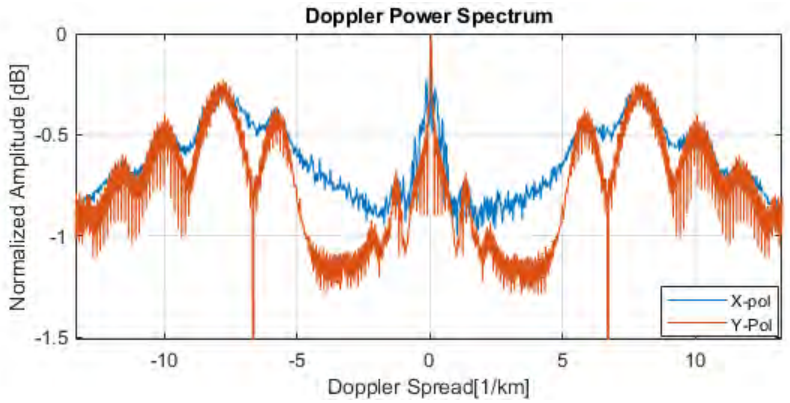

Figure 153. Power Delay Profiles in relation to Polarization

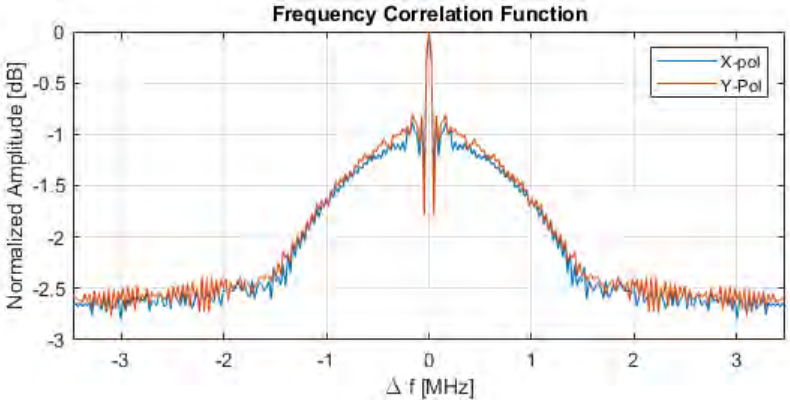

Figure 154. Frequency Correlation functions in relation to Polarization

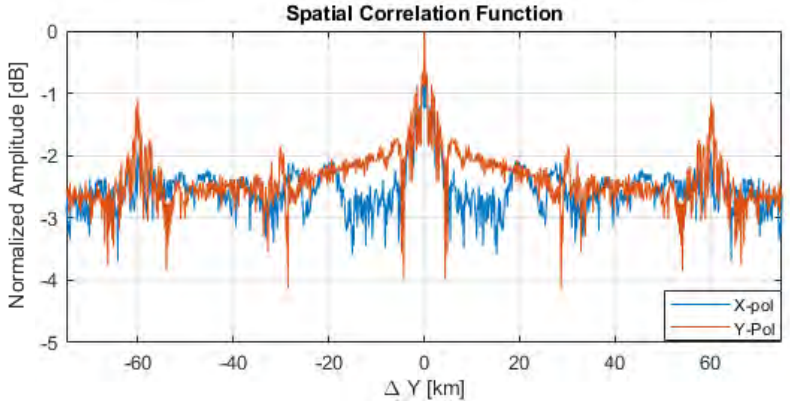

Figure 155. Spatial Correlation Functions in relation to Polarization

Comparisons of the power distributions between the single flute and stochastic flute cases reveal subtle differences. The power delay is clearly greater in magnitude with multiple scattering sources present in the propagation channel as is the case of the stochastic flute

map. The doppler power lobbing characteristics observed previously in the y-pol. stochastic map case is also present in the single flute case in addition to a significant increase in the depth of the power level decay along the doppler spread. The profile of the spatial correlation and frequency correlation functions appear to be the same for both flute maps. The second order peaks appear to occur along the same regions of the grid in the spatial correlation function.

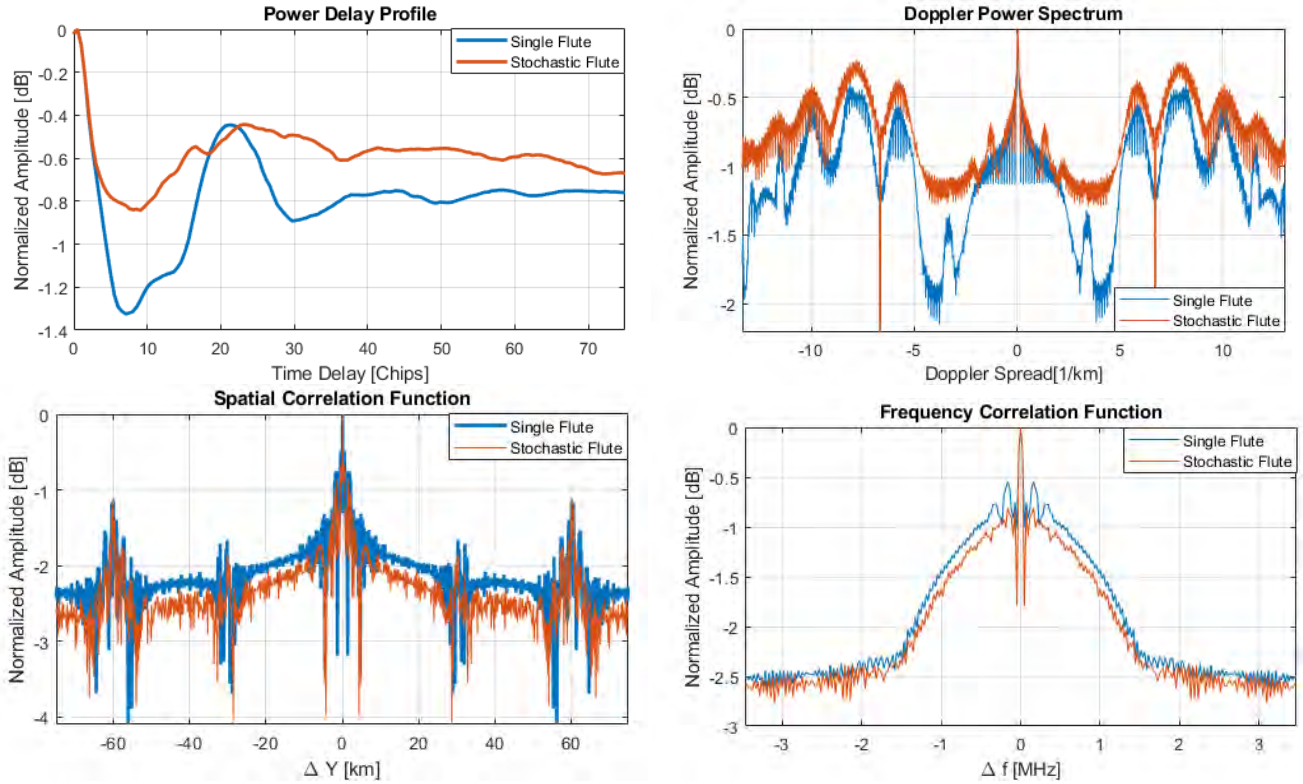

Figure 156. Secondary Calculation comparisons between Single Flute and Stochastic Flute Results

Based on these results, it is clear that changes to the frequency and polarization causes more significant differences observed in the secondary calculations than the physical characteristics of the flute structures within the density map. The single flute and stochastic flute map differences are primarily revealed in the power spectrum

magnitudes, whereas the features of those distributions are largely dependent on the frequency and polarization.

The following results compare the scattering characteristics of the Kolmogorov and Flute structures. These results are shown for the *x*-pol. cases in which the flute structure had the most subtle features observed previously. Additionally, the Kolmogorov phase cube has a low phase variance, sufficient to for creating weak scattering conditions. It is evident that the flute can cause more significant broadening in the peak power distributions over spatial and frequency variations. However, the Kolmogorov structure causes a greater spectral broadening and smaller spatial coherence and coherence bandwidths. The quantitative results to these observations are provided in Figure 158.The combination of flute and Kolmogorov phase cubes are demonstrated in Chapter 5.

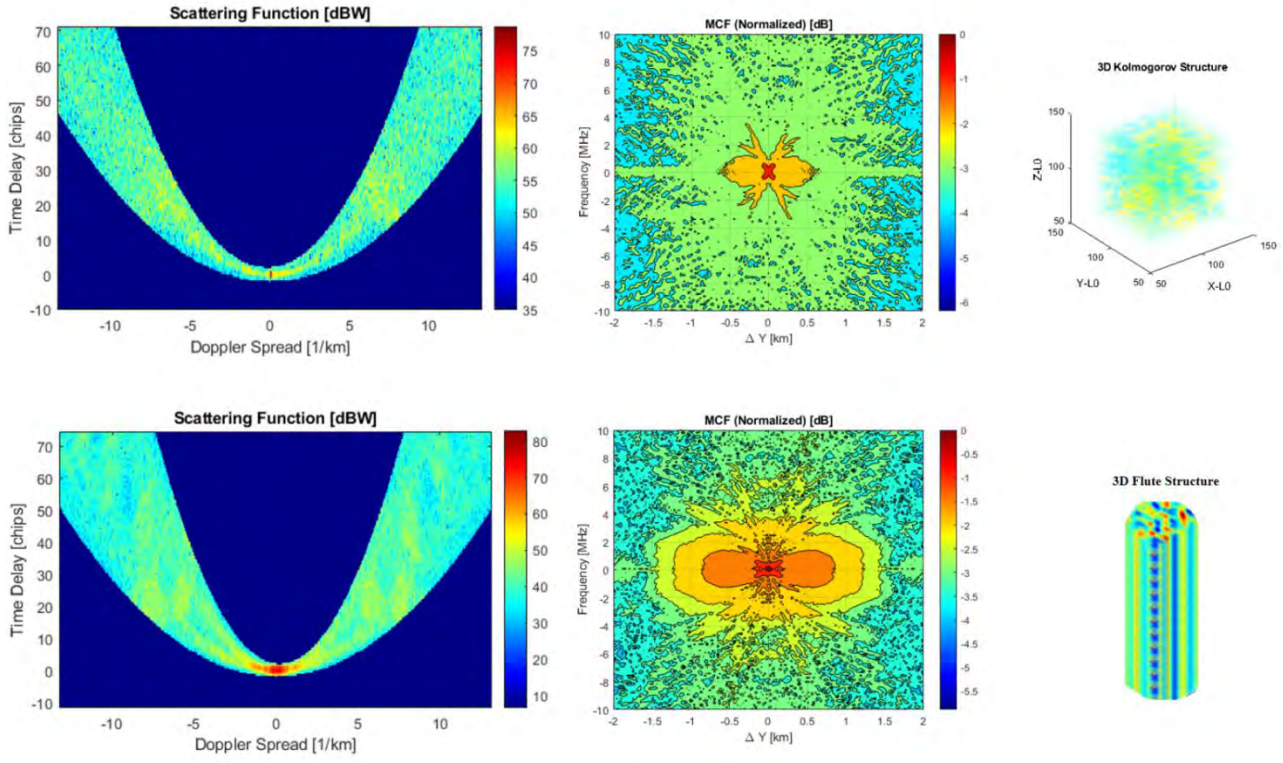

Figure 157. Scattering Function and Mutual Coherence Comparisons between Kolmogorov and Stochastic Flute Results

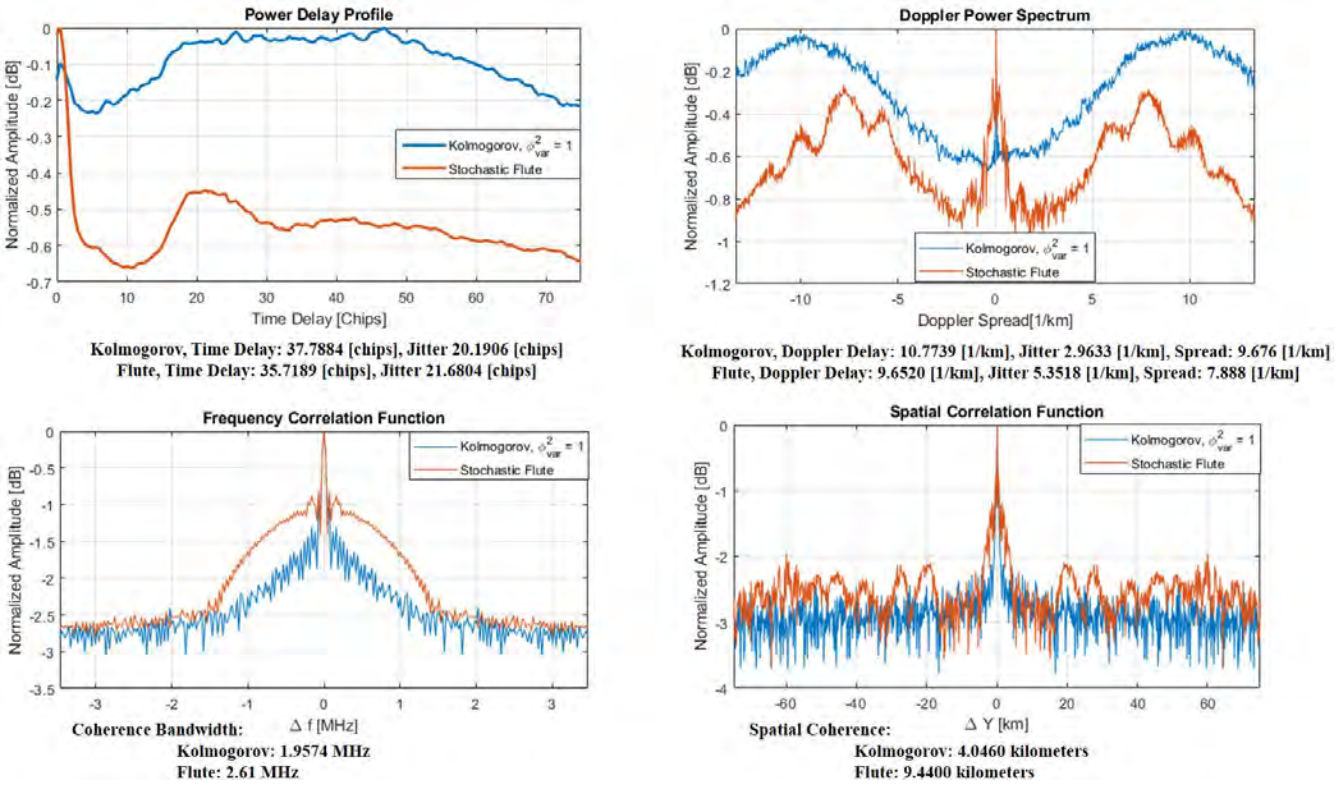

Figure 158. Secondary Calculation comparisons between Kolmogorov and Stochastic Flute Results

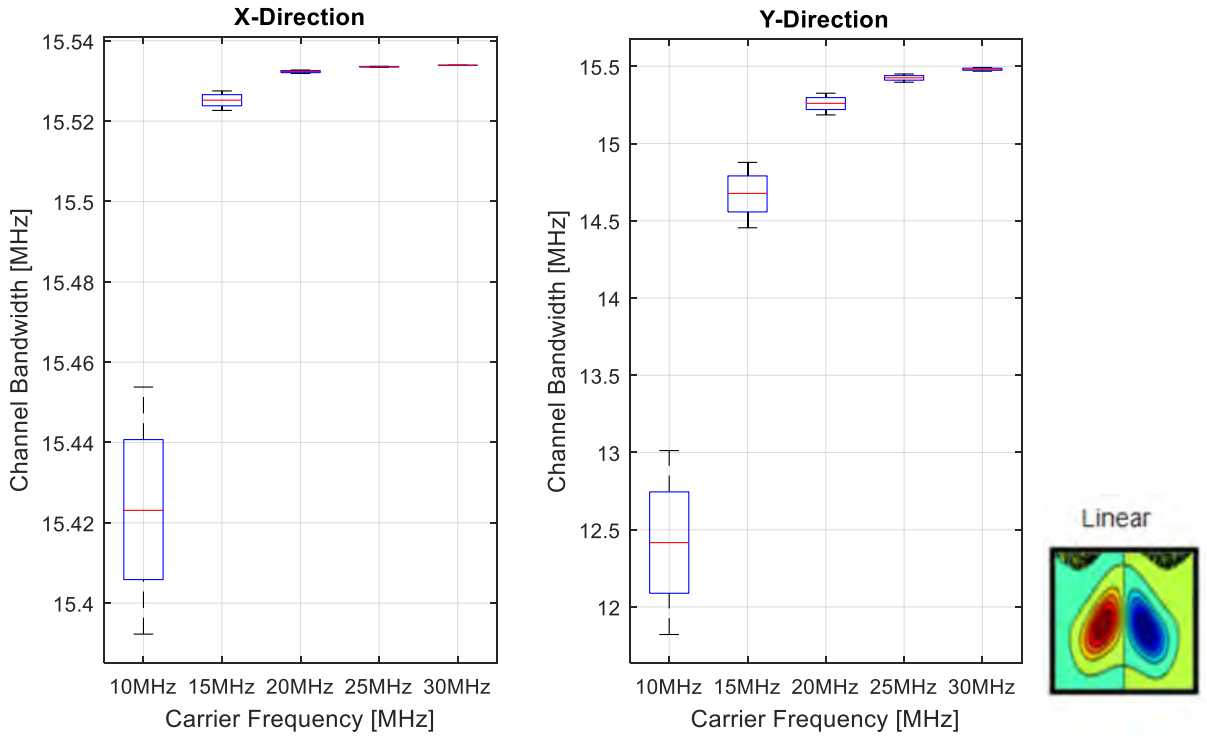

Figure 159. Coherence Bandwidth Frequency Sweep for Isolated Flute Channel

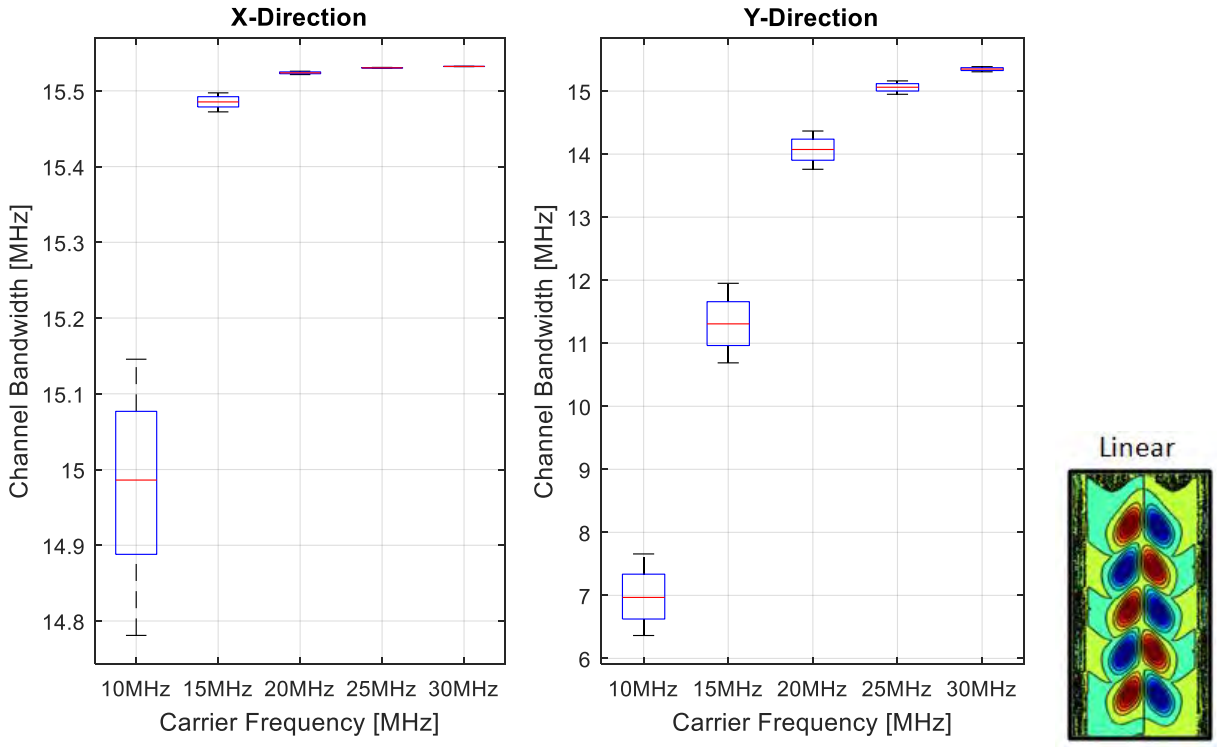

Figure 160. Coherence Bandwidth Frequency Sweep for Flute Array Channel

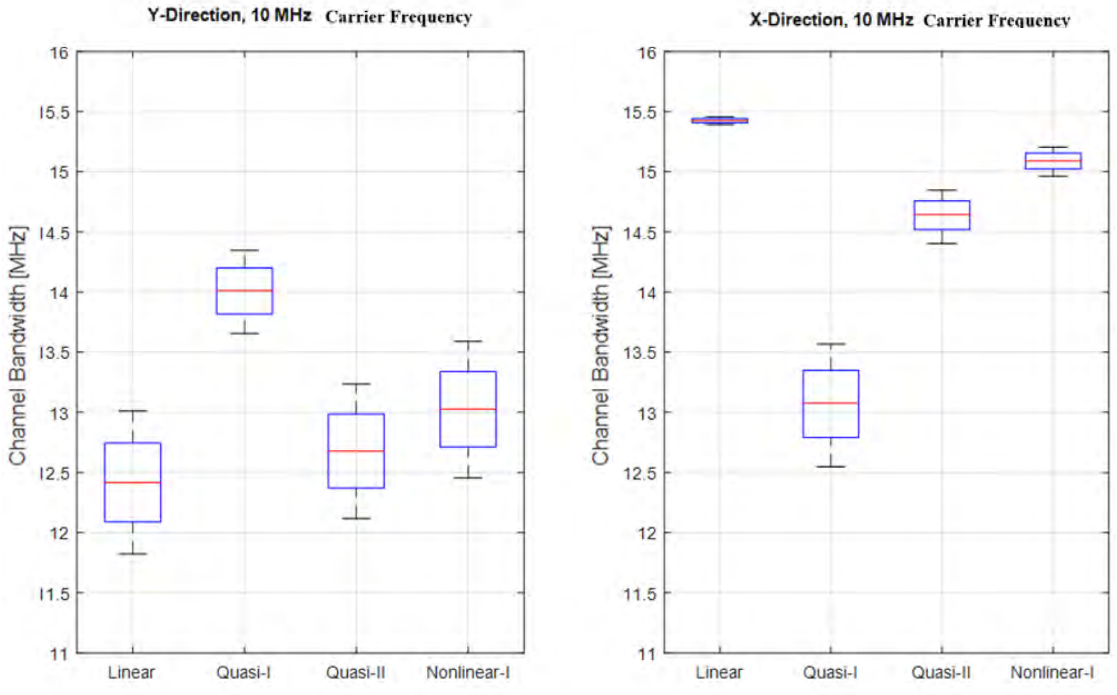

Figure 161. Phase Scintillation averaged over propagation distance for Isolated Flutes

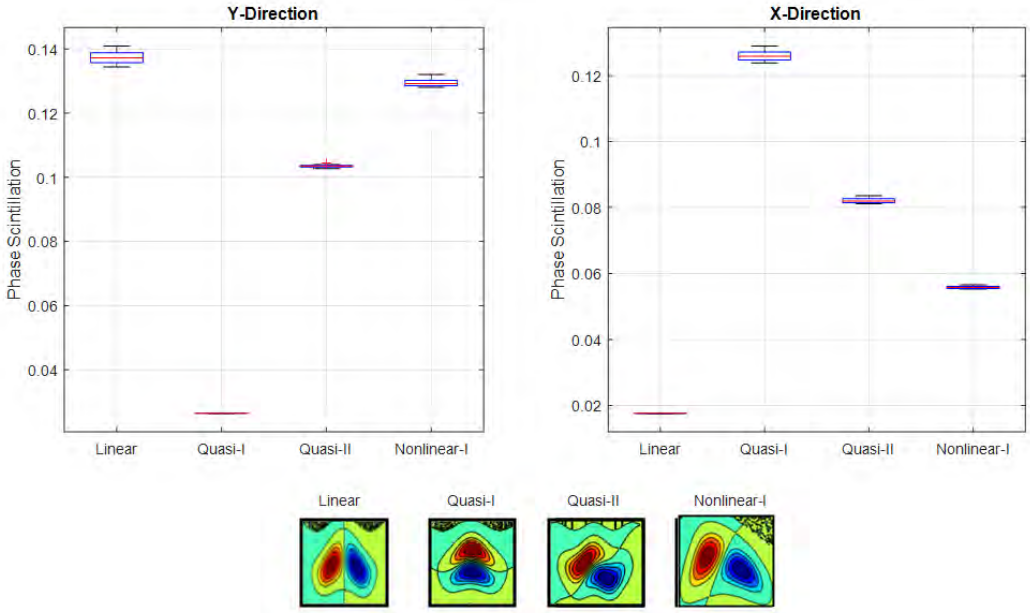

Figure 162. Phase Scintillation averaged over propagation distance for Isolated Flutes

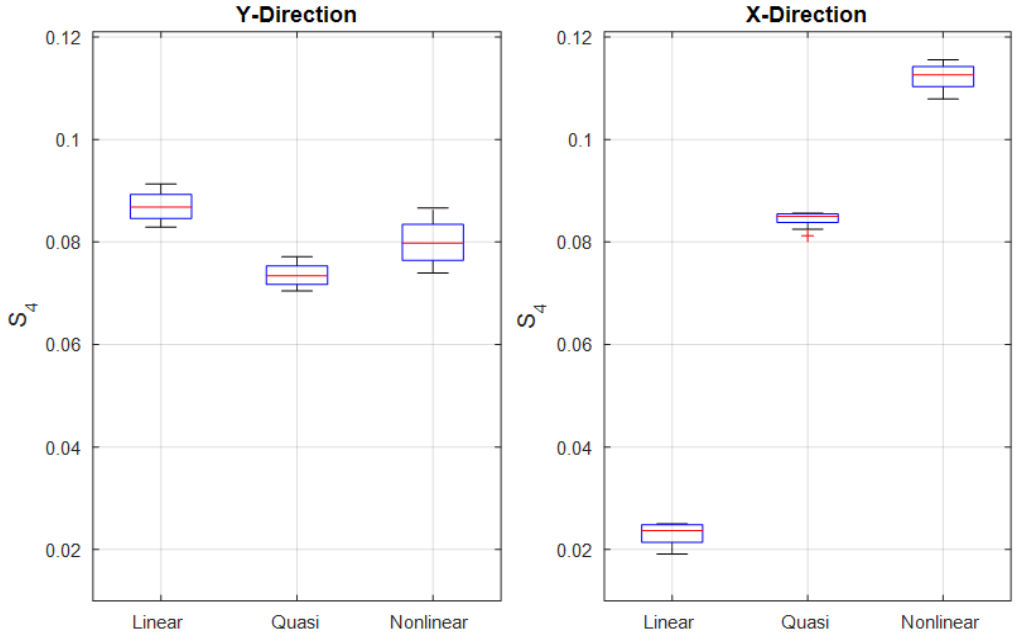

Figure 163. Scintillation Index averaged over propagation distance for Flute Arrays

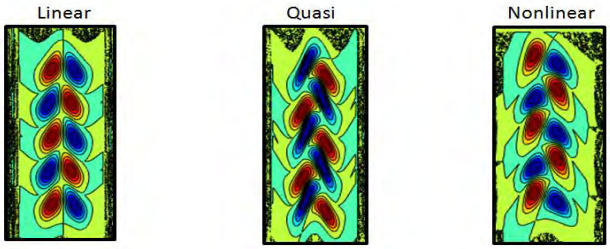

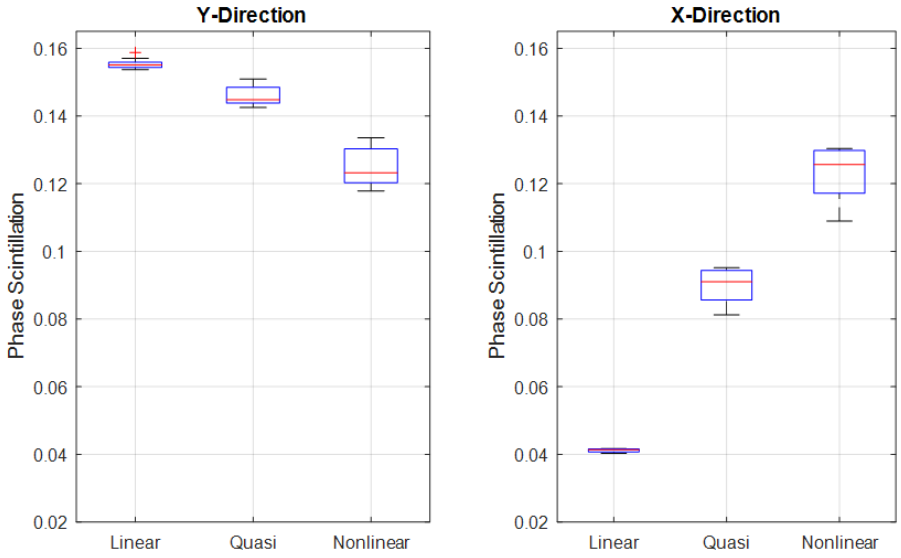

Figure 164. Phase Scintillation averaged over propagation distance for Flute Arrays

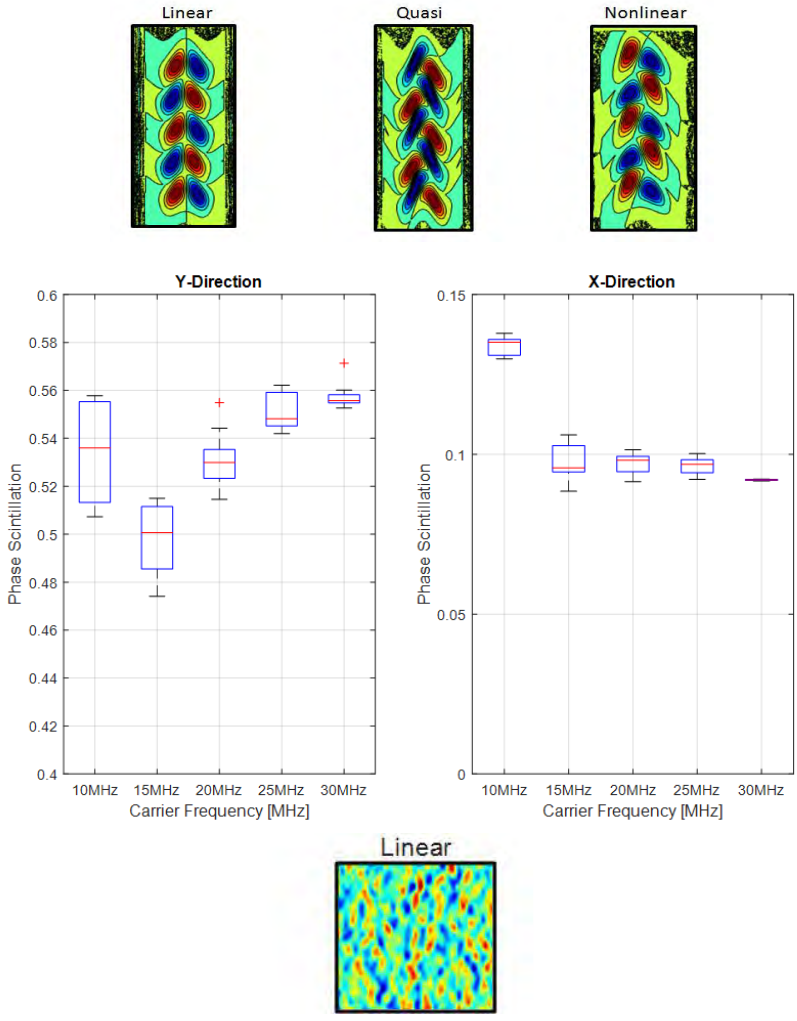

Figure 165. Phase Scintillation averaged over propagation distance for Stochastic Flute Map

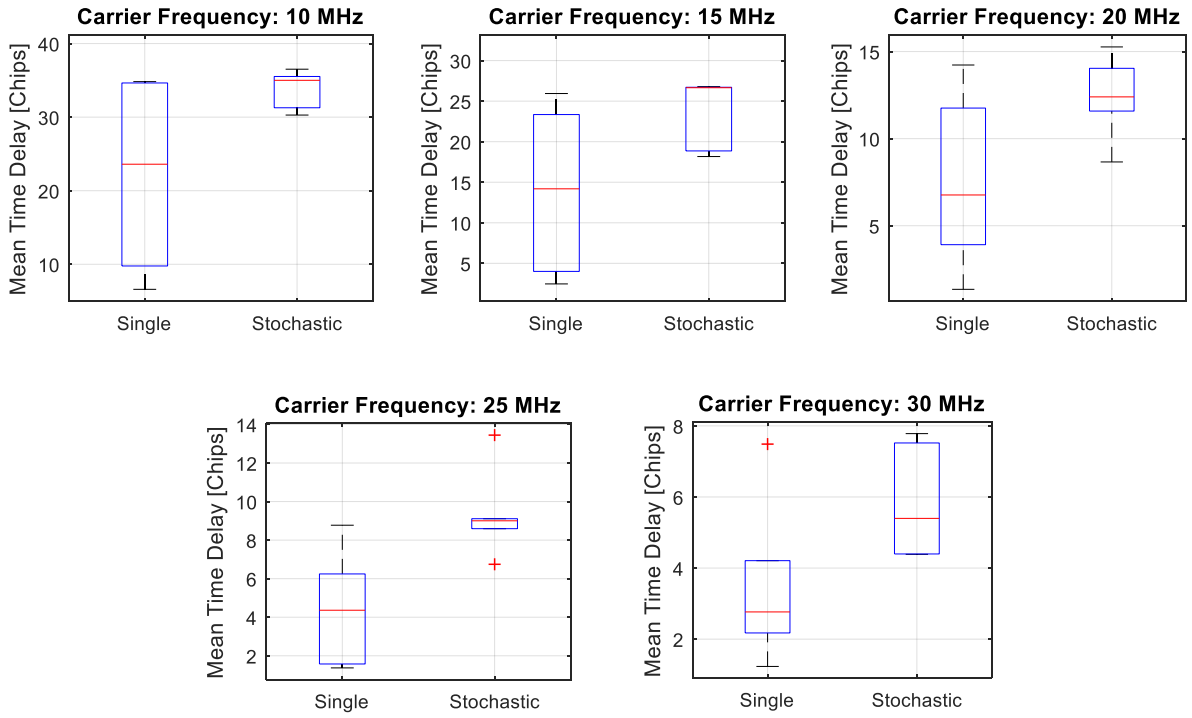

Figure 166.Time Delay averaged over propagation distance for Single and Stochastic Flute Maps

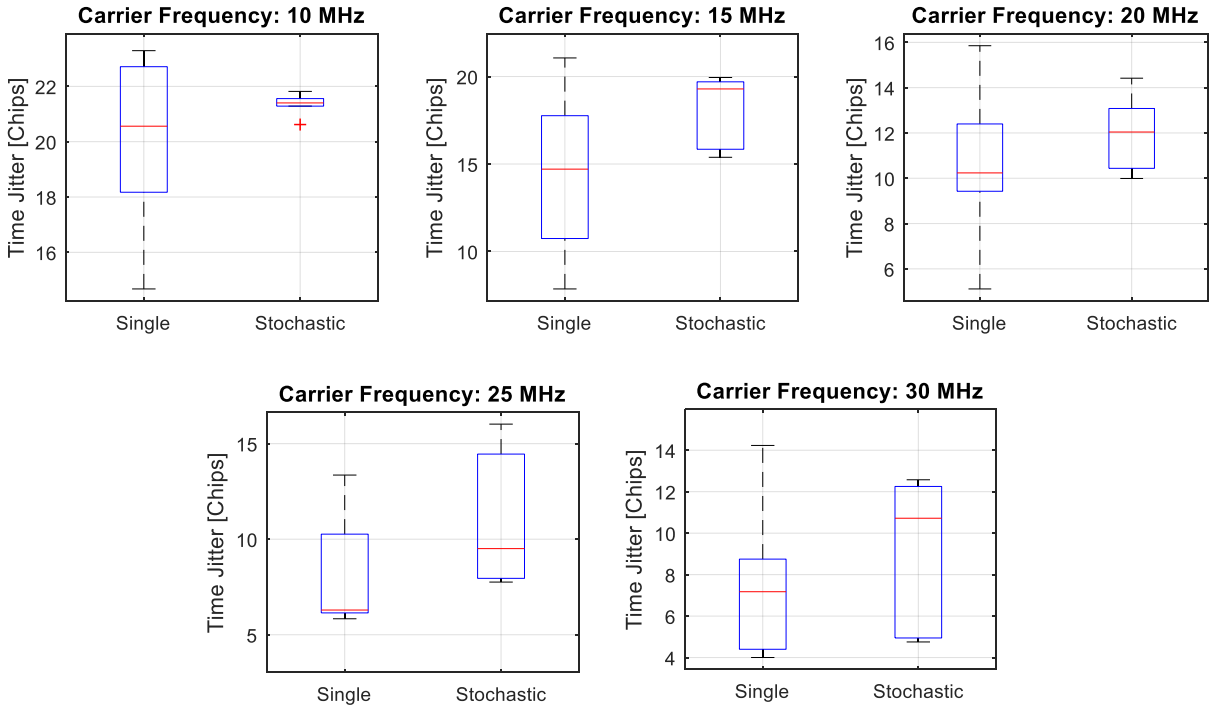

Figure 167.Time Jitter averaged over propagation distance for Single and Stochastic Flute Maps

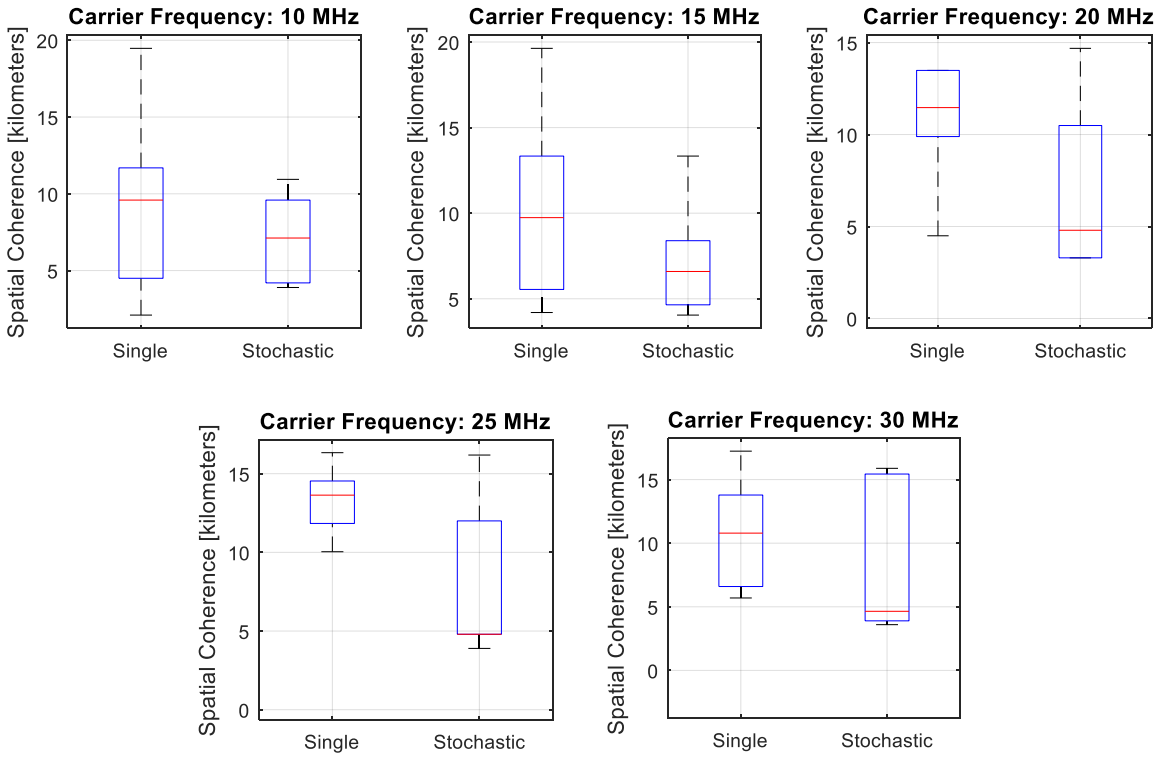

Figure 168. Spatial Coherence averaged over propagation distance for Single and Stochastic Flute Maps

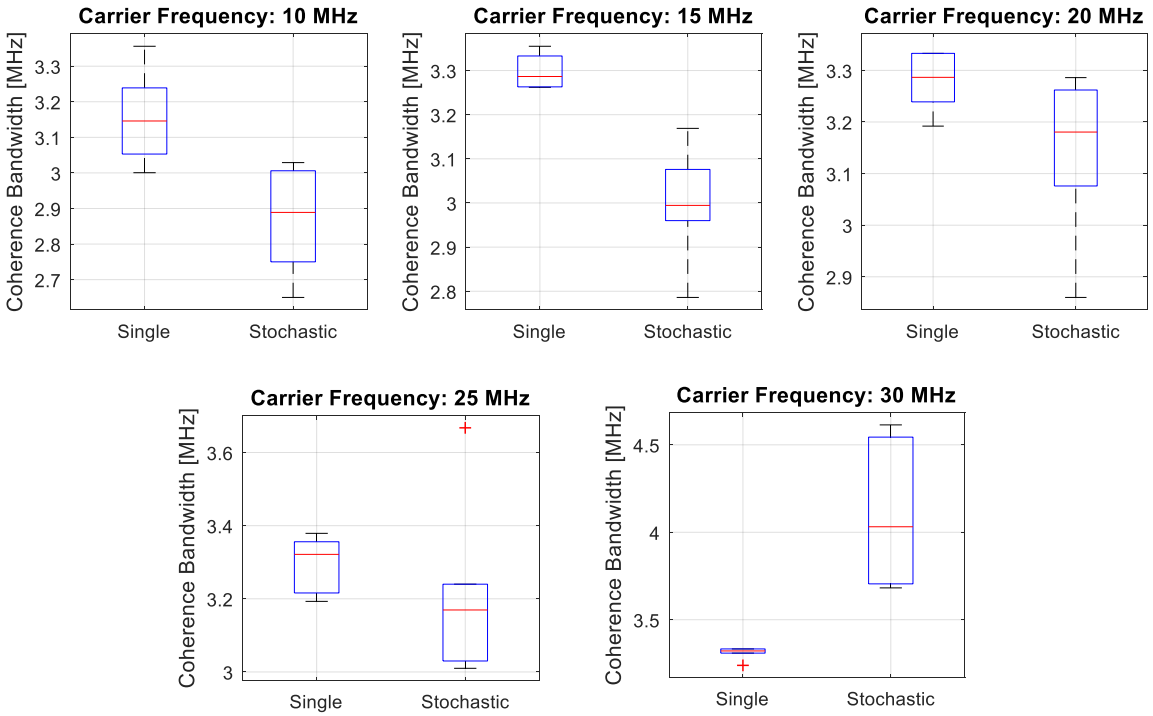

Figure 169. Coherence Bandwidth averaged over propagation distance for Single and Stochastic Flute Maps

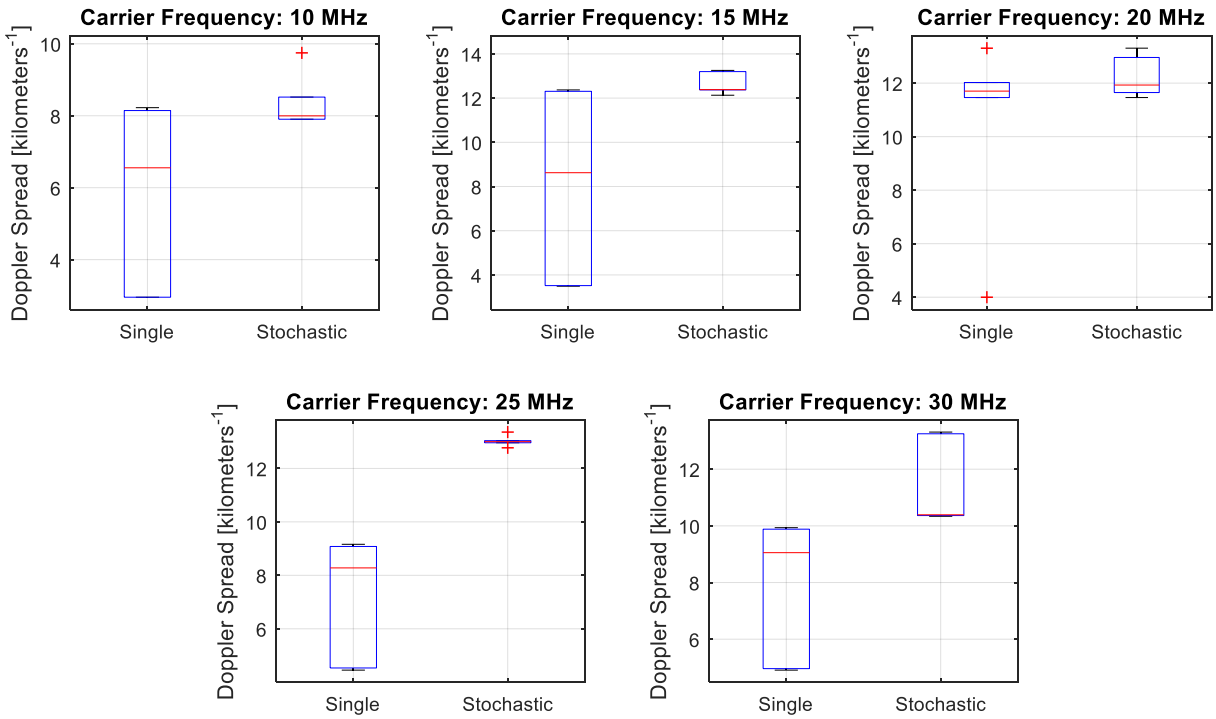

Figure 170. Doppler Spread averaged over propagation distance for Single and Stochastic Flute Maps

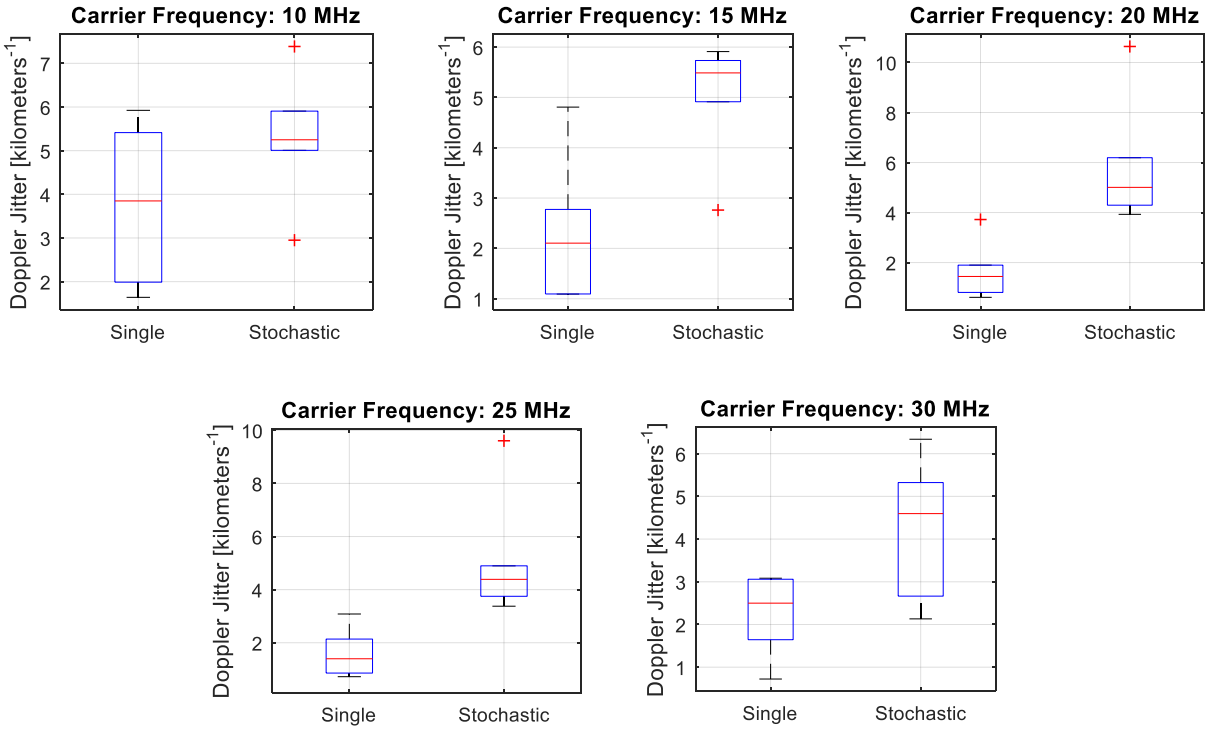

Figure 171. Doppler Jitter averaged over propagation distance for Single and Stochastic Flute Maps

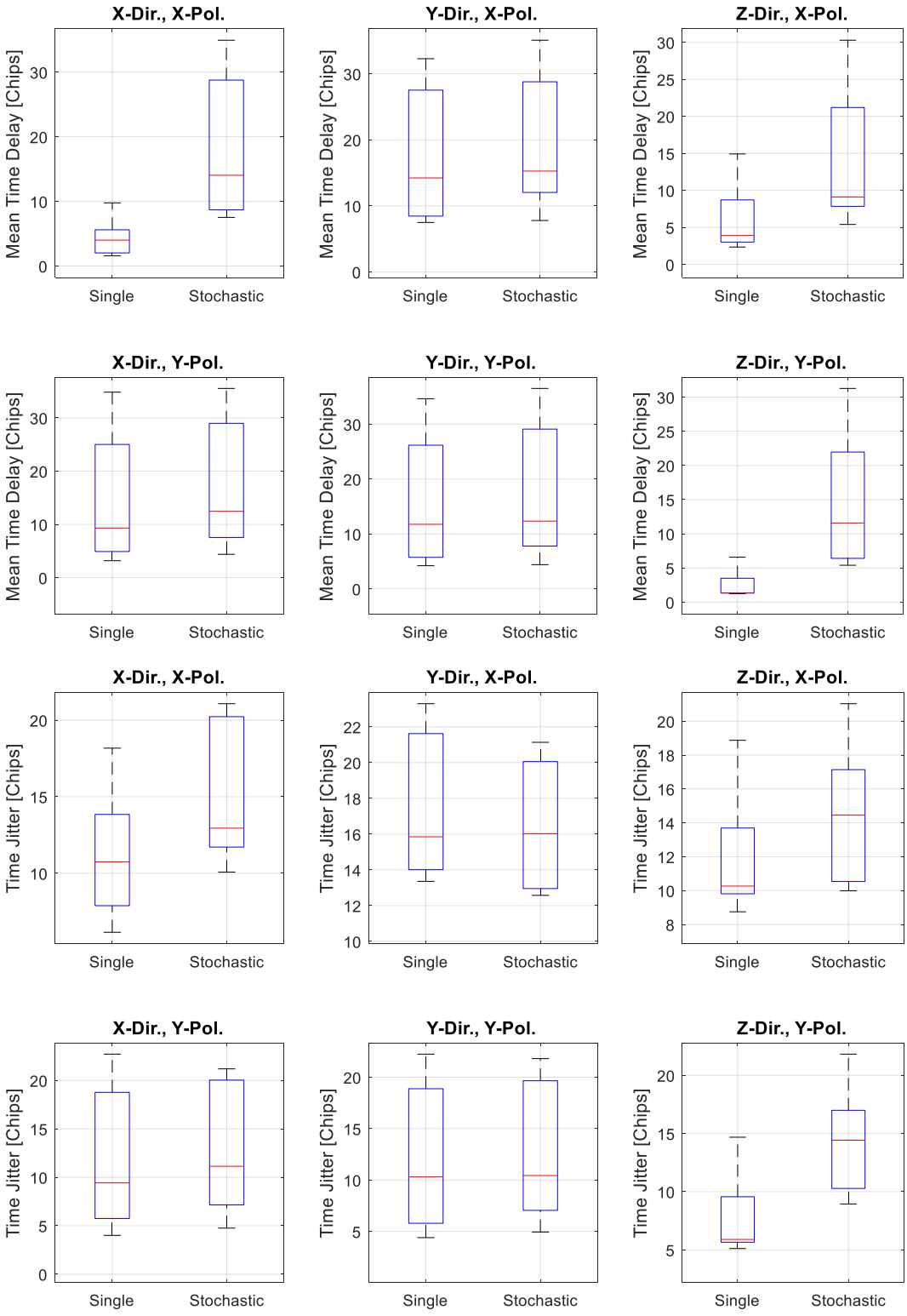

Figure 172. Mean Time Delay and Jitter averaged over propagation distance for Single and Stochastic Flute Maps for a combination of polarizations

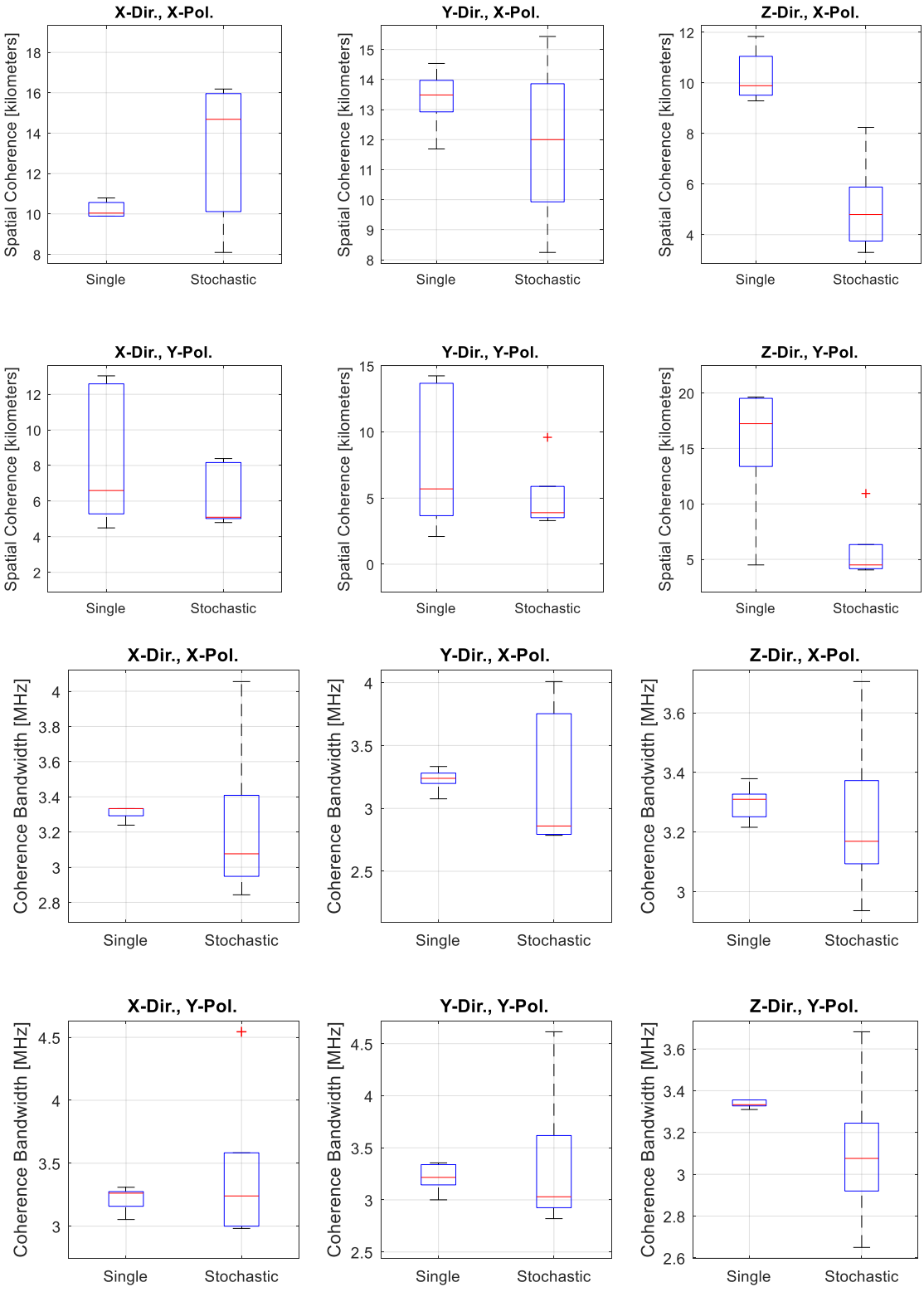

Figure 173. Spatial and Bandwidth Coherence averaged over propagation distance for Single and Stochastic Flute Maps for a combination of polarizations

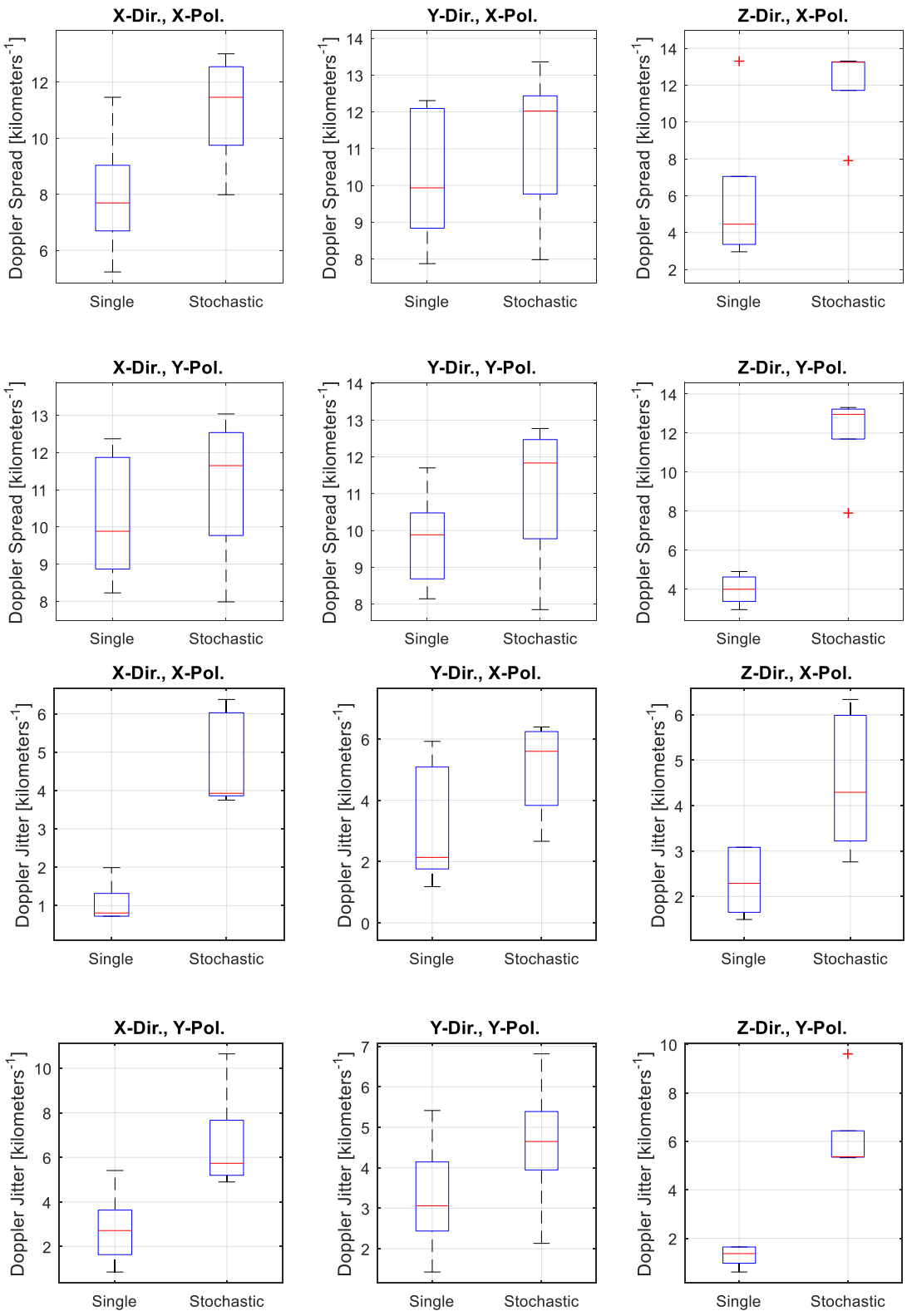

Figure 174. Doppler Spread and Jitter Coherence averaged over propagation distance for Single and Stochastic Flute Maps for a combination of polarizations

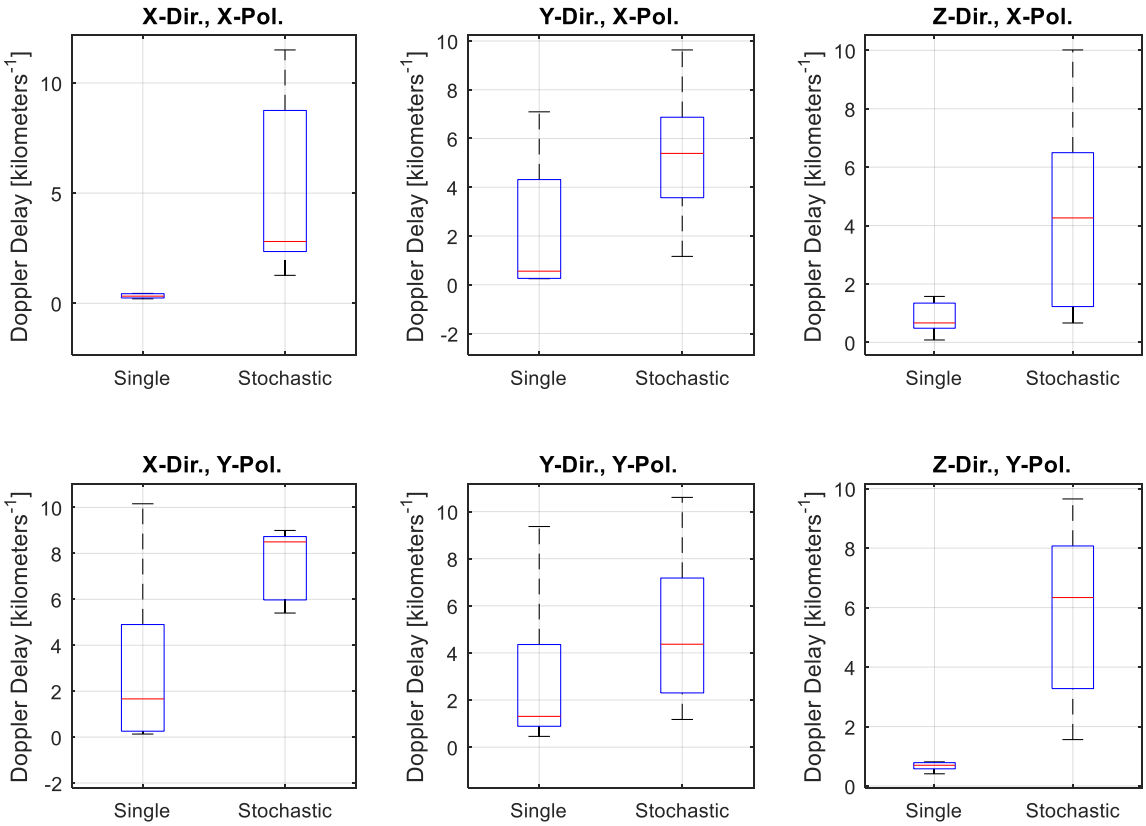

Figure 175. Doppler Delay Coherence averaged over propagation distance for Single and Stochastic Flute Maps for a combination of polarizations

APPENDIX F. 1D vs. 2D Propagation Results

The propagation effects between the 1D and 2D propagation algorithms is evident in Figure 173. At a distance of 0.5 meters, the peak intensity caused by the lens is identical. Propagation beyond this region is where the edge diffraction begins to dominate. This appears to significantly differ between the 1D and 2D propagation models at a 2 meter propagation distance. This simple example alludes to a potential cause for the differences in the flute structure model 1D and 2D results. The comparison of the results from each propagation algorithm become less coherent as the diffraction persists.

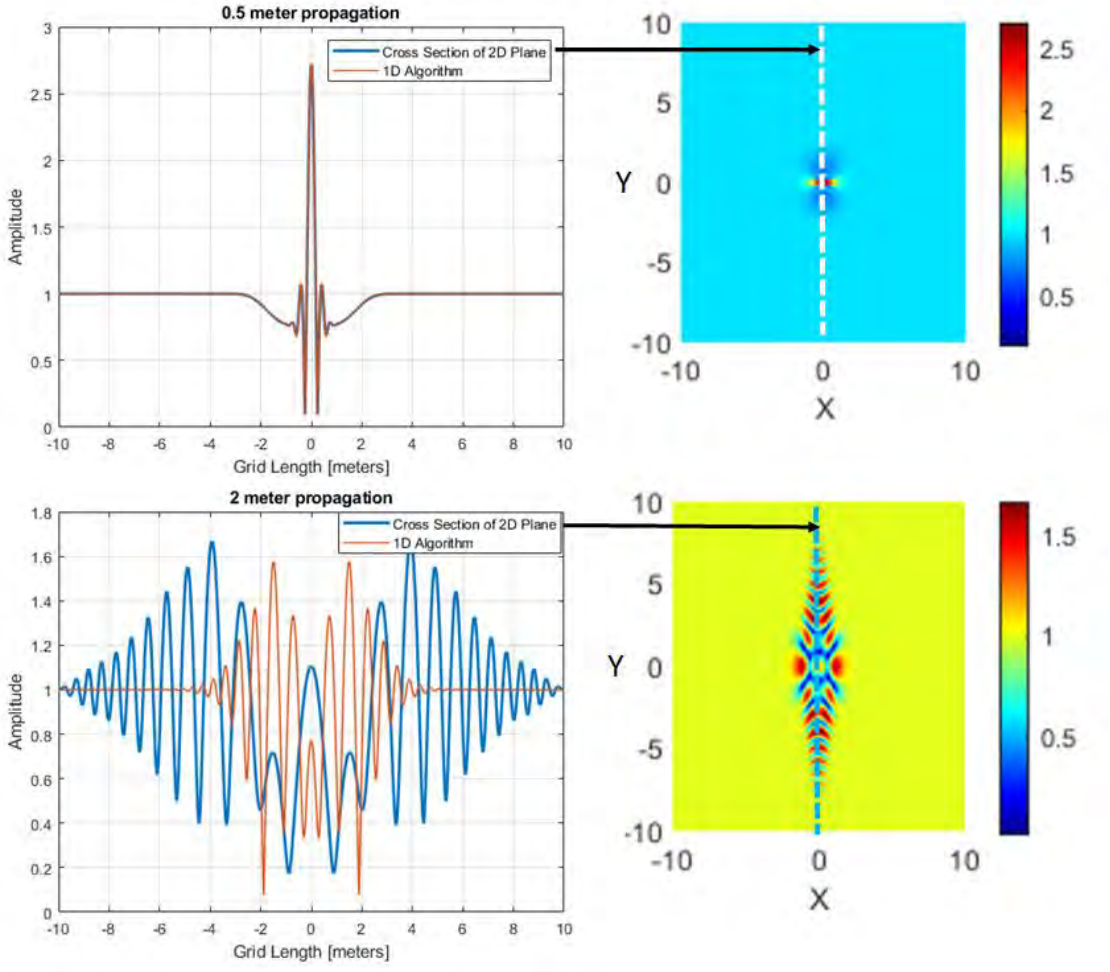

Figure 176. Gaussian Lens Effect for 1D (left) and 2D (right) Scattering Planes

APPENDIX G. Ray Trace Validation

The following results demonstrate the agreement between the ray-trace coupled phase screen approach and Snell's Law of refraction. The concept is demonstrated in a basic two-layer medium in which the ray starts in a medium of air and passes through a refractive material. Applying a variety of angles between 0 and 90 degrees at 0.5 degree increments, the polarization coefficients acquired at the final point are compared to the those determined by Snell's law. Examining the error plots in Figure 179, the error converges to ~0..01 for steeper angles that cause the most significant refraction. These differences are likely a result of the numerical error from the first order gradient differentials applied when calculating the velocity vectors.

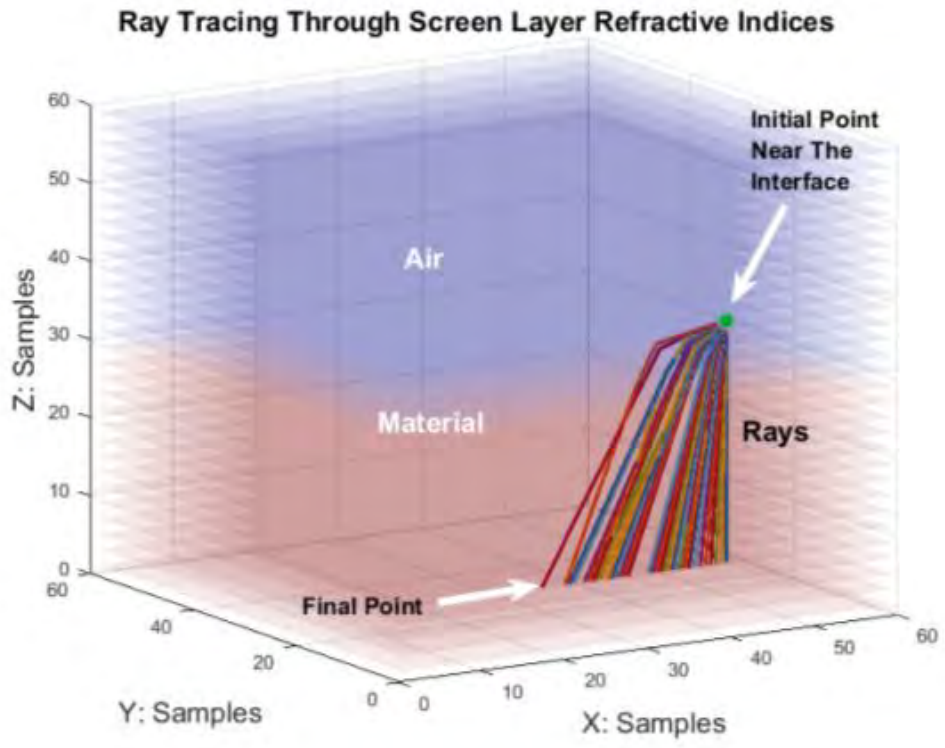

Figure 177. Phase Screen - Ray Trace Validation Model

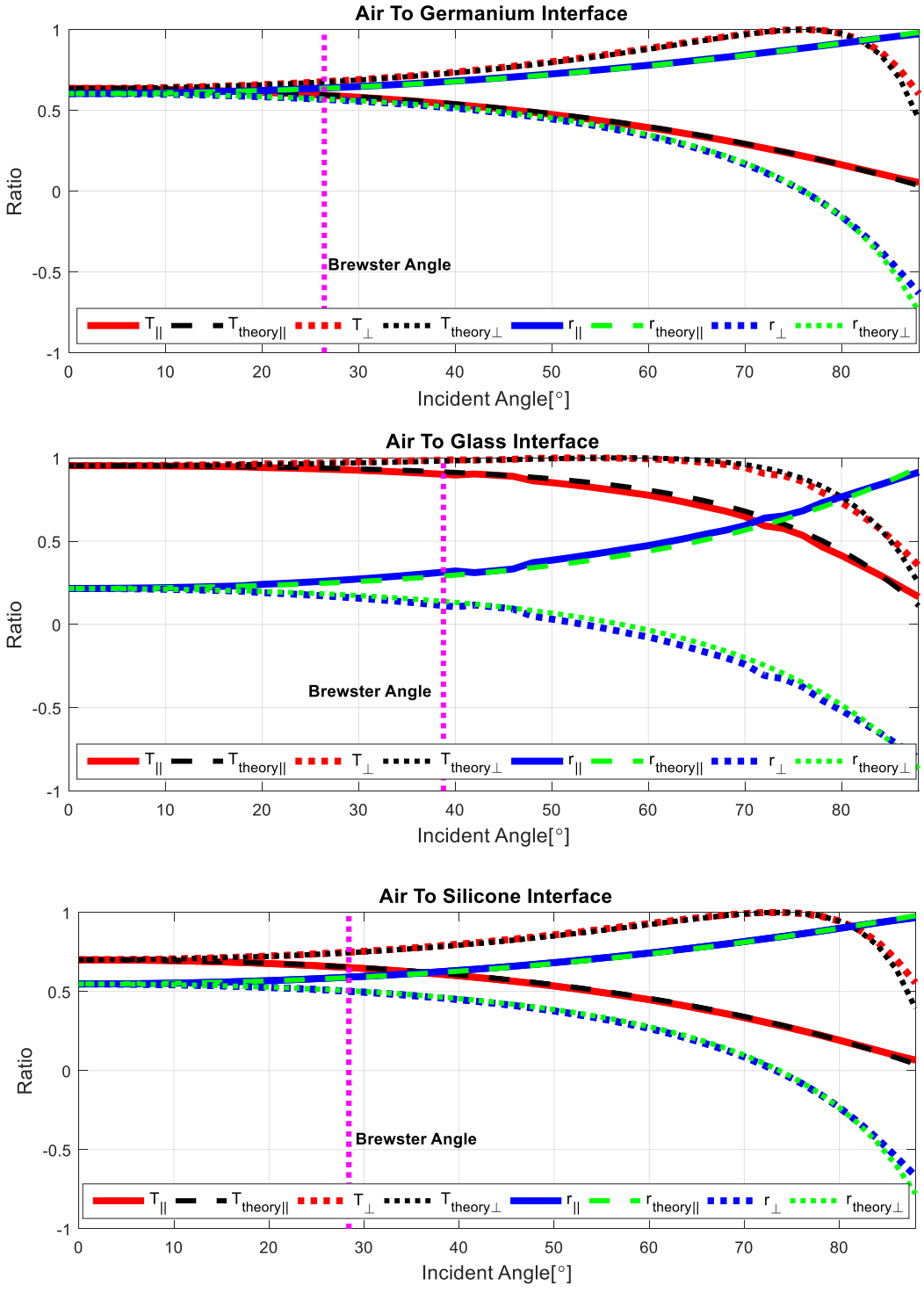

Figure 178. Refractive Interfaces and Corresponding Polarization Coefficients

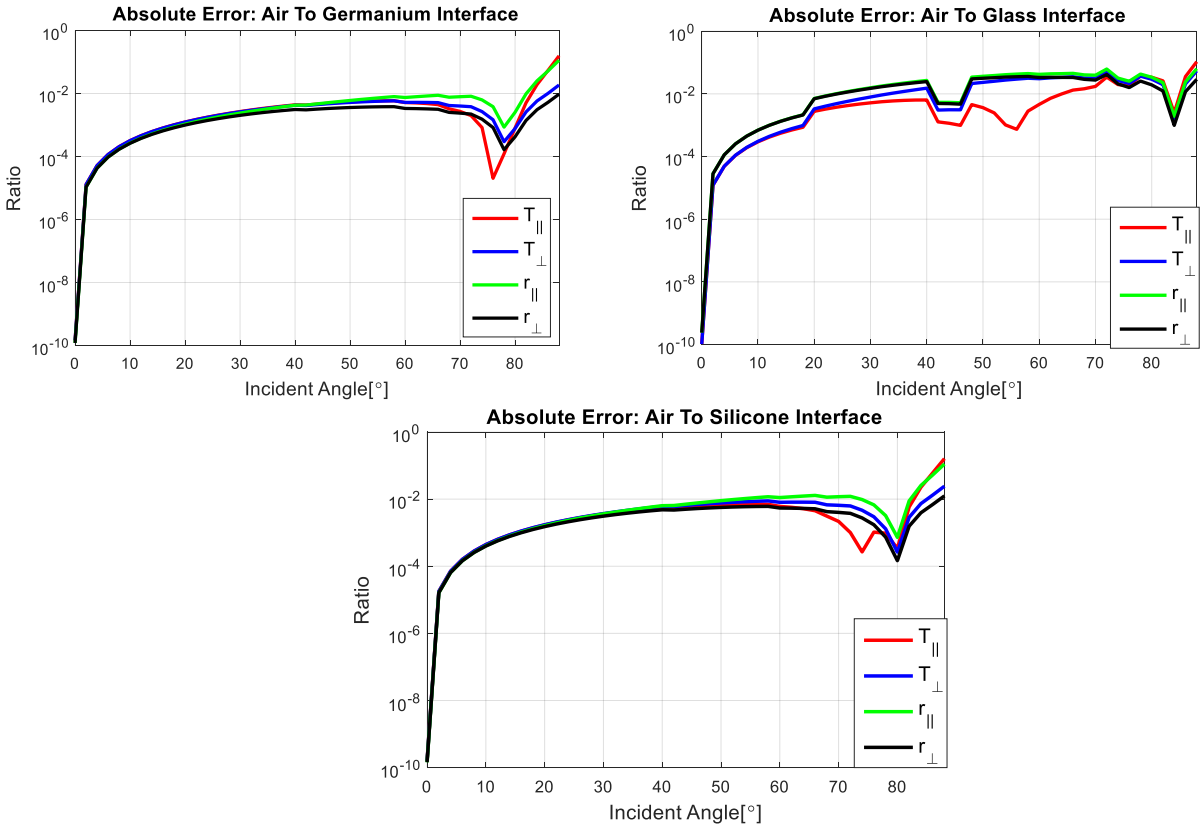

Figure 179. Error Calculations of the Ray Tracer Compared to Snell's Law

Bibliography

[1]. V. Sotnikov, T. Kim, J.Lundberg, I. Paraschiv, and T. Mehlhorn, "Scattering of electromagnetic waves by vortex density structures associated with interchange instability: Analytical and large scale plasma simulation results,"*Physics of Plasmas*, 21(5), 052309, 2014.

[2]. V. Sotnikov, T. Kim, E. Mishin, W. Amatucci, G. Ganguli, and T. Mehlhorn, "Low Frequency Plasma Turbulence as a Source of Clutter in Surveillance and Communication", *Advanced Maui Optical and Space Surveillance Technologies Conference*, 2012.

[3]. J. Nycander, and V. P. Pavlenko, "Localized flute vortices in plasmas," *Physica Scripta*, vol. 43, no. 1, pp. 95–99, 1991. doi:10.1088/0031-8949/43/1/016.

[4]. Yasin, Essam, "Modulational Instability and Electromagnetic Wave Scattering of Plasma Flute Modes", Dissertation, University of Nevada, Reno, 2010 https://scholarworks.unr.edu/handle/11714/4428.

[5]. R.O. Dendy, *Plasma Dynamics*, Oxford University Press, USA, 1990

[6]. R. Schunk, A. Nagy, *Ionospheres: Physics, Plasma Physics, and Chemistry*, Cambridge University Press, 2nd edition, 2009

[7]. M. J.Keskinen, "The structure of the high-latitude ionosphere and magnetosphere," *Johns Hopkins APL Technical Digest*, vol. 5, 1984, pp. 154–158.

[8]. L. S. Wagner, J. A. Goldstein, M. A. Rupar, and E. J. Kennedy, "Northern Exposure 1992: An investigation of transauroral HF radio skywave propagation", *NRL*, 1993.

[9]. K. C. Yeh, and C. H. Liu, "Radiowave scintillations in the ionosphere," *Proc. IEEE*, 70, 324-360, 1982.

[10]. E. D. Tereshchenko, M. O. Kozlova, Evstafiev, O. V., B. Z. Khudukon, T. Nygrén, M. Rietveld, and A. Brekke, "Irregular structures of the F layer at high latitudes during ionospheric heating," *Ann. Geophys*., 18, 1197–1209, https://doi.org/10.1007/s00585-000-1197-1, 2000.

[11]. H. Mounir, A. Berthelier, J. C. Cerisier, D. Lagoutte, and C. Beghin, "The small-scale turbulent structure of the high latitude ionosphere - Arcad-Aureol-3 observations," *Annales Geophysicae*, vol. 9, 1991, pp. 725–737.

[12]. J. M. Cordes, B. J. Rickett, D. R. Stinebring, and W. A. Coles, "Theory of parabolic arcs in interstellar scintillation spectra," *Astrophys. Journal*. 637, 346–365, 2006.

[13]. K. C. Yeh and C. H. Liu, "An investigation of temporal moments of stochastic waves," *Radio Science*, vol. 12, no. 5, pp. 671-680, Sept.-Oct. 1977, doi: 10.1029/RS012i005p00671.

[14]. Y. Béniguel, V. Romano, L. Alfonsi, M. Aquino, A. Bourdillon, P. Cannon, G. De Franceschi, S. Dubey, B. Forte, V. Gherm, N. Jakowski, M. Materassi, T. Noack, M. Pozoga, N. Rogers, P. Spalla, H. J. Strangeways, E. M.Warrington, A. Wernik, V. Wilken, N. Zernov, "Ionospheric scintillation monitoring and modeling". *Ann. Geophys*. [Internet]. 2009Apr.25 [cited 2021Jul.30];52(3-4):391-416. Available from: https://www.annalsofgeophysics.eu/index.php/annals/article/view/4595

[15]. Caltech. (2013, October 14). Chapter 19 Magnetohydrodynamics. pmaweb.caltech.edu . http://www.pmaweb.caltech.edu › 1219.2.K.pdf.

[16]. J. Pedlosky, *Geophysical Fluid Dynamics*, 2nd ed, Springer-Verlag, New York, 1987.

[17]. S. Fielding, "The Basics of Fluid Dynamics" (PDF). Durham University. Retrieved 22 December 2019.

[18]. J. J. Y. Hsu, "Visual and computational plasma physics," New Jersey: World Scientific, 2015.

[19]. H. Bhatia, G. Norgard, V. Pascucci, et al., "The helmholtz-hodge decomposition-a survey. Visualization and Computer Graphics," *IEEE Transactions*, 2013, 19(8): 1386-1404.

[20]. I. Horvath, E. A. Essex. "Vertical E x B drift velocity variations and associated low-latitude ionospheric irregularities investigated with the TOPEX and GPS satellite data," *Annales Geophysicae*, European Geosciences Union, 2003, 21 (4), pp.1017-1030. hal-00317049

[21]. P. Satyanarayana, P. N. Guzdar, J. D. Huba, and S. L. Ossakow, "Rayleigh-Taylor instability in the presence of a stratified shear layer," *J. Geophys. Res*., 89(A5), 2945–2954, 1984, doi:10.1029/JA089iA05p02945.

[22]. T. J. M. Boyd and J. J. Sanderson, *The Physics of Plasmas*. Cambridge: Cambridge University Press, 2003.

[23]. I. Sandberg, Zh. N. Andrushchenko, and V. P. Pavlenko, Phys. Plasmas 12, 042311 (2005). https://doi.org/10.1063/1.1883183

[24]. Makoto Sasaki,Naohiro Kasuya, Shinichiro Toda, Takuma Yamada, Yusuke Kosuga, Hiroyuki Arakawa, Tatsuya Kobayashi, Shigeru Inagaki, Akihide Fujisawa, Yoshihiko Nagashima, Kimitaka Itoh, Sanae-I Itoh, "Multiple-Instabilities in Magnetized Plasmas with Density Gradient and Velocity Shears," *Plasma and Fusion Research*, 2017, Volume 12, Pages 1401042, Released November 28, 2017, Online ISSN 1880-6821, https://doi.org/10.1585/pfr.12.1401042, https://www.jstage.jst.go.jp/article/pfr/12/0/12_1401042/_article/-char/en

[25]. Lehnert, *Basic Features of Plasma Instabilities*, 1972

[26]. T. Tajima, W. Horton, P. J. Morrison, J. Schutkeker, T. Kamimura, K. Mima, and Y. Abe, "Instabilities and vortex dynamics in shear flow of magnetized plasmas, "*Physics of Fluids B: Plasma Physics* 3, 938-954 (1991) https://doi.org/10.1063/1.859850

[27]. A. S. Richardson, "NRL Plasma Formulary", *Naval Research Laboratory*, 2019

[28]. Pen, Ue-Li & Levin, Yuri. "Pulsar scintillations from corrugated reconnection sheets," *ISM. Monthly Notices of the Royal Astronomical Society*. 442. 10.1093/mnras/stu1020, 2013.

[29]. D. Stinebring, B. Rickett, and S. Ocker,"The Frequency Dependence of Scintillation Arc Thickness in Pulsar B1133+16," 2018.

REPORT DOCUMENTATION PAGE

Form Approved
OMB No. 074-0188

1. REPORT DATE *(DD-MM-YYYY)*	2. REPORT TYPE	3. DATES COVERED *(From – To)*
01-09-2021	Dissertation	September 2018– September 2021

TITLE AND SUBTITLE

Ionospheric F-Layer Dipole Flute Instability Effects on Electromagnetic Scattering in a Magnetohydrodynamic Plasma

5a. CONTRACT NUMBER

5b. GRANT NUMBER

5c. PROGRAM ELEMENT NUMBER

6. AUTHOR(S)

Knisely, Andrew J.

5d. PROJECT NUMBER

5e. TASK NUMBER

5f. WORK UNIT NUMBER

7. PERFORMING ORGANIZATION NAMES(S) AND ADDRESS(S)
Air Force Institute of Technology
Graduate School of Engineering and Management (AFIT/ENG)
2950 HobsonWay, Building 640
WPAFB OH 45433-8865

8. PERFORMING ORGANIZATION REPORT NUMBER

AFIT-ENG-DS-21-M-009

9. SPONSORING/MONITORING AGENCY NAME(S) AND ADDRESS(ES)
AGENCY Air Force Research Lab, Plasma Physics Simulation Lab
ADDRESS 2241 Avionics Cir, Wright-Patterson AFB, OH, 45433 Avionics Cir, Wright-Patterson AFB, OH 45433
PHONE and EMAIL vladimir.sotnikov.1@us.af.mil
ATTN: POC Dr. Vladimir Sotnikov

10. SPONSOR/MONITOR'S ACRONYM(S)

AFRL/RYMF

11. SPONSOR/MONITOR'S REPORT NUMBER(S)

12. DISTRIBUTION/AVAILABILITY STATEMENT
DISTRUBTION STATEMENT A.APPROVED FOR PUBLIC RELEASE; DISTRIBUTION UNLIMITED.

13. SUPPLEMENTARY NOTES
This material is declared a work of the U.S. Government and is not subject to copyright protection in the United States.

14. ABSTRACT

The ionosphere has significant impact on radio frequency (RF) applications such as satellites, over-the-horizon radar, and commercial communication systems. The dynamic processes effecting the behavior of the ionic content leads to a variety of instabilities that adversely affect the quality of RF signals. In the F-layer ionosphere, flute instability persists, appearing as two radial regions of high and low density perturbations elongated along the earth's geomagnetic field lines. The sizes of flute structures are comparable to the wavelengths in the high frequency spectrum. The objective is to characterize the high frequency scattering of an incident field by developing a 3D propagation model that incorporates a phase cube coupled ray tracer approach to discretize the phase effects of a two-fluid magnetohydrodynamic (MHD) dipole flute density perturbation model. A single fluid MHD model simulates a variety of plasma flow and shear effects to alter the ideal flute's physical features, creating a subset of unique flutes. A unique phase screen approach is presented to generate stochastic flute density maps. The phase power spectrums reveal a power law relationship similar to Kolmogorov turbulence. The electric field propagation results demonstrate that specific arrangements of the flutes can cause weak to strong scattering conditions. Additional frequency domain analysis of the received field scattering functions demonstrates the existence of parabolic scintillation arcs, significant broadening in the doppler power spectrum, and narrow coherence bandwidths indicating frequency selectivity in the propagation channels that adversely impact the quality of high frequency electric fields.

15. SUBJECT TERMS
Dipole Flutes, Ionosphere, Kolmogorov, Phase Screens, Phase Cube, Propagation, Spectral

16. SECURITY CLASSIFICATION OF:			17. LIMITATION OF ABSTRACT	18. NUMBER OFPAGES	19a. NAME OF RESPONSIBLE PERSON
a. REPORT	b. ABSTRACT	c. THIS PAGE			Dr. Andrew J. Terzuoli, AFIT/ENG
U	U	U	UU	306	19b. TELEPHONE NUMBER *(Include area code)* (937) 255-6565, ext xxxx (NOT DSN) (terzuoli@afit.edu)

Standard Form 298 (Rev. 8-98)
Prescribed by ANSI Std. Z39-18